# Orbital Rashba contribution to spin-orbit torques at 3d transition metals|Al interfaces : the particular case of Co|Al

Nicolas Sebe

université PARIS-SACLAY

# Orbital Rashba contribution to spin-orbit torques at 3d transition metals|Al interfaces : the particular case of Co|Al

*Contribution Rashba orbitale aux couples de spin-orbite aux interfaces métaux de transition 3d|Al : le cas particulier de Co|Al*

**Thèse de doctorat de l'université Paris-Saclay**

École doctorale n° 564, physique en Île-de-France (PIF)
Spécialité de doctorat : Physique
Graduate School : Physique. Référent : Faculté des sciences d'Orsay

Thèse préparée au **: Laboratoire Albert Fert**, (CNRS, Thales, Université Paris-Saclay), sous la direction de **Henri-Yves JAFFRES**, directeur de recherche CNRS et la co-direction de **Vincent CROS**, directeur de recherche CNRS

**Thèse soutenue à Paris-Saclay, le 7 novembre 2025, par**

**Nicolas SEBE**

## Composition du jury

Membres du jury avec voix délibérative

| | |
|---|---|
| **Jean-Eric WEGROWE**<br>Professeur, LSI | Président |
| **Matthieu BAILLEUL**<br>Directeur de recherche CNRS, IPCMS<br>Université de Strasbourg | Rapporteur & Examinateur |
| **Jon GORCHON**<br>Chargé de recherche CNRS, Institut Jean Lamour<br>Université de Lorraine | Rapporteur & Examinateur |
| **Hélène BEA**<br>Maîtresse de conférences, SPINTEC<br>Université Grenoble Alpes | Examinatrice |

THESE DE DOCTORAT
NNT : 2025UPASP134

université PARIS-SACLAY | ÉCOLE DOCTORALE Physique en Île-de-France (PIF)

**Titre :** Contribution Rashba orbitale aux couples de spin-orbite aux interfaces métaux de transition 3d|Al : le cas particulier de Co|Al

**Mots clés :** Rashba-orbite, Couple orbital, spin-orbite

**Résumé :** Cette thèse de doctorat se concentre sur le domaine de la spinorbitronique, en particulier sur l'étude expérimentale du couple spin-orbite (SOT) pour la commutation magnétique dans les dispositifs avancés SOT-MRAM. Le mécanisme SOT est crucial car il décrit l'interaction entre un courant de spin, contrôlé par un courant de charge, et une aimantation locale qui agit comme un bit de mémoire dans le dispositif. Ce sujet est d'une grande actualité en spintronique, tant pour ses aspects fondamentaux que pour ses applications potentielles dans une nouvelle génération de dispositifs spintroniques, tels que les dispositifs logiques et les mémoires. Le SOT est associé à plusieurs mécanismes de conversion spin-charge, notamment l'effet Hall de spin (SHE) dans les métaux de transition lourds comme le platine (Pt), le tantale (Ta) et le tungstène (W), ainsi que l'effet Rashba-Edelstein (REE) aux interfaces. Ces effets influencent l'amplitude et les symétries des différentes composantes du SOT. L'objectif principal est d'utiliser le SOT pour la commutation avec une densité de courant critique typique de l'ordre de jc=$10^{11} A/m^2$ ou moins. Un des buts majeurs de cette thèse est de réduire les densités de courant critique en s'appuyant sur un fort effet Rashba orbitalaire découvert à l'interface entre le Co et l'Al. Ce programme de thèse sera principalement développé au laboratoire Albert Fert, CNRS, Thales (LAF), où divers équipements seront utilisés, tels que la pulvérisation cathodique, la micro et nano lithographie, les méthodes de second harmonique f-2f et les mesures de commutation avec l'utilisation d'un cryostat 9T.

**Title :** Orbital Rashba contribution to spin-orbit torques at 3d transition metals|Al interfaces : the particular case of Co|Al

**Keywords :** Orbital Rashba, Orbital torque, spin-orbit

**Abstract :** This doctoral thesis focuses on the field of spin-orbitronics, particularly on the experimental study of spin-orbit torque (SOT) for magnetic switching in advanced SOT-MRAM devices. The SOT mechanism is crucial as it describes the interaction between a spin current, controlled by a charge current, and a local magnetization that acts as a memory bit in the device. This topic is highly relevant in spintronics, both for its fundamental aspects and for its potential applications in a new generation of spintronic devices, such as logic devices and memories. SOT is associated with several spin-charge conversion mechanisms, notably the spin Hall effect (SHE) in heavy transition metals like platinum (Pt), tantalum (Ta), and tungsten (W), as well as the Rashba-Edelstein effect (REE) at interfaces. These effects influence the amplitude and symmetries of the different components of SOT. The main objective is to use SOT for switching with a typical critical current density on the order of jc=$10^{11} A/m^2$ or less. One of the major goals of this thesis is to reduce the critical current densities by leveraging a strong orbital Rashba effect discovered at the interface between Co and Al. This thesis program will be primarily developed at the laboratory of the Laboratoire Albert Fert, CNRS, Thales (LAF), where various equipment will be used, such as cathodic sputtering, micro and nano lithography, f-2f second harmonic methods, and switching measurements using a 9T cryostat.

# Table des matières

# 1 - Acknowledgements

Ce manuscrit présente l'aboutissement de trois belles années au sein du laboratoire Albert Fert. Avant de décrire en détail les expériences que nous avons menées, j'aimerais remercier chaleureusement l'ensemble des personnes qui ont permis le succès de ce travail de recherche.

En premier lieu, je souhaite remercier les membres du jury de cette thèse. En particulier le président Jean-Eric Wegrowe pour les riches discussions sur la physique des couples spin-orbite que nous avons eues. Je veux également adresser mes remerciements aux deux rapporteurs Matthieu Bailleul et Jon Gorchon pour avoir revu en détail ce manuscrit et pour nos échanges stimulants pendant la soutenance. De plus, je veux remercier Hélène Béa pour la rigueur de ses précieux commentaires.

Cette thèse a été permise par le financement du PEPR électronique. Je tiens donc à exprimer ma gratitude à ses deux coordinateurs : Isabelle Sagnes et Thomas Ernst. Je remercie spécialement les pilotes du projet EMCOM Manuel Bibes, Louis Hutin et Kévin Garello pour leur confiance. Grâce au PEPR, j'ai eu accès à des formation de qualités et mes travaux ont été diffusés auprès de l'ensemble de la communauté de l'électronique française. A cet égard, je veux remercier Agnès Antoine et la grande Maéva Lubin.

Je veux maintenant écrire ma reconnaissance envers les deux directeurs de cette thèse, Henri Jaffrès et Vincent Cros. C'est vous qui avez choisi ma candidature et qui m'avez transmis les outils pour réussir ce travail de recherche. Henri, je te remercie chaleureusement pour m'avoir fait découvrir la spintronique il y a cinq ans. Je te remercie pour ta disponibilité et la qualité de nos échanges. J'ai été porté pendant ces trois ans par la profondeur de ta vision de la physique et par le niveau de détail de tes modèles. Je veux souligner ta grande générosité, pourvoyeuse de nombreuses feuilles A3 mises en équation et de verres lorsque l'heure est plus tardive. Vincent, je te suis reconnaissant pour ton accueil au labo, pour l'organisation des collaborations au sein de l'équipe et pour nos discussions. Grâce à toi, nous avons conduit ce travail avec rigueur, un certain pragmatisme et je veux te remercier particulièrement pour tes conseils sur la communication de nos résultats. Merci à tous les deux.

Je remercie également spécialement Kévin Garello qui au cours de nos échanges m'a aidé à situer notre travail dans la recherche et le développement des dispositifs SOT-MRAM. De retour au laboratoire Albert Fert, je veux aussi exprimer ma gratitude envers Jean-Marie Georges et Nicolas Reyren. Nos discussions à l'angle des couloirs m'ont permis de gagner un certain recul. Je suis aussi reconnaissant envers Sophie Collin et Florian Godel pour leur aide sur les dépôts, la fabrication des échantillons et la générosité avec laquelle ils partagent leur expertise des matériaux.

I am now about to write a very meaningful paragraph for very important postdocs. This thesis would not have been as successful without Sachin Krishnia who taught me everything when I arrived at the lab. Thank you, Sachin, for showing me the techniques necessary for this study. Thank you as well for always being supportive and available for a good time. I am grateful to Sougata for our teamwork and the quality of your nanofabrication. I

also want to thank the two Brazilians of the team : Nicholas for your help with the measurements and Torrao for our cooperation and your commitment at the end of the thesis. I warmly thank Armando for giving me insights into what DFT can achieve and adding a lot to this work.

Le laboratoire Albert Fert est un endroit merveilleux où travailler. On y trouve toujours quelqu'un de disponible pour aider ou pour discuter, de physique ou pas. Des gourmandises sont toujours disponibles en salle café. Des nombreuses rencontres que j'y ai faites, je pense particulièrement à Kévin S. qui m'a tenu la main lors de mes premiers trajets bureau-café et a su élever mon niveau de course à pied. Activité que j'ai maintenu grâce à la *running team* avec laquelle nous avons arpenté le plateau de Saclay : Sarah, Meghan, William, Théophile, Santiago, Vincent H... Dans un autre domaine, ma thèse a beaucoup bénéficié d'une escapade brésilienne accompagné de Benjamin, Katia et des grands Sylvão, Frederic et Alberto. Je ne peux pas citer toutes les belles rencontres mais j'aimerais quand même dénoncer Laurette pour sa littérature, Marie-Blandine (je suis ton fan), Mohammed pour ses smashs bien sentis, Arnaud pour python, l'optique, le ML, la musique... Diana pour les SOT puis pour nos discussions sur l'après thèse, Vincent H. pour ton aide aux moments clefs, Hugo, Maxime, Gabriel, Hadi avec qui j'ai partagé les plaisirs de la rédaction, Benjamin qui a éclairé avec six mois d'avances le chemin tortueux de la thèse sur les effets orbitaux... Pour conclure ce paragraphe j'aimerais faire deux tirs groupés. Merci à l'équipe 2D pour sa chaleur, sa jovialité et sa générosité. Et je veux enfin remercier la suprateam des señor Villegas, Briatico, Trastoy, Mesoraca et Humbert pour son accueil généreux autour de quelques suprabeers. Ce fut un honneur. J'ai beaucoup apprécié votre convivialité en semaine et le weekend.

Cette thèse a vu l'émergence d'un phénomène assez particulier au rez-de-chaussée de TRT. Avec vue sur le jardin ensoleillé d'un côté et rythme effréné du couloir de l'autre, autour d'un arrangement de cinq tables en mélaminé, dont une franchement moins bien que les autres, est apparu le "M...d Office". Je dois l'avouer, cette association de malfaiteurs fut le réel pilier de la thèse. Addition rare du flegme de Hao, de la philosophie provençale de Sylvain, de la sagesse germanique de Frederic, de l'énergie et de la générosité de Satya Rama Naga Greeshmani Doddi, des aventures improbables d'Iñes et bien sûr de Malik, l'homme du XXIe siècle. Je suis immensément fier d'avoir été de ceux-là. Il ne fait aucun mystère que nous ayons survolé chaque compétition organisée au laboratoire. La physique mondiale n'a pas fini de nous entendre. Bien sûr, le M... Office s'est construit au gré de nombreuses visites. Nous étions toujours heureux de voir franchir notre porte par l'immense, le formidable, le magnifique Hadi, par le gaulois Mudit, par l'intense et profond William, par Monsieur Laxman, par l'indispensable Sarah, et par tous les autres. Je vous souhaite tout le meilleur pour la suite de vos aventures. Mon café et mon chocolat seront toujours les vôtres.

En dehors du laboratoire, certaines relations ont spécialement compté. En premier lieu bien sûr mon coloc, Gabriel. Nous avons parcouru la thèse ensemble. Nous nous sommes épaulés lors de nuits blanches et je suis encore impressionné par ta soutenance. Par

ailleurs, mon palais doit énormément à ta cuisine, espagnole, brésilienne ou fainéante, elle est toujours généreuse, savoureuse et réconfortante. Nous souhaitons aussi à Henri le meilleur pour l'après thèse. Les trois années de cette thèse ont été ponctuées de séances d'escalade, de bouffes et de vélo avec mes chers Benjamin D et Otaro. Je dois également beaucoup à un autre Benjamin, bordelais celui-ci, j'ai toujours éprouvé beaucoup de plaisir à venir vous voir avec Alice. Vos fêtes d'Halloween sont presque aussi effrayantes que l'inénarrable Elias. Voilà presque dix ans qu'il est mon repère, mon soutien, mon dulciné.

En plus de ces belles amitiés, j'ai toujours été entouré de ma famille. Merci à mes parents d'avoir toujours suivi mon parcours. Merci à mes grands-parents pour l'intérêt porté à ma thèse, j'en suis très touché. Merci à Marie-Bénédicte pour avoir suivi ma recherche et à Stéphanie d'être venue assister au bouquet final. Je continuerai à suivre de près les aventures de Clémence qui a aussi fait le beau choix de la thèse. Et j'ai hâte de voir Antoine changer d'avis…

L'apothéose de ces remerciements sera pour toi Ming Ming,

> Le revers de ton gi fait le tour de mon cœur,
> Un kumi-kata en douceur,
> Randori du temps, berceau nocturne et sûr,
> Et si je ne sais plus tout ce que j'ai vécu
> C'est que ton ippon m'a encore eu

# 2 - Introduction

## 2.1 . Non volatile spintronic memories

This thesis is financed by the *programme d'equipement prioritaire de recherche électronique* (PEPR Electronics). This public funding included in the France 2030 initiative, intends on fostering academic research related to electronics in order to increase the technology readiness levels of new technology concepts. Among all electronics applications, this thesis work belongs to the PEPR subproject focusing on applications to computing. I am especially part of the EMCOM project aiming at developing emerging magnetic random access memories.

Semiconductor industry managed to increase chips computing power at an outstanding pace since 1970 thanks to two scaling laws : the famous Moore's law and Dennard's scaling. Both those scaling laws are related to incremental improvements of the complementary metal oxide semiconductor (CMOS) technology. Moore's law states that the number of transistor on a given chip area doubles every two years. It is due to progresses both in transistor design and fabrication techniques, notably lithography. Dennard's scaling estimated that the energy consumption per unit of chip area would remain constant. The combination of those two laws enabled for a very rapid growth of the computing power per Joule.

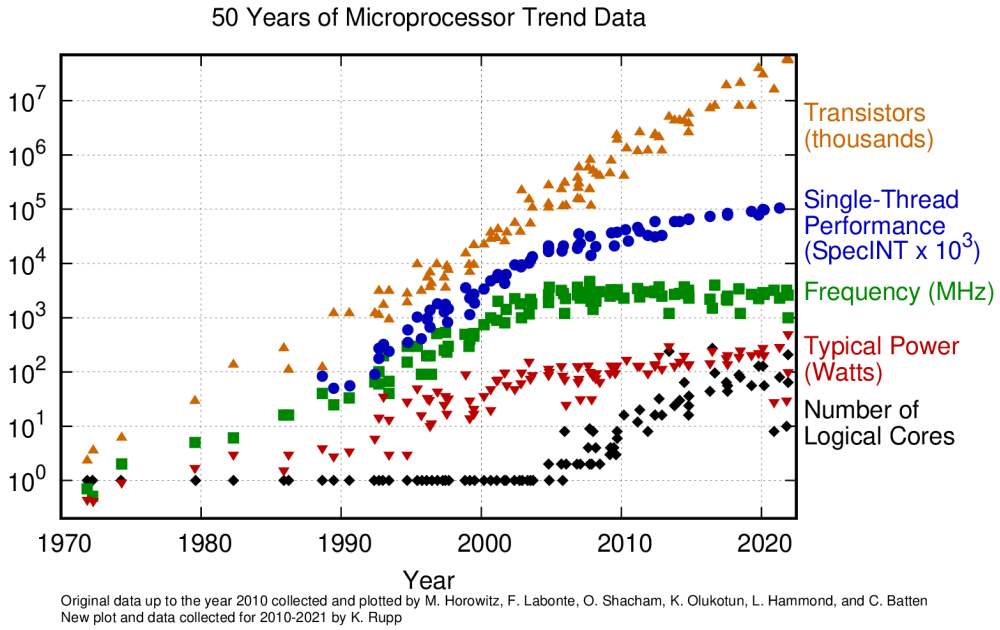


Figure 2.1 – Evolution of microprocessor specifications since 1970, from Ref. [Rupp, 2022]

However, while Moore's law still stands undenied, Dennard's scaling ceased around 2006. As illustrated figure 2.1, exponential trends in performance, frequency and typical power

for microprocessor broke around then. These inflexions are all related to arising energy management difficulties when the transistor size shrinks. Notably, transistor leakage currents and saturation voltage don't scale well. This worsens chip heating during operation and therefore prevents the acceleration of CPU clock speed.

To overcome these limitations, non volatile memory stands as a promising route. Unlike SRAM transistor so far, non volatile memories retain information even without power supply, hence eliminating static current leakages. Concept proposed for non volatile memories include resistive RAM, phase change memories and magnetic random acces memory (MRAM). Among those different ideas, MRAM standouts in terms of endurance. Indeed, information in MRAM is stored in a magnetization orientation rather than material parameters (oxidation or crystalline phase). Hence, writing and reading cycles do not involve atomic motion.

## 2.2 . From GMR to MRAM technology

At the origins of MRAM lies the pionneer effect in spintronics, namely the giant magnetoresistance (GMR) effect. Discovered in 1988 simultaneously by Albert Fert and Peter Grünberg teams, GMR is a property of thin films multilayers alternating ferromagnet and normal metals. Such films exhibit a drastically different resistance when the ferromagnetic layers have their magnetizations parallel compared to antiparallel [Baibich et al., 1988, Binasch et al., 1989]. Hence, GMR allows to probe electrically the magnetization orientation of a magnetic layer. It was thus integrated only a decade after its discovery, into hard disk drives reading heads [Dieny et al., 1993]. The magnetoresistance is usually quantified through the MR ratio defined as :

$$MR = \frac{R(\uparrow\downarrow) - R(\uparrow\uparrow)}{R(\uparrow\downarrow)}$$

GMR magnetoresistance ratio typically can reached up to 100 % at room temperature in multilayers [Chappert et al., 2007]. This discovery was followed by an even larger magnetoresistance : the tunneling magnetoresistance (TMR). TMR arises in magnetic tunnel junctions (MTJ) made of two ferromagnetic layers separated by an insulating layer. Spin filtering of the electronic wave functions at a crystalline MgO tunnel barrier allows for much larger magnetoresistance ratios than GMR [Zhang and Butler, 2004]. This effect was first measured in 1974 [Julliere, 1975]. TMR ratios were measured as large as 600 % at 300 K [Ikeda et al., 2008].

MTJs displaying such large TMR ratio became at the heart of a new technology proposal in spintronics : MRAM. In MRAM, the MTJ does not act as a read head of a hard disk drive but rather constitutes the information bit itself. MTJs indeed have two stable states and TMR makes reading the MTJ state relatively easy. In an industrial MRAM MTJ, the magnetization of one of the ferromagnetic layers is pinned via a synthetic antiferromagnet so that its magnetization is fixed : it is the reference layer. The other layer, referred to as free

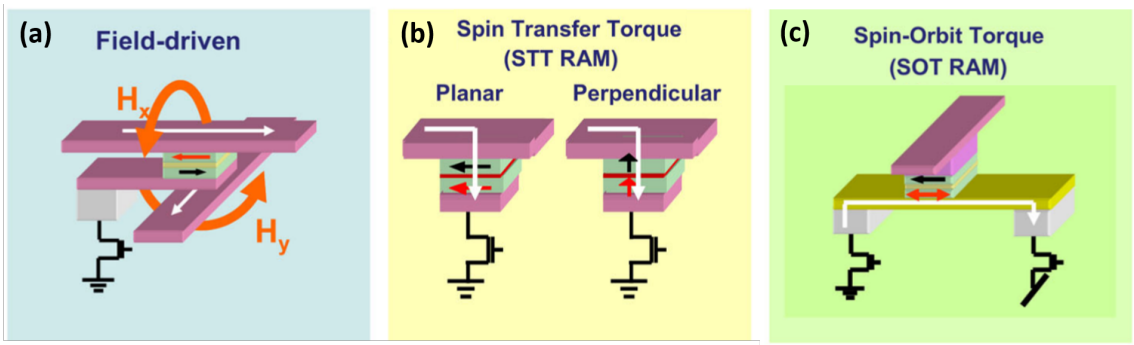


Figure 2.2 – The three MRAM concepts discussed in the text : **a**) field MRAM **b**) STT-MRAM and **c**) SOT-MRAM. *Adapted from Ref. [Dieny and Chshiev, 2017]*

layer, defines the state of the MTJ through its orientation that can be either parallel or antiparallel to the reference. MTJ are the common element to the three MRAM principles depicted in figure 2.2.

Another important MRAM challenge is the writing operation. Physically, this consists in switching the MTJ free layer magnetization from parallel to antiparallel and vice versa. Several routes have been proposed and experimented [Bhatti et al., 2017]. The first was the field MRAM. In this view, the free layer magnetization is manipulated by a magnetic field induced via an electrical current flown through a dedicated wire in the chip (figure 2.2 **a**). This design however is limited in terms of achievable memory density. If the MTJs are too close to each other, it is no longer possible to address them separately.

The next MRAM generation introduced the effect of spin transfer torque for the writing operation of the MTJ bit, as schematized in figure 2.2 **b**). This design benefits from a simple two-terminal architecture, where electrical contacts at both ends of the magnetic tunnel junction (MTJ) enable both reading and writing through a tunneling current in a current-perpendicular-to-plane configuration. While readout relies on the tunneling magnetoresistance (TMR) effect, writing is governed by STT. This torque arises when a current passes through the MTJ stack, exerting a force on the free layer's magnetization. When electrons flow from the reference layer to the free layer, the torque favors alignment into the parallel state ; reversing the current instead promotes the antiparallel configuration.

STT-MRAM were first commercialized by Everspin technology in 2018. Despite being currently deployed for targeted applications, this technique still has two main drawbacks preventing mass adoption. First, STT is zero when the magnetization of the two layers are perfectly aligned. This gives a upper bound to the writing speed : the incubation time. It is typically of a few ns [Devolder et al., 2008]. Second, STT writing mechanism involves flowing substantial electrical current through the MTJ insulating barrier. As a result, breakdown probability increases and device endurance shortens.

The next MRAM design generation overcomes those two challenges. Spin orbit torque

(SOT) MRAM possess three terminals (figure 2.2 **c**). It still consists in a MTJ whose state is read through TMR, but writing operation differs from STT. In SOT, the free layer magnetization switches due to torques arising when a current is flown in an adjacent so-called SOT layer. In this design, no electrical current flows through the tunnel barrier for writing and no incubation time is required. As a consequence, SOT-MRAM is promising for increasing both MRAM writing speed and endurance.

A key challenge in SOT-MRAM operation is the need for an external in-plane magnetic field to achieve deterministic magnetization switching in perpendicularly magnetized MTJs. This requirement, absent in STT-MRAM devices, stems from the symmetry of the torque generated by in-plane pure spin currents (from spin Hall effects). To overcome this limitation and enable field-free switching, several strategies have been proposed [Krizakova et al., 2022].

Moreover, in the aim of reducing the electrical current required for switching, which physical effect is the most efficient is still an open debate. Notably, Orbital Hall Effect (OHE) and the Orbital Rashba Edelstein Effect (OREE) have been considered as two possible promising mechanisms to enhance torques, without the need to use rare and expensive heavy metals. Theoretical investigations suggested first that the orbital degree of freedom can be large in the 3*d*, 4*d*, and 5*d* transition metal series, which was corroborated by experiments lead on MTJs in a series of recent works [Gupta et al., 2025, Yao et al., 2025].

The EMCOM project, part of the PEPR Electronics initiative, is dedicated to advancing the development of SOT-MRAM technologies. While several alternative approaches—such as optical switching, voltage control of magnetic anisotropy, and thermally induced switching—are under exploration, this thesis focuses specifically on the optimization and characterization of spin–orbit torque (SOT). As discussed in Section 3, SOT generally emerges in systems with strong spin–orbit coupling. However, recent hypotheses suggest that orbital effects could enable even greater SOT in systems composed of light metals. The objective of this PhD work is to investigate how a specific orbital Rashba effect, observed at the Co/Al interface, contributes to SOT enhancement and to assess its potential integration into industrial device architectures.

## 2.3 . Outline of this thesis

In this manuscript, we first provide chapter 3 an overview of the different physical concepts driven by spin-orbit coupling that are key to SOT-MRAM and the experimental study of SOT. We notably describe different magnetoresistances, the emergence of magnetic anisotropy and the SOT response to an applied electric field. Chapter 4, we focus on the orbital Rashba Edeslstein effect, both proposing a toy model and reviewing a few experiments. Next, we explain chapter 5 the protocols we used to measure SOT experimentally throughout our investigation.

Relying on these methods, we delve into the characterization of Co|Al interface chapter 6.

We demonstrate thanks to experiments combined with a semiclassical transport model the occurrence of large interfacial SOT in this system. Chapter 7, we present two *ab initio* investigations that were lead on this system and forecast a large orbital Rashba Edelstein effect in the interfacial band structure between Co and Al. Those two chapters constitute a demonstration with theoretical and experimental arguments that orbital Rashba Edelsrein effect leads to large SOT at Co|Al interface.

We then try to experimentally disturb this system so as to investigate its robustness on material parameters. We present chapter 8 an experimental campaign where SOT is enhanced in Co|Al via ultrathin Pt addition between the two layers. We measure that it is detrimental to SOT and perpendicular magnetic anisotropy. However, in chapter 9, we modify the ferromagnetic layer by engineering it with CoFeB alloy and we show non zero interfacial torques as well as substantial perpendicular magnetic anisotropy. In a last experimental chapter, we perorm magnetization switching experiments in our multilayers and demonstrate that Co|Al orbital torques improve magnetization switching energy efficiency. We sum up our conclusions chapter 11 and expose a few perspectives to this study.

# 3 - Basic principles

In this section, we present the main physical concepts in spintronics and orbitronics which are mandatory to understand the key features of magnetic torques, the central topic of this thesis. We consider various concepts spanning from the spin-orbit interactions to Rashba effects involving either spin or orbital momentum locking as well as spin-orbit torques.

## 3.1 . Spin-orbit coupling (SOC)

### 3.1.1 . Spin and orbital degrees of freedom in condensed matter

Spin and orbital angular momentum are two main electronic degrees of freedom that appear in the quantum mechanics framework. They are quantified with their respective quantum numbers :

$$S = m_s\hbar,\, m_s \in \left\{-\frac{1}{2}, \frac{1}{2}\right\} \quad \text{and} \quad L = m_l\hbar,\, m_l \in \{-l, \ldots, 0, \ldots l\}$$

Both electronic spin and orbital angular momentum lead to respective magnetic moments :

$$\mu_S = -g_s\mu_B S \quad \text{and} \quad \mu_L = -g_L\mu_B L$$

where $\mu_B$ is Bohr magneton. In vacuum or in systems with low spin-orbit coupling, $g_s \simeq 2$ while $g_L = 1$. This is a correct approximation to the case of light metals or 3*d* transition metals investigated in this thesis.

In a crystalline lattice, a combination of the Pauli exclusion principle and Coulomb interactions leads to the emergence of the Heisenberg exchange interaction between neighbouring atoms electrons. Depending on its sign, it makes alignment of outer shells electrons spin energetically favorable, either in the same direction (ferromagnetic case) or in the opposite directions (antiferromagnetic material). In a ferromagnetic material, the sign of this interaction is such that, under a transition temperature called Curie temperature, it tends to align spins in a single direction, the majority spins direction.

The energy difference between majority and minority spin electrons leads to a spin-split band structure, resulting in different transport properties for each spin channel. Especially, majority and minority electrons possess different conductivities : $\sigma_\uparrow \neq \sigma_\downarrow$ owing to the difference in their density of states at the Fermi level. As a consequence, when a current flows through a ferromagnet, it is spin polarized. The spin current can be written : $J = J_\uparrow - J_\downarrow = (\sigma_\uparrow - \sigma_\downarrow)\,\mathbf{E}$ with $\mathbf{E}$ the electric field equal for the two spin directions.

### 3.1.2 . Spin-orbit coupling in a crystal

A key interaction for the description of spin dependent properties of electrons in metal is their interaction with the crystal orbitals : the spin-orbit coupling (SOC). This interaction emerges through the Lorentz transformation of the orbital electric field into an effective

magnetic field in the electron frame.

$$\mathbf{B}_{SOC} = -\frac{\mathbf{v} \times \mathbf{E}}{c^2}$$

The electron spin and this effective magnetic field interact in the Hamiltonian as :

$$\hat{\mathcal{H}}_{SOC} = -\hat{\mu}_S \cdot \mathbf{B}_{SOC}$$

Noting that the electric field derives from the potential ($V(\mathbf{r})$) : $\mathbf{E} = -\nabla V$ and the velocity writes $\mathbf{v} = \mathbf{p}/m$, we can derive :

$$\hat{\mathcal{H}}_{SOC} = -\hat{\mu}_S \cdot \mathbf{B}_{SOC} = -g_S \left( \frac{e\hbar}{2m^2c^2} \right) \hat{\mathbf{S}} \cdot (\mathbf{p} \times \nabla V)$$

Since the crystalline potential emerges from atomic orbitals, a realistic assumption is to treat the potential $V(\mathbf{r}) = V(r)$ as radial. This leads to considering $\nabla V = |\nabla V| \mathbf{e_r}$. This assumption allows to let the orbital angular momentum operator appear in $H_{SOC}$ :

$$\hat{\mathcal{H}}_{SOC} = \eta_{SOC}\, \mathbf{L} \cdot \mathbf{S} \quad \text{with} \quad \eta_{SOC} = -g_S \frac{e\hbar}{2m^2c^2} \left\langle \frac{\nabla \mathbf{V}(\mathbf{r})}{r} \right\rangle \tag{3.1}$$

SOC lifts the spin degeneracy in the band structure similarly to a Zeeman term induced by the orbit field. In the hydrogen atom case, the factor $\eta_{SOC}$ can be shown to be proportional to $Z^4$, $Z$ being the atomic number. However, in crystals, calculations accounting for screening by inner shells electrons lead to a $Z^2$ dependence [Landau and Lifchits, 1958, Heide et al., 2009]. SOC is therefore expected to be the especially strong in heavy metals corresponding to large Z.

### 3.1.3 . Magnetic anisotropy

In general, magnetic properties depend on the orientation of the magnetization. Notably, all magnetization orientations are not equivalent energy-wise. One axis has usually a minimal energy : the easy axis. This magnetic anisotropy arise from different sources. We discuss mostly three : the shape anisotropy, common to all magnetic samples in a non spherical shape and particularly relevant in thin films, the magneto-crystalline anisotropy, which is SOC dependent together with the surface anisotropy term.

#### Shape anisotropy

Maxwell equations impose that $\mathrm{div}\,(\mathbf{B}_{total}) = 0$. However, noting $\hat{\mathbf{m}}$ the magnetization vector, at the surface of a magnetic sample, $\mathrm{div}\,(\hat{\mathbf{m}}) = -\hat{\mathbf{n}} \cdot \hat{\mathbf{m}}$. Except for the magnetization to be always orthogonal to the surface normal $\hat{\mathbf{n}}$, this is non zero. It is allowed since the vector that has to respect Maxwell equations is the sum of the magnetization and the magnetic field $\mathbf{m} + \mathbf{H}$. As a result, a magnetization component orthogonal to the sample

surface comes with a magnetic field which is opposed to it. It is thus denoted $\mathbf{H_D}$, the demagnetizing field. A solution to minimize the induced energy is the apparition of magnetic domains. The sample magnetization has a different orientation in each domain, notably to avoid components orthogonal to the surfaces.

However, microscopically, the demagnetizing field is a consequence of the two magnetic dipoles interaction (Biot and Savart law). At short scales, it is negligible against the exchange energy, or exchange stiffness $A$. Thus, under a distance of the order of $\sqrt{A/\left(2\pi M_s^2\right)}$, the magnetization is uniform despite demagnetizing field. Especially, in thin films, magnetic domain may arise within the plane but not across the thickness.

For a monodomain magnetic sample, the demagnetizing field is related to the magnetization through the $3 \times 3$ demagnetizing tensor : $\mathbf{H_D} = -\left[N_D\right]\mathbf{m}$. The resulting term in the energy writes $E_D = -\frac{1}{2}\mathbf{m}\left[N_D\right]\mathbf{m}$.

The case of a magnetic thin film can be approximated to an infinite magnetic plane. It can be demonstrated that in that case, $H_D = -m_z$. The shape anisotropy energy for a magnetic thin film is thus :

$$E_D = \frac{1}{2}\mu_0 m_z^2 = \frac{1}{2}\mu_0 M_s^2 \cos^2\theta \tag{3.2}$$

with $\theta$, the polar angle that $\hat{\mathbf{m}}$ forms with the film plane normal direction.

### Bulk magnetocrystalline anisotropy

The magnetocrystalline anisotropy, generally quantified by a certain volume energy $K$ is a consequence of SOC in a perfect crystal. Since this interaction couples the spins to the electronic wave functions, it induces a coupling between the magnetic order and the crystalline lattice [Coey, 2010]. For instance, in a cubic crystal, [100], [010] and [001] are equivalent. Hence, the magnetocrystalline energy has to be symmetric in the magnetization components $m_x$, $m_y$ and $m_z$ in the crystal. Since a cubic crystal also respects inversion symmetry, energy must be even in each $m_i$. The possible terms to sixth order are :

$$E_{MC} = K_0\left(m_x^2 + m_y^2 + m_z^2\right) + K_1\left(m_x^2 m_y^2 + m_y^2 m_z^2 + m_x^2 m_z^2\right) + K_2\left(m_x^2 m_y^2 m_z^2\right)$$

with $K_1$ the anisotropy constant calculated at the order 4 of the perturbation and $K_2$ corresponding to the order 6, generally much smaller.

Nevertheless, in the case of sputtered samples, due to the reduced symmetry of the structure (in general of a polycrystalline quality), we have only to consider the unidirectional anisotropy introduces surfaces and interfaces, that we call surface anisotropy terms.

### Surface anisotropy

The magnetocrystalline anisotropy is not of relevance in this thesis because our samples mostly are polycrystalline since they are grown by sputtering. Another origin of magnetocrystalline anisotropy is the bond distribution in metallic alloys or in thin multilayers, as extensively explored in this thesis samples. This interfacial bonds give rise to the surface anisotropy [Néel, 1954].

The symmetry breaking at an interface induces a different anisotropy for the atoms in the layer concomitant to the interface due to band hybridization or lattice mismatch. The main symmetry axis of an interface being the normal axis, the equivalent volume energy due to surface anisotropy writes :

$$E_s = \frac{K_s}{t_{FM}} \sin^2 \theta \tag{3.3}$$

where $t_F$ is the ferromagnetic layer thickness. Surface anisotropy is especially large at the interfaces of transition metals thin films and heavy metals due to the enhanced SOC of the latter [Givord et al., 1996]. Large surface anisotropy also arises at the interface between transition $3d$ ferromagnetic metals and light metals oxides, which will be more extensively detailed in section 6.1.2.

### Effective anisotropy field

The sum of surface anisotropy, shape anisotropy and a magnetocrystalline term experimented by a magnetic thin film yields the total energy :

$$E = \left( \frac{K_\mathcal{V}}{M_s} + \frac{K_s}{M_s t_F} - \frac{1}{2}\mu_0 M_s \right) M_s \sin^2 \theta \tag{3.4}$$

From this equation, we define an effective anisotropy field $H_k^{eff}$ (in Si units ) :

$$H_k^{eff} = \left( \frac{2K_\mathcal{V}}{\mu_0 M_s} - M_s \right) + \frac{2K_s}{\mu_0 M_s t} \tag{3.5}$$

If this effective field is positive, the sample possesses a perpendicular magnetic anisotropy (PMA). The minimization of equation 3.4 yields $\theta = 0 \text{ or } \pi$. The magnetization points favorably along the direction perpendicular to the plane. If a magnetic field $H_{app}$ is applied in the sample plane, the magnetization will saturate parallel to the latter for $H_{app} > H_k^{eff}$.

Conversely, a magnetic sample such that $H_k^{eff} < 0$ possesses an in-plane magnetization. Without external field, energy minimization brings the magnetization in the sample plane. It will saturate parallel to an external field orthogonal to this plane for $H_{app} > |H_k^{eff}|$.

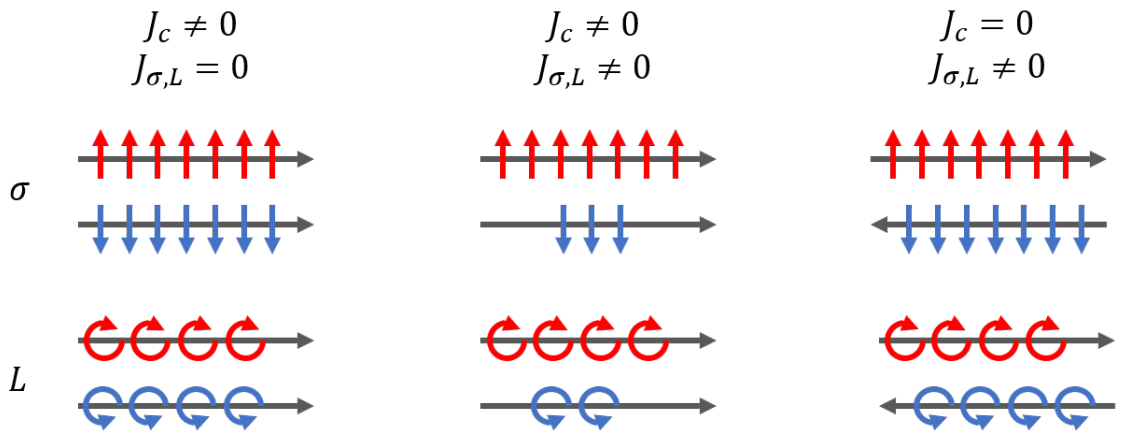


Figure 3.1 – Representation of the three different cases discussed in section 3.1.4. It shows how charge currents on one hand and spin or orbital angular momentum currents on the other hand are either null or finite. In particular, a pure spin, or orbital, current with zero charge current is achievable.

### 3.1.4 . Charge and angular momentum flows in solids

In electronics, information is mostly conveyed by flows of electronic charges. In a quantum framework such electronic currents are described by the anti-commutator :

$$\hat{\mathcal{J}}_i = \frac{\left\{q\hat{I}, \hat{v}_i\right\}}{2}$$

with $\left\{\hat{A}, \hat{B}\right\} = \hat{A}\hat{B} + \hat{B}\hat{A}$ is the anti-commutator of the respective $\hat{A}$ and $\hat{B}$ operators ($\hat{I}$ and $\hat{v}_i$ are the respective identity and velocity (along the $i$ axis) operators).

In spintronics, information is conveyed by the other degrees of freedom of electrons : mostly the spin $\sigma$, and, recently, the orbital angular momentum $\mathbf{L}$. Spin and orbital currents operators can be defined similarly to the charge current, giving the following tensors :

$$\hat{j}_\sigma = \frac{\{\hat{\sigma}, \hat{v}\}}{2} \quad \text{and} \quad \hat{j}_L = \frac{\left\{\hat{L}, \hat{v}\right\}}{2}$$

where $\hat{j}_\sigma$ is the spin-current, $\hat{j}_\sigma$ is the orbital-current, and $\hat{v}$ is the velocity operators. Spin current can also be defined relatively to a quantization axis. We also define $\mathcal{J}_\sigma = \mathcal{J}_\uparrow - \mathcal{J}_\downarrow$ while $\mathcal{J} = \mathcal{J}_\uparrow + \mathcal{J}_\downarrow$ the (mean or expectation values of the) spin-current and total current densities. From this picture, we understand three distinct situations as represented in figure 3.1. Further on, we will note the same quantities without the 'hat' symbol as the quantum average (or classical) values of the corresponding operators.

Firstly, if the flows of $\uparrow$ and $\downarrow$ electrons are equal, as when an electric field is applied to a normal metal, there is a finite charge current but no spin current. That is a standard charge current. Secondly, let's consider a ferromagnetic metal. The population of majority

spins $\uparrow$ and of minority spins $\downarrow$ are different. As a consequence, when an electric field is applied, $\mathcal{J}_\uparrow$ and $\mathcal{J}_\downarrow$ are finite but different. In this case both charge and spin currents arise. Both flow toward the same direction. This case is designated as polarized current. Thirdly, we will encounter situations were $\mathcal{J}_\uparrow = -\mathcal{J}_\downarrow$. This is the pure spin current case. Overall charge current is zero but a finite spin current occurs. It is still debated to what extent the same three cases may be defined replacing the electrons spin by their orbital angular momentum [Valet et al., 2025].

## 3.2 . Magnetoresistances of single ferromagnetic film

It is well known that the resistance of a thin film is dependent on the amplitude and orientation of an external applied magnetic field. The effects involved in this conductance variations are several amongst which : the Hall effect (HE), Lorentz magnetoresistance, anisotropy of magnetoresistance (AMR) and planar Hall effect (PHE), magnetic accumulation effects. Moreover, the terms that arise in the conductivity of a magnetic sample are expected to respect the symmetries defined in the equation derived in [Goldberg and Davis, 1954] :

$$\mathbf{j} = \sigma_0\mathbf{E} + \alpha\mathbf{E}\times\mathbf{H} + \beta\mathbf{E}|\mathbf{H}|^2 + \gamma\mathbf{H}(\mathbf{E}\cdot\mathbf{H}) + \delta M\mathbf{E}$$

where $\sigma_0$, $\alpha$, $\beta$, $\gamma$ and $\delta$ represent here the respective coefficients for the bare conductivity, AHE, Lorentz MR, AMR (or PHE) and accumulation effects.

In the case of a magnetic film, in the presence of a magnetization, a same kind of expression is valid (hereafter called anomalous effects) when the external field is formally replaced by the magnetization vector giving then rise to the so-called anomalous Hall effects (AHE) $\alpha_{AHE}\mathbf{E}\times\mathbf{M}$ to give :

$$\mathbf{j} = \sigma_0\mathbf{E} + \alpha_{AHE}\mathbf{E}\times\mathbf{M} + \tilde{\beta}\mathbf{E}|\mathbf{M}|^2 + \tilde{\gamma}\mathbf{M}(\mathbf{E}\cdot\mathbf{M}) + \tilde{\delta}M\mathbf{E}$$

after having introduced corresponding coefficients.

It turns out that the overall conductivity of a magnetic thin film is thus anisotropic. Assuming the magnetization lying along $\hat{z}$, it can be written as a $3\times3$ matrix as following :

$$\sigma = \begin{pmatrix} \sigma_{xx} & \sigma_{xy} & \sigma_{xz} \\ \sigma_{yx} & \sigma_{yy} & \sigma_{yz} \\ \sigma_{zx} & \sigma_{zy} & \sigma_{zz} \end{pmatrix}$$

where $\sigma_{xx} = \sigma_{yy} \neq \sigma_{zz}$ and the off diagonal are antisymmetric : if $i \neq j$, $\sigma_{ij} = -\sigma_{ji}$.

### 3.2.1 . Anisotropic magnetoresistance and planar Hall effect

Anisotropic magnetoresistance (AMR) and planar Hall effect (PHE) are a first consequence of SOC in a single ferromagnetic material. AMR is measured experimentally as a difference

between the longitudinal resistivity of a ferromagnet when the current is applied either parallel to the magnetization ($\rho_{\parallel}$) or transverse ($\rho_{\perp}$) to it. The AMR ratio is usually defined as :

$$\frac{\Delta\rho}{\rho} = \frac{\rho_{\parallel} - \rho_{\perp}}{\rho_{\perp}}$$

It is generally positive, meaning that the transverse case is more conductive than the parallel configuration [Fert and Campbell, 1971]. To model the conductivity of a ferromagnet, scattering is assumed to be mostly due to conductive the $4s$ bands scattering with localized $4p$ and $3d$ bands in $3d$ materials. Since majority and minority spins present different band structure at the Fermi level, this scattering induces different resistances : $\rho_{\uparrow}$ and $\rho_{\downarrow}$. A spin mixing resistance has to be added to represent scattering events affecting the spin orientation. In this two current framework, the resistivity of a ferromagnet writes [Campbell et al., 1967, Fert and Campbell, 1968] :

$$\rho = \frac{\rho_{\uparrow}\rho_{\downarrow} + \rho_{\uparrow\downarrow}\left(\rho_{\uparrow} + \rho_{\downarrow}\right)}{\rho_{\uparrow} + \rho_{\downarrow} + 4\rho_{\uparrow\downarrow}}$$

with $\rho_{\uparrow,\downarrow}$ the respective majority and minority spin resistance channels. The resistivity anisotropy is not apparent in this expression. It comes from spin orbit coupling induced mixing of spin polarized and orbital polarized wavefunctions. In [Campbell et al., 1967], the authors present a simplified model predicting AMR. They introduce the spin-orbit coupling and show through perturbation theory that it causes scattering events mixing $d_{\uparrow}$ and $d_{\downarrow}$ orbitals. Since the spin-orbit coupling in equation 3.1 is the product of those orbitals angular momentum (influenced by the applied electric field $\mathcal{E}$) and electrons spins (quantified along magnetization direction), this scattering term is anisotropic. This lead the authors to :

$$\frac{\Delta\rho}{\rho} = \frac{\gamma\left(\rho_{\downarrow} - \rho_{\uparrow}\right)\rho_{\downarrow}}{\rho_{\uparrow\downarrow} + \rho_{\uparrow\downarrow}\left(\rho_{\uparrow} - \rho_{\downarrow}\right)}$$

where $\gamma$ is the square of the ratio of SOC and the Heisenberg exchange. [Kokado et al., 2012] presents a more refined two conduction model where $s-s$ scattering is included as well as spin dependence of the electrons effective mass to derive the AMR ratio.

This first consequence of SOC on electronic transport in ferromagnet also affects the transverse resistance through the planar Hall effect (PHE). For the magnetization aligned to $\hat{x}$, AMR can be described by the conductivity tensor :

$$\sigma_0 = \begin{pmatrix} \sigma_{xx} & 0 \\ 0 & \sigma_{yy} \end{pmatrix}$$

Rotating the magnetization in the plane by a certain azimuthal angle $\varphi$ changes the conductivity tensor as $\sigma(\varphi) = R_{\varphi}^{-1}\sigma_0 R_{\varphi}$ with $R_{\varphi}$ the rotation matrix. As a consequence,

$$\sigma(\varphi) = \begin{pmatrix} \sigma_{xx}\cos^2\varphi + \sigma_{yy}\sin^2\varphi & \frac{1}{2}\left(\sigma_{xx} - \sigma_{yy}\right)\sin 2\varphi \\ \frac{1}{2}\left(\sigma_{xx} - \sigma_{yy}\right)\sin 2\varphi & \sigma_{xx}\sin^2\varphi + \sigma_{yy}\cos^2\varphi \end{pmatrix}$$

This tensor makes clearly apparent the existence of a transverse resistance $R_{xy} = R_{PHE} \sin 2\varphi$.

### 3.2.2 . Anomalous Hall effect (AHE)

The anomalous Hall effect (AHE) arises in ferromagnetic samples. It is analogous to the classical Hall effect which predicts that when an electric field is applied on a metallic sample inside a magnetic field, a voltage arises transversely to both fields. In the anomalous Hall effect, instead of an external magnetic field, the transverse voltage is proportional to the magnetization component orthogonal to the current according to :

$$R_{xy}^{(z)} = R_{AHE} \ (\hat{\mathbf{e}}_m \times \mathbf{E}) \cdot \hat{y}$$

for $\mathbf{E} = E_x$ with $\mathbf{e_m}$ the magnetization unit vector, indicating here a specific choice of the spin quantization along the $\hat{z}$ direction normal to the plane.

Yet, the amplitude of $R_{AHE}$ of ferromagnetic metals is generally much larger than the transverse resistance expected from the classical Hall effect. The actual underlying mechanisms to AHE are still debated but two types of effects have been identified, either intrinsic or extrinsic. The intrinsic origin of AHE was first suggested by Karplus and Luttinger in 1954 [Karplus and Luttinger, 1954]. They explain AHE solely by the electronic band structure. They show that from the Berry curvature, when an electric field is applied, electrons acquire a momentum component transverse to both the electric field and the magnetization. This theory is designated as intrinsic because it emerges from the perfect crystal Hamiltonian and does not involve any impurity scattering.

However, in 1955, Smit reported that AHE vanishes at low temperatures [Smit, 1955, Smit, 1958]. From this experimental assessment, he concluded that intrinsic effects alone do not give the full AHE picture. He thus noted that in the presence of SOC, scattering events become anisotropic, inducing a transverse voltage. He proposed two mechanisms : through skew-scattering, an electron gets a transverse momentum proportional to $\mathbf{E} \times \mathbf{S}$ when scattered. Since in a ferromagnet there is an imbalance between $\mathbf{S} = 1/2$ and $\mathbf{S} = -1/2$ spin population, this generates a finite transverse current giving a transverse conductivity $\sigma_{xy}$.

Another mechanism exits, the side-jump scattering. During such scattering events, electrons experience a small lateral displacement whose direction is determined by their spin orientation. At the macroscopic scale in a ferromagnet, this mechanism also results also in a transverse voltage with a same signature than the intrinsic mechanism (independent of the impurity scattering rate).

Besides being a powerful tool to electrically probe a ferromagnetic sample's magnetization orientation, AHE conveys information on the sample's material properties itself. For instance, it can be used to detect a finite magnetization arising in a metallic layers deposited on a ferromagnetic layer through magnetic proximity effect [Dang et al., 2020].

In the next section, we turn to the description of the charge-to-spin conversion effects which are at the heart of the spin-orbit torque phenomena.

## 3.3 . Charge to spin conversion : the spin Hall effect

The spin Hall effect (SHE) results in a transverse flow of electrons spins in a metallic sample in response to an applied electric field. It arises from the bulk conducting states. SHE allows to electrically create a spin flux which is of interest for many spintronics applications. Notably, it can be used to inject a spin current in a neighbouring metallic layer.

Analog to AHE, SHE is due to the perturbation introduced by the SOC of the electronic band structure itself (intrinsic) as well as/or the change of the electronic scattering introduced by the SOC (extrinsic). It is hence especially large in metallic materials with large SOC such as heavy metals Pt, W and Ta. However, contrarily to AHE, SHE arises in metals without the occurrence of any electron spin-polarization in the longitudinal current and thus does not lead to any transverse charge current.

To distinguish extrinsic and intrinsic contributions, SHE, it can be quantified with two parameters : an extrinsic skew-scattering angle $\alpha_{SS}$ (generally called spin-angle angle) plus a contribution arising from an intrinsic SHE conductivity $\sigma_{SHC}^{int}$ to give the general formula [Sagasta et al., 2016] :

$$-\rho_{SH} = \alpha_{SS}\rho_{xx} + \sigma_{SHC}^{int}\rho_{xx}^2$$

Note that the SHC terms also may include the extrinsic side-jump component because the latter is known to be independent on the electronic scattering time. Confounding extrinsic and intrinsic contributions, SHE in a given material is often quantified through an effective spin Hall angle $\theta_{SHE}^{*}$ which relates the charge current density (along a longitudinal direction) to the induced transverse (pure) spin-current :

$$\mathcal{J}_s = \theta_{SHE}^{*}\mathcal{J}_c$$

$\mathcal{J}_s$ is expressed in charge units so that $\theta_{SHE}^{*} = \left(\alpha_{SS} + \sigma_{SHC}^{int}\rho_{xx}\right)$ is dimensionless. In heavy metals, reported $\theta_{SHE}$ are typically of the order of 1 to 20 %, with significant variations between the different studies [Sinova et al., 2015].

Systems exhibiting SHE are also host to the inverse SHE (ISHE). It consists in the conversion of an injected pure spin current into a transverse charge current $\mathcal{J}_c = \theta_{ISHE}\mathcal{J}_s$ (or vice versa for the SHE whereby $J_s$ and $J_c$ interchange in the latter expression). Note however that the out-of-equilibrium injection of a spin-current into such metal from a neighboring ferromagnet may induce a transverse charge current by current proximity effect. This will be more largely emphasized further on in the section 6.4.2.

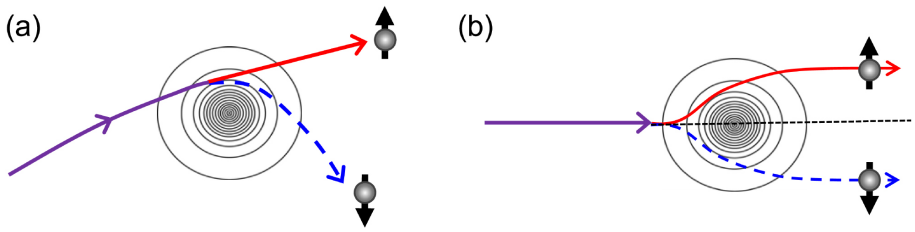


Figure 3.2 – Representation of **a)** skew scattering and **b)** side jump mechanism on a potential center. From [Niimi and Otani, 2015].

### 3.3.1 . Intrinsic origin of SHE

As for the AHE, the intrinsic mechanism derives from a perfect crystal Hamiltonian in the presence of SOC. With these ingredients, it is especially large in systems where SOC induces a spin-dependent band splitting such that the Fermi level lies in between the resulting bands.

This mechanism is similar to Karplus and Luttinger model for AHE and its relation to band structure topology through the Berry connection and the Berry phase was established by [Jungwirth et al., 2002]. The model was extended to non magnetic SHE systems by [Murakami et al., 2003, Sinova et al., 2004].

Through Kubo formalism, the spin Hall effect amplitude can be evaluated for a variety of materials. Especially, it has been reported that it is the dominant contribution in heavy metal Pt [Guo et al., 2008]. Moreover, first principles calculations of the intrinsic SHE in $4d$ and $5d$ transition metals predict opposite signs for Pt on one hand and W or Ta on the other hand.

### 3.3.2 . Extrinsic origin of SHE

The extrinsic processes for SHE are the different types of scattering events which yield anisotropic outcomes under SOC. They are described via two families : skew scattering and side jump scattering.

#### Skew scattering

Skew scattering occurs when the outcome of an electron scattering event is biased toward one direction transverse to the incident flow, according to its spin orientation. It is sketched figure 3.2 **a)**. This anisotropic scattering can be obtained by including SOC in a disorder potential [Sinova et al., 2015]. This scattering leads electrons of opposite spin orientation to acquire opposite transverse velocities. Through skew scattering, a transverse spin current thus arises.

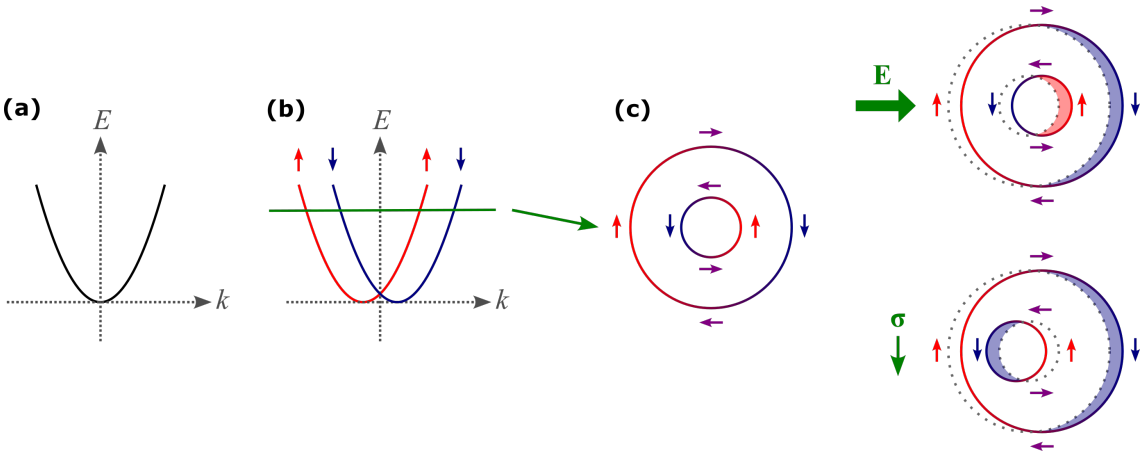


Figure 3.3 – **a**) Parabolic dispersion. **b**) Lift of degeneracy due to Rashba spin-orbit Hamiltonian term. **c**) Projection of the two different helical Rashba states onto the Fermi surface and response of the projected spin or orbital polarization to an applied electric field or a spin injection.

### Side-jump scattering

Sketched figure 3.2 **b)**, side jump scattering is a different type of process. SOC and disorder also lead to an anisotropic outcome. But during side jump, the out coming electronic momentum is parallel to the incident wave vector. Still, the real space wave function is shifted transversely to the electronic flow. For opposite spins, the shift is opposite.

Averaged over conducting electrons, this mechanism results in a transverse spin current when an electric field is applied.

#### 3.3.3 . Experimental measurements of SHE

The first experimental evidence of SHE was obtained by optical Kerr microscopy on GaAs [Kato et al., 2004]. First successful transport experiments soon followed by non local spin injection in Al [Valenzuela and Tinkham, 2006] and damping alteration measured through ferromagnetic resonance in Pt|NiFe [Ando et al., 2008]. [Liu et al., 2012b] demonstrated that SHE induced spin current by $\beta-$Ta is sufficient to drive magnetization switching of an in plane magnetic layer.

## 3.4 . Spin charge conversion at interfaces : Rashba Edelstein effect

The Rashba-Edesltein effect (hereafter designed as REE) is another effect causing conversion of a charge current into a spin flux. The specificity of REE is that it is an interfacial effect. REE arises solely onto the interfacial electronic Rashba (or topological) state band structure in response to an applied electric field.

At the interface between two different material layers, the vertical symmetry is broken.

This allows for the existence of an effective vertical electric field $\mathbf{E_{int}}$ between the two layers due to the occurrence of an electrical dipole. For an interfacial Bloch state of wave vector $\mathbf{k}$, the Lorentz transformation of $\mathbf{E_{int}}$ gives rise to an effective magnetic field $-\left(\mathbf{v}\times\mathbf{E_{int}}\right)/c^2$. The Zeeman interaction between the electronic state spin and this effective magnetic field writes as a spin orbit term in the Hamiltonian according to :

$$\hat{\mathcal{H}}_R = -\alpha_R\,\hat{\sigma}\cdot(\hat{z}\times\mathbf{k})$$

leading to the definition of the so-called Rashba Hamiltonian $\hat{\mathcal{H}}_R$ with $\alpha_R$ the Rashba constant in unit of energy $\times$ length (eV.nm).

As a consequence of this Hamiltonian, for a given wave vector $\mathbf{k}$, the spin degeneracy is lifted according to the projection of the spin on the in plane direction orthogonal to $\mathbf{k}$. Considering the electronic states at the Fermi level, this is manifested by the "spin-momentum locking" or SML. This term designates the fact that spin and wave vector are orthogonal for Fermi level states. Note that this explanation of the origin of Rashba splitting is simplistic and an actual derivation can be performed more accurately through tight-binding calculation techniques. Typically, spin-momentum locking also arises on the interfacial states of topological insulators described by a single single helical state, unlike a Rashba texture, emanating from the SOC Hamiltonian free of any kinetic interaction.

The application of an electric field along the $\hat{x}$ direction in such system, as represented in figure 3.3, results in a certain population increase of the electron density with spin pointing along $-\hat{y}$ together with a depletion of those pointing towards $\hat{y}$. This is the so-called Rashba-Edelstein effect leading to charge-spin interconversion.

The inverse effect also emerges from equivalent band structures. If the spin population pointing along one direction is injected, the Fermi contours are effectively shifted in the direction transverse to the spins. This is spin to charge conversion through the inverse Rashba-Edelstein effect (or IREE). IREE is usually quantified via a certain Rashba-Edelstein length $\lambda_{REE}$ [Sánchez et al., 2013] that compares the generated 2D current density confined in the 2D interface to the 3D spin-current density injected within the neighbouring metal :

$$\lambda_{IREE} = \left(\frac{\mathcal{J}_C^{2D}}{\mathcal{J}_s^{3D}}\right)$$

Regarding the REE efficiency (direct effect), it is sized by a scaling wave vector $q_{REE}$ according to $q_{REE} = \left(\frac{\mathcal{J}_s^{3D}}{\mathcal{J}_C^{2D}}\right)$ [Rojas-Sánchez and Fert, 2019].

We note that contrarily to ISHE, IREE does not induce a 3D charge flow but rather a 2D current, confined near the interface. From a current perpendicular to plane, no vertical spin current directly emerges from REE, i.e. from the linear response theory. Instead, REE ge-

nerates a spin accumulation inside the interface, characterized by a population imbalance of one spin direction. This accumulation may still couple to metallic neighbouring layers, through diffusion processes, generating a subsequent spin-current whose amplitude is scaled by a characteristic spin-relaxation time $\tau_{s,I}$.

IREE has been first measured in systems involving Bi and Ag interfacing. Spin momentum locking was measured by angular resolved photoemission spectroscopy [Ast et al., 2007] and IREE was measured in [Sánchez et al., 2013, Sangiao et al., 2015]. Spin momentum locking was also shown to arise inside 2D electron gases between oxides layers [Lesne et al., 2016]. This system in particular presents the interest that the sign of the spin charge conversion can be electrically tuned, paving the way to new device concepts [Noël et al., 2020]. Regarding transition metals, spin REE has been shown to arise at the interface with oxides, especially in CoFeB|MgO [Rousseau et al., 2021]. Studies even suggest that spin momentum locking of interfacial states has a strong contribution to perpendicular magnetic anisotropy (PMA) [Barnes et al., 2014]. Regarding topological insulators, Bi alloys were exploited to achieve large REE charge-to-spin conversion and measure the resulting torques on a magnetic layer [Khang et al., 2018, Mellnik et al., 2014].

## 3.5 . Out-of-equilibrium orbital angular momentum generation

SHE, spin REE and reciprocals, have in common that they convert an applied electric current into a spin current. However, recent calculations demonstrate that similar effects, of the same geometry, lead to orbital angular momentum currents and accumulations (polarization) rather than spin. It has been claimed that the advantage of such orbital generation over spin is that, since orbitals are directly coupled to the electric field, the orbital response to a charge current is not expected to be proportional to SOC [Go et al., 2018]. It may thus give rise to larger responses. However, this result is still being questioned [Valet et al., 2025].

Those effects are divided in two categories : orbital Hall effect (OHE) that induces an orbitally polarized current transverse to a charge current. It is the counterpart to SHE and OREE which is interfacial and leads to orbital angular accumulation (polarization) when an electric field is applied.

### 3.5.1 . OREE : equilibrium orbital texture at interfaces

OREE shares the same geometry and electronic band structure as spin REE. Instead of SML, electronic states onto the Fermi surface exhibit orbital momentum locking (OML). This means that they bear an orbital angular momentum instead of spin, orthogonal to the wave vector and in the plane (see figure 3.4). From this OML, an orbital accumulation arises under an applied electric field through the same mechanism as REE described figure 3.3 **c**).

The underlying mechanisms to the occurrence of OML are actually analogous to the ones giving rise to REE but without the need to involve any SOC. It relies on the inversion sym-

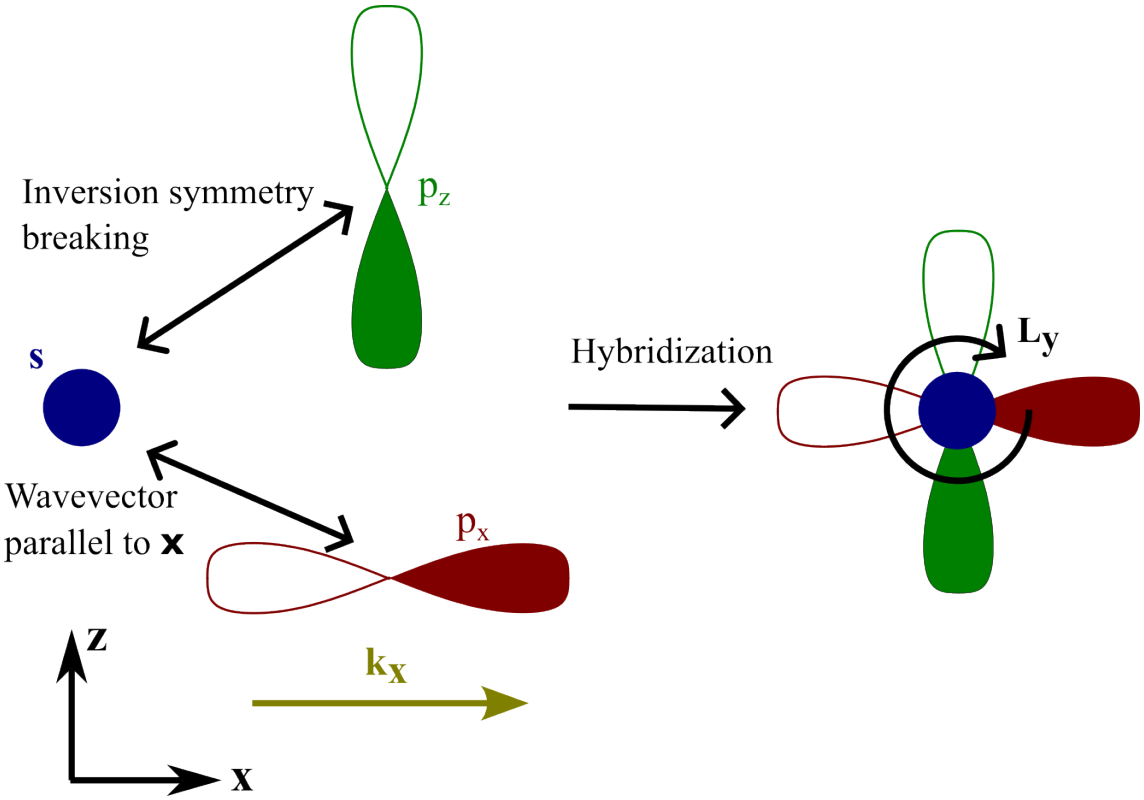


Figure 3.4 – Representation of the hybridization of conducting $s$ orbitals with $p_z$ orbitals due to inversion symmetry breaking and $p_x$ for a Bloch state of wave vector parallel to $\hat{x}$. This results in an electronic state bearing angular momentum along $\hat{y}$. Over the Fermi contour, this model yields OML.

metry breaking characteristic of the interface. In [Go et al., 2017], the authors propose a mechanism for materials involving $s$ and $p$ conduction bands, as schemed in figure 3.4. For an electronic state propagating toward the $\hat{x}$ direction, the two $s$ and $p_x$ orbitals couple. Simultaneously, the inversion symmetry breaking allows now the hybridization of the two $s$ and $p_z$ orbitals, which is forbidden otherwise. The resulting orbital nature of the Bloch state is mixed between $s$, $p_x$ and $p_z$ resulting in the occurrence of a certain orbital angular momentum along the $\hat{y}$ direction. This is the OML. Same result can be obtained from this model with $s$ and $d$ bands.

This demonstrate that OML may exist at equilibrium. Once this is verified, it follows from linear response theory that a finite orbital angular momentum accumulation arises under the application of an electric field.

#### 3.5.2 . OHE : out of equilibrium orbital current

OHE underlying physics is more difficult to catch and the actual microscopic mechanisms are still ongoing debate. It is indeed in apparent contradiction with one result of solid state physics : in crystals, orbital angular momentum is quenched due to symmetries [Mohn, 2006, Tinkham, 2003]. However, modelling the interband couplings allowed when an electric field is applied leads to uncover a finite out of equilibrium orbital angular momentum current [Go et al., 2018].

This effect arose interest because, unlike SHE, it has been predicted to be particularly large in light metals which had not been investigated for SHE [Salemi and Oppeneer, 2022]. Yet, the experimental detection of orbital currents or accumulation is a challenge. On the one hand, most of spintronics measurements techniques rely on the magnetization response to an excitation (magnetization switching, oscillations...). But orbital angular momentum is usually negligible in transition metals ferromagnets (4.5 % in Fe and 3.4 % in Co [Goering*, 2005]). As a consequence, without a strong SOC inside the ferromagnet, the response to an orbital excitation is generally too low to measure. On the other hand, when OREE and OHE are primary present and SOC is non zero, they actually cause their spin counterparts, REE and SHE, through electronic states perturbation. In experiments, it seems thus complicated to disentangle both effects separately.

### 3.6 . Spin-orbit torques (SOT)

SHE, REE and reciprocal effects, OHE and OREE all result in the generation of an out-of-equilibrium angular momentum flows or out-of-equilibrium angular momentum accumulations, for either the spin or orbital degree of freedom of the electrons. When a ferromagnetic material is involved, such angular momentum couples to the magnetization, resulting in a torque being applied on the latter : the so-called spin-orbit torques (SOT). This triggers magnetization dynamics, leading to, as for instance, controlled magnetization oscillations or back-and-forth magnetization switching.

However, before evoking some aspects of SOT physics, we first address the case of the

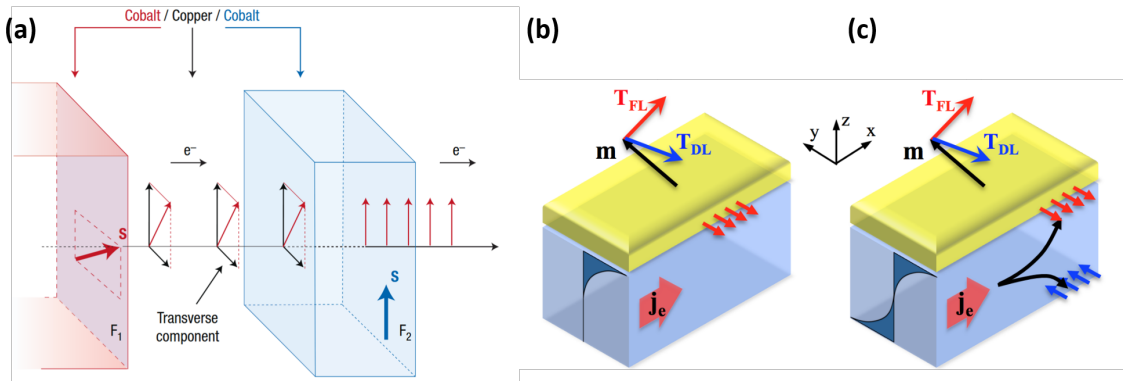


Figure 3.5 – **a**) Representation of the spin-transfer torque effect (STT). A flow of electrons crosses a magnetic multilayer. In the first layer $\mathrm{F}_1$ it gets spin polarized along the magnetization direction. It then relaxes in $\mathrm{F}_2$, exerting a torque on the magnetization as large as its transverse component. Extracted from [Chappert et al., 2007] **b**) Representation of the SOT geometry, in the case of a Rashba-like interfacial spin accumulation. **c**) SOT induced by SHE-like spin current injection. *Figures **b**) and **c**) are extracted from [Manchon et al., 2019].*

spin-transfer torque (STT). STT is the phenomenon at the core of STT-MRAM writing operation actually at play in commercial devices.

### 3.6.1 . Spin-transfer torque (STT)

In this geometry, a current is injected through a magnetic multilayer perpendicular to the interfaces plane (refer to figure 3.5 **a**). The electron flow goes across the first magnetic layer before entering a second one, possibly by tunneling effects in magnetic tunnel junction (MTJ) devices. The conduction electrons bearing this current get spin polarized according to the majority spins inside the first layer. At this point, it is thus in the case of a polarized current : both charge current and spin current are non zero. This current then penetrates into the second layer. Inside, the electrons bearing majority spin orientation of the first layer relax toward the majority spin direction of the second layer generating a magnetic torque on the local magnetization by reaction process. This occurs via the following mechanism, first predicted in Refs. [Slonczewski, 1996, Berger, 1996].

The spin current entering into a ferromagnetic layer is subject to the ferromagnet exchange field. Subsequently, electron spins precess around the magnetization direction $\hat{\mathbf{m}}$; this is the Larmor precession. However, incident spin flow is the superposition of Bloch states of different wave vectors $\mathbf{k}$. All those wave vectors point toward the inside of the ferromagnetic layer but can have any orientation within the corresponding half space. For a given depth inside the ferromagnet, the precession of the spins of two electronic states of different $\mathbf{k}$ is generally incoherent. Hence, on average, only the spin component parallel to the magnetization remains after a few atomic planes [Stiles and Zangwill, 2002].

This means that the injected spin current component transverse to the magnetization vanishes. To satisfy conservation of angular momentum, this relaxation is accompanied by

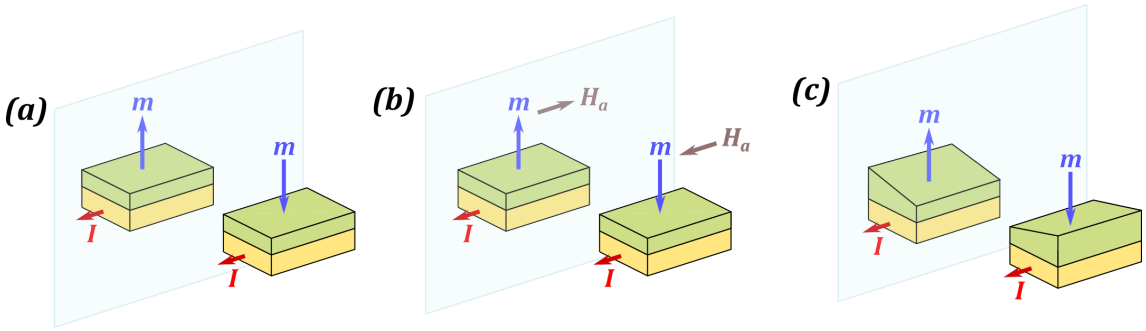


Figure 3.6 – **a**) SOT configuration for a bilayer consisting of a PMA ferromagnet. When a current is applied, up and down magnetization states are symmetric with respect to a mirror. For SOT induced switching to be deterministic, this symmetry can be broken by **b**) applying an in plane field or **c**) by introducing an asymmetry in the bilayer fabrication. *Inspired from [Yu et al., 2014].*

a torque on the second layer magnetization. This is STT. This torque corresponds to the absorbed part of the injected spins transverse component. It is convenient to decompose it into two different components. The damping-like component $\tau_{DL} \propto \hat{\mathbf{m}} \times (\hat{\mathbf{m}} \times \sigma)$ is the prominent term caused by spin transfer in the case of thick ferromagnetic layers. The field-like torque $\tau_{FL} \propto \hat{\mathbf{m}} \times \sigma$ is a correcting term interpreted as the exchange field induced by incoming electrons [Zhang et al., 2002] or as the spin tilt that electrons undergo when crossing an interface [Barnaś et al., 2005]. Nevertheless, as described in the following chapters, the field-like torque may become dominant over the damping-like torque in the case of ultrathin ferromagnetic layers, at interfaces with oxides and, as one important result of this thesis, at the interface with Al.

If the charge current is reversed (in sign), the sign of STT is also reversed. STT thus allows for electrical control of a magnetization's direction. This property was quickly demonstrated experimentally after the first theoretical proposals : first for spin waves excitation [Tsoi et al., 1998], and then then following studies reported switching of magnetic multilayers from quasi-parallel magnetization state to the quasi-antiparallel configuration [Albert et al., 2000, Grollier et al., 2001].

### 3.6.2 . The SOT mechanism

The spin-orbit torque (SOT) differs from STT through its geometry. While STT spin-current is parallel to the charge current, SOT spin current is transverse to it (figure 3.5). In SOT, the spin current incoming into the ferromagnetic layer arises from a neighboring layer or at the interface between these two. It is either the result of SHE or REE. Moreover, even though OHE and OREE generate orbital angular momentum current or/and accumulation instead of spin, they can still couple to the magnetization through SOC [Go and Lee, 2020, Go et al., 2023].

As a result, four different effects lead to SOT although the orbital contributions have been

overlooked for about two decades. Generally, it is likely that the observed SOT in a given system is a combination of several of them. Disentangling the four contributions is however not an easy task because assigned to the same symmetry signatures.

As STT, SOT can be used for spin wave excitation [Demidov et al., 2017] and magnetization switching [Miron et al., 2011, Liu et al., 2012a, Liu et al., 2012b, Baumgartner et al., 2017]. An important consideration regarding SOT-driven magnetization switching of a perpendicular magnetic layer is that to be deterministic, it requires breaking of mirror symmetry as displayed in figure 3.6.

### 3.6.3 . Action of the two components of the torques on the SOT in PMA ferromagnets

In a macrospin model, the dynamics of the magnetization vector $\mathbf{M}$ obeys the Landau Lifshitz-Gilbert (LLG) equation :

$$\frac{d\mathbf{M}}{dt} = \gamma \left(\mathbf{B}_{eff} + \mathbf{B}_{FL}\right) \times \mathbf{M} + \frac{\alpha}{M_s}\mathbf{M} \times \frac{d\mathbf{M}}{dt} + \mathbf{\Gamma}_{DL} \tag{3.6}$$

with $M_s$ the magnetization/unit volume and where the first term to the right involves the field like field torque ($\mathbf{B}_{FL}$), the second term is the damping (or Gilbert) term with $\alpha$ the damping parameter and the last term is the damping like torque ($\mathbf{\Gamma}_{DL}$). The magnetization equilibrium of the magnetic layer is reached when the total torque equals zero. When the damping like torque term is large due to the application of a current, the magnetization tends to align in the sample plane, i. e. parallel to the injected spin direction. For a PMA sample, it results in a certain indeterminacy of the out-of-plane magnetization when SOT is relaxed, between up or down direction.

The application of an external in-plane magnetic field $\mathbf{B}_x$ allows to lift this orientation degeneracy by stabilizing the magnetization either in the up or down perpendicular direction depending on the sign of $\mathbf{B}_x$. Consequently, the switching properties of PMA ferromagnetic material depends on both the current density injected and the value of the in-plane field $\mathcal{B}_x$ which seems mandatory for reliable switching operations. Moreover, the value of the critical currents $J_c$ is dependent of both the Damping-like and field-like terms. Some models have expressed $J_c$ as :

$$J_c = \frac{2eM_s t_F \sqrt{\alpha}}{\mu_0 \hbar \zeta_{DL} \sqrt{\beta\left(2+\alpha\beta\right)}\sqrt{2B_k^2 - B_x^2}}$$

with $\zeta_{DL}$ the DL torque efficiency, $\beta$ is the field like over damping like ratio, $B_k$ the effective PMA anisotropy field [Taniguchi et al., 2015, Krizakova et al., 2022].

## 3.7 . Linear response theory in electronic transport

We present in this section the main results describing the linear response theory for a future description of the Rashba-Edelstein response. Generally, one searches for the res-

ponse function of a given operator $\hat{\mathcal{O}}$ under a certain excitation described by an interaction Hamiltonian $\hat{\mathcal{H}}_{int} = \int \hat{\mathcal{B}}\mathcal{F}(t)d^3rdt$ where $\hat{\mathcal{B}}$ is a quantum operator (*e.g* the velocity $v_{\mathbf{k}}$) and $\mathcal{F}(t)$ is a classical source (*e.g.* the electric field $\mathbf{E}$).

In the limit of the DC transport regime induced by $\mathbf{E}$, the the response tensor $\chi_{ij}$ reads :

$$\delta\mathcal{O}^i = \chi_{ij}\ \mathbf{E}^j$$

Following the Kubo formula [Salemi et al., 2021] :

$$\chi_{ij} = ie\int_{\Omega_{\mathbf{k}}} \frac{d\mathbf{k}}{\Omega_k} \sum_{n,l} \left(\frac{f_{\mathbf{k},n} - f_{\mathbf{k},l}}{\hbar\omega_{\mathbf{k},nl}}\right) \frac{\mathcal{O}^i_{\mathbf{k},nl} v^j_{\mathbf{k},ln}}{\omega_{\mathbf{k},nl} - i\tau^{-1}} \tag{3.7}$$

with $\Omega_k$ the volume of the unit-cell of the reciprocal lattice, $\hbar\omega_{\mathbf{k},nl} = \epsilon_{\mathbf{k}n} - \epsilon_{\mathbf{k}l}$ the difference between the two eigenvalues $\epsilon_{\mathbf{k}n,l}$ at the $\mathbf{k}$ point, $v^j_{\mathbf{k},ln} = \langle\psi_{l,\mathbf{k}}|\hat{v}_j|\psi_{n,\mathbf{k}}\rangle$, $f_{\mathbf{k},n} = 1/(e^{(\epsilon_{\mathbf{k},n}-\epsilon_F)/k_BT}+1)$ the Fermi-Dirac occupation and $\mathcal{O}^i_{\mathbf{k},nl} = \langle\psi_{n,\mathbf{k}}|\hat{\mathcal{O}}_i|\psi_{l,\mathbf{k}}\rangle$ and $\tau$ the *intraband* electron relaxation time for $n = l$ and responsible for the dissipative contribution. The terms $n \neq l$ represent the intrinsic *interband* contribution whereas $n = m$ represents the intraband contribution (with $\omega_{k,nl} \to 0$) with a response scaling linearly with the scattering relaxation time $\tau$.

In the following chapters, we extensively use this formalism to predict with the orbital-Rashba and torkance in the different structures investigated.

## 3.8 . Conclusion

This first chapter has provided an overview of the fundamental concepts and phenomena central to the study of spin-orbit interactions and their implications for electrical control of magnetization. We covered the basics of spin and orbital degrees of freedom, explored the details of spin-orbit coupling in crystalline structures, and examined magnetic anisotropy and distinct transport properties. We then addressed charge to spin conversion through SHE and spin REE. Out-of-equilibrium orbital dynamics in OHE or OREE underscore the open questions raised by spintronics recent development. The resulting spin-orbit torques are powerful to control magnetic states at the nanoscale. Finally, the introduction to linear response theory provided the main framework we will use throughout this thesis to theoretically investigate electronic transport in these systems. In the next chapter, we discuss more extensively Rashba-Edelstein effects, notably OREE which is at the core of this thesis main results.

# 4 - Emergence of the orbital Rashba phenomenon

## 4.1 . Introduction and motivations

The so-called orbital-Hall effect (OHE) and orbital Rashba effect (OREE) have been recently considered as very promising efficient mechanisms to produce orbital currents allowing enhancement of the magnetic torques, effect which could benefit to the SOT-MRAM technologies. Recent experimental findings have corroborated such novel potential introduced by the orbital degree of freedom provided by "light" materials in heterostructures designed for enhanced torque devices. However, whereas OHE is a *bulk effect* which requires a certain minimum thickness to be efficient, OREE appears as a pure interfacial effect which can be more easily implemented in heterostructures consisting of ultrathin layers. Moreover, the OREE appears without the need of any spin-orbit coupling which opens new opportunities to light metals in the spintronic industry technology.

In this chapter, we first present a minimum tight-binding model able to describe the occurrence of the orbital moment locking texture and subsequent ORE before discussing the first experimental realizations proving the occurrence of ORE.

## 4.2 . OREE derivation in a simple system

Orbital momentum locking (OML) can be derived within a tight-binding framework considering a $s-p$ alloy in a two dimensional square lattice [Go et al., 2017] in the $(\hat{x},\hat{y})$ plane. Denoting $n = p_x,\ p_y,\ p_z \text{ and } s$ and $|\phi_{n,\mathbf{R}}\rangle$ the $n-$different Wannier functions centered on a certain lattice vector $\mathbf{R}$, we can conveniently choose the electronic states as :

$$|\varphi_{n,\mathbf{k}}\rangle = \frac{1}{\sqrt{N}} \sum_{\mathbf{R}} e^{i\mathbf{k}\cdot\mathbf{R}} |\phi_{n,\mathbf{R}}\rangle$$

constituting the Bloch wave functions basis satisfying the translation symmetry. The tight-binding Hamiltonian in the reciprocal space is a $4\times 4$ matrix :

$$\hat{\mathcal{H}}(\mathbf{k}) = \begin{pmatrix} H_p(\mathbf{k}) & h(\mathbf{k}) \\ h^\dagger(\mathbf{k}) & H_s(\mathbf{k}) \end{pmatrix}$$

where $H_p(\mathbf{k})$ is a diagonal Hamiltonian containing the energies of each of the three $p$ orbitals $E_{p_x}(\mathbf{k})$, $E_{p_y}(\mathbf{k})$ and $E_{p_z}(\mathbf{k})$, $H_s(\mathbf{k}) = E_s(\mathbf{k})$, whereas $h(\mathbf{k})$ and $h^\dagger(\mathbf{k})$ are the off-diagonal terms describing hopping between $p$ and $s$ orbitals. Because of the particular symmetry of a 2D surface, $h(\mathbf{k})$ can be written as :

$$h(\mathbf{k}) = \left(i\gamma_{sp}\sin(k_x a),\ i\gamma_{sp}\sin(k_y a),\ V_z(\mathbf{k})\right)^{\mathrm{T}}$$

with $\gamma_{sp}$ the hopping term between nearest neighbor $s$ and the respective $p_x$ or $p_y$ orbitals, $V_z(\mathbf{k})$ the hopping between $s$ and $p_z$. $V_z(\mathbf{k})$ results from a potential gradient across the plane of the two dimensional lattice.

To derive an effective orbital Rashba Hamiltonian, we consider $\mathbf{k}$ small and consider only its first order ($\sin(k_i a) \simeq k_i a$) expression. We then treat $h(\mathbf{k})$ as a perturbation to the

Hamiltonian of parameters $\mathbf{k}$ and $V_z(0)$. From the perturbation theory, the tight-binding Hamiltonian eigenstates are respectively given by :

$$\left|\varphi'_{p_x,\mathbf{k}}\right\rangle = \left|\varphi_{p_x,\mathbf{k}}\right\rangle + \frac{i\gamma_{sp}k_x a}{E_s(0) - E_{p_x}(0)}\left|\varphi_{s,\mathbf{k}}\right\rangle$$
$$\left|\varphi'_{p_y,\mathbf{k}}\right\rangle = \left|\varphi_{p_y,\mathbf{k}}\right\rangle + \frac{i\gamma_{sp}k_y a}{E_s(0) - E_{p_y}(0)}\left|\varphi_{s,\mathbf{k}}\right\rangle$$
$$\left|\varphi'_{p_z,\mathbf{k}}\right\rangle = \left|\varphi_{p_z,\mathbf{k}}\right\rangle - \frac{V_z(0)}{E_s(0) - E_{p_z}(0)}\left|\varphi_{s,\mathbf{k}}\right\rangle$$

$$\left|\varphi'_{s,\mathbf{k}}\right\rangle = \left|\varphi_{s,\mathbf{k}}\right\rangle + \frac{i\gamma_{sp}k_x a}{E_s(0) - E_{p_x}(0)}\left|\varphi_{p_x,\mathbf{k}}\right\rangle + \frac{i\gamma_{sp}k_y a}{E_s(0) - E_{p_y}(0)}\left|\varphi_{p_y,\mathbf{k}}\right\rangle + \frac{V_z(0)}{E_s(0) - E_{p_z}(0)}\left|\varphi_{p_z,\mathbf{k}}\right\rangle$$

From these eigenstates, one can compute an effective Hamiltonian : $\mathcal{H}_{eff}(\mathbf{k})$ :

$$\hat{\mathcal{H}}_{eff}(\mathbf{k}) = \begin{pmatrix} H^p_{eff}(\mathbf{k}) & 0 \\ 0 & H^s_{eff}(\mathbf{k}) \end{pmatrix}$$

$H^p_{eff}$ actually takes the form $H^p_{eff}(\mathbf{k}) = H_p(\mathbf{k}) + H_{OR}(\mathbf{k})$. $H_{OR}$ is an orbital Rashba Hamiltonian expressed by :

$$\hat{\mathcal{H}}_{OR}(\mathbf{k}) = \frac{\alpha_{OR}}{\hbar}\hat{\mathbf{L}} \cdot (\mathbf{z} \times \mathbf{k})$$

Assuming the three on-site energies be all equal for the $p$ orbitals for a perfect cubic lattice, $E_{p_x}(0) = E_{p_y}(0) = E_{p_{xy}}(0)$, $\alpha_{OR}$ can be expressed with the tight-binding parameters as :

$$\alpha_{OR} = a\gamma_{sp}V_z(0)\left(\frac{1}{E_{p_{xy}}(0) - E_s(0)} + \frac{1}{E_{p_z}(0) - E_s(0)}\right)$$

The orbital operator arises in the basis

$$\mathbf{L_x} = \hbar\begin{pmatrix} 0 & 0 & 0 \\ 0 & 0 & -i \\ 0 & i & 0 \end{pmatrix},\ \mathbf{L_y} = \hbar\begin{pmatrix} 0 & 0 & i \\ 0 & 0 & 0 \\ -i & 0 & 0 \end{pmatrix},\ \mathbf{L_z} = \hbar\begin{pmatrix} 0 & -i & 0 \\ i & 0 & 0 \\ 0 & 0 & 0 \end{pmatrix}$$

This tight binding model derived in a simple square lattice illustrates how an orbital Rashba arises through inversion symmetry breaking acting onto the $s - p$ hybridization. [Petersen and Hedegård, 2000] proposes a similar approach considering $sp$ type orbitals whereas [Park et al., 2013] demonstrate from equivalent tight-binding formalism the emergence of an orbital Rashba Hamiltonian in Co|Pt bilayers, requiring only $d$-type orbitals.

In the next section, we introduce some of the first experimental evidences of the occurrence of the orbital momentum locking and OREE phenomena in electronic band structure.

## 4.3 . Evidences of OML and OREE

### 4.3.1 . Cu|oxide interfaces

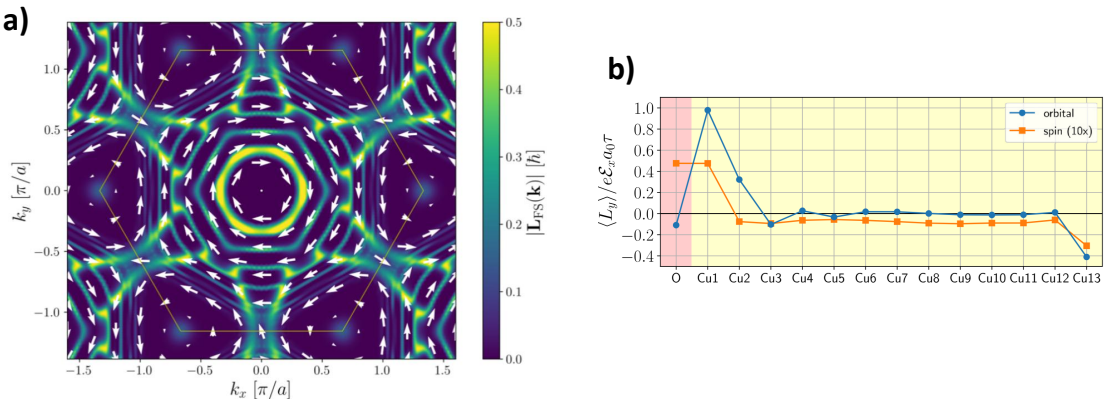


Figure 4.1 – **a)** Orbital momentum locking at a Cu and O interface computed by DFT. **b)** Resulting orbital angular momentum emerging at the Cu layer in contact with the oxygen. Note that although spin accumulation is non zero, it is ten times lower. [Go et al., 2021]

One of the first system and interface investigated experimentally for its OREE property is the interface of a Cu thin film with its oxide (Cu|CuOx), and more generally with an oxide layer (Cu|Ox). Spin torque FMR experiments reported in 2016 showed an enhancement of SOT with an optimized oxidization of a Cu layer deposited on top of NiFe [An et al., 2016]. This work was followed in 2018 by a study of [Gao et al., 2018] in which is demonstrate that the origin of the SOT is purely interfacial, suggesting a Rashba like phenomenon arising at the interface between the ferromagnet and the Cu oxide.

It is in 2021 that DFT was performed considering an interface between a Cu layer and oxygen atoms [Go et al., 2021] (figure 4.1). Those first principles calculations lead to the conclusion that the interface between Cu and an oxide is host to OREE. The occurrence of OREE was later confirmed by so called OREE magnetoresistance in NiFe|Cu|CuOx [Ding et al., 2022].

OREE magnetoresistance is an effect observed on an orbital Rashba system on the longitudinal conductivity. It is analogous to the SHE magnetoresistance [Chen et al., 2013, Choi et al., 2017] having the same symmetry terms. These effects result from the addition of the direct angular momentum generating effect and its inverse. In the case of OREE magnetoresistance, an applied electric field induced charge current would become orbitally polarized through OREE. Polarized carriers scattering at the interface with a ferromagnetic layer depends on the magnetization direction. This scattering in turns contributes to longitudinal charge current via IOREE (inverse orbital Rashba-Edelstein effect). This mechanism is represented figure 4.2 **a)** and **b)**. All in all, the longitudinal resistance depends on the magnetization direction : hence OREE magnetoresistance. [Ding et al., 2022] reports longitudinal resistance angular dependences consistent with this scenario. They are re-

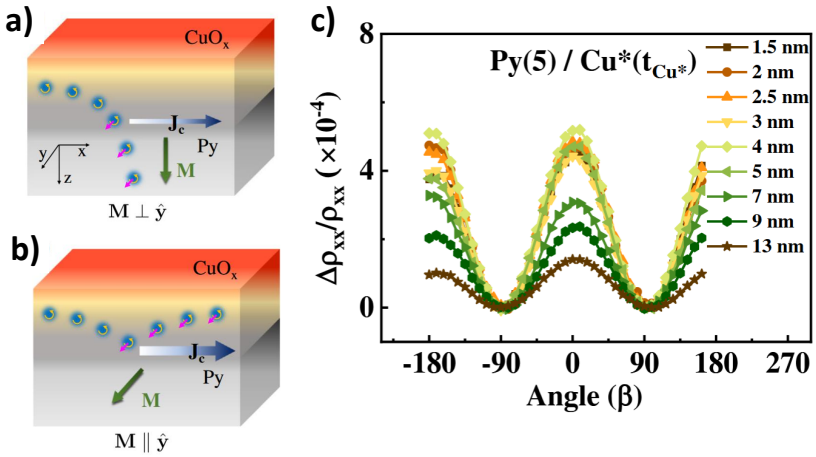


Figure 4.2 – Representation of the OREE magnetoresistance in the configuration **a**) where the magnetization is orthogonal to the OREE induced orbital angular momentum and **b**) where they are parallel. **c**) Dependence of the longitudinal resistance on the angle $\beta$ of the magnetization with the sample plane. $\beta$ is defined as the magnetization angle with the sample normal in the $y, z$ plane. Extracted from [Ding et al., 2022].

produced figure figure 4.2 **c)**.

In the studies reported above, the interface Cu|oxide is made of the boundary between metallic Cu and naturally air oxidized $Cu_2O$. However, large SOT have been also shown to arise at the interface between Cu and aluminium oxide [Kim et al., 2021]. In this study, spin torque FMR was conducted on CoFe|Cu|$Al_2O_3$ thin films as well as CoFe|Cu|$Bi_2O_3$.

In the latter structures, it was found that the torque on the magnetization is due to spin REE since Bi is an heavy atom inducing large SOC. In CoFe|Cu|$Al_2O_3$ however, no heavy element is present and only OREE is expected to give rise to torques. The FMR measurement show torques on the magnetic layer to be one order of magnitude larger with Cu|$Al_2O_3$ compared to Cu|$Bi_2O_3$ (figure 4.3). Moreover, the SOT in FM|Cu|$Al_2O_3$ are shown to have a marked dependence on the ferromagnetic material, an orbital angular momentum SOT feature. This study illustrates the versatility of Cu as a platform for OREE generation.

Those demonstrations of SOT generated from low atomic number materials raise the question of to what extent it can be made more efficient by introducing heavy metals in the multilayer. In [Ding et al., 2020], a Pt layer was inserted between air exposed Cu and TmIG, a PMA insulating magnetic material. They observe a large increase of SOT in the series of samples TmIG|Pt|Cu* compared to samples with only Pt deposited on TmIG (figure 4.4 **a**) when Pt thickness is between 0.5 and 3 nm. They confront those data to a model comprising two torque sources : SHE and OREE. From this model, they quantify that such increase in SOT is mostly of OREE origin (figure 4.4 **b**).

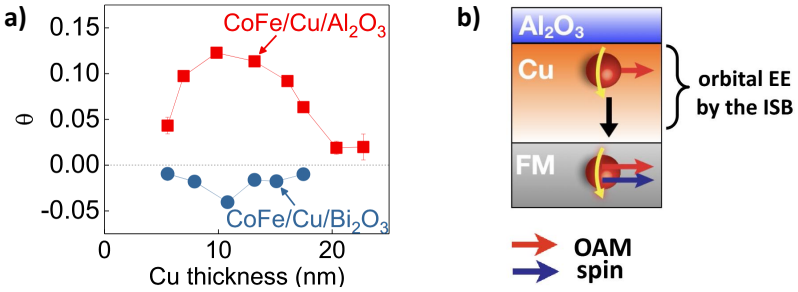


Figure 4.3 – **a**) Damping-like torque efficiencies $\theta$ measured as a function of Cu thickness in CoFe|Cu|$Al_2O_3$ and CoFe|Cu|$Bi_2O_3$. **b**) Representation of orbital angular momentum accumulation occuring at Cu|$Al_2O_3$ interface and its coupling to the magnetization inside the ferromagnetic layer. Extracted from [Kim et al., 2021].

The author explain this effect by injection of an orbital angular momentum from Cu|CuOx OREE into Pt, converted hereafter to spin through Pt large SOC. In other words, large spin-orbit materials as heavy metals may act as orbital-spin converter. The subsequent spin flow then exerts directly torques onto the magnetization. They confirm this result by OREE magnetoresistance measurement where the signal is enhanced by a factor of 10 in the Pt thickness range where the torques are observed to increase.

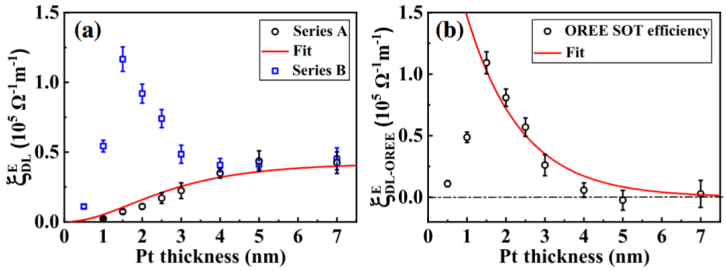


Figure 4.4 – **a**) Damping-like torque efficiencies $\xi^E_{DL}$ as a function of Pt thickness in TmIG|Pt|Cu* (series B, blue squares) and TmIG|Pt (series A, blue squares). **b**) Damping like torque efficiency attributed to OREE by the authors in TmIG|Pt|Cu*. Extracted from [Ding et al., 2020].

However, the picture of an out-of-equilibrium flux of orbital angular momentum flowing from the OREE interface to the ferromagnetic layer is currently under debate. Yet, this study demonstrates at least that Cu OREE and Pt SHE can be made to act constructively together in exerting torques on a magnetization.

At Laboratoire Albert Fert, in the frame of Benjamin Bony thesis, the study [Krishnia et al., 2024] compared the different systems comprising Cu OREE superimposed to spin generation and acting onto Co $3d$ transition metal. We reproduce figure 4.5 the damping like torques measured in the different systems. In those figures, the damping-

like effective field is plotted as a function of the current density in the Pt layer (or Cu* for the sample without Pt). The steeper is the slope, the larger is the SOT.

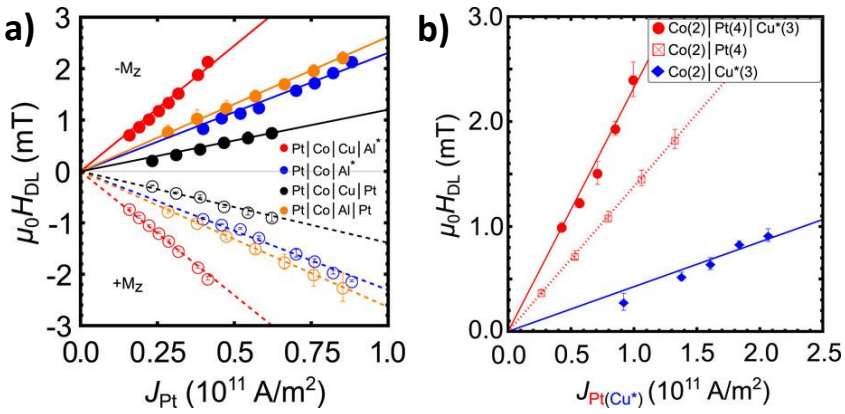


Figure 4.5 – **a)** and **b)** SOT measurements reported in [Krishnia et al., 2024]

In figure 4.5 **a**), Pt|Co|Cu|Al* is shown to have the largest torques compared to the other samples. This confirms the existence of SOT induced by OREE at the Cu|AlOx interface. Especially, this structure has larger torques than Pt|Co|Al* (Al* means Al fully naturally oxidized), confirming that the interface Cu|AlOx plays a peculiar role. Pt|Co|Al* and Pt|Co|Al|Pt exhibit similar SOT while Pt|Co|Cu|Pt has the lowest damping-like torque of the samples measured [Krishnia et al., 2023]. Those three samples will be the object of a more extensive discussion in this manuscript, chapter 6.

From the same study, figure 4.5 **b**) reports on the damping-like torque acquired in three multilayers. Co|Cu* has the lowest torque compared to Co|Pt. This shows that interfacial Cu|CuOx OREE induced torques in Co do not exceed those due to Pt SHE. However, the third samples Co|Pt|Cu* presents the largest torques, confirming that in this system, OREE from Cu|CuOx and intermediate Pt SHE add up to have a maximal effect on the magnetization. More experimental SOT results on Cu|CuOx an be found in [Bony et al., 2025].

We also conclude from those considerations that Pt|Co|Cu|Pt, where no interface is expected to host OREE, having the lowest SOT is also a manifestation of the absence of SOT generation in bulk metallic Cu. The need for the interface with an oxide confirms the OREE origin.

## 4.4 . A phenomena common to many spintronics materials?

Besides Cu and oxides interfaces, OREE has been shown to arise in other systems that are at the foundations of latest findings in spintronics. Notably, [Go et al., 2017] demonstrated theoretically $BiAg_2$ is not only a seminal platform for spin REE but is also host to a non zero

OREE. They find a significant orbital momentum locking in the opposite direction to the spin momentum locking.

Regarding oxides 2D electron gases, systems, [Kim et al., 2014] applies tight-binding model to surface states of $SrTiO_3$ and $KTaO_3$ oxide materials and finds a significant OREE. Recently, OREE was also reported from spin pumping experiments in epitaxial $LaAlO_3|SrTiO_3$ oxide systems [El Hamdi et al., 2023]. This latter work notably demonstrate from DFT calculations different response symmetry for spin REE and OREE. In epitaxial films, it is thus possible to disentangle spin and orbital REE through angular dependence of spin pumping.

Another crucial system for interfacial physics are the topological insulators. Their electronic surface states have been extensively studied for hosting spin momentum locking. In a work of 2012 probing those surface states via angular resolved photoemission spectroscopy with circularly polarized light, authors report orbital angular momentum locking at the surface of $Bi_2Se_3$, opposite to SML. They accompany this experimental results with DFT calculation that confirm this conclusion [Park et al., 2012].

Finally, a theoretical work of 2011 suggests that OREE is actually more fundamental than spin REE [Park et al., 2011]. The authors derive a model where the interfacial electric field due to the inversion symmetry breaking induces a non zero orbital angular momentum in the interfacial states. This yields orbital angular momentum locking causing OREE. In turn, spin momentum locking emerges due to coupling with this texture rather than from the effective Zeeman potential mentioned section 3.4.

## 4.5 . Conclusion

In this section, we have explored the different aspects of OREE physics. We proceeded to a theoretical derivation of the orbital Rashba Hamiltonian in a simplified system, under general assumptions. It illustrates the microscopic mechanism at play at the origin of this effect as well as how general this effect may be to interfaces. We then reported various demonstration and calculations of OREE at Cu|oxide interfaces. This gives insights into how this effect manifest and how it can be optimized through materials engineering. We briefly extended this discussion to consider whether OREE is common across various spintronics materials. OML and subsequent OREE are key concepts of this thesis since one of the main result is the discovery of such effect at the interface between metallic Co and Al. In the next chapter, we describe the experimental method that we employ to quantify SOT in magnetic thin films. Such measurements will allow us to precisely assess the out of equilibrium spin and orbit properties of the samples investigated throughout this thesis.

# 5 - Metrology of spin orbit torques

## 5.1 . Introduction

An accurate measurement of the two SOT components is mandatory for both fundamentals and applied spintronic and orbitronic research. A fine knowledge of both components dependence on materials and metallic structures parameters allows to draw conclusions regarding their physical origin as well as investigate the potential of a given structure for electric control of magnetization dynamics and optimize it. Several methods are available.

One of them is spin-transfer torque (STT) ferromagnetic resonance (FMR) or STT-FMR [Liu et al., 2011]. Even though FMR has been extensively studied in spintronics, this experiment is made difficult to employ because it requires radio-frequency circuits and set-ups besides a cautious analysis to disentangle the different rectification effects.

Another technique is two measure SOT induced magnetization oscillations or magnetization switching via optical Kerr effect [Fan et al., 2016, Tsai et al., 2018]. The drawback of optical detection of the magnetization perturbation by SOT is the strong detection sensitivity required and that, in PMA samples, it usually allows for only one component to be accurately measured.

Measuring SOT can also be achieved by harnessing critical magnetization switching currents. However those critical currents depend on a variety of factors else than SOT. Especially, considering magnetization switching as that of a single magnetic domain requires the fabrication of small magnetic elements (less than 100 nm typically) which involves demanding processes.

It can also be stressed that ongoing research on ultrafast picosecond pulses enables the precise temporal resolution needed to directly observe the dynamics of SOT driven magnetization dynamics. By synchronizing these pulses with pump-probe techniques, researchers can disentangle thermal and spin contributions to SOT, offering unprecedented insights into energy-efficient spintronics [Jhuria et al., 2020]. This approach however requires ultrafast optics and simulation developments.

In this thesis, we will thus rely on harmonic Hall techniques [Pi et al., 2010, Hayashi et al., 2014, Garello et al., 2013] to investigate SOT. Those techniques involves only electrical measurements, are relatively quick to operate and allow for a precise disentanglement of the two SOT components with an appropriate model.

Throughout this chapter and manuscript we will not $\alpha$ and $\theta$ the respective azimutal and polar angles of the unit magnetization vector $\mathbf{m}$ with the $\hat{z}$ direction corresponding to the normal direction to the layers. In the same way, $\alpha_H$ and $\theta_H$ will correspond to the azimutal and polar angles of the external applied magnetic field.

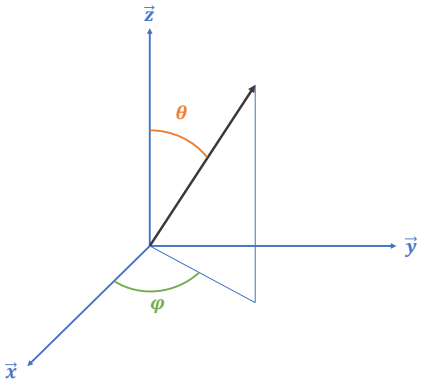


Figure 5.1 – Definition of polar $\theta$ and azimuthal $\varphi$ angles that we use in this thesis. The plane $(\mathbf{x}, \mathbf{y})$ is the sample plane.

## 5.2 . Quantifying SOT with Harmonic Hall measurements

### 5.2.1 . Harmonic Hall measurements principle

The transverse resistance $R_{xy}$ of a magnetic sample arises from the combined effects of Anomalous Hall Effect (AHE) and Planar Hall Effect (PHE). The amplitude of these magnetoresistances depend differently on the Euler angle, the respective azimuthal ($\varphi$) and polar ($\theta$) angles of the magnetization vector $\hat{\mathbf{m}}$ (vectors represented figure 5.1). When an alternating electrical current is applied to the sample at a certain frequency or pulsation $\omega$, the spin-orbit torque (SOT) becomes time dependent, leading to periodic variations in $\theta$ and $\varphi$ at the same frequency. As a consequence, $V_{xy}$ also exhibits this time dependence, written as :

$$V_{xy}(t) = R_{xy}(t) I_0 \sin(\omega t) \tag{5.1}$$

If the applied current pulsation $\omega$ is much smaller than magnetization dynamics (that are typically in the GHz range), both angles $\theta$ and $\varphi$ oscillate mainly in-phase with the AC current. This allows us to express them as : $\theta = \theta_0 + \Delta\theta \sin \omega t$ and $\varphi = \varphi_0 + \Delta\varphi \sin \omega t$. Assuming small variations of $\theta$ and $\varphi$, the transverse resistance can be approximated to the first order as : $R_{xy} = R_0(\theta_0, \varphi_0) + \frac{\partial R_0}{\partial \theta} \Delta\theta \sin \omega t + \frac{\partial R_0}{\partial \varphi} \Delta\varphi \sin \omega t$. Substituting this expression into equation 5.1, we thus obtain :

$$V_{xy}(t) = \left( R_0 + \frac{\partial R_0}{\partial \theta} \Delta\theta \sin \omega t + \frac{\partial R_0}{\partial \varphi} \Delta\varphi \sin \omega t \right) I_0 \sin(\omega t)$$

Thus,

$$V_{xy}(t) = -R_{2\omega} I_0 + R_0 I_0 \sin(\omega t) + R_{2\omega} I_0 \cos 2\omega t \tag{5.2}$$

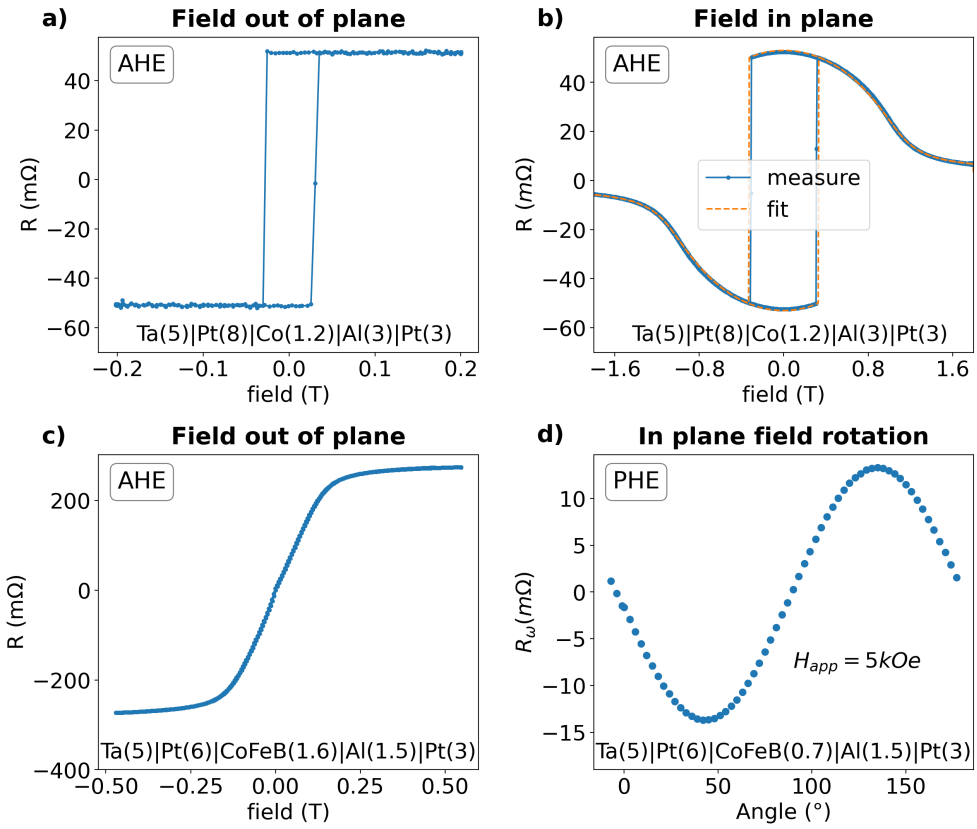


Figure 5.2 – **First harmonic resistance acquired respectively on OOP (a and b) and IP (c and d) magnetized samples : a)** out of plane hysteresis loop of a sample having PMA. **b)** In plane hysteresis loop of the same sample. Experimental data in blue and fit with Stoner-Wohlfarth model in orange. Parameters for the fit : $R_{AHE}$, $H_k^{eff}$ and $\theta$. **c)** out of plane hysteresis loop of a sample having in-plane anisotropy. **d)** In plane rotation of the field over 360°. The amplitude of the signal is $R_{PHE}$.

The second harmonic resistance $R_{2\omega}$ is given by :

$$R_{2\omega} = -\frac{1}{2}\left(\frac{\partial R_0}{\partial \theta}\Delta\theta + \frac{\partial R_0}{\partial \varphi}\Delta\varphi\right) \tag{5.3}$$

Hence, the second harmonic of $V_{xy}$ is directly linked to the transverse resistance changes due to magnetization oscillations. By expressing this dependence in terms of the SOT effective fields, one can extract respectively the damping-like $\mathbf{H_{DL}}$and the field-like $\mathbf{H_{FL}}$components from transport measurements according to specific experimental configuration.

### 5.2.2 . Parameters extracted from the first harmonic Hall signal

The transverse resistance $R_0$ in equation 5.2 stems from the superposition of AHE and PHE within the sample. This relationship is expressed as :

$$R_0 = R_{AHE}\cos\theta + R_{PHE}\sin^2\theta\sin 2\varphi \tag{5.4}$$

From this equation, we note that when a magnetic field, sufficiently strong to force the magnetization direction (saturation regime), is applied in the sample plane, $R_0 = R_{PHE}\sin 2\varphi$. This allows for precise measurement of the PHE amplitude (figure 5.2 **d**). Additionally, by applying a field perpendicular to the sample plane and sweeping it from positive values to negative values yields a signal proportional to the $\hat{z}$ component of the magnetization through the AHE. If the maximum applied field is strong enough to saturate the magnetization along $\hat{z}$, $R_{xy}$ spans from $-R_{AHE}$ to $+R_{AHE}$. This measurement provides an accurate value of the $R_{AHE}$ (figure 5.2 **b-c**).

The equilibrium values of $\theta$ and $\varphi$ are determined by minimizing the energy when a magnetic field $\mathbf{B} = \mu_0\mathbf{H^{app}}$ is applied. The application of such a magnetic field introduces a term $-\hat{\mathbf{m}}\cdot\mathbf{H^{app}}$ in the magnetization energy. Assuming no in plane axis anisotropy, the azimuthal angles of the magnetization and of the applied field align, i.e., $\varphi_H = \varphi_m$. Consequently, the energy term simplifies to $-\mu_0\hat{\mathbf{m}}\cdot\mathbf{H^{app}} = -\mu_0 M_s H^{app}\cos(\theta_H - \theta)$.

In the samples investigated in this thesis, two additional energy terms must be considered. On one hand, the demagnetizing field of a thin film produces an energy cost of $\Delta E = \frac{1}{2}\mu_0 M_s^2\cos^2\theta_m$. This energy term tends to minimize the magnetic moment inside the sample to reduce the magnetostatic energy cost. It tends to drive the magnetization in the plane of the sample. On the other hand, our exhibit an interfacial anisotropy favoring a magnetization out of the sample plane, contributing to the energy as : $\Delta E = \frac{K_s}{t_{FM}}\sin^2\theta$

The overall energy incorporating those different contributions is given by :

$$E = -\mu_0 M_s H^{app}\cos(\theta_H - \theta) - \mu_0\frac{M_s H_k^{eff}}{2}\cos^2\theta \tag{5.5}$$

where the effective anisotropy field $H_k^{eff}$ is defined in equation 3.5.

Given the magnetic parameters of the sample and the applied magnetic field, the angle $\theta$ can be determined through numerical minimization of the energy. However, experimentally, the unknown variable is the effective anisotropy field $H_k^{eff}$. It can be determined conversely from AHE by acquiring the first harmonic transverse resistance while sweeping the magnetic field or rotating it out of the sample plane and fitting that signal with equation 5.4. In this procedure, $\theta_H$ is known and $\theta$ estimated by energy minimization with $H_k^{eff}$ as a free parameter.

Thus, the analysis of the first harmonic allows for the experimental and independent measurement of $R_{AHE}$, $R_{PHE}$ and $H_k^{eff}$.

### 5.2.3 . Second harmonic of Hall voltage

For the $2^{\text{nd}}$ harmonic component, following equation 5.3, it is necessary to differentiate $R_0$ and estimate the amplitudes of the magnetization oscillations $\Delta\theta$ and $\Delta\varphi$. The first step yields :

$$R_{2\omega} = -\frac{1}{2}\left[(-R_{AHE} + 2R_{PHE}\cos\theta\sin 2\varphi)\sin\theta\Delta\theta + 2R_{PHE}\sin^2\theta\cos 2\varphi\Delta\varphi\right] \tag{5.6}$$

To compute $\Delta\theta$ and $\Delta\varphi$ amplitudes, an effective field approach has been used. At equilibrium, the angles $\theta$ and $\varphi$ align with an effective field $H_{eff}$, which results from magnetic anisotropy and applied magnetic field $H^{app} = \frac{1}{\mu_0}B$. To determine this effective field, we have to derive a relationship expressing the change in the magnetization angles $\delta\theta$ and $\delta\varphi$ as a function of a perturbation of the applied field $H^{app}(\theta_H, \phi_H)$ by a small transverse field $\delta H_\perp^\theta$ (polar) or $\delta H_\perp^\varphi$ (azimuthal).

The change in $\theta$ (resp. $\varphi$) is only related to $\delta H_\perp^\theta$ (resp. $\delta H_\perp^\varphi$). Assuming these perturbation fields are small compared to the applied field and the anisotropy effective field, we have :

$$\delta\theta \simeq \tan\delta\theta = \frac{\delta H_\perp^\theta}{H_{eff}^\theta} \qquad \text{and} \qquad \delta\varphi \simeq \tan\delta\varphi = \frac{\delta H_\perp^\varphi}{H_{eff}^\varphi} \tag{5.7}$$

These relations define the two effective field components $H_{eff}^\theta$ and $H_{eff}^\varphi$. Regarding the polar angle $\varphi$, assuming no in plane easy axis, the only field competing with a perturbation field $\delta H_\perp^\varphi$ is the in-plane component of the applied field, whose norm is $H_{ip}^{app} = H^{app}\sin\theta_H$. Consequently $H_{eff}^\varphi = H^{app}\sin\theta_H$ giving :

$$\delta\varphi = \frac{\delta H_\perp^\varphi}{H^{app}\sin\theta_H}$$

For the azimuthal angle $\theta$, the out-of-plane anisotropy must be considered. We use the energy functional to derive $\delta\theta$. The equilibrium value of $\theta$ minimizes the energy given by equation 5.5. Therefore,

$\frac{1}{\mu_0}\frac{\partial E}{\partial\theta} = -M_s H^{app}\sin(\theta_H - \theta) + M_s H_k^{eff}\sin\theta\cos\theta = 0$

$$H^{app}\sin(\theta_H - \theta) = \frac{H_k^{eff}}{2}\sin 2\theta \tag{5.8}$$

Differentiating this equation, we obtain :

$$H^{app}\cos(\theta_H - \theta)(\delta\theta_H - \delta\theta) = H_k^{eff}\cos 2\theta\,\delta\theta$$

leading to :

$$\delta\theta = \left(\frac{H^{app}\cos(\theta_H - \theta)}{H^{app}\cos(\theta_H - \theta) + H_k^{eff}\cos 2\theta}\right)\delta\theta_H \tag{5.9}$$

This formula relates $\delta\theta$ to $\delta\theta_H$. $\delta\theta$ is a small variation of the magnetization azimuthal angle while $\delta\theta_H$ is a small change in the applied magnetic field polar angle. Such small change $\delta\theta_H$ in the applied field orientation is equivalent to apply a field orthogonal to $\mathbf{H^{app}}$ of amplitude $\delta H^{app,\perp} = \delta\theta_H H^{app}$. The projection of this field on the azimuthal vector of the magnetization yields $\delta H_\theta^\perp = H^{app,\perp}\cos(\theta_H - \theta) = H^{app}\cos(\theta_H - \theta)\delta\theta_H$. Thus the numerator of equation 5.9 is $H_\theta^\perp$. We thus identify equation 5.9 to equation 5.7, and find :

$$H_\theta^{eff} = H^{app}\cos(\theta_H - \theta) + H_k^{eff}\cos 2\theta \tag{5.10}$$

In Cartesian coordinates, the SOT effective fields are expressed as follows :

$$\mathbf{H_{DL}} = H_{DL}\hat{\mathbf{m}} \times \hat{y} = H_{DL}\begin{vmatrix} -\cos\theta \\ 0 \\ \sin\theta\cos\varphi \end{vmatrix} \quad and \quad \mathbf{H_{FL}} = H_{FL}\begin{vmatrix} 0 \\ 1 \\ 0 \end{vmatrix} \tag{5.11}$$

Projecting SOT effective fields on azimuthal and polar vectors, we obtain :

$$H_\theta^{SOT} = H_{FL}\sin\varphi\cos\theta - H_{DL}\cos\varphi \tag{5.12}$$

$$H_\varphi^{SOT} = H_{FL}\cos\varphi + H_{DL}\sin\varphi\cos\theta \tag{5.13}$$

Dividing those SOT effective fields by the equilibrium effective fields computed above, we derive :

$$\Delta\theta = \frac{H_{FL}\sin\varphi\cos\theta - H_{DL}\cos\varphi}{H^{app}\cos(\theta_H - \theta) + H_k^{eff}\cos 2\theta} \tag{5.14}$$

$$\Delta\varphi = \frac{H_{FL}\cos\varphi + H_{DL}\sin\varphi\cos\theta}{H^{app}\sin\theta_H} \tag{5.15}$$

### 5.2.4 . SOT measurement through in-plane angular dependence (IP)

To measure SOT, a possible experimental protocol involves rotating the applied magnetic field within the plane of the sample, with its amplitude stronger than the anisotropy effective field. Under these conditions, the magnetization polar angle $\theta$ aligns with the field, such that $\theta = \theta_H = \frac{\pi}{2}$. Applying equations 5.6, 5.14 and 5.15 results in :

$$R_{2\omega} = \frac{1}{2}\left[R_{AHE}\frac{H_{DL}}{H^{app} - H_k^{eff}}\cos\varphi + 2R_{PHE}\frac{H_{FL}}{H^{app}}\left(2\cos^3\varphi - \cos\varphi\right)\right] \tag{5.16}$$

In the previous formula, the contributions of $H_{DL}$ and $H_{FL}$ are expressed as two orthogonal trigonometric functions of $\varphi$. Hence, it is straightforward to separate them during a full in-plane rotation measurement of $R_{2\omega}$. By measuring these two components for different values of applied field $H^{app}$ and knowing the anisotropy field, one can accurately estimate the two SOT effective fields $H_{DL}$ and $H_{FL}$.

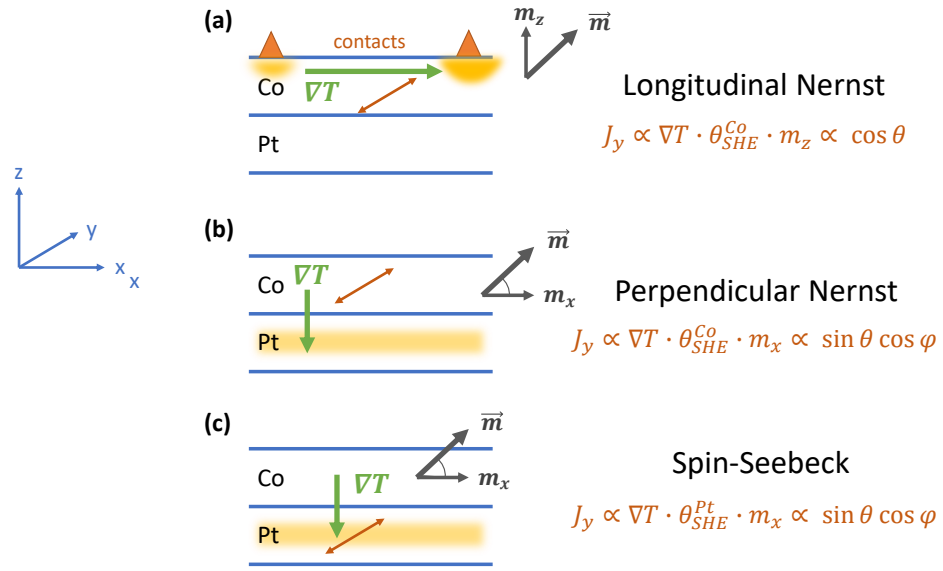


Figure 5.3 – Representation of the different thermal effects leading to a transverse current in a typical Co | Pt bilayer. **(a)** Nernst effect induced by an in plane thermal gradient, a common consequence of asymmetric electrical contacts. **(b)** Nernst effect arising from a vertical thermal gradient. This thermal inhomogeneity typically results from higher conductivity in Pt than Co. **(c)** Spin-Seebeck effect occurring due to a vertical thermal gradient.

### 5.2.5 . SOT measurement through magnetic field dependence (OOP)

Regarding samples with PMA, the in-plane rotation protocol requires the application of very large magnetic fields. A more practical approach is to apply the field slightly off-axis within the plane of the sample and sweep its amplitude from positive values (exceeding the anisotropy) to negative values. When the field surpasses the anisotropy, the magnetization aligns to it. Conversely, when it is zero, the magnetization becomes perpendicular to the sample plane. The magnetization response to SOT is maximized when the applied field amplitude is close to the effective anisotropy field where the magnetization has an intermediate position. This approach is similar to that presented [Garello et al., 2013].

The magnetization response to this experimental protocol can be simulated with good precision. By energy minimization, we determine the equilibrium position of the magnetization, which in turn gives the first harmonic transverse voltage. Calculating it with a perturbing SOT field allows to estimate the second harmonic signal. Experimental measurements are then fitted to this simulation on the whole field range to extract values for SOT effective field. A fully analytical approach is proposed in [Hayashi et al., 2014].

### 5.2.6 . Thermal effects in harmonic Hall measurements

Injecting a high current density into metallic thin films and stacks results in Joule heating. In general, this heating is not homogeneous and temperature gradients may arise

from cooler to warmer areas. Those thermal gradients in turn generate a flow of charge carrier from the warmer regions to the coolers. Consequently, Joule heating causes additional spin and charge currents that may contribute to the transverse voltage through anomalous Nernst effect (ANE), planar Nernst effect (PNE) and spin-Seebeck effect (SSE) [Bauer et al., 2012].

Among the possible configurations, in-plane temperature gradients are expected to arise due to asymmetries in the electrical contacts. This is typically a likely consequence of wire bonding. Inside the Co layer, the ensuing charge current contributes to the transverse voltage similarly to AHE (figure 5.3 **(a)**). This contribution is a component of the anomalous Nernst effect.

Besides longitudinal gradients, vertical temperature gradients arise inevitably and are expected to be larger than in-plane counterparts. Indeed , there is a manifest discrepancy between the heat dissipated to the substrate and the heat dissipated at the surface that is in contact to air or vacuum. This discrepancy creates an out of plane temperature gradient. Moreover, since each deposited metallic layer has a different conductivity, the current densities differ from layer to layer. Since Joule heating scales with the current density squared, this induces temperature gradients between the different layers.

In Co|Pt bilayer, this typically induces two additional transverse currents. One occurs in Co due to Co SHE. This is the perpendicular ANE figure 5.3 **(b)**. This component is not expected to be significant in the studied samples of this thesis as Co thickness does not exceed 2 nm. However, the same temperature gradient in Pt also adds to the transverse voltage via Pt SHE. This is the spin-Seebeck effect (figure 5.3 **(c)**).

ANE and SSE lead to transverse charge currents in the form of :

$$\mathbf{I}_{\nabla \mathbf{T}} = -\alpha_T \nabla \mathbf{T} \times \hat{\mathbf{m}} \tag{5.17}$$

with $\alpha_T$ a certain thermal prefactor. From this expression, we see that vertical thermal gradients induce a transverse current proportional to the longitudinal component of the magnetization $m_x$ while longitudinaal thermal inhomogeneity drives a current proportional to $m_z$. In the open circuit conditions, those currents add to the trnasverse volatge $V_{xy}$ that we measure in harmonic Hall measurements.

Moreover, the thermal gradient $\nabla T$ is proportional to $R_s I^2$, the power dissipated by the applied electrical current. Consequently, the current induced by $\nabla T$ obeys

$$I_{\nabla T} \propto \alpha R_s I(t)^2 \propto \alpha \frac{I_0^2}{2} \left[1 - \cos 2\omega t\right]$$

From this equation, It is evident that thermal effects affect both the offset and the second harmonic component of the transverse voltage.

In harmonic Hall measurements, it is therefore crucial to account for these thermal effects and distinguish between the signature of the torques and that of thermal gradients.

In the following sections, we explain how these considerations are addressed in our experimental protocols.

## 5.3 . Experimental procedure

### 5.3.1 . Sample preparation and measurements

After deposition of the multilayers using magnetron sputtering, the samples are patterned into 5 µm wide Hall bars for electrical transport measurements. The patterning process involves UV lithography and ion beam etching. Once patterned, the samples are mounted onto a sample holder and wire bonded to its pads. They are then loaded into a magnetotransport setup adapted for harmonic Hall measurements.

The two setups used during my thesis (figure 5.4) can generate a controlled and uniform magnetic field across the sample area. One setup employs a standard electromagnet capable of producing 0.7 T magnetic field, while the other uses a superconducting coil specified for 9 T measurements. Both setup allow for sample rotation within the magnetic field. The electromagnet setup can rotate the sample along one axis, either out of plane or in plane, depending on the chosen sample holder head. The superconducting coil setup features a "3D" head that can rotate along to orthogonal axes, enabling any orientation of the sample within the magnetic field.

Electrical currents are applied to the samples using AC current sources of typically 19 Hz frequency (choosing another frequency under 1kHz was not found to affect the measure), and the transverse or longitudinal voltages are measured with the help of lock-in amplifiers. These amplifiers not only reduce noise but also allow for the measurement of any harmonic of the applied current frequency. Hence they are well suited for harmonic Hall measurement techniques.

### 5.3.2 . Measuring torques in in-plane magnetized samples

#### Protocol description

For samples with in-plane magnetization, the most practical method to measure SOT is to rotate an applied magnetic field within the sample plane ($\theta = 90°$ and $\phi$ spans $0°$ to $360°$ range). This approach requires relatively low field to saturate the magnetization. During a full rotation of the sample, the first and second harmonic signals are given by the following equations (from 5.4 and 5.16) :

$$R_\omega = R_{PHE} \sin 2\varphi \tag{5.18}$$

$$R_{2\omega} = \Theta \cos\varphi + \Phi \left(2\cos^3\varphi - \cos\varphi\right) \tag{5.19}$$

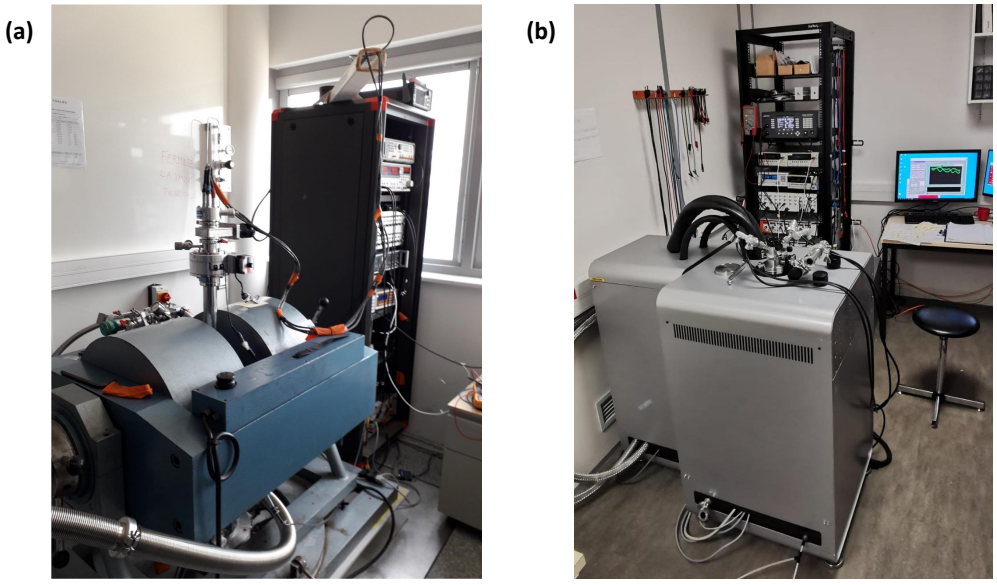


Figure 5.4 – Picture of the setups used for transport measurement. **(a)** 0.7 T transport setup. The electromagnet, the cryostat tube containing the sample holder as well as the electronics rack behind are visible. **(b)** System designed for up to 9T magnetic field. The sample holder is plugged in the cryostat, allowing for 3D sample rotation.

where

$$\Theta = \frac{1}{2}\left[R_{AHE}\frac{H_{DL}}{H^{app} - H_k^{eff}} + I_0\alpha\nabla T\right]$$
$$\Phi = R_{PHE}\frac{H_{FL}}{H^{app}}$$

It is thus convenient to deduce from the first harmonic signal the origin of $\varphi$ and $R_{PHE}$ and then extract both $\Theta$ and $\Phi$ through a decomposition of the signal into orthogonal trigonometric functions. Since the vertical magnetization component is constant in this measurement $m_z = 0$, thermal effects appear on the component proportional to $\cos\varphi$ as they are proportional to the longitudinal magnetization $m_x$ [Avci et al., 2014].

Notably, the terms containing SOT depend on the applied field $H^{app}$ whereas the thermal effects term $I_0\alpha\nabla T$ does not. This holds true as long as the applied magnetic field is strong enough to saturate the magnetization parallel to it. In order to extract the spin-orbit torques (SOT) using this technique, we therefore follow this sequence/protocol :

1. Estimate $R_{PHE}$ from first harmonic transverse resistance with rotating in plan field as large as possible (figure 5.5 **(a)**).
2. Rotate the field in sample plane for several magnetic field amplitudes stronger than the anisotropy.
3. Extract $\Theta$ and $\Phi$ for each applied field value (figure 5.5 **(b)**).
4. Plot $\Theta$ as a function of $\frac{1}{H^{app}-H_k^{eff}}$ and $\Phi$ as a function of $\frac{1}{H^{app}}$.

5. Extract $H_{DL}$ and $H_{FL}$ as the slopes of the resulting lines (figure 5.5 **(c)**).

### Uncertainty estimation

When we apply this protocol to a given sample, for each in plane magnetic field value, we typically measure second harmonic signals at four different applied current amplitudes. This gives four different values of $\Theta$ and $\Phi$. They are proportional to the current amplitude. Each point figure 5.5 **c)** is thus the outcome of a linear fit of four measurements. The actual values of the two SOT components are then calculated from another linear fit, represented by the grey lines figure 5.5 **c)**.

On the example figure 5.5, this process yields SOT estimates of :

- $H_{FL} = 0.80 \pm 0.01$ Oe/mA
- $H_{DL} = 5.03 \pm 0.05$ Oe/mA

The uncertainties reported here are the outcome of scipy.optimize *curve_fit* procedure. It propagates the uncertainties between the different fits. They are relatively very small, of around 1 %.

However, there is another notable uncertainty source in our measurements as the sample plane is not perfectly aligned to the field. Due to this misalignment, $\theta \neq 90^o$ and equation 5.19 is not exact. We assume this misalignment is less than 5°, which is already considerable.

Figure 5.6, we represent the second harmonic signal calculated by our semi analytical model for an in plane field rotation having a 5° disorientation (dashed blue line). We assume in plane magnetization ($H_k^{eff} = -100$ Oe), an applied field of 6000 Oe, an AHE resistance of 1 $\Omega$ and PHE of 0.5 $\Omega$. For SOT, we choose $H_{DL} = -H_{FL} = 16$ Oe. We then fit this simulation as we would experimental values, with equation 5.19. The fit outcome is : $H_{FL} = 15.77$ Oe and $H_{DL} = 15.63$ Oe. This is a relative error of less than 2.3 %.

To conclude, after combining these two uncertainty sources, it is safe to consider that this SOT measurement protocol comes with less than 4 % relative uncertainty on each torque component.

#### 5.3.3 . Measuring torques in out-of-plane magnetized samples

### Protocol description

Even though the same protocol can be applied to samples with PMA, it requires very large magnetic fields to saturate the magnetization in the sample plane. Therefore, we have chosen an alternative method to measure the two components of SOT in PMA samples : sweeping the applied magnetic field from positive values stronger than the anisotropy to negative values along two orthogonal axes within the sample plane (represented figure 5.7 **b)** and **c)**).

During this field sweep, equilibrium magnetization state results of a trade-off between applied magnetic field and anisotropy. Magnetization almost aligns with the field $\mathbf{H^{app}}$

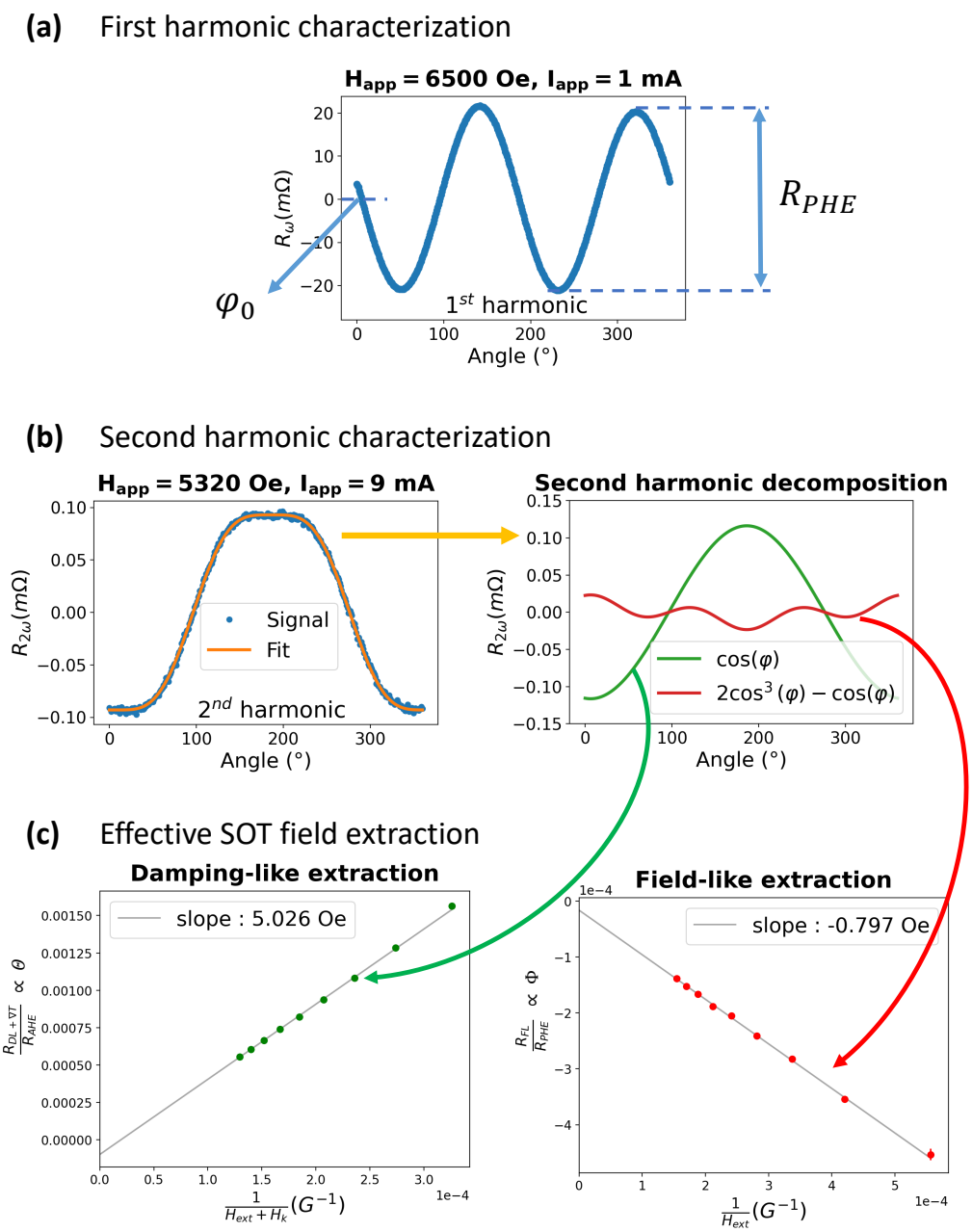


Figure 5.5 – Electrical measurements performed to measure SOT in an in-plane geometry for in-plane magnetized samples. The multilayer is Ta(5)|Pt(8)|Co(0.3)|CFB(1.1)|Al(3)|Pt(3) **(a)** First harmonic of the transverse resistance when magnetic field is rotated in the plane. **(b)** Second Harmonic signal and its decomposition according to equation 5.19. **(c)** Field like and damping like torqued extracted from second harmonic measurements at different applied magnetic fields. Each point in magnetic field results from a range of measurements of applied current amplitudes between 5 and 10 mA peak. The amplitude of $R_{2\omega}$ being assumed to be linear in current.

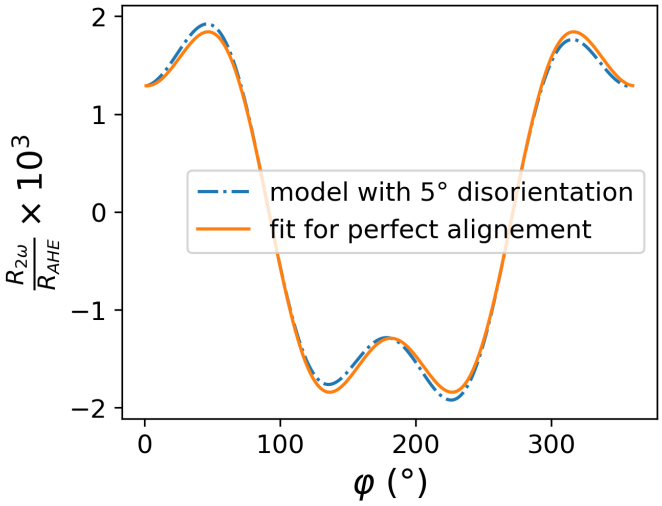


Figure 5.6 – Caption

when it exceeds the anisotropy. As the field decreases below the anisotropy, the magnetization tilts increasingly out of the sample plane. When $\mathbf{H}^{\mathbf{app}} = \mathbf{0}$, the magnetization is perpendicular to the sample plane. As $\mathbf{H}^{\mathbf{app}}$ becomes negative, the magnetization tilts in the opposite direction. It is convenient to set the field direction slightly out of the sample plane, by 4° for instance. This causes the magnetization to switch when the applied field becomes sufficiently strong in the opposite side of the sample. When the field is swept to negative values, the magnetization undergoes the same cycle on the other side of the sample.

By monitoring the magnetization position through AHE during this cycle as a function of $\mathbf{H}^{\mathbf{app}}$,the effective anisotropy field value can be extracted via fitting (figure 5.7 **a)**). This is achieved by fitting the experimental transverse resistance (proportional to the $\hat{z}$ component of the magnetization) to numerical simulations.

The second harmonic signal is proportional to the SOT induced modulation of the magnetization around its equilibrium position. The signal is small when the field is either larger or much smaller than the anisotropy, as the magnetization is dominated respectively by the applied field or the anisotropy. However, when the applied field amplitude is close to the effective anisotropy, the magnetization oscillations are then maximized.

The component of magnetization variations that drive the larger second harmonic signal is $\Delta\theta$. As a consequence, when magnetic field is transverse to the applied current ($\varphi = 90\,\mathrm{deg}$), the dominant term in the second harmonic voltage is due to field-like torque component (figure 5.7 **b)**). Thus, $R_{2\omega}^{xy}$ is even in magnetic field. However, when field and current are parallel ($\varphi = 0\,\mathrm{deg}$) it is the damping-like torque, which is odd in magnetic field (see figure 5.7c).

Accounting for the thermal effects in this measurement protocol is not as straightfor-

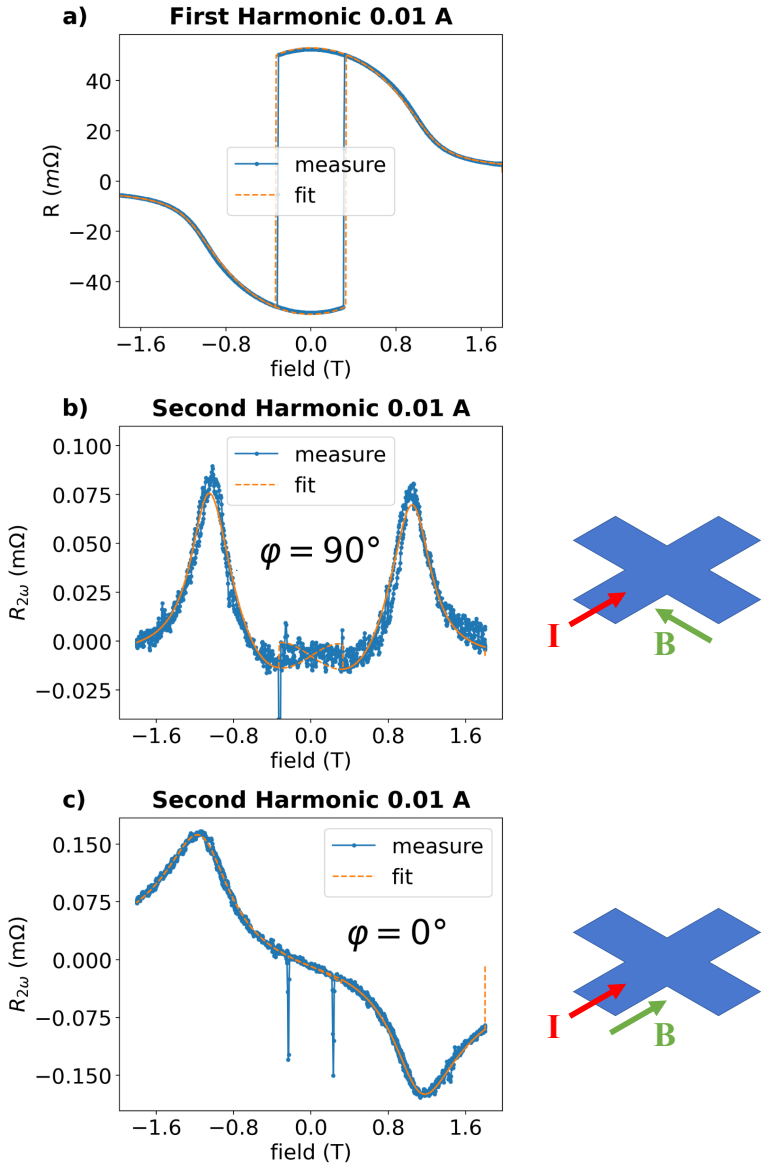


Figure 5.7 – Electrical measurements performed to measure SOT in an out of plane geometry. **a)** First harmonic response of the transverse resistance when magnetic field is scanned in the sample plane. **b)** Second harmonic signal with external magnetic field parallel to applied current. (Ta(5 nm)|Pt(8 nm)|Co(0.9 nm)|Al(3 nm)|Pt(3 nm)) **c)** Second harmonic signal with external magnetic field orthogonal to applied current.

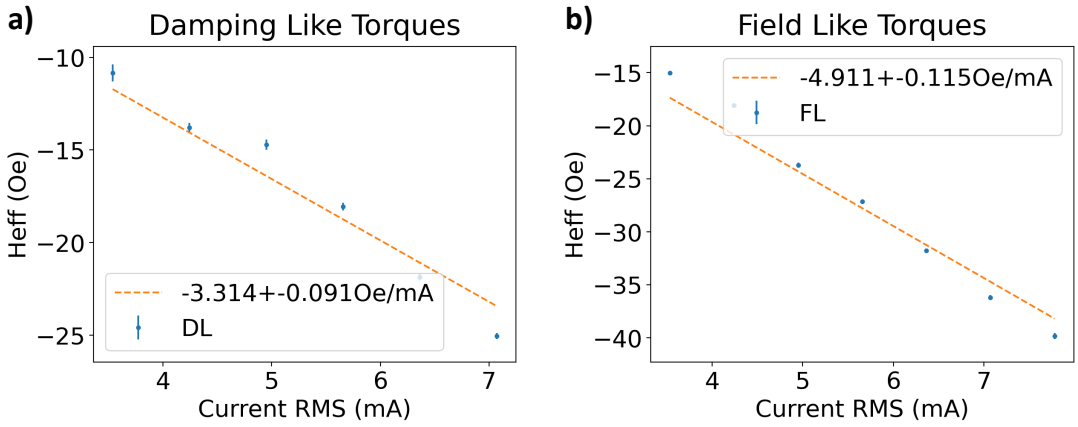


Figure 5.8 – Effective SOT fields (**a)** damping like and **b)** field like) extracted by fitting our model to the measurements displayed figure 5.7 (Ta(5 nm)|Pt(8 nm)|Co(0.9 nm)|Al(3 nm)|Pt(3 nm))

ward as in the in-plane case. Thermal effects indeed vary as the magnetization orientation changes. According to equation 5.17, a transverse thermal induced current is the sum of a term proportional to $m_x$ and a term proportional to $m_z$. The latter is hence proportional to the first harmonic $R_\omega$ signal ($\propto m_z\ R_{AHE}$). It can be removed by subtracting a term $-\tilde{\alpha}R_\omega$ such that there is no "opening" in $R_{2\omega}$ at $H^{app} = 0$.

To extract the SOT from a given metallic structure according to this method, we actually repeated the process described above for different applied currents (typically between 4 and 10 mA). We then extract an estimation of the effective SOT fields as the slope of the straight formed by $H_{SOT}$ as a function of $I$, in Oe per applied mA (see figure 5.8).

### Uncertainty estimation

To evaluate the uncertainty on the parameters extracted from the measurement described above, we distinguish two types of uncertainties. Type A uncertainty is evaluated from the measurements performed in the same conditions at different applied currents. For a quantity $x$ independent of the current estimated from a series of measurement $x_i$,

$$U_A(x) = \sqrt{\mathrm{Var}(x_i)}$$

For a quantity $x$ linear in the current $I$, as the SOT effective fields, we assimilate this uncertainty to the uncertainty on the slope of $x(I)$ (figure 5.8).

Type B uncertainty on each parameter measurement is evaluated from the covariance matrix returned by scipy.optimize *curve_fit* procedure. Each measurement at a certain applied current outcomes an estimation $x_i$ and a type B uncertainty for it $U_{B,i}$ (on figure 5.8, this is the error bar of each blue point).

The overall uncertainty is evaluated as :

$$U(x) = \sqrt{U_A(x)^2 + \sum_i u_{B,i}^2} \tag{5.20}$$

Here are the values that we find for the quantities extracted figures 5.7 and 5.8 :

| Quantity | Estimated value | Absolute uncertainty | Relative uncertainty |
|---|---|---|---|
| $H_k^{eff}$ | 17000 Oe | 200 Oe | 1.2 % |
| $\theta(DL)$ | 85.1° | 0.2° | 2 % |
| $\phi(DL)$ | 1.8° | 0.9° | not relevant |
| $H_{DL}$ | -3.3 Oe/mA | 0.3 Oe/mA | 9 % |
| $\theta(FL)$ | 87.8° | 0.1° | < 1 % |
| $\phi(FL)$ | 89.9° | 0.5° | not relevant |
| $H_{FL}$ | -4.9 Oe/mA | 0.3 Oe/mA | 6 % |

To conclude, we can safely estimate that the uncertainty of our measurements of each SOT component is of less than 10 %.

## 5.4 . Conclusion

In this chapter, we examine two essential methods for measuring and quantifying SOT, both relying on harmonic Hall measurements principle. We detail how the transverse resistance contains information regarding magnetoresistances and magnetic anisotropy. We then derive to a certain extent the equations governing the second harmonic transverse resistance of a magnetic layer subject to alternating current and subsequent SOT. We present two protocols based on this derivation to measure SOT field like and damping like components. One relies on the angular dependence of the signal while the second exploits the field amplitude dependence. We use these two protocols across this thesis to accurately characterize the two SOT components of various magnetic multilayers of interest.

# 6 - Contribution of Co|Al interface to SOT

## 6.1 . SOT involving 3*d* transition and light metals

### 6.1.1 . SOT optimization in ultrathin PMA multilayers

The prospect of designing an efficient SOT magnetic random access memory (SOT-MRAM) devices implies identifying a material combination that exhibits both optimized PMA for data retention and large SOT for energy efficient writing. As both properties are significantly enhanced by exploiting SOC at the interfaces of the free magnetic layer, most advanced SOT-MRAM proposals include a SOT track constituted of a thin 5*d* heavy metal layer such as $\beta$-W, Ta or Pt [Garello et al., 2018, Yasin et al., 2024].. Another free layer property to account for in designing MRAM is the magnetic damping but this will be not investigated in this thesis.

There are two primary avenues for tuning SOT and PMA. The first is to optimize PMA through the surface anisotropy that arises between a ferromagnetic material and a metal oxide. This approach is already utilized in industrial processes with the CoFeB/MgO stack, which demonstrates both good PMA and tunneling magnetoresistance (TMR), another key property for MRAM. For a recent review, refer to [Dieny and Chshiev, 2017].

The second avenue focuses on engineering the SOT line of the device to leverage new concepts and materials, aiming for improved writing energy efficiency. Among numerous materials possibilities, topological insulators stand out for enabling notably large charge to spin conversion as a SOT track. Moreover, 2D materials may allow to fabricate sharpest interfaces, either being used as the tunneling barrier, ferromagnetic layers, or SOT track [Dieny et al., 2020, Yang et al., 2022].

Regarding new physical concepts, orbital effects OREE and possibly OHE are gaining increased interest. Yet, systems exhibiting strong orbital effects adding up to spin contributions, such as observed recently in copper (Cu), tend to display in-plane magnetization [Sala and Gambardella, 2022, Bose et al., 2023, Fukunaga et al., 2023, Kim et al., 2023, Krishnia et al., 2024, Bony et al., 2025, Xu et al., 2025]. Hence, in order to fully harness the potential of orbital effects in generating spin-orbit torque (SOT), it is essential to identify multilayer structures combining these effects keeping however significant perpendicular magnetic anisotropy (PMA) [Gupta et al., 2025].

In the following two sections, we explain why our attention was drawn to Al. At the interface with a ferromagnet, its oxidized form $Al_2O_3$ has indeed previously been proven to induce a strong PMA (section 6.1.2) and was recently identified as a source of Dzyaloshinskii–Moriya interaction (DMI), an interaction associated to SOC (section 6.3.2).

### 6.1.2 . Co|AlOx for PMA

In spintronics, both Co and Al are already at the core of the discovery of a system made of low-SOC materials (light elements) exhibits strong SOC related properties : Co|AlOx interface. Back to 2002, Ref. [Monso et al., 2002] found that the magnetic anisotropy in Pt|CoFe|AlOx samples becomes perpendicular for a certain oxidization degree of Al. This result drew a lot of attention because of the large PMA observed.

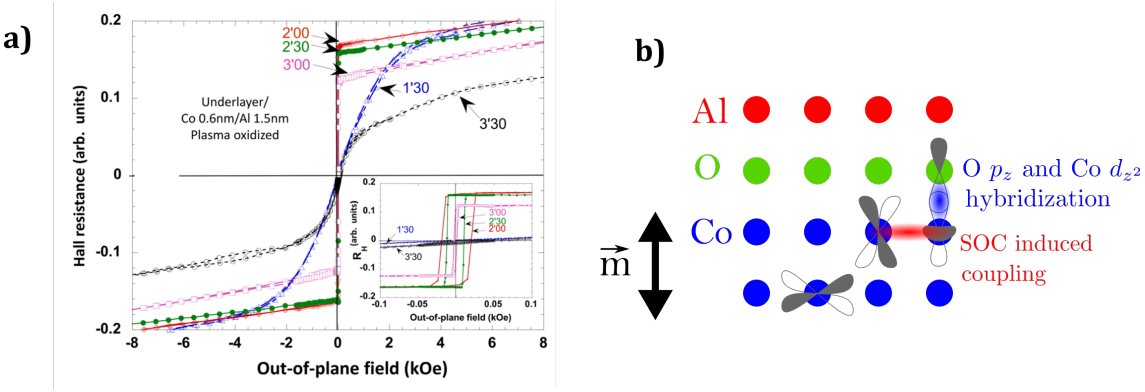


Figure 6.1 – **a)** Out of plane hysteresis loops measured by AHE in Pt(3 nm)|Co(0.6 nm)|Al(1.5 nm) for different exposition times to oxygen plasma [Rodmacq et al., 2003]. **b)** Representation of Bruno model explanation of interfacial PMA at Co|AlOx

Soon after this discovery, similar results were obtained in Pt|Co|AlOx [Rodmacq et al., 2003] (figure 6.1 **a)**), as well as in Pt|Co|MOx structures where M is a varying light metal (Al, Mg, Ta, etc...), especially as described in [Manchon et al., 2008]. The authors of these different studies found out that the PMA could be optimized through the tuning of the oxidization degree of the capping metallic layer. This indicated that the PMA was resulting from the oxygen atoms concentration at the Co interface.

Further characterizations studies through X-ray absorption spectroscopy (XAS) and X-ray photo-emission spectroscopy (XPS) exhibited the creation of Co-O bonds at the interface [Manchon et al., 2008]. The authors correlate the maximum amplitude of PMA with the most uniform oxidization at Co interface. These experimental conclusions suggest that the interfacial PMA is thus originating from Co and O orbital bonding and hybridization. It is emphasized in [Balan et al., 2024] where it is demonstrated through X-ray photoelectron spectroscopy that gate voltage control of the PMA in Pt|Co|AlOx is to be attributed to oxygen atom migration within the metallic layers.

Ab-initio calculations were able to reproduce those trends. Those calculations also find out that this property is very robust : it can be observed varying both the transition metal and the oxide. Among the different theoretical studies investigating the different anisotropy terms reported in the review [Dieny and Chshiev, 2017], we only report one relevant interpretation of the PMA catching the main physical ideas.

Based on a model coined by Patrick Bruno in the 90s [Bruno, 1993], hereafter quantitatively confronted to DFT in later studies [Liang et al., 2014, Kanai et al., 2014], the PMA arising at transition metal oxides interface is a consequence of both SOC and hybridization of $p_z$ oxygen orbitals with $d_{z^2}$ 3*d* transition metal orbitals.

The mechanism is as follows : in the bulk of fcc transition metals (Co or Fe), the charge

distribution is quasi-isotropic, meaning there is no preferred axis for the orbital magnetic moment. Consequently, there is no specific uniaxial crystalline anisotropy. However, at the interface with an oxide, the $3d_{z^2}$ orbitals of transition metal hybridize with the $2p_z$ orbitals of oxygen. This outcomes in a depletion of $3d_{z^2}$ electron population. However, due to spin-orbit coupling, the $3d_{z^2}$ also mix with $3d_{xz}$ and $3d_{yz}$ orbitals; $3d_{xz}$ and $3d_{yz}$ orbitals occupations are reduced, as electrons preferentially occupy the $2p_z$ orbital of oxygen. As a result, the most occupied orbitals in the ferromagnet are the $3d_{x^2-y^2}$ and $3d_{xy}$ orbitals leading to an out-of-plane orbital magnetic moment. In the presence of SOC, this causes the out of plane magnetization orientation to minimize energy. Therefore, this redistribution of electrons causes a PMA at the interface (figure 6.1 **b**).

## 6.2 . Growth and material characterization

The fabrication by sputtering and characterizations of ultrathin layers of Co, Pt and Al are critical in the assessment of their physical properties. Notably, these ultrathin films are particularly susceptible to interlayer atomic diffusion, which can significantly affect their structural and magnetic properties at very small thicknesses. To ensure the high quality and reliability of our samples, an extensive characterization is mandatory. In this regard, we employed a range of advanced characterization techniques to thoroughly assess the quality of our metallic layers. Growth was performed using Magnetron Sputtering and charactrizations relied on X-Ray Reflectometry (XRR), X-Ray Photoelectron Spectroscopy (XPS), Scanning Transmission Electron Microscopy (STEM), and Superconducting Quantum Interference Device (SQUID) measurements. Each of these methods provides unique insights into the structural, chemical, and magnetic properties of the films. Our comprehensive analysis consistently indicated the excellent quality of our samples, demonstrating well-defined layers with minimal intermixing as well as large magnetic moments in the ultrathin limit. In this section, we outline the methodologies and findings that underscore the integrity and potential of our ultrathin Pt, Co, Al and Cu films.

### 6.2.1 . Magnetron sputtering

The different stacks were grown using Plassys MP900S magnetron sputtering system at Laboratoire Albert Fert. This technique is industry compatible due to its ability to achieve excellent resolution for each layer's thickness over a large area, while also allowing for relatively quick growth, low roughness and limited chemical interdiffusion.

Sputtering refers to the process where atoms are ejected from a material's surface due to collisions with energetic particles from a plasma. This phenomenon was first observed by Sir William Grove in 1852 as a "dirt effect" during his experiments on electric discharge in gaseous media. Advances in vacuum technology have since enabled the exploitation of this effect to grow thin films on substrates. A significant technological improvement has been the use of a magnetron. In a magnetron sputtering chamber, a plasma is generated by applying an electrical voltage between the target and the vacuum chamber. To enhance the collision rate of plasma particles while maintaining low pressure, a magnetron

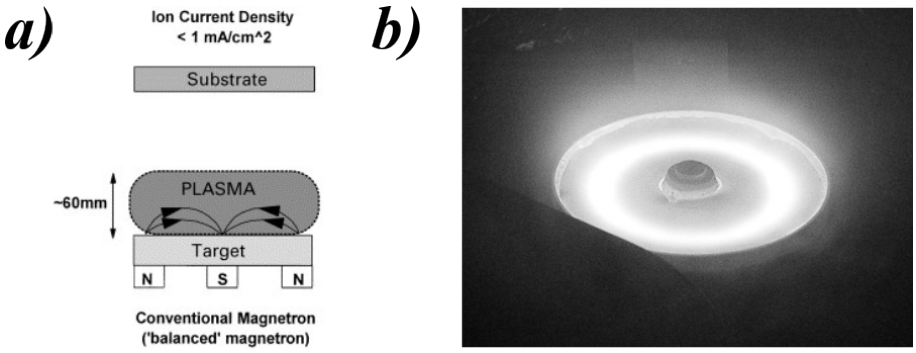


Figure 6.2 – **a)** Representation of the plasma's electrons trajectories, from [Kelly and Arnell, 2000] **b)** Picture of an operating magnetron sputtering target, extracted from [Bräuer et al., 2010].

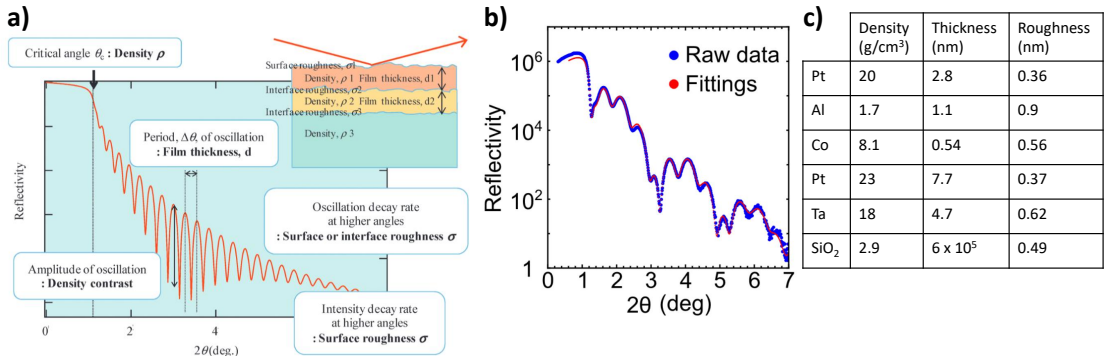


| | Density (g/cm³) | Thickness (nm) | Roughness (nm) |
|---|---|---|---|
| Pt | 20 | 2.8 | 0.36 |
| Al | 1.7 | 1.1 | 0.9 |
| Co | 8.1 | 0.54 | 0.56 |
| Pt | 23 | 7.7 | 0.37 |
| Ta | 18 | 4.7 | 0.62 |
| $SiO_2$ | 2.9 | 6 x $10^5$ | 0.49 |

Figure 6.3 – **a)** Summary of the different quantities available from an XRR measurement, from [Yasaka, 2010]. **b)** XRR measurement (blue) and fit (red) performed on a Pt(8 nm)|Co(0.7 nm)|Al(1.4 nm)|Pt(3 nm) sample. Parameters of that fit [Krishnia et al., 2023]

confines secondary electrons near the target.

At the Laboratoire Albert Fert, the magnetron plasma is generated from Ar atoms at a pressure of $2.5 \times 10^{-3}$ mbar and a DC power of less than 100 W. The chamber can accommodate up to seven targets simultaneously, allowing multilayered samples to be grown without air exposure. The substrate is positioned 75 mm away from the target, resulting in thickness inhomogeneities of less than 2 % across a 2-inch wafer. All samples presented in this thesis were grown at room temperature on Si|$SiO_2$ silicon substrates with thermally oxidized surfaces of 250 nm thickness. I conducted myself the growth of most of this thesis's samples.

### 6.2.2 . X-Ray Reflectivity (XRR)

X-Ray Reflectometry (XRR) is a non-destructive optical characterization technique for thin films. It measures parameters such as layer thickness, density, surface roughness, and

interface width. XRR is suitable for analyzing crystalline, polycrystalline, or amorphous samples with a total thickness of less than one micrometer.

An XRR measurement involves shining X-rays onto the sample's surface at varying incidence angles $\theta$ and measuring the specular reflection intensity at angle $\pi - \theta$. The resulting spectrum is expressed as a function of $2\theta$, the angle between the X-ray source and the detector. Since X-ray refractive index of silicon is slightly smaller than 1, the light undergoes total reflection below a certain angle $\theta_C$ (typically less than 1°, related to material density). Above this angle, the X-rays penetrate in the thin films and the intensity of the reflected beam decreases sharply. For $SiO_2$, no total reflection occurs (refractive index greater than 1).

As illustrated figure 6.3 **a**, the reflected beam results from the interference of rays reflected at the sample's different interfaces. As a consequence, varying $\theta$ produces oscillations patterns in the intensity, known as the Kiessig fringes. The period of these oscillations is inversely proportional to the thickness of each layer. Additionally, the decay of the total signal as well as the decrease of oscillations period with increasing $\theta$ are due to the various interfaces roughness [Yasaka, 2010].

The resulting XRR measurement is thus a complex signal which can be fitted to theoretical functions that account for the information contained in the reflectivity. Figure 6.3 **b** shows the XRR measurement of on one of our samples (Pt(8 nm)|Co(0.7 nm)|Al(1.4 nm)|Pt(3 nm)). The fit, obtained using dedicated software, extracts as parameters the thicknesses of the sample's different layers, and finds values slightly thinner than the nominal ones. We consider this differences to be reasonable since they are of less than 10 %.

Furthermore, this procedure reveals a typical roughness of about 0.37 nm at Pt|Co interface and 0.56 nm at Co|Al interface. Given the roughness of 0.49 nm at the substrate interface $SiO_2$|Ta, the roughness of the sputtering grown layers remains reasonable. XRR measurement of that sample has been performed by Sachin Krishnia.

### 6.2.3 . X-Ray Photoelectron Spectroscopy (XPS)

X-Ray Photoelectron Spectroscopy (XPS) is a powerful technique used to determine the chemical nature of elements in a sample as well as their bonding states. This method relies on the photoelectric effect, where an incoming radiation causes electrons to be emitted from the sample. During an XPS measurement, the energy of the incident photons is known, and the emitted electrons flux is measured as a function of their kinetic energy. This allows for the calculation of the binding energy $E_{binding}$ using the following equation :

$$E_{binding} = E_{photon} - E_{kinetic} \tag{6.1}$$

The binding energy represents the energy required to remove the electron from its electronic environment within the material. By analysing the spectrum, which exhibits peaks at the binding energies of the system's electrons, one can accurately identify the present

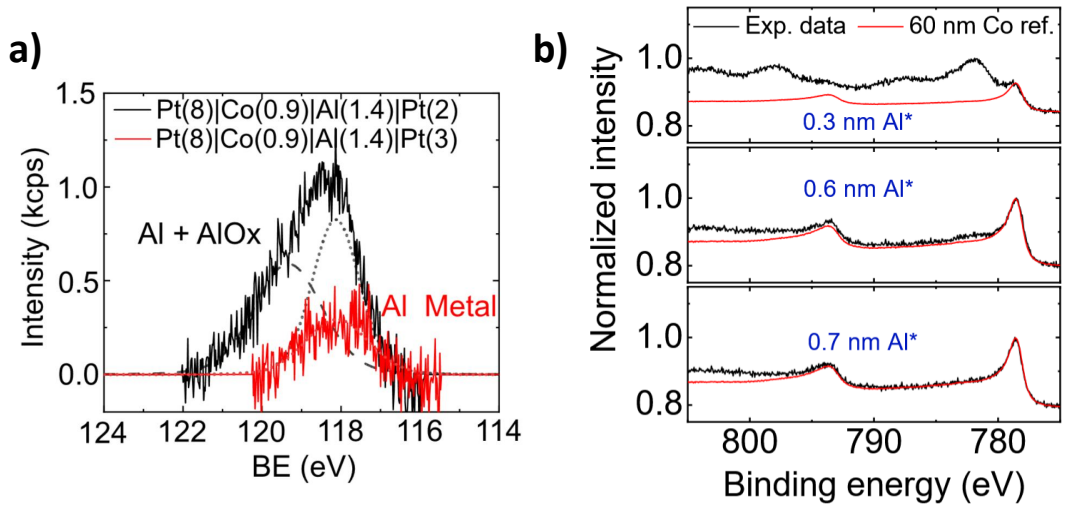


Figure 6.4 – **a**) XPS measurement carried out on our sample of Pt(8 nm)|Co(0.7 nm)|Al(1.4 nm)|Pt(3 nm) in red and Pt(8 nm)|Co(0.7 nm)|Al(1.4 nm)|Pt(2 nm), with thinner Pt capping, in black, from [Krishnia et al., 2023]. **b**) XPS spectra of Pt(8 nm)|Co(0.9 nm)|Al* with Al* thicknesses of 0.3, 0.6 and 0.7 nm near Co 2p binding energy, on our samples. Reference spectrum for 60 nm Co is shown in red. [Krishnia et al., 2025]

elements as well as their chemical bonds. However, a limitation of XPS is its surface sensitivity; electrons emitted from depths larger than nanometers are likely to scatter before reaching the surface and therefore are not collected by the detector.

Still, since our samples are in total a few nanometers thick, XPS is relevant for characterizing the oxidization state of the different buried layers. For instance, we have conducted a study to determine the thickness of Pt capping layer necessary to fully prevent the oxidization of Al. We measure the photoemission spectra around the Al 2s binding energy (around 118 eV) in samples Pt(8 nm)|Co(0.9 nm)|Al(1.4 nm)|Pt($t_{Pt}$), as shown in figure 6.4 **a**. For the sample with $t_{Pt} = 2\ nm$, the XPS peak could be fitted as a superposition of the Al 2s peak and Al 2s peak shifted due to Al-O bonding. However, when $t_{Pt} = 3\ nm$, only the Al 2s peak is present. From these results, we have concluded that a 3 nm Pt capping is sufficient to maintain the Al layer fully metallic, preventing its oxidization. Consequently, this is the Pt thickness that we have used for the capping layer in all our samples.

We have also used XPS to determine the oxidization degree of Co in Pt(8 nm)|Co(0.9 nm)|Al*($t_{Al*}$), where Al* represents Al exposed to air. As we reproduce figure 6.4 **b**), with 0.7 nm deposited Al*, the XPS spectrum around Co 2p binding energy matches very well that of 60 nm Co reference sample. However, with $t_{Al*} = 0.3$ nm (topmost plot), the XPS spectrum around Co 2p binding energy significantly deviates from the reference. This indicates Co oxidization. Notably, we observe a additional peak at 781.9 eV, that we attribute to CoO $2p_{3/2}$ electronic orbital. We interpret those results

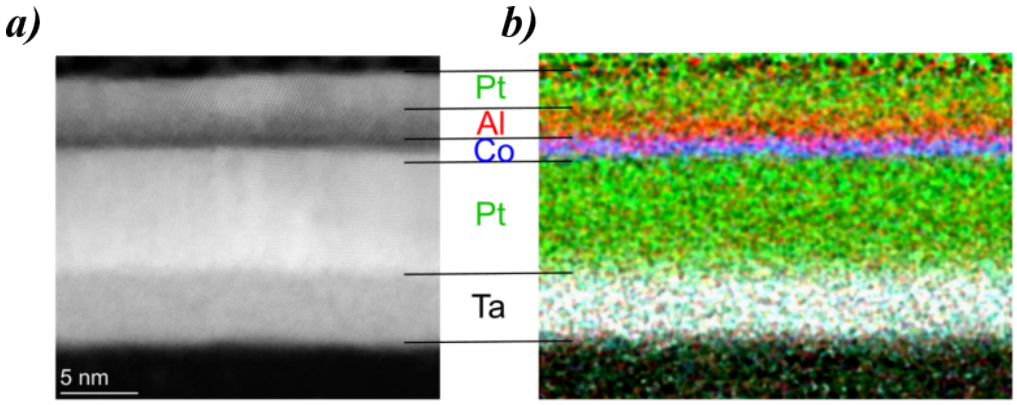


Figure 6.5 – **a)** HAADF image of a Pt(8 nm)|Co(0.7 nm)|Al(1.4 nm)|Pt(3 nm) and **b)** EDX elemental map of the same sample.

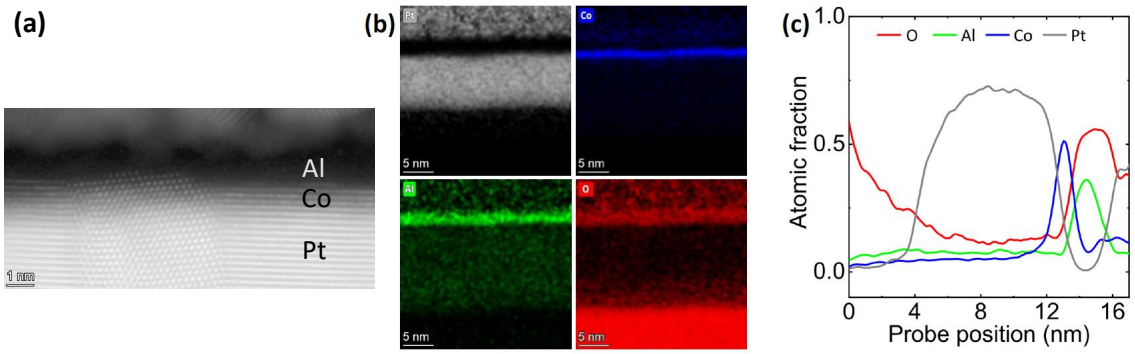


Figure 6.6 – **a**) HAADF image of Pt(8 nm)|Co(0.9 nm)|Al*(0.7 nm) sample. **b**) EDX element map of Pt (light gray), Co (blue), Al (green) and O (red) spatial distribution. **c**) Depth-profile of Pt, Al, Co and O atomic fractions integrated along the thickness. *Adapted from Ref. [Krishnia et al., 2025].*

as 0.7 nm of deposited $t_{Al*}$ to be enough to prevent any oxidization of Co. Besides, we measured the spectrum for $t_{Al*} = 0.6$ nm and noticed it exhibits a small peak at 781.9 eV. Hence, we conclude that 0.7 nm is the minimum Al thickness needed to maintain fully unoxidized metallic Co in samples free of any Pt capping.

### 6.2.4 . Scanning transmission electron microscopy

Scanning Transmission Electron Microscopy (STEM) is an imaging technique that offers very fine spatial resolution. The principle is to focus an electron beam, typically less than 1 Å in size, onto the sample [Crewe and Wall, 1970, Muller, 2009]. From the interaction of this beam with the sample, various signals can be collected and analysed, providing structural and chemical information at the atomic scale.

The interaction between the electron beam and the sample generates characteristic X-Rays [Goldstein et al., 2017] among other emitted radiations. Specifically, an electron from

the beam can eject an inner orbital (in K or L shell) electron from a sample atom, leaving it in an excited ionic state. One possible relaxation mechanism involves an outer shell electron transitioning to the inner orbital, emitting a photon with a precisely defined energy.

The X-rays emitted during a STEM experiment can be collected through Energy Dispersive X-ray spectroscopy (EDX) which measures the X-ray occurrence as a function of the photon's energy. This results in a spectrum with sharp peaks corresponding to the available energy transitions of the present atoms. From such a spectrum, the chemical nature of the atomic species present under the beam's spot can be accurately determined.

For even higher spatial resolution, High Angle Annular Dark Field (HAADF) imaging can be employed. This technique relies on collecting electrons from the incoming beam that have scattered on the nuclei of the sample's atoms [Otten, 1991]. These electrons are transmitted through the samples at wide angles, depending on the atomic number of the sample's atom. Measuring these electrons produces an image of the sample with sharp contrast between the different chemical species, although it provides less information about each element than EDX. Therefore the two techniques complement each other.

These experiments were conducted on our Pt|Co|Al|Pt ultrathin multilayers at the Forschungszentrum Jülich Ernst Ruska-Centre for Microscopy and Spectroscopy with Electrons, in collaboration with T. Denneulin. In figure 6.5 **a**), the sharp contrast between Pt, Al and Co layers is clearly visible. Additionally, figure 6.5 **b**), shows the elemental distribution obtained from EDX. We can clearly observe well separated Pt, Co and Al layers at the scale of the colorbar window. This indicates minimal intermixing between the layers and no oxidization of Al or Co.

In order to further assess the quality of our multilayers, we have also performed these characterisations on Pt(8 nm)|Co(0.9 nm)|Al*(0.7 nm) samples without Pt capping (figure 6.6). Here, Al is oxidized, in contrast with samples exhibited figure 6.5. On the HAADF image figure 6.6 **a**), we identify Pt and Co polycristalline nature and evaluate the typical grain size to be around 4 nm. The interfaces between the layers are still very sharp, indicating that intermixing is low. Pt atomic planes are even visible to be parallel to the surface, revealing the (111) orientation of Pt. The different elements distribution probed by EDX are displayed 6.6 **b-c**). The Co and AlOx layers are clearly distinct and the interface between the two is sharply marked.

## 6.3 . Magnetic properties of Pt|Co|Al* and Pt|Co|Al structures

Besides those detailed structural characterizations, measurements of the samples magnetic properties as well as *ab initio* caluclations were conducted. Saturation magnetization $M_s$ was measured using Superconducting Quantum Interference Device (SQUID) which enables to quantify the total magnetic moment of a sample. To gain further insights on the nature of magnetism, these measurements of the total magnetization have been complemented by X-Ray Magnetic Circular Dichroism (XMCD). This latter technique

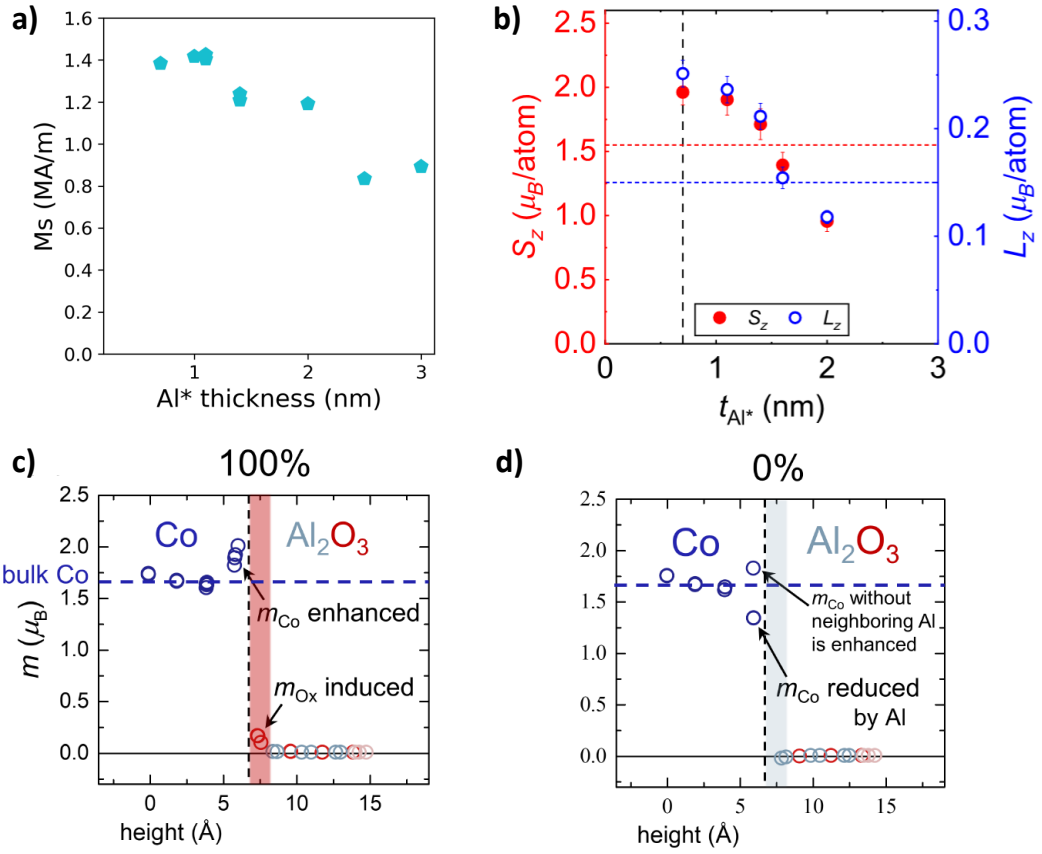


Figure 6.7 – **a**) Spontaneous magnetization measured by SQUID in Pt(8 nm)|Co(0.9 nm)|Al*($t_{Al*}$) samples. **b**) Spin magnetic moment (in red) and orbital moment (in blue) per atom deduced from XMCD measurements on the same samples. **c**) *Ab initio* profile of the magnetic moments expected at the fully oxidized interface between a Co layer and an Al layer. **d**) Same estimation via DFT for a fully metallic interface. *Adapted from Ref. [Krishnia et al., 2025].*

consists in measuring the difference in the sample absorption spectra for two X-Ray beams having opposite circular polarization. Through the "sum-rules" applied to the absorption rate at the $L_{2,3}$ edges, information can be deduced on the spin and orbital moments born per atoms of the magnetic sample. XMCD was performed at the DEIMOS line of the synchrotron SOLEIL in collaboration with Philippe Ohresser and Nicolas Jaouen.

The outcome of SQUID and XMCD combined investigations led on Pt|Co|Al* are shown figure 6.7 **a-b**). They are represented as a function of the air exposed Al* layer thickness. We show through XPS section 6.2.3 that as this thickness increase, the oxidization degree of the Co|Al interface decreases from full oxidization below $t_{Al*} = 0.7$ nm to full metallic character.

We observe a monotonous decrease in both $M_s$ and magnetic moment per atom when the Al* layer is grown thicker. Figure 6.7 **a)**, the $M_s$ decreases from 1.4 to 0.8 MA/m between 0.7 nm Al* (oxidized Co|Al* interface) and 3 nm Al* (metallic Co|Al* interface). This is a 70 % decrease. Figure 6.7 **b)**, spin magnetic moment per atom (red dots) drops from 1.9 $\mu_B$ to 0.9 $\mu_B$ while the orbital moment (blue circles) declines from 0.25 $\mu_B$ to 0.12 $\mu_B$. This is a reduction of a factor of two for those two quantities, larger than the $M_s$ reduction amplitude. We note that the proportion of orbital moment over spin moment remains roughly constant. The dotted horizontal lines figure 6.7 **b)** represent the magnetic moments, both spin (red) and orbital (blue) per atom of bulk Co.

From DFT calculations, this trend is reproduced as the oxidization degree of Co|Al interface is set from 100 % to 0 %. Calculations exhibit a competition between two effects occurring together and causing this magnetization weakening.

Most significantly, at oxidized Co|Al interface, interfacial Co spin magnetic moment is risen by 15 % (blue circles figure 6.7 **c**) and oxygen atoms acquire a magnetic moment, around 0.1 $\mu_B$ (red circles figure 6.7 **c)**). On the contrary, when the interface is fully metallic, interfacial Co is predicted to lose magnetic moment (blue circle figure 6.7 **d)**) and no moment arises in Al. This predicts a diminution of moment per atom as well as $M_s$ when increasing Al* thickness.

In opposition to this effect, metallic Al is expected to exert a positive strain on the Co layer. This positive strain is found from DFT calculations to induce a small increase of the magnetic moment born by Co. However, when transitioning from oxidized Co|Al* interface to the metallic case, this increase of magnetic moment is negligible compared to the increase predicted above [Krishnia et al., 2025]. Thus, *ab initio* calculations explain qualitatively the experimental trend.

Besides this Al* thickness dependence of the magnetic properties, we also conduct $M_s$ characterization, via room temperature SQUID, of samples with Pt capping and thus fully metallic Al. The resulting $M_s$ values are reported as a function of the Co thickness figure 6.8. We consider two series of samples : one with 1.4 nm Al : $\mathrm{Ta}(5\ \mathrm{nm})|\mathrm{Pt}(8)|\mathrm{Co}(t_{Co})|\mathrm{Al}(1.4)|\mathrm{Pt}(3)$ (fuchsia circles) and one with 3 nm Al :

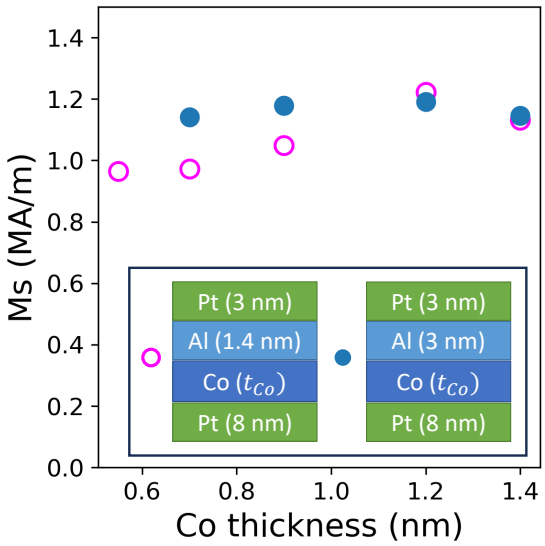


Figure 6.8 – Saturation magnetization measured by SQUID on two series of samples : $\mathrm{Ta(5\ nm)|Pt(8)|Co}(t_{Co})\mathrm{|Al(1.4)|Pt(3)}$ (fuchsia circles) and $\mathrm{Ta(5)|Pt(8)|Co}(t_{Co})\mathrm{|Al(3)|Pt(3)}$ (blue disks).

$\mathrm{Ta(5\ nm)|Pt(8)|Co}(t_{Co})\mathrm{|Al(1.4)|Pt(3)}$ (blue dots).

The two series were measured to have $M_s$ around 1.1 MA/m. Regarding the samples with 1.4 nm Al, we note a small increase in the $M_s$ values from 0.95 MA/m for 0.5 nm Co to 1.1 MA/m for 1.4 nm Co. The samples with 3 nm Al have $M_s$ values nearly independent on Co thickness. They are a little larger than that of 1.4 nm Al series and lie between 1.1 and 1.2 MA/m. We attribute the difference between the two series by the exalted strain exerted on the Co layer by 3 nm Al compared to 1.4 nm Al. This is consistent with the DFT calculations predicting an enhanced $M_s$ for a larger strain.

Together, XRR, XPS, XMCD, HAADF, EDX and SQUID demonstrate the high quality of the films we have grown with magnetron sputtering. The interfaces are very flat and each layer is well defined, with low intermixing. Moreover, the magnetic properties of Co are consistent with DFT calculations for layers as thin as less than 1 nm.

### 6.3.1 . PMA property

The PMA properties have been investigated in all characterized samples using first harmonic hysteresis loops of Hall resistance. As discussed in the section 6.1.2, PMA is expected to be maximal in samples with optimized Co|Al oxidization, where Co-O bonds are uniformly formed without in depth Co oxidization. From our XPS analysis, we have identified this condition to be reached for the Pt|Co|Al*(0.7 nm) sample (refer to section 6.2.3).

However, our study reveal a strikingly more complex behavior. The red dots figure 6.9 **a**) show that the measured magnetic anisotropy of Co in Pt|Co|Al* decreases when Al* is

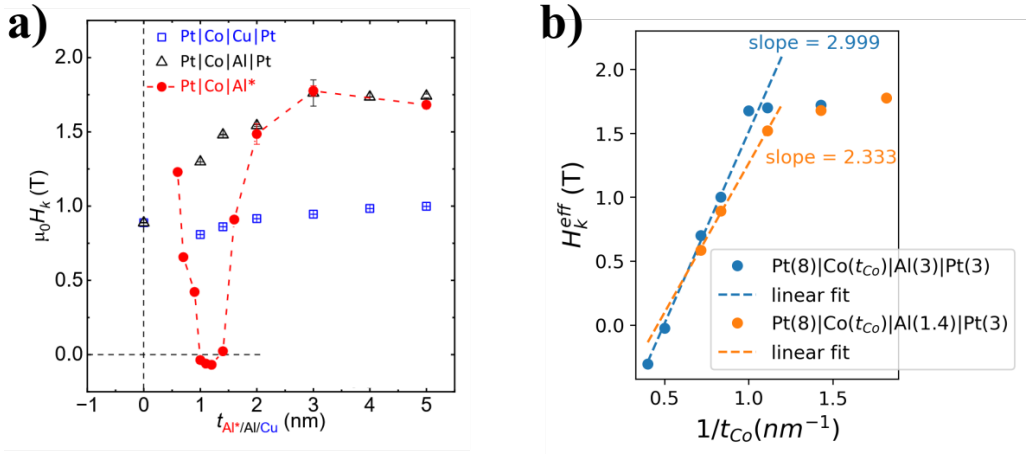


Figure 6.9 – **a**) Magnetic anisotropy effective fields measured in three series of sample. One reference series of Pt(8 nm)|Co(0.9 nm)|Cu($t_{Cu}$)|Pt(3 nm); a series of Pt(8 nm)|Co(0.9 nm)|Al($t_{Al}$)|Pt(3 nm) where Co|Al is metallic in all samples; and one series Pt(8 nm)|Co(0.9 nm)|Al*($t_{Al*}$) where oxidization of the interface varies with Al* thickness. *Extracted from Ref. [Krishnia et al., 2025].* **b**) Magnetic anisotropy effective fields in series where the Co layer thickness varies. Both series have Pt capping and they differ by the Al layer thickness.

grown thicker than 0.7 nm down to losing PMA for Al* thicker than 1 nm. Yet, in samples with $t_{Al*} > 1.4\,nm$, the anisotropy undergoes another sign change. The samples with $t_{Al*} > 1.4\,nm$ possess strong PMA, stronger than Pt|Co|Al*(0.7 nm), despite their pure metallic Co|Al interface.

The evolution of anisotropy in this sample series can be compared to those capped with 3 nm Pt, preventing any oxidization of Al as described earlier. When the Al thickness is varied, Al remains metallic, and the anisotropy corresponds to out of plane magnetization without exhibiting any sign change (black triangles on figure 6.9 **a**). Compared to the reference sample without Al (Pt(8 nm)|Co(0.9 nm)|Pt(3 nm)), whose anisotropy is $H_k^{eff} = 0.75\,T$, the effective anisotropy field increases with the addition of Al, reaching a maximum of $1.72$ T at $t_{Al} = 3\,nm$. It is remarkable that the metallic Al induced anisotropy surpasses that induced by Pt or AlOx.

For Al layers thicker than 2 nm, the effective anisotropy of Pt capped and uncapped samples perfectly overlap. This indicates that the mechanism leading to the second PMA sign change in the Pt|Co|Al* series does not involve oxygen orbitals and that metallic Al grown on Co plays a particular role.

Additionally, we compare figure 6.9 **a**) the anisotropy arising from Co|Al interface with samples without Al : Pt|Co|Cu|Pt, represented by blue squares. While increasing Cu thickness, the anisotropy remains stable and roughly equal to reference sample Pt|Co|Pt. In contrast, it increases by roughly a factor 2 when $t_{Al}$ is raised. We confirm from that com-

parison that the anisotropy strength in Al samples can not be explained by sole Pt|Co interface, which is common to the two series, and highlight the crucial role played by Al atoms in this system while Cu remains neutral regarding PMA.

In figure 6.9 **b**), the effective anisotropy fields are plotted as a function of the inverse of Co thickness. For Co thicknesses comprised between 0.9 nm and 2.5 nm (1.1 $nm^{-1}$ and 0.4 $nm^{-1}$), it exhibits a linear relationship of the form $t_{Co}^{-1}$. That is consistent with the model distinguishing bulk anisotropy, demagnetizing field and surface anisotropy (equation 3.5) :

$$H_k^{eff} = \left(H_k^{\mathcal{V}} - M_s\right) + \frac{1}{\mu_0}\frac{K^s}{M_s t_{Co}} \tag{6.2}$$

Fitting a straight line to these experimental data, we find that the slope of the series with 1.4 nm of Al is of 2.3 T.nm, a fifth lower than that of samples with 3 nm Al (3.0 T.nm). This confirms that the maximum in anisotropy as a function of Al thickness for $t_{Al} = 3$ nm figure 6.9 **a**) stems from surface anisotropy. We note that samples with Co thinner than 0.8 nm do not fit with the same straight line. Still, their anisotropy is also linear in $t_{Co}^{-1}$.

In conclusion, our measurements of PMA varying the thicknesses of different layers in our samples demonstrate that the coupling between Co and Al generates an additional magnetic surface anisotropy. This anisotropy can not arise from the same mechanism than previously proposed for Co|AlOx. It involves neither oxygen nor strong SOC material.

### 6.3.2 . DMI in Co|AlOx

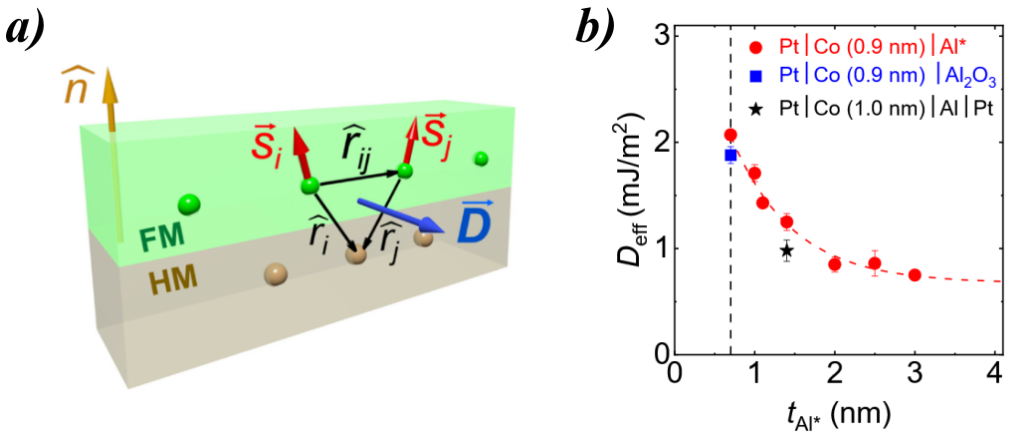


Figure 6.10 – **a**) Scheme of DMI at a ferromagnetic and heavy metal interface. Anti-symmetric exchange is mediated by the heavy metal SOC [Kuepferling et al., 2023]. **b**) Values of DMI reported in [Krishnia et al., 2025] in Pt|Co(0.9 nm)|Al* (red dots). The blue square is Pt|Co(0.9 nm)|$Al_2O_3$ from Ref. [Belmeguenai et al., 2015] and the star is Pt|Co(1.0 nm)|Al(1.4 nm)|Pt(3 nm), where Al is purely metallic, from [Ajejas et al., 2022] corrected for ferromagnetic thickness.

Apart from the PMA properties previously described, the interfacial Dzyaloshinskii–Moriya Interaction (i-DMI) is also at the forefront of actual nanomagnetism research. Also known

as antisymmetric exchange, the DMI between two spins is represented in the following Hamiltonian :

$$\mathcal{H}_{DMI} = \mathbf{D}_{ij} \cdot (\mathbf{S}_i \times \mathbf{S}_j) \tag{6.3}$$

To be non-zero, this interaction requires inversion symmetry breaking in the presence of SOC and is hence expected to arise at the interfaces of ferromagnetic layers and heavy metals [Fert, 1990]. DMI is anticipated to play a crucial role in the development of spintronic technologies since it determines a chirality in the spin texture. This chirality has been shown to stabilize topological spin textures such as skyrmions [Fert et al., 2013], enable fast domain wall motion [Thiaville et al., 2012] and play a role in magnetization switching [Baumgartner et al., 2017].

In addition to PMA, DMI has been measured to be particularly strong in Pt|Co|AlOx systems, with values of $D$ close to 2 pJ/m [Belmeguenai et al., 2015, Kuepferling et al., 2023]. However, studies involving the Co|AlOx interface have reported a broad range of different values, from 0.5 to 2.5 pJ/m [Kim et al., 2017, Lo Conte et al., 2017]. Therefore, our system provides an excellent platform for investigating DMI as a function of the oxidization degree of Co|Al interface.

The i-DMI has been evaluated in our samples by Brillouin light scattering (BLS) (collaboration with A. Thiaville, LPS, Orsay). It was measured in Pt|Co|Al* samples, where Al* is a layer of aluminium exposed to air of varying thicknesses, as shown figure 6.10 **b)**. We show that sample Pt|Co(0.9 nm)|Al*(0.7 nm) has a strong effective DMI greater than 2 mJ/m$^2$. DMI then decreases as Al* thickness is increased from 0.7 nm to 2 nm where it reaches a saturation value of 0.8 mJ/m$^2$ (refer to figure 6.10 **b**) [Krishnia et al., 2025]. The i-DMI measured in our samples closely match measurements from previous studies in the oxidized regime (blue square figure 6.10 **b**, [Belmeguenai et al., 2015]) and metallic regime (black star, [Ajejas et al., 2022]).

This DMI reduction as the interfacial oxidization decreases is predicted from DFT calculations performed by our collaborators from SPINTEC (L., Vojacek, M. Chshiev). The calculations show that as the oxygen content of the interface is increased, a charge transfer operates from Co atoms to O. This induces interfacial charge dipole. Such dipole is responsible for an i-DMI which adds up to that emerging at bottom Pt|Co interface. This occurs through the Rashba type i-DMI mechanism [Belabbes et al., 2016, Yang et al., 2018]. More details on this experiment and calculations can be found in [Krishnia et al., 2025].

## 6.4 . Transport properties (AHE) of SOT layers

In this section, we describe in details the anomalous Hall effect (AHE) properties of the multilayers used in SOT characterizations. Our motivation is guided by the particular aspect that in CIP, both electron and spin experience the same boundary conditions (reflection/transmission/loss) than in a normal injection geometry adapted to model SOT (CPP).

We introduce two types of electronic processes to describe the relevant scattering events. On one hand, spin-current proximity effects are generated throughout the structures in the CIP geometry. On the other hand, we propagate the out-of-equilibrium Fermi distribution from interfaces. This is denominated as the "non-local (transverse) conductivity" as proposed by [Zhang and Butler, 1995], pioneered by the so-call Fuchs-Sondheimer [Sondheimer, 2001] approach and extended it to the case of two spin-channels.

### 6.4.1 . Spin-dependent scattering properties

In ferromagnetic layers, AHE via the acquisition of both longitudinal ($R_{xx}$) and transverse ($R_{xy}$) resistances, provide a deep knowledge of bulk and interface physical properties. It makes the most of the relation between spin-orbit assisted electron scattering at the nanometer scale within each layer's bulk (magnons, phonons, impurities...) and scattering at the interfaces. These different contributions can be modeled in an "extended Fuchs-Sondheimer" model involving spin polarized conducting electrons (Camley-Barnas framework [Camley and Barnaś, 1989]) and spin-orbit mediated interactions.

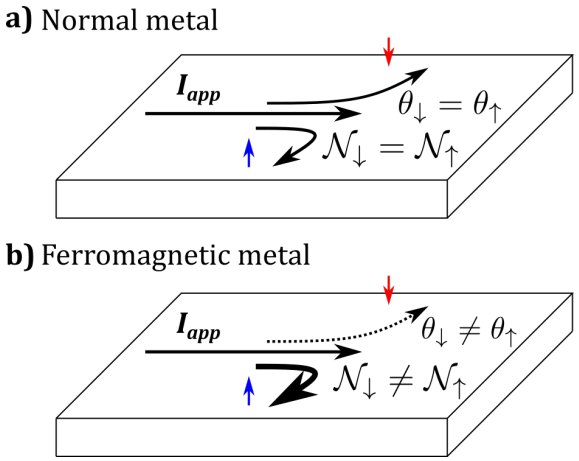


Figure 6.11 – Comparison between **a**) in plane SHE in a normal metal and **b**) in plane AHE in a ferromagnetic metal. $\mathcal{N}_\uparrow$ and $\mathcal{N}_\downarrow$ respectively designate $up$ and $donw$ spins.

For this thesis, we thus model AHE resistances in a spin-dependent in-plane current geometry (CIP) transport model. The longitudinal and transverse resistances of Hall bars of dimensions $L \times W$ are respectively given by [Dang et al., 2020] :

$$R_{xx} = \frac{L}{W} \frac{1}{\sum_{i,s} \sigma_{xx}^{i,s} t_i} \tag{6.4}$$

and

$$R_{xy} = \frac{\sum_{i,s} \sigma_{xy}^{i,s} t_i}{\left(\sum_{i,s} \sigma_{xx}^{i,s} t_i\right)^2} \tag{6.5}$$

with $\sigma_{xx}^{i,s} = \sigma_{xx}^{i,\uparrow,\downarrow}$, $\sigma_{xy}^{i,s} = \sigma_{xy}^{i,\uparrow,\downarrow}$ and $t_i$ the respective spin-dependent longitudinal, transverse conductivities and thickness of each layer ("$(i)$") constituting the stack.

Following T.-H. Dang et al. [Dang et al., 2020], in the CIP geometry, the strategy for the AHE calculations in multilayers consists in :

1. A representation of the profile of the charge and spin polarized current channels inside the whole multilayer through an out-of-equilibrium Fermi distribution $f_s(z,k) = f_{s,0}(z,k) + \delta f_s(z,k)$ with $\delta f_s(z,k) = \sum g_s^{i,j}(z,k)$ a perturbation of the distribution function introduced by interfaces between two materials (of index 'i' and 'j=i$\pm$ 1'). The source of spin currents in this system is the spin-polarization of the bulk part of the ferromagnet. In turn, it leads to spin injection in the adjacent non magnetic layers by proximity effect such that spin currents are not strictly confined into the ferromagnet. Nevertheless, the spin-dependent interfacial transmission is also included in the present model.
2. Accounting for the occurrence of electron scattering at the different interfaces, described by spin dependent reflections and transmissions which are partially non-specular [Stewart et al., 2003].
3. The presence of heavy metal layers (such as Pt) introduces an additional contribution to the spin-orbit assisted scattering processes to the ones existing in the Co layer, and is another source of transverse current.

According to those considerations, the procedure to obtain the change in the AHE originating from interfaces is to consider a self-consistent solution for $g_s(z,\mathbf{k})$ in each separate layer satisfying :

$$g_s(z,\mathbf{v}) = \begin{cases} \frac{eE_x\tau^s}{m^*}\frac{\partial f_{s,0}(\mathbf{v})}{\partial v_x}\left[1 + A_-^s(\mathbf{v})\exp\left(-\frac{z}{\tau^s|v_z|}\right)\right] & \text{for } v_z > 0 \\ \frac{eE_x\tau^s}{m^*}\frac{\partial f_{s,0}(\mathbf{v})}{\partial v_x}\left[1 + A_+^s(\mathbf{v})\exp\left(+\frac{z}{\tau^s|v_z|}\right)\right] & \text{for } v_z < 0 \end{cases} \tag{6.6}$$

with $m^*$ the effective mass, $v_z$ the electron velocity at the Fermi level, $\tau_s$ the spin-dependent momentum scattering time, and where $A_+^s(\mathbf{k})$ and $A_-^s(\mathbf{k})$ are the two spin-dependent constants to find to match the boundary conditions ($E_x$ is the electric field along the $\hat{x}$ direction), leading to exponential evanescence of the distribution functions near interfaces. The current density for the spin $s$ is given by :

$$J_s(z) = e\left(\frac{m^*}{\hbar}\right)^3 \int_{\mathcal{V}} v_x g_s(z,\mathbf{v})\, d^3\mathbf{v}$$

where $\mathcal{V}$ is the unit volume of the 3D velocity space and including the result that $f_s(z,\mathbf{k}) = f_{s,0} + g_s(z,\mathbf{k})$ ($f_{s,0}$ is the Fermi-Dirac distribution at equilibrium ).

In the following, we use this model to extract transport parameters of our multilayers from experimentally obtained values of AHE as a function of the different layers thicknesses. Section 6.6, we rely on those parameters to model the SOT arising in Pt|Co|Al|Pt thin films.

### 6.4.2 . Extracting interfacial parameters from AHE

We model the interlayer spin-dependent electronic diffusion in our multilayers applying equivalent multiscattering approach, as than the one described more extensively in section 6.6 for CPP transverse spin-currents. This framework accounts for the considerations explained above as well as multiscattering processes experimented at the various interfaces. From this model, we are able to quantitatively predict AHE in three series of samples reported in figure 6.12

Figure 6.12 presents AHE resistances ($\mathrm{R_{AHE}}$) measurements obtained for various stacking sequences as a function of layer thicknesses. In figure 6.12 **a**) the dependence of AHE on the Co thickness ($t_{Co}$) in $\mathrm{Ta(5)|Pt(8)|Co}(t_{Co})\mathrm{|Al(1.4)|Pt(3)}$ and $\mathrm{Ta(5)|Pt(8)|Co}(t_{Co})\mathrm{|Al(3)|Pt(3)}$ is displayed. It emphasizes an increase of AHE with $t_{Co}$ for the two series (Al 1.4 and Al 3 nm). Regarding equation 6.5 numerator $\sigma_{xy,\mathrm{Co}}$, such $R_{xy}$ behavior manifests the gradual rise of the spin-current polarization in ultrathin Co as Co layer is made thicker [Bony et al., 2025]. This polarization is smaller in the thinnest samples due to spin-memory loss occurring during electron scattering at interfaces (Fuchs-Sondheimer model). From the denominator $\sigma_{xx,\mathrm{Co}}t_{Co}$ perspective, once electronic polarization saturates at $t_{Co} > 2.5$ nm (mean-free path of the electrons in Co), $R_{xy}$ decreases proportionally to $1/t_{Co}$. We do not reach this regime in figure 6.12**a** but observe the saturation of $R_{AHE}$.

We also note that AHE appears larger for 1.4 nm Al compared to 3 nm Al. This is partially to be assigned to an additional current shunting channel in Al. Note that Al in itself has also previously been observed to be detrimental to spin transmission between Co and Pt, also as reported in [Sharma et al., 2008]. We investigate this property in figure 6.12**b**) through AHE resistance $R_{xy}$ as a function of Al thickness in $\mathrm{Ta(5)|Pt(8)|Co(0.9)|Al}(t_{Al})\mathrm{|Pt(3)}$. We observe a rapid drop of $R_{xy}$ from 120 mΩ to 55 mΩ when a thin 1 nm Al (or thinner) is inserted between Co and the top Pt. This behavior confirms that Al prevents the electron spin transmission between Co and Pt. AHE then reduces slowly as $t_{Al}$ increases since Al does not contribute to transverse transport but only causes a small current shunting in this "thin" regime ($t_{Al} < 5$ nm).

Finally, figure 6.12 **c**) shows how AHE is dependent on the thickness ($t_{Pt}$) of bottom Pt SHE layer. AHE decreases from $130\ m\Omega$ to $26.5\ m\Omega$ when bottom Pt thickness is increased from 2 nm to 8 nm. Since the thicknesses of Pt in those samples are typically larger than the spin mean-free path ($\lambda^{Pt} \simeq 1.5$ nm), the resulting decrease of AHE with $t_{Pt}$ is due to current shunting in added Pt.

The analysis of the AHE data using our scattering model (dotted lines figure 6.12) allow us

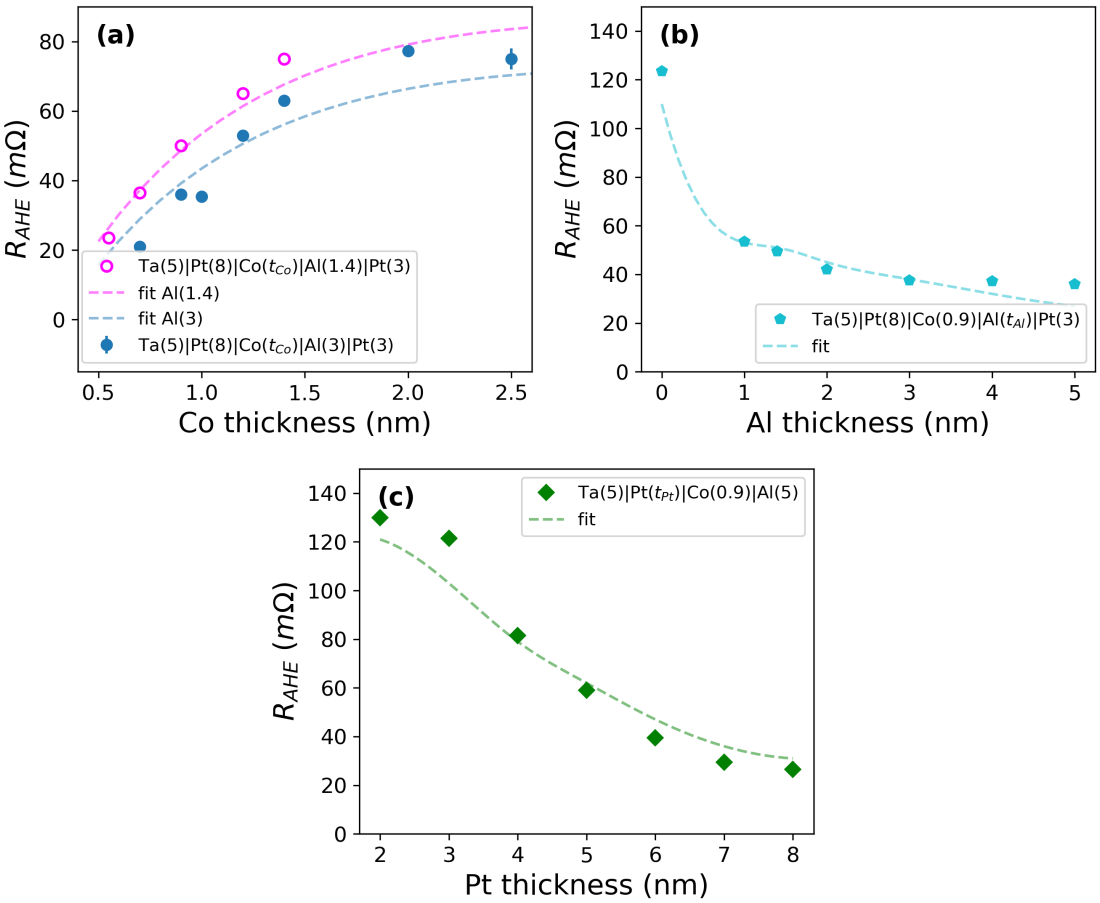


Figure 6.12 – AHE resistances measured in series of multilayers. **a**) Co thickness variations in $\mathrm{Ta}(5)|\mathrm{Pt}(8)|\mathrm{Co}(t_{Co})|\mathrm{Al}(1.4\text{ or }3)|\mathrm{Pt}(3)$. **b**) Plot of AHE resistance as a function of Al thickness in $\mathrm{Ta}(5)|\mathrm{Pt}(8)|\mathrm{Co}(0.9)|\mathrm{Al}(t_{Al})|\mathrm{Pt}(3)$. **c**) The thickness of bottom Pt layer is varied in $\mathrm{Ta}(5)|\mathrm{Pt}(t_{Pt})|\mathrm{Co}(0.9)|\mathrm{Al}(5)$. Fits obtained from our model are represented by the dotted lines.

to estimate the parameters at the various interfaces. These parameters are reported in table 6.1 along with the corresponding error bars.

The transmission coefficients that we induce from AHE are especially helpful for a SOT model. We find them to be particularly spin polarized in the Pt|Co and Co|Cu interfaces (0.9 for majority spins in the two case and respectively 0.4 and 0.3 for minority spins). In contrast, we find a considerably lower transmission for both spin channels at Co|Al interface. Regarding the capping Pt layer, we come up with a relatively large transmission of 0.6 between Pt and Cu while it is significantly quenched to the value of 0.2 when Cu is replaced by Al. This is consistent with the picture of Al preventing spin diffusion between Co and Pt while Cu is relatively transparent.

We also arrive at quantifying the spin memory loss parameters $\delta$, with notably $\delta = 0.4$ at Pt|Co and Cu|Pt interfaces and $\delta = 0.25$ at Co|Cu. This corresponds to depolarization probabilities (1-$e^{-\delta}$) of respectively 33 % and 22 %. The derived $\delta$ value for Co|Cu is close to the estimation of 0.25 in [Eid et al., 2002], while we find significantly lower $\delta$ for Pt|Co and Cu|Pt than [Nguyen et al., 2014] (0.9 for Pt|Co) [Kurt et al., 2002] (0.9 for Cu|Pt at low temperature).

These information are precious for a fair determination of the SOT extracted from our model 6.6. In particular, the role of the specularity in both reflection and transmission will be largely discussed in the chapter 9 dealing with CoFeB.

| Parameters | Symbols | Values for ↑ spin | Value for ↓ spin |
|---|---|---|---|
| Co conductivity | $\sigma_{Co}$ | $\frac{\sigma_{Co}}{2(1-\beta_{Co})} = 7.4 \pm 1.0 \times 10^6$ | $\frac{\sigma_{Co}}{2(1+\beta_{Co})} = 1.6 \pm 0.3 \times 10^6$ |
| Cu conductivity | $\sigma_{Cu}$ | $1.3 \pm 0.3 \times 10^7$ | $1.3 \times \pm 0.310^7$ |
| Pt conductivity | $\sigma_{Pt}$ | $2.5 \pm 0.5 \times 10^6$ | $2.5 \pm 0.5 \times 10^6$ |
| Al conductivity | $\sigma_{Al}$ | $7 \pm 1 \times 10^6$ | $7 \pm 1 \times 10^6$ |
| | | | |
| mean free path of Co | $\lambda_{Co}$ | $7.0 \pm 1$ | $2.0 \pm 0.3$ |
| mean free path of Cu | $\lambda_{Cu}$ | $7.0 \pm 1$ | $7.0 \pm 1$ |
| mean free path of Pt | $\lambda_{Pt}$ | $2.0 \pm 0.5$ | $2.0 \pm 0.5$ |
| mean free path of Al | $\lambda_{Al}$ | $6.0 \pm 1.5$ | $6.0 \pm 1.5$ |
| | | | |
| Pt/Co int. transmission | $\mathcal{T}_{Pt/Co}$ | $\frac{\mathcal{T}_{Pt/Co}}{1-\gamma_{Pt/Co}} = 0.9 \pm 0.1$ | $\frac{\mathcal{T}_{Pt/Co}}{1+\gamma_{Pt/Co}} = 0.4 \pm 0.1$ |
| Co/Cu int. transmission | $\mathcal{T}_{Co/Cu}$ | $\frac{\mathcal{T}_{Co/Cu}}{1-\gamma_{Co/Cu}} = 0.9 \pm 0.05$ | $\frac{\mathcal{T}_{Co/Cu}}{1+\gamma_{Co/Cu}} = 0.3 \pm 0.1$ |
| Co/Al int. transmission | $\mathcal{T}_{Co/Al}$ | $\frac{\mathcal{T}_{Co/Al}}{1-\gamma_{Co/Al}} = 0.1 \pm 0.05$ | $\frac{\mathcal{T}_{Co/Al}}{1+\gamma_{Co/Al}} = 0.1 \pm 0.05$ |
| Cu/Pt int. transmission | $\mathcal{T}_{Cu/Pt}$ | $\mathcal{T}_{Cu/Pt} = 0.6 \pm 0.1$ | $\mathcal{T}_{Cu/Pt} = 0.6 \pm 0.1$ |
| Al/Pt Interface transmission | $\mathcal{T}_{Al/Pt}$ | $\mathcal{T}_{Al/Pt} = 0.2 \pm 0.1$ | $\mathcal{T}_{Al/Pt} = 0.2 \pm 0.1$ |
| | | | |
| Pt/Co spin-memory loss | $\delta_{Pt/Co}$ | $0.4 \pm 0.1$ | |
| Co/Cu spin-memory loss | $\delta_{Co/Cu}$ | $0.25 \pm 0.1$ | |
| Cu/Pt spin-memory loss | $\delta_{Cu/Pt}$ | $0.4 \pm 0.1$ | |
| Co/Al spin-memory loss | $\delta_{Co/Al}$ | negligible | |

Table 6.1 – Physical parameters for bulk Pt, Co, Cu and Al and their interfaces extracted from our AHE fitting procedure. The conductivities $\sigma$ are given in the unit of S.cm$^{-1}$ and the electronic mean free path ($\lambda$) in the unit of nm. $\gamma_{A/B}$ is the spin-asymmetry coefficient at the interface between layers A and B. $\delta$ is the corresponding spin-memory loss coefficient.

## 6.5 . SOT integrating metallic Co|Al interface

In this section, we present the main experimental spin-orbit torque (SOT) results integrating Co|Al interfaces. We also describe a theoretical description and model of transverse spin-currents (inducing torque) within the whole structures. Unlike the previous section, which focused on spin currents associated with the AHE in the CIP configuration, this analysis addresses the dynamics of spin currents in the CPP geometry.

### 6.5.1 . SOT enhancement from Co|Al interface light metal thickness dependence

In Figure 6.14 we present the effective SOT fields measured in the series of samples Pt|Co|Al($t_{Al}$)|Pt and Pt|Co|Cu($t_{Cu}$)|Pt (as the reference sample series). The results for the two series are drastically different. Compared to quasi-symmetric reference sample Pt|Co|Pt ($\mathrm{t_{Al/Cu}} = 0\,\mathrm{nm}$), inserting Cu on top of cobalt slightly increases both SOT components. However, increasing the thickness of this Cu layer from 1 nm to 5 nm does not significantly affect the SOT.

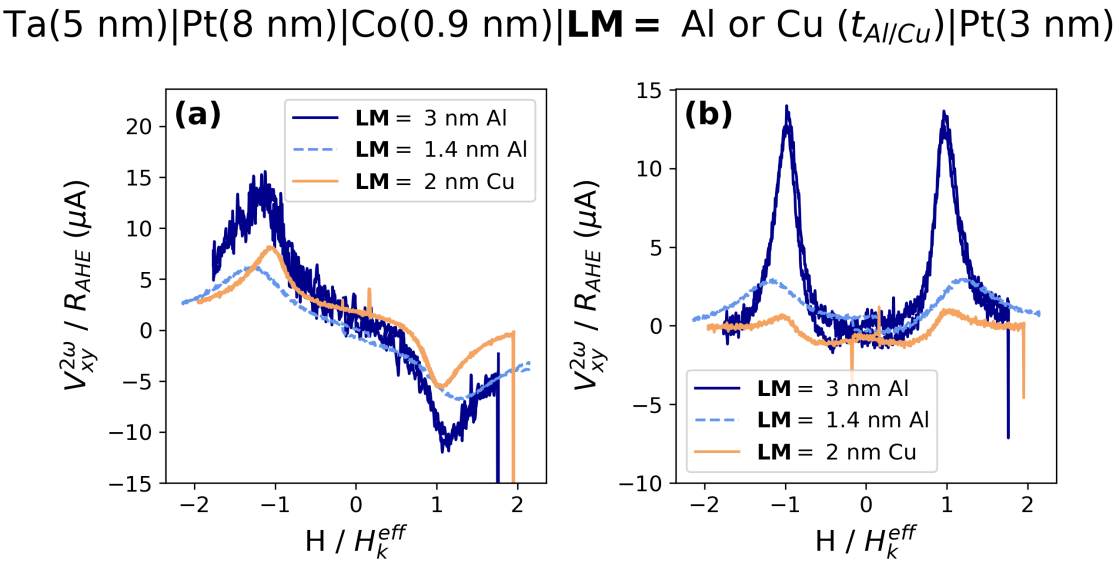


Figure 6.13 – **a**) Raw second harmonic signals obtained while applying a magnetic field parallel to the current lines ("damping-like torque" configuration) with a slight out of plane disorientation in Ta(5 nm)|Pt(8 nm)|Co(0.9 nm)|**LM**|Pt(3 nm). **LM** being 3 nm Al, 1.4 nm Al or 2 nm Cu. **b**) Same with field applied orthogonal to current ("field-like torque" configuration)

In contrast, when Al is grown between Co and the capping Pt layer, SOT increase considerably. The Damping-like torque effective field increases by a factor of five, while the field like component increases by one order of magnitude. This substantial increase in SOT can be partially attributed to Al preventing spin propagation from the capping Pt layer into the

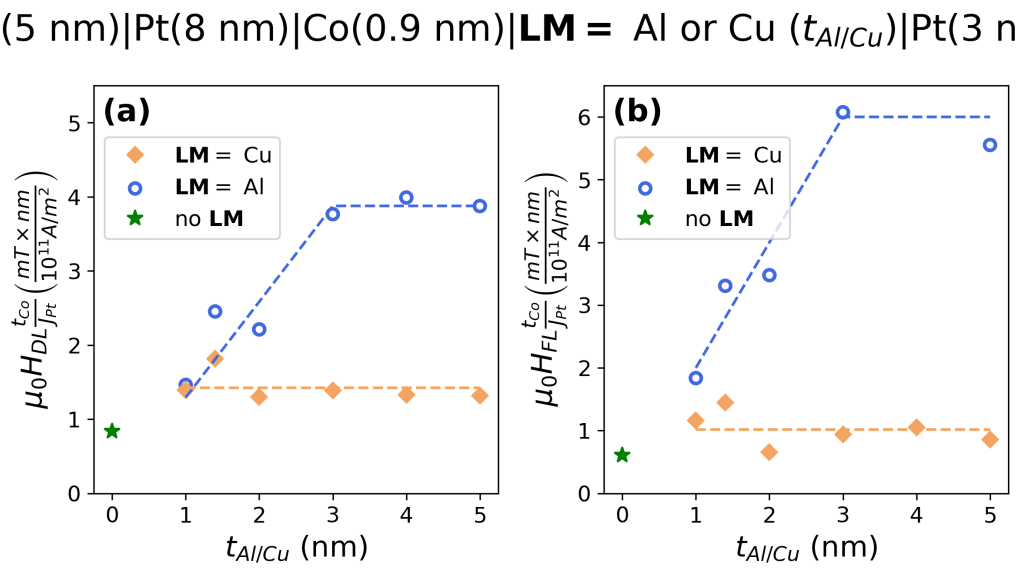


Figure 6.14 – **c)** Damping-like torque effective fields measured in Pt(8 nm)|Co(0.9 nm)|Al($t_{Al}$)|Pt(3 nm) (red dots) and Pt(8 nm)|Co(0.9 nm)|Cu($t_{Cu}$)|Pt(3 nm). **d)** Field-like torque effective fields measured in the same series of samples. *Adapted from Ref. [Krishnia et al., 2023].*

Co layer, as previously discussed.

Indeed, in our multilayers, significant SOT arises from SHE in Pt. In the reference sample Pt(8 nm)|Co|Pt(3 nm), SHE from the two Pt layers partially cancels out by 60%. We can model this with an effective spin Hall angle $\theta_{SHE}^{eff}$ summing the bottom and capping Pt contributions :

$$\theta_{SHE}^{eff} = \theta_{SHE}^{Pt} \exp(-\delta) \left(\mathcal{F}(t_{Pt} = 8 \text{ nm}, \mathcal{T}_{Co|Pt}) - \mathcal{F}(t_{Pt} = 3 \text{ nm}, \mathcal{T}_{Co|LM|Pt})\right) \quad (6.7)$$

where $\delta$ is the interfacial spin memory loss and $\mathcal{F}(t_{Pt}, \mathcal{T})$ quantifies the spin-backflow in Pt and the interface transmission. It approximates to :

$$\mathcal{F}(t_{Pt}, \mathcal{T}) = \frac{(\mathcal{T} G_{sh})\, r_s^{Pt} \tanh\left(\frac{t_{Pt}}{2\lambda_{sf}^{Pt}}\right)}{1 + (\mathcal{T} G_{sh})\, r_s^{Pt} \coth\left(\frac{t_{Pt}}{\lambda_{sf}^{Pt}}\right)}$$

where $\lambda_{sf}^{Pt}$ and $r_s^{Pt} = \rho_{Pt} \times \lambda_{sf}^{Pt}$ are the respective spin-diffusion length and spin-resistance of Pt. $(\mathcal{T} G_{sh}) = G_{\uparrow\downarrow}$ is the so-called spin-mixing conductance, product of the Sharvin conductance ($G_{sh}$) with the transmission coefficient of the transverse spin component ($\mathcal{T}$). It is clearly visible from those equations that preventing transmission from capping Pt to Co enhances SOT. We attribute part of the SOT increase in the Al based samples to this effect : $\mathcal{T}_{Co|Al|Pt}$ diminishes when Al thickness increases as shown by AHE measurements

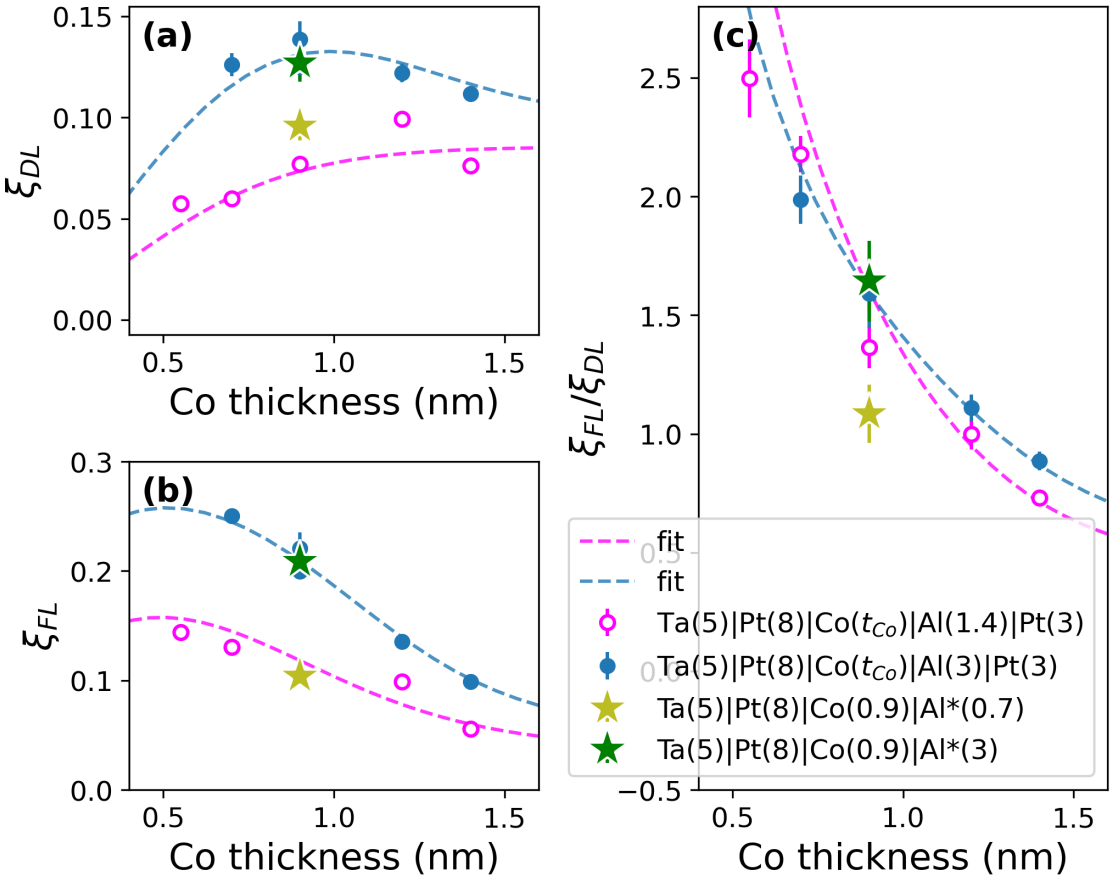


Figure 6.15 – **a**) Damping-like SOT efficiencies measured in Pt(8 nm)|Co($t_{Co}$)|Al(1.4 nm)|Pt(3 nm) (pink empty circles) and Pt(8 nm)|Co($t_{Co}$)|Al(3 nm)|Pt(3 nm) (blue filled circles). The two stars correspond to samples without Pt capping, with 0.9 nm Co thickness and 0.7 or 3 nm of air exposed Al. **b**) Field-like SOT efficiencies. **c**) Ratio of the two components.

(cf. figure 6.12 **(b)**). Meanwhile, the Cu layer is mostly transparent to spin diffusion over a few nanometers. $\mathcal{T}_{Co|Cu|Pt}$ barely varies with Cu thickness and is close to $\mathcal{T}_{Co|Pt}$ (table 6.1). As a consequence, there is a much smaller increase in the SOT with Cu inserted. A more detailed description of our electronic transport model can be found section 6.6.

### Co thickness dependence

To further understand SOT generation in our system, we also measure the dependence of SOT on the cobalt layer thickness $t_{Co}$. We display figure 6.15 the obtained SOT efficiencies $\xi_{DL/FL}$. Those are dimensionless quantities corrected for magnetization variations

between the different samples through integration over the Co thickness :

$$\xi_{DL/FL} = \frac{2e}{\hbar} M_s t_{Co} \left( \frac{\mu_0 H_{DL/FL}}{\mathcal{J}_{Pt}} \right)$$

Figures 6.15 **a**) and **b**), we plot respectively the damping like and the field like torque efficiencies in two series of samples of varying Co thickness : one with 1.4 nm of Al grown between Co and capping Pt an one with 3 nm Al. Regarding the damping like efficiency, the series with 1.4 nm Al (fuchsia open dots) saturates around $\xi_{DL} \simeq 0.08$ for $t_{Co}$ thicker than 1.2 nm. The series with 3 nm, blue dots, presents a maximum of $\xi_{DL} = 0.131 \pm 0.005$ for $t_{Co} = 0.9$ nm.

The field efficiencies that we report figures 6.15 **b**) exhibit a similar decreasing trend in the two series as the Co layer is grown thicker.

Consistently with the Al thickness dependence shown in figure 6.14 where SOT is maximized at $\mathrm{t_{Al}} = 3\,\mathrm{nm}$, we observe larger SOT in samples with 3 nm Al than in those with 1.4 nm Al for all Co thicknesses investigated. For $t_{Co} = 0.9$ nm, $\xi_{DL} = 0.131 \pm 0.005$ and $\xi_{FL} = 0.21 \pm 0.01$ with 3 nm Al, which compares to $\xi_{DL} = 0.077 \pm 0.002$ and $\xi_{FL} = 0.105 \pm 0.007$ with 1.4 nm Al. We fit our transport model (described section 6.6) to those SOT efficiencies and represent it as dashed lines figures 6.15 **a**) and **b**).

From this model, we extract a typical transverse spin penetration length inside our Co layers of $1.2 \pm 0.1$ nm. This length is larger than a previous estimation of 1.7 nm based on Spin Pumping Ferromagnetic Resonance (SP-FMR) measurements [Taniguchi et al., 2008].

Figure 6.15 **c**) displays the ratio between the two SOT components $\xi_{FL}/\xi_{DL}$. This ratio reaches high values in the thinnest samples as large as 2.5 for $t_{Co} = 0.7$ nm. This is unexpected for Pt|Co. Indeed, in Pt|Co, SOT originates from SHE in Pt and the spin mixing conductance at the interface is mostly real, which results in a stronger Damping-like component [Stiles and Zangwill, 2002].

Additionally, in figure 6.15 we also include the SOT efficiencies measured in samples without Pt capping (green and olive stars). With 0.7 nm of air exposed Al, for which Al is fully oxidized while Co is not, the torque efficiencies do not match those measured in Pt|Co|Al|Pt samples. In particular, the value of the ratio is smaller than for the two capped samples ($\xi_{DL} = 0.096 \pm 0.007$ and $\xi_{FL} = 0.103 \pm 0.005$, giving a ratio of $1.07 \pm 0.09$ significantly smaller than $1.5 \pm 0.1$).

Conversely, with 3 nm of Al exposed to air, where we had shown that the interface is fully metallic, we find exactly the same SOT efficiencies as in the Pt capped series : $\xi_{DL} = 0.127 \pm 0.009$ and $\xi_{FL} = 0.21 \pm 0.02$ (compared to $\xi_{DL} = 0.131 \pm 0.005$ and $\xi_{FL} = 0.21 \pm 0.01$ with capping).

This additional considerations allow enable two important validations. First, the same SOT measured in Pt|Co|Al|Pt and Pt|Co|Al*(3 nm) rule out any role of the capping Pt layer in

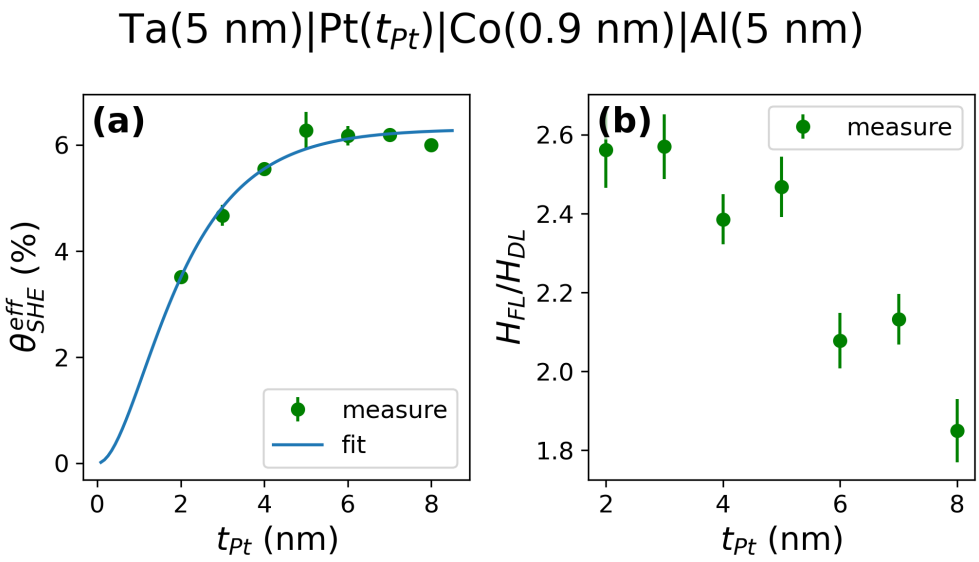


Figure 6.16 – **a**) Effective spin Hall angle $\theta^{eff}_{SHE}$ extracted from our torque measurements. Fit in continuous line. **b**) Ratio of the two SOT components for varying bottom Pt thickness.

the SOT generation for sufficiently thick Al interlayer. This confirms that thick Al prevents spin transmission and diffusion from capping Pt to Co layers. Second, the different SOT efficiencies in Co|Al*(0.7 nm) highlight that physics at play at metallic Co|Al interface are different than the already extensively investigated oxidized Co|AlOx system.

### Pt thickness dependence in Pt($t_{Pt}$)|Co|Al|Pt

In order to accurately quantify the contribution of the bottom Pt layer to the SOT, we also measured the SOT in Pt($t_{Pt}$)|Co(0.9 nm)|Al(5 nm) series in which Al is metallic at its interface with Co. In figure 6.16 **a**), we plot the effective SHE angle $\theta^{eff}_{SHE}$ extracted from our measurements as the damping-like torque efficiency corrected by a transmission coefficient as discussed equation 6.7. Since Co and Al layers remain unchanged in this series of samples, their contribution is constant. $\theta^{eff}_{SHE}$ increases as Pt layer thickens and reaches a plateau above 5 nm. We can fit this behavior with our model, a Pt spin diffusion length of 1.5 nm and $\theta^{Pt}_{SHE} \simeq 0.08$ in agreement with previous studies [Rojas-Sánchez et al., 2014].

Comparing figure 6.16 **a**) to figure 6.16 **b**), we note that the $H_{FL}/H_{DL}$ ratio has an opposite trend to the Pt SHE. This ratio remains larger than one in all samples and decreases as Pt SHE rises up to its maximum. This trend further indicates that an explanation based on the sole SHE Pt contribution is not fully satisfactory. However, those measurements clearly show that $H_{FL}/H_{DL}$ increases while SHE decreases (small Pt thickness), emphasizing the Rashba origin of the strong Field-like torque.

## 6.6 . Transverse spin-transport model for SOT

In this section, we describe in details our model used for qualifying the transverse spin accumulations and spin-currents in metallic multilayers. It is used to understand the origin of the SOT. The case of Rashba angular moment polarization (at Co|Al interface) will be also investigated with additional input given in the next two chapters (7 and 8) dealing with density functional theory (DFT) developments.

In the following description of the spin-transport model, we will note :

- $\hat{y}$ is the direction of the spin flow.
- $\check{\mu} = \mu_x + i\mu_y$
- $\check{\mathcal{J}}_\sigma = \mathcal{J}_{\sigma,x} + i\mathcal{J}_{\sigma,y}$

with '✓' hat marker on the top indicating the respective spin-density and spin-currents transverse to the local magnetization direction $\hat{e}_m$ (assumed to be oriented along the $z$ axis) and where $\hat{x}$ corresponding to the incident spin-current direction.

### 6.6.1 . From complex decoherence length to SOT

#### Introducing complex decoherence lengths

We propose a model enabling to understand the relation between the transverse spin accumulation and the resulting SOT components. This model adapts the drift-precession-diffusion theory framework as first proposed in the pioneering work of Ref. [Zhang et al., 2002, Stiles and Zangwill, 2002] which shows how an exchange interaction between the magnetization and the spin accumulation may explain SOT. This approach was later complemented by introducing complex spin diffusion lengths accounting for spin precession in a ferromagnetic layer of finite thickness [Petitjean et al., 2012, Shchelushkin and Brataas, 2005]. Following those principles, we have derived the equations in systems comprising a ferromagnet and a light metal.

In [Amin and Stiles, 2016], it is shown that this approach can be handled through generalized spin-dependent Boltzmann equations. This simplification for the treatment of the specific spin degree of freedom is possible in the limit of vanishing SOC (case of 3*d* ferromagnet). The same qualitative conclusion in favor of a generalized diffusion scheme for the transverse spin component is also deduced from the Keldysh framework [Pauyac et al., 2018].

We assume that in the Co ferromagnetic layer, besides the *transverse* momentum relaxation time $\tau_p$, the spin-relaxation is described by : a longitudinal relaxation (spin-flip) time $\tau_{sf}$ (generally quite long), a transverse decoherence term (e.g. from magnon emission/absorption) $\tau_\Delta$ (generally short), and a certain Larmor time $\tau_J$ due to precession. Noting $\check{\mu} = Tr\,\langle\Psi_{kn}|\hat{\sigma}|\Psi_{kn}\rangle$, the out-of equilibrium spin density and $\check{\mathcal{J}}_\sigma = Tr\,\langle\Psi_{kn}|\{\hat{\sigma},\hat{\mathcal{J}}\}|\Psi_{kn}\rangle$ the spin current, their coupled dynamics are given by [Jungwirth et al., 2014] :

$$\frac{\partial \check{\mu}}{\partial t} = -\frac{\check{\mu}}{\tau_\Delta} - \frac{\check{\mu}}{\tau_{sf}} - \frac{\check{\mu} \times \hat{e}_m}{\tau_J} - \nabla_z \check{\mathcal{J}}_\sigma \tag{6.8}$$

$$\frac{\partial \check{\mathcal{J}}_\sigma}{\partial t} = -\frac{\check{\mathcal{J}}_\sigma}{\tau_\Delta} - \frac{\check{\mathcal{J}}_\sigma}{\tau_p} - \frac{\check{\mathcal{J}}_\sigma \times \hat{e}_m}{\tau_J} - \frac{\mathcal{D}_\perp}{v_F^2 \tau_p} \nabla_z \check{\mu} \tag{6.9}$$

where $\hat{e}_m$ is the unit vector of the local magnetization $\hat{\mathbf{m}}$. For the following calculations, we remind the notation for the reduced complex spin accumulation $\check{\mu} = v_F (\mu_x + i\mu_y)$ and complex transverse spin-current $\check{\mathcal{J}}_\sigma = \mathcal{J}_{\sigma_x} + i\mathcal{J}_{\sigma_y}$. $\mathcal{D}_\perp$ is the diffusion constant for the transverse component of the spin angular momentum.

In the steady state regime, $\frac{\partial}{\partial t} = 0$, equations 6.8 and 6.9 become :

$$\check{\mu} \left( \frac{1}{\lambda_\Delta} + \frac{1}{\lambda_{sf}} - \frac{i}{\lambda_J} \right) + \nabla_z \check{\mathcal{J}}_\sigma = 0 \tag{6.10}$$

$$\check{\mathcal{J}}_\sigma \left( \frac{1}{\lambda_\Delta} + \frac{1}{\lambda_p} - \frac{i}{\lambda_J} \right) + \frac{\mathcal{D}_\perp}{v_F^2 \tau_p} \nabla_z \check{\mu} = 0 \tag{6.11}$$

Here, the correspondence between a characteristic time time $\tau_i$ and the characteristic length $\lambda_i$ is : $\lambda_i = v_F \tau_i$. We define $\tilde{\lambda}_\mu = \left( \frac{1}{\lambda_\Delta} + \frac{1}{\lambda_{sf}} - \frac{i}{\lambda_J} \right)^{-1}$ and $\tilde{\lambda}_\mathcal{J} = \left( \frac{1}{\lambda_\Delta} + \frac{1}{\lambda_p} - \frac{i}{\lambda_J} \right)^{-1}$ two complex scaling length. Noting that $\left( \frac{v_F^2 \tau_p}{3} \right) = \mathcal{D}_\perp$ the diffusion constant, the combination of the two equations yields :

$$\check{\mu} = \left( \tilde{\lambda}_p \right)^2 \frac{\partial^2 \check{\mu}}{\partial z^2} \quad \text{and} \quad \check{\mathcal{J}}_\sigma = \left( \tilde{\lambda}_p \right)^2 \frac{\partial^2 \check{\mathcal{J}}_\sigma}{\partial z^2} \tag{6.12}$$

where $\tilde{\lambda}_p$ is the common *propagation* scaling length. It is defined by $\tilde{\lambda}_p^2 = \left( \frac{\tilde{\lambda}_\mu \tilde{\lambda}_\mathcal{J}}{3} \right)$. Its real part represents the decay of the transverse spin components (accumulation and current) in the ferromagnet while its imaginary part represents its precession feature.

### Generalized complex spin-resistance

The characteristic lengths described above are specific to each layer. In order to accurately model diffusion between different layers, it is needed to include in the model the different electrical resistivities. This is dealt with by introducing a selective layer spin-resistance $r^s$. Generalizing the approach used to describe non-collinear spin transport in [Cosset-Cheneau, 2022], we define $r^s$ as :

$$r^s = \frac{1}{G_{sh}} \sqrt{\frac{\tilde{\lambda_\mu}}{\tilde{\lambda_J}}} \tag{6.13}$$

Regarding non magnetic materials, where $\lambda_\Delta$ and $\lambda_J$ are zero, this writes : $(G_{sh}r^s) = \sqrt{\frac{\tau_{sf}}{\tau_p}}$. For instance, in Pt, $(G_{sh}r^s) \simeq 2$ as obtained from THz emission experiment [Krishnia et al., 2024]. It is greater than 1 as in all materials where $\tau_{sf} > \tau_p$. Notably, in low SOC materials as Cu or Al, it is typically larger than 10. In non collinear ferromagnets, the spin-resistance is complex, rendering spin precession.

### Relation between SOT and spin currents

The two components of the integrated spin-orbit torques (SOT) $\check{\tau}_{SOT}$ are defined as the time variation of the volume integral of the local magnetization vector, defined as $\mathbf{M}$, when an out-of-equilibrium spin current occurs which is opposite to the torque generated on the spin-accumulation $\check{\mu}$ (in the limit of small SOC). From total angular momentum conservation, the sign of the cross product term has then to be opposite to that of equation 6.8 :

$$\check{\tau}_{SOT} = \int_{\mathcal{V}} \frac{\partial \mathbf{M}}{\partial t} d\mathcal{V} = -\int_{\mathcal{V}} \frac{\hat{e}_m \times \check{\mu}}{\tau_J} d\mathcal{V} \tag{6.14}$$

Moreover, equation 6.8 rewrites in the steady-state regime of spin-injection :

$$\frac{v_F \check{\mu}}{\tilde{\lambda_\mu}} = -\frac{\partial \check{\mathcal{J}}_\sigma}{\partial y}$$

From this equation,

$$\check{\mu} = -\left(\frac{1}{\frac{1}{\tau_\Delta} + \frac{1}{\tau_{sf}} - \frac{i}{\tau_J}}\right) \frac{\partial \check{\mathcal{J}}_\sigma}{\partial z} = -\tau_J \left(\frac{i + \tau_J\left(\frac{1}{\tau_\Delta} + \frac{1}{\tau_{sf}}\right)}{1 + \left[\tau_J\left(\frac{1}{\tau_\Delta} + \frac{1}{\tau_{sf}}\right)\right]^2}\right) \frac{\partial \check{\mathcal{J}}_\sigma}{\partial z}$$

Noting that in our framework $\check{\mu} \times \hat{e}_m = -i\check{\mu}$, we can derive :

$$\int_{\mathcal{V}} \frac{\check{\mu} \times \hat{e}_m}{\tau_J} d\mathcal{V} = \int_{\mathcal{V}} -\frac{i}{\tau_J} \check{\mu}\, d\mathcal{V} = -\int_{\mathcal{V}} \frac{1 + i\tau_J\left(\frac{1}{\tau_\Delta} + \frac{1}{\tau_{sf}}\right)}{1 + \left[\tau_J\left(\frac{1}{\tau_\Delta} + \frac{1}{\tau_{sf}}\right)\right]^2} \frac{\partial \check{\mathcal{J}}_\sigma}{\partial z}$$

The integral over the volume of $\frac{\partial \check{\mathcal{J}}_\sigma}{\partial y}$ yields the integrated torque $\check{\tau}_{SOT}$ in the FM thickness we are searching for :

$$\check{\tau}_{SOT} = \left(\frac{1 + i\tau_J\left(\frac{1}{\tau_\Delta} + \frac{1}{\tau_{sf}}\right)}{1 + \left[\tau_J\left(\frac{1}{\tau_\Delta} + \frac{1}{\tau_{sf}}\right)\right]^2}\right) \left(\check{\mathcal{J}}_\sigma^{in} - \check{\mathcal{J}}_\sigma^{out}\right) \tag{6.15}$$

This equation teaches us that the torques applied on the ferromagnetic layer are proportional to the balance between spin current *entering* through one interface $\check{\mathcal{J}}_\sigma^{in}$ and outgoing through the other interface $\check{\mathcal{J}}_\sigma^{out}$. The proportionality constant is complex, accounting for precession of the spin current around the magnetization. The real part of the resulting $\check{\tau}_{SOT}$ is the damping like torque component while the imaginary part is the field like torque. In the following, we will propagate the spin currents between the different layers of our samples.

From the latter equation, we can observe that the ratio between the Field-like and the Damping-like torques are closely dependent on the ratio between $\tau_J$ and $\tau_\Delta$. For thick FM layers, thicker than the decoherence length, an increase of the decoherence rate $\tau_\Delta^{-1}$ enhances the Field-like term (from almost zero) and reduces the Damping-like component.

### 6.6.2 . Multiple scattering approach (case of ultrathin layers)

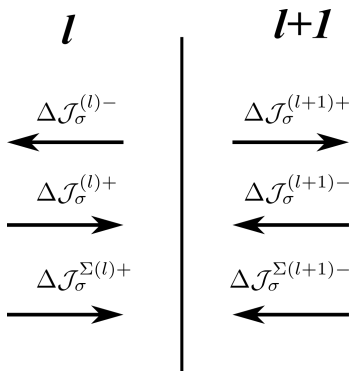


Figure 6.17 – Spin currents definition at one interface

Estimating the spin currents $\check{\mathcal{J}}_\sigma^{in}$ and $\check{\mathcal{J}}_\sigma^{out}$ in the ferromagnetic layer of Pt|Co|Al|Pt is challenging due to the presence of different spin current sources and multiple interfaces scattering. We have to consider multiple scattering processes at several interfaces and boundaries. Our approach consists in a multiscattering formalism that enables to write a super-scattering matrix $\mathbb{S}$ from each individual interface scattering matrix $\tilde{\mathcal{S}}$. We describe this approach in this section.

In the following, we note the out-of-equilibrium spin-polarized current by $\Delta\check{\mathcal{J}}_\sigma(z) = (\mathcal{J}_\uparrow - \mathcal{J}_\downarrow)$. Those are generated by the diffusion of the out-of-equilibrium spin-accumulation $\check{\mu}(z)$.

Let's consider a single interface between layers $l$ and $l+1$ (figure 6.17). The purpose of a scattering matrix is to write a linear relationship between the two *outgoing* spin-accumulation flow (spin-currents) to the left and to the right, respectively $\Delta\check{\mathcal{J}}_\sigma^{(l)-}$ and $\Delta\check{\mathcal{J}}_\sigma^{(l+1)+}$, connected to the two *in-going* spin-current $\Delta\check{\mathcal{J}}_\sigma^{(l)+}$ and $\Delta\check{\mathcal{J}}_\sigma^{(l+1)-}$. This also may involve two sources terms (SHE) generated from either side materials $\check{\mathcal{J}}_\sigma^{\Sigma(l)+}$ and $\check{\mathcal{J}}_\sigma^{\Sigma(l+1)-}$. Because the source term imposes different boundary conditions, we need two

scattering matrices $\mathcal{S}$ and $\tilde{\mathcal{S}}$ :

$$\left| \begin{array}{l} \Delta\check{\mathcal{J}}_\sigma^{(l)-} \\ \Delta\check{\mathcal{J}}_\sigma^{(l+1)+} \end{array} \right. = \mathcal{S} \left| \begin{array}{l} \check{\mathcal{J}}_\sigma^{\Sigma(l)+} \\ \check{\mathcal{J}}_\sigma^{\Sigma(l+1)-} \end{array} \right. + \tilde{\mathcal{S}} \left| \begin{array}{l} \Delta\check{\mathcal{J}}_\sigma^{(l)+} \\ \Delta\check{\mathcal{J}}_\sigma^{(l+1)-} \end{array} \right.$$

We employ a superscattering approach to propagate this single interface equation to a whole multilayer. Following this approach , we derive a superscattering matrix $\mathbb{S}$ such that :

$$\left| \begin{array}{l} \vdots \\ \Delta\check{\mathcal{J}}_\sigma^{(l)-} \\ \Delta\check{\mathcal{J}}_\sigma^{(l+1)+} \\ \vdots \end{array} \right. = \mathbb{S} \left[ \begin{array}{ccc} \ddots & & \\ & \tilde{\mathcal{S}}_l^{-1}\mathcal{S}_l & \\ & & \ddots \end{array} \right] \left| \begin{array}{l} \vdots \\ \check{\mathcal{J}}_\sigma^{\Sigma(l)+} \\ \check{\mathcal{J}}_\sigma^{\Sigma(l+1)-} \\ \vdots \end{array} \right. \tag{6.16}$$

where the right hand term can be computed from assumptions on spin current sources, transmission and reflection at interfaces.

### 6.6.3 . Single interface scattering matrix

Each single scattering matrix at a given interface between two semi-infinite materials is written as :

$$\tilde{\mathcal{S}}_l = \begin{bmatrix} \tilde{\mathcal{R}}_l & \tilde{\mathcal{T}}_l' \\ \tilde{\mathcal{T}}_l & \tilde{\mathcal{R}}_l' \end{bmatrix} \quad \text{and} \quad \mathcal{S}_l = \begin{bmatrix} \mathcal{R}_l & \mathcal{T}_l' \\ \mathcal{T}_l & \mathcal{R}_l' \end{bmatrix} \tag{6.17}$$

where $\tilde{\mathcal{R}}_l$ (resp. $\mathcal{R}_l$) is the reflection coefficient for a spin-current (resp. for a source term) arriving from layer $l$ to the interface between $l$ and $l+1$; whereas $\tilde{\mathcal{T}}_l$ (resp. $\mathcal{T}_l$) is the corresponding transmission coefficient for a spin current (resp. for a source term) arriving from layer $l$ to the interface between $l$ and $l+1$. The coefficients noted with $'$ are the equivalent coefficients for the opposite flow direction on the same interface.

We have derived those coefficients from the boundary conditions that we impose on the interface. The general self-consistent solutions can then be solved by using either $\check{\mathcal{J}}_\sigma^{(l)\pm}$ or $\Delta\check{\mu}_\sigma^{(l)\pm}$ as relevant physical quantities. We chose the $\Delta\check{\mathcal{J}}_\sigma^{(l)\pm}$ basis able to treat both SHE and REE. Those are :

(i) the continuity of the total current when the spin-memory loss is zero giving :

$$\check{\mathcal{J}}_\sigma^{\Sigma(l)+} - \Delta\check{\mathcal{J}}_\sigma^{(l)-} + \Delta\check{\mathcal{J}}_\sigma^{(l)+} = -\check{\mathcal{J}}_\sigma^{\Sigma(l+1)+} + \Delta\check{\mathcal{J}}_\sigma^{(l+1)+} - \Delta\check{\mathcal{J}}_\sigma^{(l+1)-} \tag{6.18}$$

(ii) equality between diffusive spin-current and interfacial spin-current parameterized by the spin-mixing conductance ($G_{\uparrow\downarrow} = G_{Sh}\mathcal{T}$) according to :

$$\check{\mathcal{J}}_\sigma^{\Sigma(l)+} - \Delta\check{\mathcal{J}}_\sigma^{(l)-} + \Delta\check{\mathcal{J}}_\sigma^{(l)+} = G_{\uparrow\downarrow}\left[r^{s(l)}\left(\Delta\check{\mathcal{J}}_\sigma^{(l)-} + \Delta\check{\mathcal{J}}_\sigma^{(l)+}\right) - r^{s(l+1)}\left(\Delta\check{\mathcal{J}}_\sigma^{(l+1)-} + \Delta\check{\mathcal{J}}_\sigma^{(l+1)+}\right)\right] \tag{6.19}$$

when the spin-memory loss is absent.

(iii) When necessary, the introduction of a fictitious layer interface of evanescent thickness $t_{loss}$ with spin-diffusion length $\lambda_{loss}$ taking into account the previously defined spin-memory loss parameter $\delta$ owing to $\delta = \left(\frac{t_{loss}}{\lambda_{loss}}\right)$.

This yields the formulae of $\tilde{\mathcal{R}}_l$ and $\tilde{\mathcal{T}}_l$ as a function of material and interface parameters according to :

$$\tilde{\mathcal{T}}_l = \frac{2\, T_{\uparrow\downarrow}\, \tilde{r}_s^{(l)} \left(\frac{\delta}{\sinh \delta}\right)}{1 + \delta \coth(\delta) T_{\uparrow\downarrow} \left(\tilde{r}_s^{(l)} + \tilde{r}_s^{(l+1)}\right) + \delta^2 T_{\uparrow\downarrow}^2 \tilde{r}_s^{(l)} \tilde{r}_s^{(l+1)}} \tag{6.20}$$

$$\tilde{\mathcal{R}}_l = \frac{1 + \delta \coth(\delta)\, T_{\uparrow\downarrow} \left(\tilde{r}_s^{(l+1)} - \tilde{r}_s^{(l)}\right)}{1 + \delta \coth(\delta) T_{\uparrow\downarrow} \left(\tilde{r}_s^{(l)} + \tilde{r}_s^{(l+1)}\right) + \delta^2 T_{\uparrow\downarrow}^2 \tilde{r}_s^{(l+1)} \tilde{r}_s^{(l+1)}} \tag{6.21}$$

Regarding $\mathcal{S}$ matrices dealing with the scattering of the source terms, the current discontinuity equation remains unchanged. However, contrary to the previous case, the source term does not solely derive from a spin accumulation. $\mathcal{R}_l$ and $\mathcal{T}_l$ then become :

$$\mathcal{T}_l = \frac{T_{\uparrow\downarrow}\, \tilde{r}_s^{(l)} \left(\frac{\delta}{\sinh \delta}\right)}{1 + \delta \coth(\delta) T_{\uparrow\downarrow} \left(\tilde{r}_s^{(l)} + \tilde{r}_s^{(l+1)}\right) + \delta^2 T_{\uparrow\downarrow}^2 \tilde{r}_s^{(l)} \tilde{r}_s^{(l+1)}} \tag{6.22}$$

$$\mathcal{R}_l = \frac{1 + \delta \coth(\delta)\, T_{\uparrow\downarrow}\, \tilde{r}_s^{(l+1)}}{1 + \delta \coth(\delta) T_{\uparrow\downarrow} \left(\tilde{r}_s^{(l)} + \tilde{r}_s^{(l+1)}\right) + \delta^2 T_{\uparrow\downarrow}^2 \tilde{r}_s^{(l)} \tilde{r}_s^{(l+1)}} \tag{6.23}$$

From these expression, one can extract the total spin-loss $\mathcal{A}_l$ at the interface $l$ according to : $\mathcal{T}_l + \mathcal{R}_l + \mathcal{A}_l = 1$ (an equivalent expression exists for the tilde equations)

### 6.6.4 . Treating self-consistently back-and-forth reflections in the multiple scattering approach

In our ultrathin metallic multilayers, not only reflections and transmissions of spin at a single interface have to be taken into account but also multiple diffusion even originating from all interfaces. The single interface scattering approach described so far does not include such multiple reflections explicitly. The general solution can be solved using the multiple scattering path approach in the spirit of its use in finding the quantum electronic eigenstates in a solid.

The general solution for the self-consistent layer-resolved scattering matrices $\tilde{\mathbb{S}}$ is :

$$\tilde{\mathbb{S}}_{ln} = \tilde{S}_l\, \delta_{ln} + \tilde{S}_{ll}\, \mathbb{P}_{lm}\, \tilde{\mathbb{S}}_{mn} \tag{6.24}$$

or equivalently :

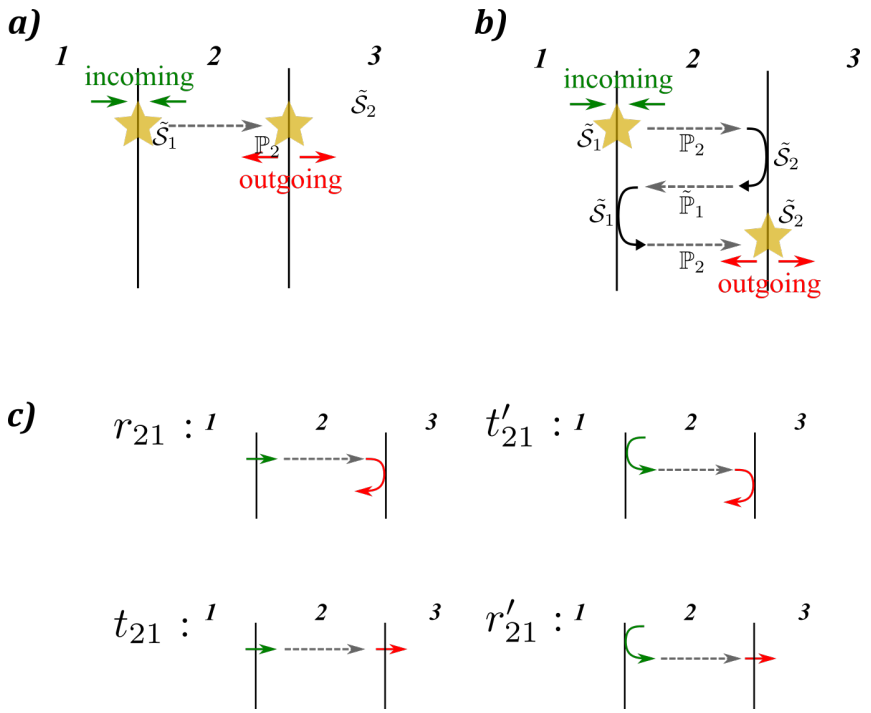


Figure 6.18 – Illustration of the scattering represented by $s_{21}$ (equation 6.28) in the two interfaces case. **a**) Zeroth order scattering represented by $\mathbb{S}_{21}^{(0)}$, **b**) First order scattering, exhibiting multiple reflections. **c**) representation of the four terms of $\mathbb{S}_{21}^{(0)}$ matrix (see equation 6.31)

$$\tilde{\mathbb{S}}^{-1} = \tilde{S}_l^{-1} - \mathbb{P} \tag{6.25}$$

with $\mathbb{P} = \mathbb{P}_{ln}$ the propagation matrix of the out-of-equilibrium spin accumulation and currents away from the interface (l) to the interface (n) or (vice versa) with the constraint $l = n \pm 1$. We remind that $\tilde{S}_l$ are the single interface scattering matrix of the interface (l) entering as a diagonal block matrix in such 'supermatrix'.

The two different (complex) propagation matrix required for $n = l + 1$ ($\mathbb{P}_{n,n+1} = \mathbb{P}_2$) and $n = l - 1$ ($\mathbb{P}_{n+1,n} = \mathbb{P}_1$) write respectively :

$$\mathbb{P}_{n,n+1} = \begin{bmatrix} 0 & 0 \\ \exp\left(-\frac{t_{n+1}}{\tilde{\lambda}_{s,n+1}}\right) & 0 \end{bmatrix}; \mathbb{P}_{n+1,n} = \begin{bmatrix} 0 & \exp\left(-\frac{t_{n+1}}{\tilde{\lambda}_{s,n+1}}\right) \\ 0 & 0 \end{bmatrix} \tag{6.26}$$

$$\tag{6.27}$$

In the following, we demonstrate that in fact it does account for it through a two interface example (figure 6.18). From equation 6.16, in the case of two interfaces, the super scattering matrix $\mathbb{S}$ can be written by blocks as :

$$\mathbb{S} = \begin{bmatrix} \tilde{\mathbb{S}}_{11} & \tilde{\mathbb{S}}_{12} \\ \tilde{\mathbb{S}}_{21} & \tilde{\mathbb{S}}_{22} \end{bmatrix} \tag{6.28}$$

In this matrix, $\tilde{\mathbb{S}}_{21}$ describes e.g. the non-local influence on the second interface (between layers 2 and 3) of incoming information on the first interface (between layers 1 and 2). From block-wise inversion of equation 6.16, we can compute $\tilde{\mathbb{S}}_{21}$ as :

$$\tilde{\mathbb{S}}_{21} = \tilde{\mathcal{S}}_2 \mathbb{P}_2 \frac{1}{1 - \tilde{\mathcal{S}}_1 \tilde{\mathbb{P}}_1 \tilde{\mathcal{S}}_2 \mathbb{P}_2} \tilde{\mathcal{S}}_1 \tag{6.29}$$

which can be developed as :

$$\tilde{\mathbb{S}}_{21} = \tilde{\mathcal{S}}_2 \mathbb{P}_2 \left[ 1 + \sum_{n=1}^{\infty} \left( \tilde{\mathcal{S}}_1 \tilde{\mathbb{P}}_1 \tilde{\mathcal{S}}_2 \mathbb{P}_2 \right)^n \right] \tilde{\mathcal{S}}_1 \tag{6.30}$$

The different terms of this sum are explicitly encoding the multiple reflections undergone between two interfaces. The first term $\tilde{\mathcal{S}}_2 \mathbb{P}_2 \tilde{\mathcal{S}}_1$ describes incoming information at the first interface contribution to information outgoing the second surface, without multiple reflections (figure 6.18 **a**). The second term is $\tilde{\mathcal{S}}_2 \mathbb{P}_2 \tilde{\mathcal{S}}_1 \tilde{\mathbb{P}}_1 \tilde{\mathcal{S}}_2 \mathbb{P}_2 \tilde{\mathcal{S}}_1$ describe an information ongoing at the first interface, undergoing one reflection on the second interface followed by a second reflection on the first interface before outgoing on the second interface (multiple reflections represented figure 6.18 **a**).

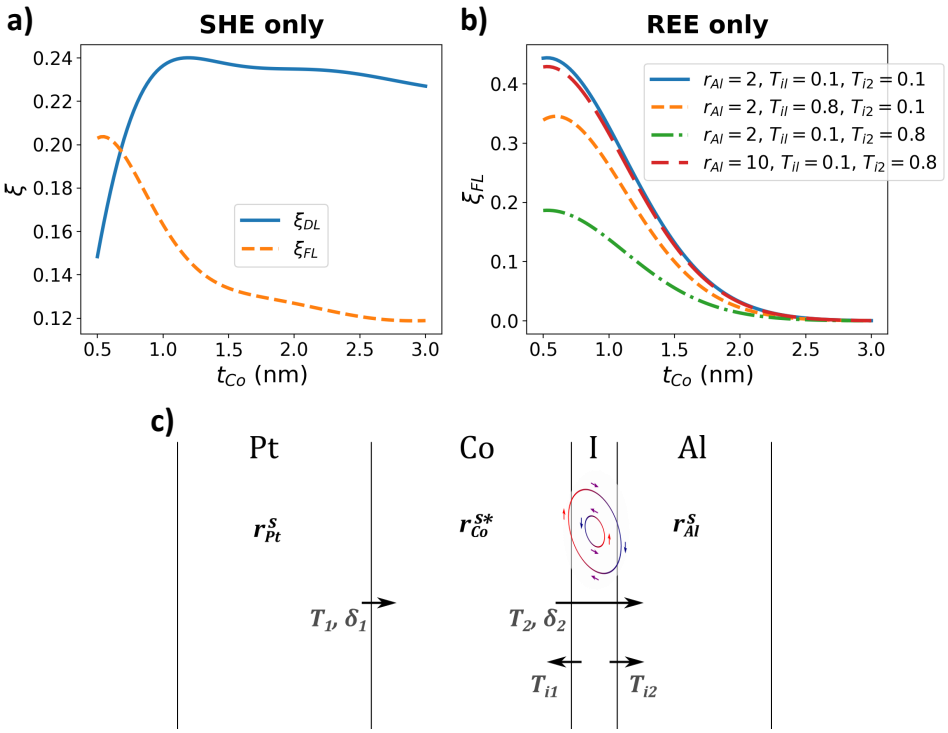


Figure 6.19 – **a**) respective Field-like and Damping-like components of SOT due to SHE, no REE, dependence on Co layer thickness. **b**) Field-like torque for different values of the parameters representing Al resistivity and the virtual Rashba layer transmission coefficients. SHE set to zero, dependence on Co layer thickness. **c**) Scheme of the model for Pt|Co|Al multilayers with relevant coefficients. $\mathcal{T}_1$ and $\mathcal{T}_2$ represent the transmission coefficient between adjacent layers whereas $\mathcal{T}_{i1}$ and $\mathcal{T}_{i2}$ represent transmission from layers to interface Rashba states. $\delta_1$ and $\delta_2$ are spin-memory loss coefficients.

To illustrate this further, let's compute the first term $\tilde{\mathbb{S}}^{(0)}_{21} = \tilde{\mathcal{S}}_2\mathbb{P}_2\tilde{\mathcal{S}}_1$ as a function of the different transmission and reflection coefficients. We derive :

$$\tilde{\mathbb{S}}^{(0)}_{21} = \begin{bmatrix} \tilde{\mathcal{R}}_2 e^{-\frac{t_2}{\lambda_2}} \tilde{\mathcal{T}}_1 & \tilde{\mathcal{R}}_2 e^{-\frac{t_2}{\lambda_2}} \tilde{\mathcal{R}}'_1 \\ \tilde{\mathcal{T}}_2 e^{-\frac{t_2}{\lambda_2}} \tilde{\mathcal{T}}_1 & \tilde{\mathcal{T}}_2 e^{-\frac{t_2}{\lambda_2}} \tilde{\mathcal{R}}'_1 \end{bmatrix} = \begin{bmatrix} r_{12} & t'_{12} \\ t_{12} & r'_{12} \end{bmatrix} \tag{6.31}$$

We identify in this matrix the effective reflections and transmissions coefficients $r_{12}$ and $t_{12}$ of a wave incoming on the first interface and outgoing at the second interface. We represent on figure 6.18 **c** the physical processes they result from.

### 6.6.5 . Semi-phenomenological modeling of SHE and REE

We choose to model Pt|Co|Al system as a stacking of four layers (see figure 6.19 **c**) : a SHE layer representing Pt (of spin resistance $r^s_{Pt}$), a ferromagnetic layer with complex relaxation lengths representing Co (of complex spin resistance $r^{s*}_{Co}$), a layer I representing

the Rashba interface and a light metal layer representing Al.

The Rashba interface is represented by a virtual "interfacial" layer possibly having small transmission coefficients toward the neighbouring layers. In case this transmission is non zero, it stands for a small coupling existing between interfacial evanescent Rashba states, which are evanescent wave functions, and bulk Bloch states. Since those two types of electronic states are in principal orthogonal, this transmission coefficient remain in any case small compared to 1. This tiny transmission results in a large spin accumulation inside this virtual layer representing the Rashba electronic states.

The overall SOT in Co is the sum of three terms : the SOT emerging from SHE integrated over the ferromagnet thickness $t_{Co}$ (equation 6.15), the SOT due to the virtual layer angular momentum accumulation, and the SOT due to diffusion of this accumulation inside the ferromagnet, which is also integrated over $t_{Co}$. The damping like component is given by the real part of the SOT while the field like is the imaginary part.

### Complex diffusion length effect on torques in the ultrathin regime

Our primary observation is that applying this model without Rashba effect is enough to explain the faster increase of the field like torque over the damping like at the lowest thicknesses of Co (figure 6.19 **a**). This can be understood noting that in equation 6.15, $\left(\check{\mathcal{J}}_{\sigma}^{in} - \check{\mathcal{J}}_{\sigma}^{out}\right) \propto \left(1 - \exp\left(-\frac{t_{Co}}{\tilde{\lambda}_{Co}}\right)\right)$. To the first order in $t_{Co}$, the imaginary part of this quantity is linear (proportional to a sine) while the real part is quadratic (cosine).

This contrasts with the usual representation of Co|Pt interface in the thick Co limit by a sole, mostly real, spin-mixing conductance $G_{\uparrow\downarrow}$ [Amin and Stiles, 2016, Brataas et al., 2006, Cosset-Chéneau et al., 2021]. While such spin mixing conductance yields stronger damping like than field like, we observe that in thin Co, this ratio is opposite and strongly depends on Co thickness. Indeed, when Co is thinner than the spin penetration length, spin transport is greatly influenced by spin precession in Co (through complex diffusion lengths) and reflections at the interfaces (through multiscattering).

### Modeling of Rashba states by an added virtual interfacial layer

We now discuss the modeling of Rashba contributions by a virtual layer. In our model, the low transmission coefficients that we impose on that layer mechanically lead to simulating a large angular momentum accumulation because spins are not able to "escape". To exhibit that clearly, we simulated four cases :

1. A case where Al spin resistance (here dimensionless) is of 2, a value close to Co resistivity (2.5) and the two transmission coefficients are set to a small value : 0.1 (blue line on figure 6.19 **c**).
2. A case (orange line on figure 6.19 **c**) where the transmission toward Co is increased to 0.8.

3. A case (green line on figure 6.19 **c**) where the transmission coefficient toward Al is risen to 0.8 while the one toward Co is kept to 0.1.
4. In the last case, the transmission coefficient toward Al is again large (0.8) but the resistivity of Al is increased to 10.

Comparing the second case to the first, we see a reduction in the field-like torque despite a better transmission of spins from the virtual layer to Co. This counter-intuitive result stems from the fact that increased transmission lowers the accumulation of spins more than it increases the angular momentum transfer. In the third case, the field like torque is the lowest because not only transmission of spins to Co is low but also electrons diffuse the best inside the Al layer where they exert no torque.

Finally, the fourth case recovers the same amplitude of field like torque as the first case due to the rise in Al resistivity. This is expected since a great resistivity difference between two consecutive layers prevents electronic diffusion equivalently to low transmission.

This model reproduces expected behavior of REE on SOT. The resulting torques are a trade off in the coupling of the Rashba states with the neighbouring metals : while better coupling with the ferromagnetic states improves transfer of angular momentum, it also decreases the lifetime of Rashba polarized electronic states and therefore the total amount of out of equilibrium momentum accumulation.

### 6.6.6 . Rashba-Edelstein effect (REE) at Co|Al interfaces

In section 6.5.1, we have reported a large increase in the ratio $\xi_{FL}/\xi_{DL}$ in Ta(5)|Pt(8)|Co($t_{Co}$)|Al|Pt(3) and Ta(5)|Pt(8)|Co($t_{Co}$)|Al* samples with ultrathin Co (figure 6.15). We have noted from the experimental results that this strong ratio is incompatible with a model comprising only Pt SHE and mostly real spin-mixing conductance at Pt|Co interface.

Additionally, we have written a multiple scattering model to model this system and fed it with parameters extracted from AHE measurement. When we only include in this model a spin current source term in the Pt layer, we reproduce this increase in the ratio $\xi_{FL}/\xi_{DL}$ (section 6.6.5, figure 6.19 **b**). It arises due to the precession of the electron spins around Co magnetization.

However, this does not match our experimental data (figure 6.20 **b**). According to our SOT measurement, the ratio $\xi_{FL}/\xi_{DL}$ is equal to 1 at $t_{Co} \simeq 1.2$ nm while the model applied with parameters consistent with the AHE resistances measured predicts this at $t_{Co} \simeq 0.5$ nm. We therefore confirm with this transport model that Pt SHE does not explain alone our experimental SOT measurements of section 6.5.1.

When the Rashba term is turned on through a non-zero source term in the virtual interfacial layer, we are able to precisely match the experimental data for each SOT component (figure 6.20 **a**). This ultimately leads us to the conclusion that there exists a strong interfacial SOT generation at Co|Al interface through spin or orbital Rashba Edelstein effect.

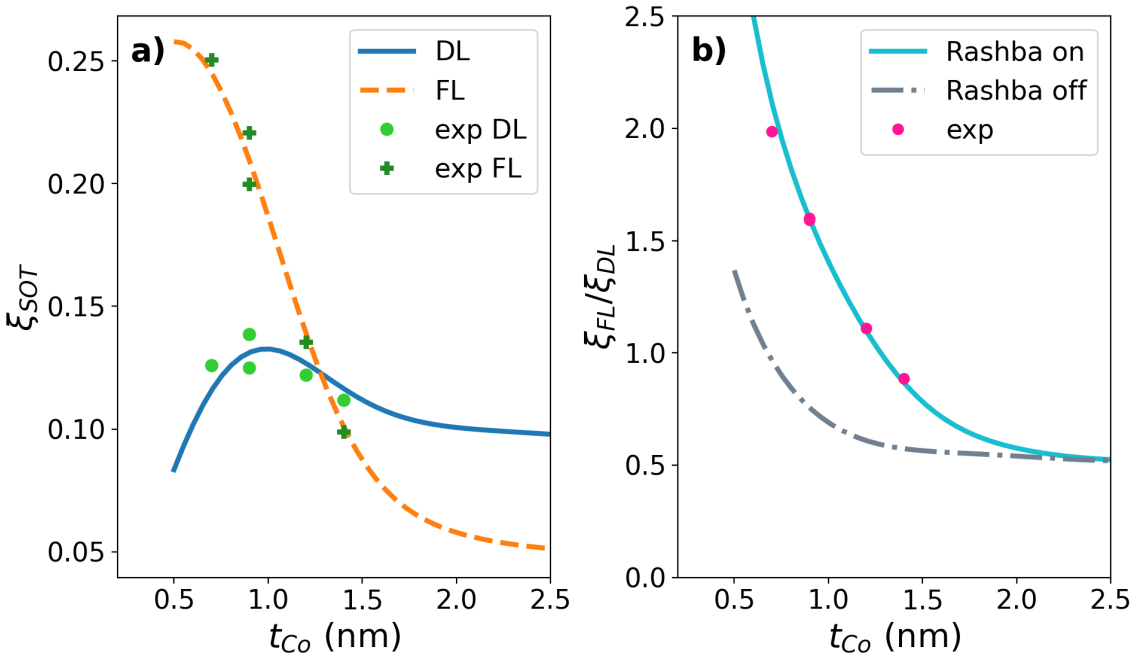


Figure 6.20 – **a**) Damping-like and field-like SOT efficiencies for Ta(5)|Pt(8)|Co($t_{Co}$)|Al(1.4)|Pt(3) and **b**) ratio of the two component as a function of Co thickness using our multiple scattering approach. The dots and crosses are experimental values. Plain and dashed lines are simulated using our multiple scattering approach and AHE compatible with AHE resistances. In **b**) is also plotted the ratio of the torques simulated with the same parameters but no Rashba effect (dashed line).

## 6.7 . Conclusion

We assess in this chapter the good quality of the magnetic thin films Ta|Pt|Co|(Al*, Al|Pt or Cu|Pt) grown with our magnetron sputtering. To this purpose, we employ XRR, XPS and TEM structural characterizations as well as XMCD and SQUID to investigate magnetic properties. This characterization unveils experimental trends compatible with DFT calculations led by collaborators. We also examine the PMA properties of these metallic structures and find a first result of this thesis : metallic Co|Al interface induces a surface magnetic anisotropy comparable to that of Pt|Co or Co|$Al_2O_3$.

We lead our investigation further with transport measurements. We first study experimentally the different trends in AHE of our different thin films structures. Combined with CIP model, we extract from these measures spin dependent transport parameters. We then use harmonic Hall techniques to evaluate SOT in our multilayers and find that the metallic Co|Al interface generates large SOT on the Co magnetization, notably of field like geometry. We disentangle this effect from the roles of Pt SHE in our samples and use a CPP model enriched by the parameters deduced from AHE to quantitatively harness SOT origin. With this study, we demonstrate the emergence of a large OREE at metallic Co|Al interface. In the next chapter, we report two DFT calculations of Co|Al interface predicting OREE in this system, quantitatively compatible with the experimental results of the present chapter.

# 7 - Insights from first principle calculations

## 7.1 . Introduction

In this section, we develop and describe our main results/calculations obtained from the density function theory (DFT) framework. These deals with (i) the emergence of the electronic band structure at Co|Al interfaces (ii) the calculation of the linear response for the orbital and spin polarization/accumulation (Rashba-Edelstein effects) and (iii) the calculations of the torquance onto Co generated by the angular momentum accumulations.

## 7.2 . Insights from DFT on the OREE emergence mechanism

The strong SOT and orbital torque (OT) evidenced at metallic Co|Al interface cannot be explained neither by standard SOT mechanisms nor by processes already explored involving oxidized light metals as *e.g.* CuO largely investigated in a recent literature. In order to gain insights onto the actual underlying physics, first principle calculations, performed by density functional theory (or DFT), are a powerful tool and seem mandatory to distinguish spin and orbital contributions. These following calculations allow to draw SOT following three consecutive steps :

- The use of DFT yields the equilibrium band structure of the system. Especially, OML or SML can be computed from this step.
- The implementation of the Kubo formalism for linear response theory is mandatory to compute out of equilibrium spin and orbit accumulations when an electric field is applied.
- The two torque components (or torkance on magnetization can be calculated and then compared to the corresponding angular momentum accumulations.

## 7.3 . Orbital momentum locking (OML) at Co|Al

The first principle calculations of metallic Co12|X12 with 'X' = 'Al', 'Cu' (the numbers refer to the number of atomic planes in an hexagonal stacking, 12 atomic plane corresponds about to 2.5 nm in thickness) were led in collaboration with Sergey Nikolaev from Osaka University, Mairbek Chsiev team from Spintec in Grenoble concerning the elctronic band structure and Rashba-Edelstein effects and Armando Pezo in Laboratoire Albert Fert regarding the band structure and torque calculation. The results of those collaborations are published in two consecutive article [Nikolaev et al., 2024] and preprint [Pezo et al., 2025].

In those works, DFT is also used to compare Co|Al to Co|Cu as in the experimental study described chapter 6 [Krishnia et al., 2023] because we learnt from this study that Co|Cu systems do not present any torque amplification (field-like) or any OML unlike Co|Al. In Ref. [Nikolaev et al., 2024] DFT is performed using the Vienna ab-initio Simulation Package (VASP) [Kresse and Furthmüller, 1996, Kresse and Joubert, 1999, Monkhorst and Pack, 1976]. From the band structure of the two metallic stacks, we exhibit the occurrence of hybridization between the $p$ orbitals of the light metal and the $d$ orbital of Co. However, the nature of this hybridization is totally different in the two systems.

In Ref. [Pezo et al., 2025], a different simulation package (SIESTA [Soler et al., 2002]) is used to perform the calculations. The energy minimization yields a slightly different lattice parameter at Co|Al interface (2.94 Å) whereas Nikolaev found 2.63 Å. Both corresponds to energy minimization. Still, concerning band structure, we don't find big changes between the two packages. The overall calculations yield same qualitative results. The main difference is that the calculations of the torkance by Wannierization techniques used in [Nikolaev et al., 2024] were very difficult to implement and converge and thus abandoned. We will present together the main results of the two studies.

### Band structure differences between Co|Cu and Co|Al

Regarding the interface between Co and the Cu or Al light metal, while a weak coupling is found in the case of Cu, it is very strong for the Co|Al interface, especially at the $K$ point of the Brillouin zone edge. This is manifested in the clear difference between the band structures of Co|Al and Co|Cu around the Fermi level as displayed in figure 7.1 **a)** (Co|Cu) and **b)** (Co|Al). Notably, at the $K-$point, we can observe electronic states in Co|Al that do not appear in Co|Cu. The band structures thus differ a lot at the edges of the Brillouin zone.

In figure 7.1 **c)**, we report a first consequence of the different hybridization of Co and Al layers compared to Co and Cu. This graph represents the computed spin magnetic moments (in red) and orbital magnetic moments (in blue) for the different Co atomic planes in Co|Al (full lines) and Co|Cu (dotted lines). In the latter case, both moments are relatively constant across the whole Co layer. Cu does not affect magnetic properties of Co.

On the opposite, a striking feature arises in Co|Al : the magnetic moment drops from 1.7 $\mu_B$ to 1.3 in the Co atomic plane in contact with Al. This is also true to orbital moment that decreases from 0.11 $\mu_B$ to 0.07 $\mu_B$. This large fall of moment per atom underlines the strength of the impact of Co-Al hybridization and is consistent with the DFT calculations reported chapter 6.

Moreover, we also note from those calculations that the out-of-plane orbital momentum in the inner Co layer respects the symmetry of honey comb packed (hcp or AB stacking) lattice (figure 7.2 **a-b**) $L_z(\mathbf{k})$. Its alternating pattern vanishes at the interfacial layer with Al, consistently with figure 7.1 **c**).

### Emergence of an orbital momentum locking (OML) at Co|Al interface

The most striking outcome of the hybridization at Co|Al interface is the emergence of an Orbital Momentum Locking (OML) texture in the 2D Brillouin zone. In figure 7.2 **a**), we clearly observe at the level of the $Co_1$ layer (first Co plane in contact with Al) a strong finite in-plane angular momentum orthogonal to the in-plane electronic wave vector $\mathbf{k}_{\|}$. Note that the amplitude of OML onto the Fermi surface reaches 0.8 $\mu_B$. This appear larger than the values observed onto topological surface states (TSS) [Pezo et al., 2024]. On the

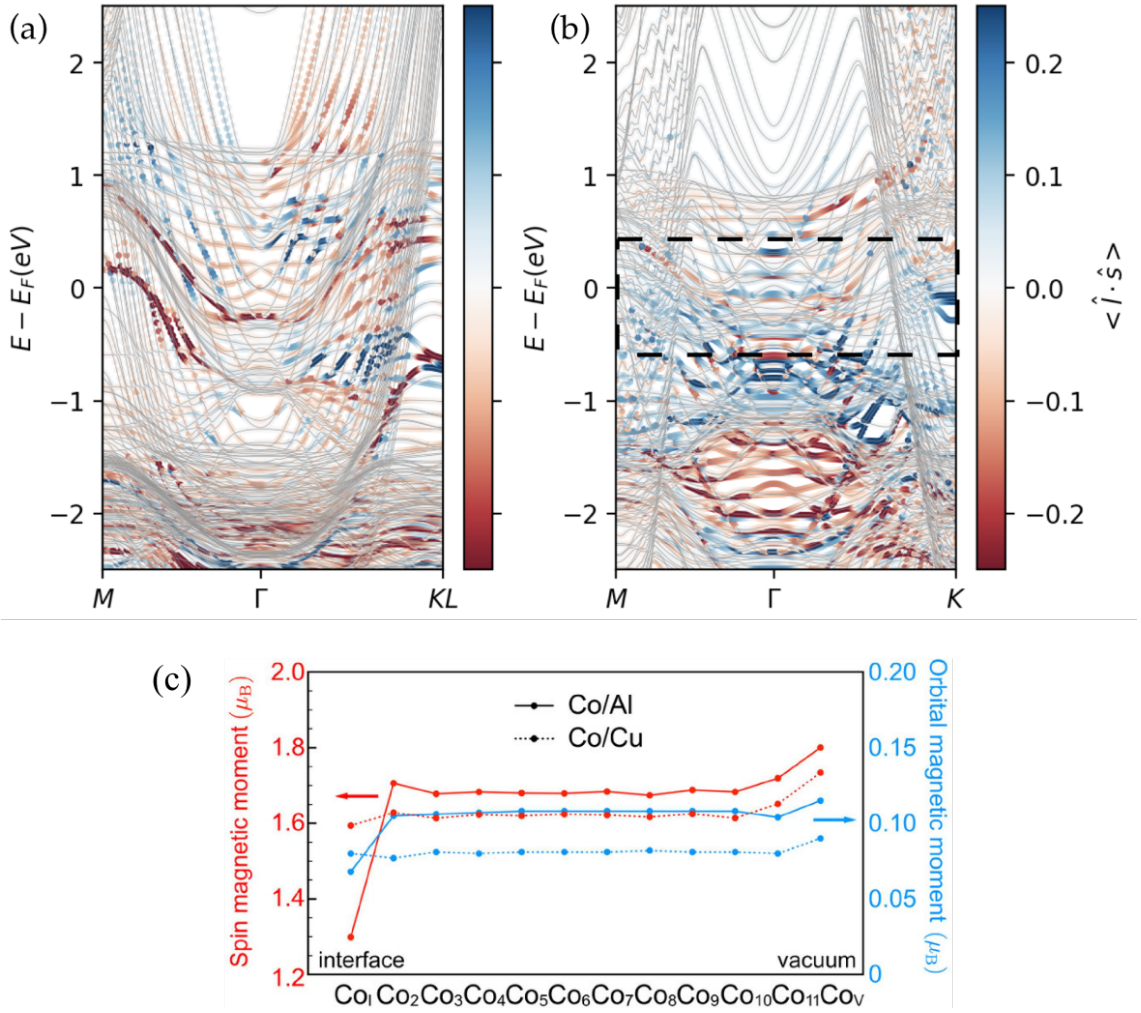


Figure 7.1 – Electronic band structure of Co(12)/Cu(12) **a**) and Co(12)/Al(12) **b**) along the high-symmetry path $M - \Gamma - K$ where the colorbar displays the mean value of the $\langle \hat{l} \cdot \hat{s} \rangle$ operator. The dashed rectangle in **b**) displays a more pronounced value for the spin-orbit interaction (SOC) operator near the Fermi level in Co/Al compared to the case of Co/Cu in **a**). Extracted from Ref. [Pezo et al., 2025] **c**) Spin and Orbital momentum computed for each layer of Co. *Adapted from Ref. [Nikolaev et al., 2024]*

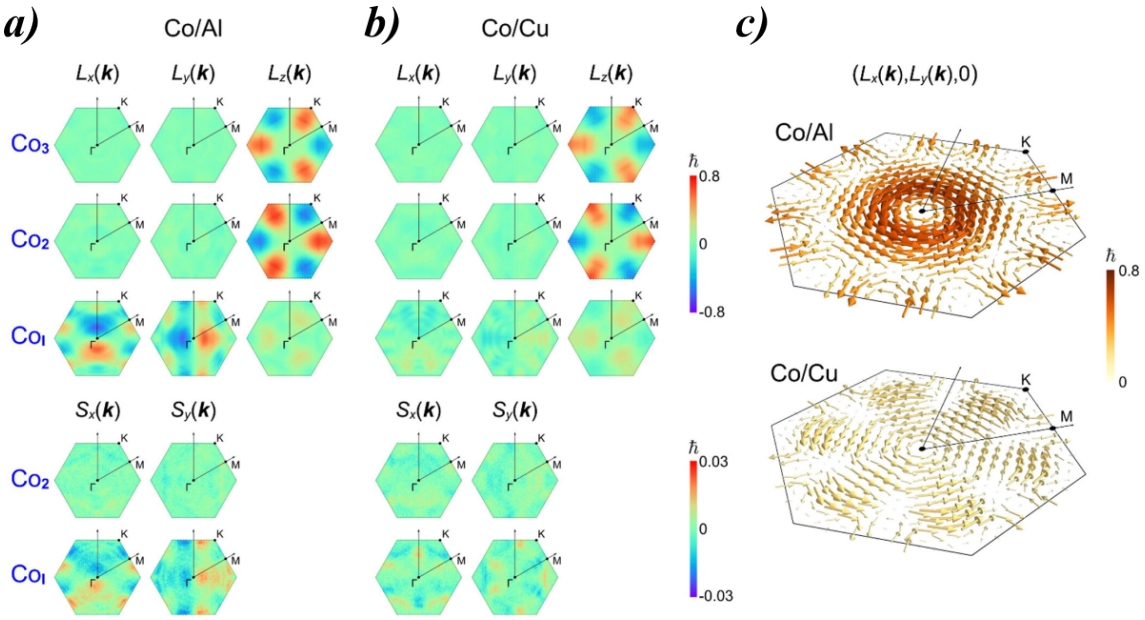


Figure 7.2 – **a**)Orbital and spin momentum computed in the Brillouin zone of Co|Al and **b**) Co|Cu. The plots on the top ($Co_i$) represent each spatial component of orbital angular momentum in the three Co layers superimposed to Al in the stack. The bottom graphs exhibit the spin momentum as a function of the wave vector. **c**) Resulting orbital texture in Co|Al and Co|Cu. Adapted from [Nikolaev et al., 2024]

contrary, in the Co|Cu system, no significant orbital texture appear, showing the absence of any OML.

In [Nikolaev et al., 2024], we report that the orbital momentum texture results from non-zero $\langle d_{z^2}|\hat{L}_x|d_{yz}\rangle$ and $\langle d_{z^2}|\hat{L}_y|d_{xz}\rangle$ transition matrix elements, this coupling being mediated by the respective $p_x$ and $p_y$ Al orbitals. This result is consistent with other mechanisms proposed for OREE emergence in Co|Pt [Park et al., 2013] and Co|CuOx [Go et al., 2021].

It was also verified by DFT that such OML persists whatever the A or B stacking order at the direct Co|Al interface. Neither is it affected by the on site Coulomb repulsion in Co, which is responsible for the energy difference between majority and minority spins. Additionally, in [Pezo et al., 2025], DFT calculations were performed for different lattice parameter values around the optimum and OML was found to emerge in each case with a maximum value close to the minimization energy corresponding to the chosen lattice parameter. Moreover, OML remains as large with switching on and off the SOC in Co layer, Al layer, or in the two layers simultaneously, proving the pure orbital nature of the underlying physical mechanisms.

Regarding the spin degree of freedom (plots at the bottom of the figure 7.2 **a**), an in-plane texture arises in Co|Al. However it is very negligible in amplitude compared to the orbital momentum previously observed (less than 4 % according to [Nikolaev et al., 2024]).

We thus demonstrate here from our band structure calculation that electronic states in Co|Cu and Co|Al at the equilibrium are of different nature. The most striking result is the prediction of a large OML, although localized in the first layer of Co in contact with Al. It is completely negligible when replacing the light metal Al with Cu. Moreover, this property seems independent of assumptions used for DFT. In the next section, we will describe how we can compute the out-of-equilibrium angular momentum accumulation resulting from OML under the application of an external electric field.

## 7.4 . Orbital Rashba-Edelstein effects : Out-of-equilibrium orbital polarization

The out-of-equilibrium orbital and spin-polarization density (accumulation) emerging from OML when an electric field $\mathbf{E} = E_x \mathbf{e_x}$ is applied can be calculated from the linear response theory as introduced section 3.7. We remind that we may define the "orbital" response $\chi^{\mathcal{L}}_{xy}$ as :

$$\langle L_y \rangle = \chi^{\mathcal{L}}_{xy} E_x$$

where the quantum average has to be performed $\langle L_y \rangle$ over the unit surface of the system in the case of a 'Rashba' quantity leading to the definition of the so-called 2-dimensional (2D) orbital accumulation $\tilde{\mu}_{\mathcal{L}} = \langle L_y \rangle$ (still) as a complex quantity with the 'tilde' symbol ($\tilde{\mathcal{O}}$) referring to the 2D density of the operator $\mathcal{O}$ (/m$^2$).

In the Kubo formalism, this quantity can be computed from the band structure (obtained by DFT) as a summation of two components. A so-called *intraband* component sums the contributions of the Fermi level electronic states whereas the so-called *interband* terms results from the virtual coupling within same bands with lower energies electronic states. The two responses are given by the following formulae :

$$\chi^{intra}_{\alpha\beta} = -e\tau \sum_{n\mathbf{k}} \left( \frac{\partial f_{n\mathbf{k}}}{\partial \epsilon_{n\mathbf{k}}} \right) \langle u_{n\mathbf{k}} | \hat{L}_\alpha | u_{n\mathbf{k}} \rangle \langle u_{n\mathbf{k}} | \hat{v}_{\beta\mathbf{k}} | u_{n\mathbf{k}} \rangle \tag{7.1}$$

$$\chi^{inter}_{\alpha\beta} = ie\hbar \sum_{n\neq m,\mathbf{k}} \frac{(f_{n\mathbf{k}} - f_{m\mathbf{k}}) \langle u_{n\mathbf{k}} | \hat{L}_\alpha | u_{m\mathbf{k}} \rangle \langle u_{m\mathbf{k}} | \hat{v}_{\beta\mathbf{k}} | u_{n\mathbf{k}} \rangle}{(\epsilon_{n\mathbf{k}} - \epsilon_{m\mathbf{k}}) (\epsilon_{n\mathbf{k}} - \epsilon_{m\mathbf{k}} - i\hbar\tau^{-1})} \tag{7.2}$$

where we remind that $\hat{v}_{\beta\mathbf{k}}$ is the velocity operator (along the direction $\beta$) at a certain $k$ point.

### Comparison with the semiclassical approach.

In this linear approximation, A. Johansson et al. [Johansson, 2024] noted that the interband contribution to REE vanishes in a system respecting time-inversion symmetry. In Co, this symmetry is broken due to the strong ferromagnetic character. This leads us

to expect a well larger contribution from the intraband since it doesn't require symmetry breaking and owing to the fact that the orbital response should be mostly insensitive to the exchange term. It is also worth noting that the intraband term corresponds to the orbital accumulation that would be computed in a semiclassical Boltzmann approach [Johansson, 2024].

To go beyond and anticipate the Rashba-Edelstein response, we can apply such semiclassical Boltzmann approach to a circular 2D contour with OML (similar to the one used in the past for topological insulators surface states). This approach consists in summing the orbital momentum of either populated or depleted electronic states when an electric field is applied. Noting that, under an electric field, the displacement of the Fermi contour is $\delta\mathbf{k} = -e\mathbf{E}\tau_p/\hbar$ ($\tau_p$ is the momentum relaxation time), and the variation in occupation factor is written $\frac{\partial f}{\partial \mathbf{k}} \cdot \delta\mathbf{k} = \frac{\partial f}{\partial \epsilon}\frac{\partial \epsilon}{\partial \mathbf{k}}\delta\mathbf{k}$, the Boltzmann approach yields :

$$\tilde{\mu}_{\mathcal{L}} = 2\,\mathcal{N}_{DOS}^{2D}\,\langle\cos^2\phi\rangle\,(ev_F\tau_p E_x)\,(\mathcal{P}_{\mathcal{L}}\hbar) \tag{7.3}$$

with $\langle\cos^2\phi\rangle = \frac{1}{2}$ in the 2D geometry and $\phi$ the azimutal angle in the plane ($\phi = 0$ in the current direction). In this expression, we used that $\frac{\partial \epsilon}{\partial \mathbf{k}} = \hbar v_F$ and introduced the 2D density of states $\frac{\partial f}{\partial \epsilon} = \mathcal{N}_{DOS}^{2D}$ as well as the mean orbital polarization of the electronic states at the Fermi level $\mathcal{P}_{\mathcal{L}}$ of the order $\simeq 0.8\ \mu_B$ (figure 7.2).

The quantities of equation 7.3 can be identified to those of the intraband term equation 7.1 as :

$$\begin{aligned}
\mathcal{P}_{\mathcal{L}}\cos\phi &\longleftrightarrow \langle\hat{L_y}\rangle \\
v_F\cos\phi &\longleftrightarrow \langle\hat{v_{x\mathbf{k}}}\rangle \\
\mathcal{N}_{DOS}^{2D} &\longleftrightarrow \left(\frac{\partial f}{\partial \epsilon}\right)
\end{aligned}$$

Noting $k_F$ the Fermi wave vector, equation 7.3 can be simplified to :

$$\chi_{xy}^{\mathcal{L}} = \frac{ek_F\tau_p}{\hbar}\,(\mathcal{P}_{\mathcal{L}}\hbar)$$

## Quantitative results

The response of Co|Al to an electric field in terms of both spin and orbital angular accumulations are computed in our Refs. [Nikolaev et al., 2024, Pezo et al., 2025]. Despite slight quantitative differences, the two studies draw the same qualitative conclusion : a large orbital response occurs in the first atomic plane of Co superposed to Al. Both calculations find a much larger susceptibility for the orbital accumulation than the spin accumulation (see table 7.1).

| | [Pezo et al., 2025] | [Nikolaev et al., 2024] |
|---|---|---|
| lattice param. (Å) | 2.94 | 2.86 |
| $\chi_{xy}^{\mathcal{L},intra}$ | 5.94 | $\simeq 2.0$ |
| $\chi_{xy}^{\mathcal{L},inter}$ | 0.20 | |
| $\chi_{xy}^{\mathcal{S},intra}$ | 0.12 | $\simeq 0.15$ |
| $\chi_{xy}^{\mathcal{S},inter}$ | -0.002 | |

Table 7.1 – Outcome of calculations performed in Refs. [Nikolaev et al., 2024, Pezo et al., 2025]. OREE response $\chi$ are given in unit of $10^{-10}\hbar\,/(V/m)$ (per atom). The orbital polarization of (orbital accumulation density) induced by OREE is then $\tilde{\mu}_{\mathcal{L}} = \chi_{xy}^{\mathcal{L}}\mathbf{E}$.

Still, one difference is worth noting. In Nikolaev et al. [Nikolaev et al., 2024], the response in spin accumulation is approximately ten times smaller than the orbital response, whereas in Pezo et al. [Pezo et al., 2025], it is smaller by a factor close to 50. Regarding the SOT generation, we need to bear in mind that the torques exerted by the orbital accumulation within Co are mediated by SOC which is typically of the order of 0.07 eV in Co.

Consequently, Ref. [Nikolaev et al., 2024] does not exclude the role of Rashba induced spin accumulation in SOT while Ref. [Pezo et al., 2025] fully rules out such contribution compared to the pure orbital momentum accumulation contribution. This difference between the two works at this point might stem from an additional approximation introduced by the Wannierization technique being used in Ref. [Nikolaev et al., 2024] (which is presently not the case in Ref. [Pezo et al., 2025]). This approximation reduces the number of bands used for computing sums 7.1 and 7.2 by focusing on electronic states and bands close to the Fermi level.

## 7.5 . SOT resulting from OML : the orbital torque

We now turn to the qualitative and quantitative description of the spin-orbit torque (SOT) and orbital torque arising from orbital and spin accumulation produced by OREE. After having described the general formalism of SOT adapted to DFT, we compare the theoretical results to our experiments with very good agreement.

### 7.5.1 . First estimation

Estimating SOT from an out-of-equilibrium orbital density (accumulation) is not straightforward. From Landau-Lifschitz standpoint, the SOT vector $\mathbf{\Gamma}$ can be defined as an effective field acting on the local magnetization $\hat{\mathbf{m}}$ such that :

$$\mathbf{\Gamma}_{SOT} = \frac{d\mathbf{M}}{dt} = \gamma_L\, \mathbf{B}_{SOT}^{eff} \times \mathbf{M} \tag{7.4}$$

with $\gamma_L = \left(\frac{e}{2m*}\right)$ the gyromagnetic factor. This equation defines the effective SOT field $\mathbf{B}_{SOT}^{eff}$. Nevertheless, in the steady-state regime of spin-current injection in a timescale

larger than the typical electronic spin relaxation time, one has to remind that such *local torque*, $\vec{\Gamma}(z)$ can be directly linked to the spin-current influx, $-\mathcal{Q}_{yz} = \nabla_z \mathcal{J}_{yz}$ derivative of the spin-current ($\hat{z}$ and $\hat{y}$ are respectively the carrier flux direction and the spin orientation). We have extensively used the latter correspondence for the establishment of our analytical semi-classical SOT model. The validity of the quantum correspondence has been given in [Go et al., 2020].

Additionally, from an effective Hamiltonian perspective, we have :

$$\hat{\mathcal{H}} = \hat{\mathcal{H}}_{kin} + \hat{\mathcal{H}}_{SOI} - \Delta_{exc} \left( \frac{\mathbf{M}}{M_s} \right) \cdot \hat{\sigma} \tag{7.5}$$

with $\hat{\mathcal{H}}_{kin}$ and $\hat{\mathcal{H}}_{SOI}$ the respective kinetic and spin-orbit terms and $\Delta_{exc}$ the *sp-d* exchange-correlation interaction energy (in unit of energy).

Applying the Ehrenfest theorem to the sum of occupied states, we find :

$$\frac{d\langle \mathbf{M} \rangle}{dt} = \frac{1}{i\hbar} \langle \left[ \mathbf{M}, \hat{\mathcal{H}} \right]_{(-)} \rangle = \left( \frac{\Delta_{exc}}{\hbar} \right) \left[ \left( \frac{\tilde{\tilde{\mu}}_s}{t_F} \right) \times \left( \frac{\mathbf{M}}{M_s} \right) \right]$$

with $\tilde{\tilde{\mu}}_s$ the 2D spin density (in unit of $\gamma\hbar/m^2$). We remind that $\mathbf{M}$ is the 3D magnetization vector). In the latter expression, we can identify the SOT effective field to $\mathbf{B}_{SOT}^{eff} = \left( \frac{\Delta_{exc}}{M_s t_F} \right) \tilde{\tilde{\mu}}_s$. However, the linear response theory applied to Co|Al as explained above yields a stronger response in orbital out of equilibrium momentum $\hat{\mathcal{L}}$ than in spin $\hat{\sigma}$. The conversion of orbital angular momentum to spin can be considered as a perturbation of the spin Hamiltonian, which, inside a ferromagnet, is mostly governed by the exchange term (compared to the SOI). In the light of this remark, we can approximate $\tilde{\tilde{\mu}}_s$ to $\left( \frac{\Delta_{SOI}}{\Delta_{exc}} \right) \tilde{\tilde{\mu}}_{\mathcal{L}}$. This results in :

$$\mathbf{B}_{SOT}^{eff} = \left( \frac{\Delta_{SOI}}{M_s t_F} \right) \tilde{\tilde{\mu}}_{\mathcal{L}} \tag{7.6}$$

Typical value of spin-orbit $\Delta_{SOC} = 70$ meV and value of electric field of $10^5$ V/m (current density of $4 \times 10^{11}$ A/m$^2$) would give a field-like torque field of about $\mathbf{B}_{FL} = 4$ mT, in very good agreement with our experimental results. More refined calculations of the two torque components will be extracted from the DFT-based linear response theory in the end of this chapter.

### 7.5.2 . SOT from the electronic band structure

If we note that, from angular momentum conservation, SOT represent the time derivative of the local magnetization due to the exchange field introduced by the out-of-equilibrium spin accumulation $\hat{\mu}(z)$, a rigorous expression of SOT can be derived from first principles [Go et al., 2020] simply by considering the commutator of the expected spin operator with the Hamiltonian according to :

$$\check{\mathcal{T}}_{SOT} = -\frac{1}{i\hbar} \langle \left[ \hat{\sigma}, \hat{\mathcal{H}} \right]_{-} \rangle \tag{7.7}$$

This representation however still admits one limit : the commutator of $\hat{H}$ with $\hat{\sigma}$ yields generally two terms, one corresponding to the local exchange field discussed just above and one representing interaction between spins and crystal wave functions via the SOC interactions. Only the former then represents the SOT we are searching for, while the latter represents angular momentum relaxation in the crystal field. However, this relaxation is proportional to SOC while SOT comes with exchange interaction. Since in a 3*d* ferromagnet like Co, SOC is negligible compared to exchange interaction, we consider that this equation 7.7 is a valid approximation.

From this formula, we can directly apply the Kubo framework to the calculation of SOT without the requirement to compute previously the out-of-equilibrium angular momentum. For DFT implementation, we can this time write both *intraband* and an *interband* torkance $\mathbf{t}$ defined as total SOT as $\check{\mathcal{T}}_{SOT} = \mathbf{t}E$. Denoting $i = x, y$ or $z$ the direction of the SOT and $j$ the direction of the applied field, we can derive :

$$t_{ij}^{inter} = \frac{e\hbar}{2\pi} \sum_{\mathbf{k},\, n \neq m} (f_n - f_m) \frac{\mathrm{Im}\left[\langle \psi_{\mathbf{k}n} | \hat{\mathcal{T}}_i | \psi_{\mathbf{k}m} \rangle \langle \psi_{\mathbf{k}m} | \hat{v}_j | \psi_{\mathbf{k}n} \rangle\right]}{(\epsilon_m - \epsilon_n)^2} \tag{7.8}$$

$$t_{ij}^{intra} = \frac{e\hbar}{2\Gamma} \sum_{\mathbf{k},\, n} \mathrm{Re}\left[\langle \psi_{\mathbf{k}n} | \hat{\mathcal{T}}_i | \psi_{\mathbf{k}n} \rangle \langle \psi_{\mathbf{k}n} | \hat{v}_j | \psi_{\mathbf{k}n} \rangle\right] \delta(\epsilon_F - \epsilon_n) \tag{7.9}$$

where $f_n$ and $f_m$ are the Fermi occupation for the respective $n$ and $m$ electronic states.

### Symmetry analysis

In this section, we discuss the main physical properties and existence rules for the occurrence of the different effects discussed previously considering simple symmetry arguments. We remind that :

- In the presence of an inversion symmetry center, *e.g.* in the bulk of a given material, the occurrence of a spin-Hall effect and/or orbital-Hall effect is possible but Rashba effects are excluded.
- Rashba effects may appear in the absence of any inversion symmetry center, *e.g.* at a surface of a material, at the interface between two materials, or in the bulk as in a ferroelectric material (GeTe,...)
- In the absence of the time reversal symmetry (magnetic materials or magnetic heterostructures), the anomalous Hall effect, that is the production of a transverse charge current, is possible.
- The occurrence of a magnetization (exchange interaction) tends to decrease the Rashba interactions in many systems.

Now, let's consider a system admitting a symmetry plane $(\hat{x},\, \hat{z})$ perpendicular to the $\hat{y}$ direction (noted $\mathfrak{M}_y$) as well as the time-reversal symmetry operation $\mathfrak{T}$ (non-magnetic structure). Assuming an electric field applied along $\hat{x}$ and the magnetization along $\hat{z}$, the torque component $\mathcal{T}_x$ represents the field-like torque and $\mathcal{T}_y$ the damping-like term. Symmetry considerations lead to :

$$\begin{array}{lll} \mathfrak{T}(v_x) = -v_x & \mathfrak{T}(\mathcal{T}_x) = \mathcal{T}_x & \mathfrak{T}(\mathcal{T}_y) = \mathcal{T}_y \\ \mathfrak{M}_y(v_x) = v_x & \mathfrak{M}_y(\mathcal{T}_x) = -\mathcal{T}_x & \mathfrak{M}_y(\mathcal{T}_y) = \mathcal{T}_y \end{array}$$

The combination of the two symmetries $\mathfrak{TM}_y$ results in the following rules :

$$\mathfrak{TM}_y(v_x) = -v_x \quad \mathfrak{TM}_y(\mathcal{T}_x) = -\mathcal{T}_x \quad \mathfrak{TM}_y(\mathcal{T}_y) = \mathcal{T}_y$$

We now apply those symmetry rules onto the interband contribution, noting that time reversal symmetry transforms a quantum state $|\psi\rangle$ into $(-i\hat{\sigma}_y)\,\hat{K}\,|\psi\rangle$ with $\hat{K}$ the complex conjugate operator :

$$\begin{aligned} t_{xx}^{inter} &= \frac{e\hbar}{\pi} \sum_{\mathbf{k},m\neq n}^{n=\text{occ}} \frac{\mathrm{Im}\left[\langle\psi_{\mathbf{k}n}|\,\hat{\mathcal{T}}_x\,|\psi_{\mathbf{k}m}\rangle\,\langle\psi_{\mathbf{k}m}|\,\hat{v}_x\,|\psi_{\mathbf{k}n}\rangle\right]}{(\epsilon_m - \epsilon_n)^2} \\ &\underset{\mathfrak{TM}_y}{=} \frac{e\hbar}{\pi} \sum_{\mathbf{k},m\neq n}^{n=\text{occ}} \frac{\mathrm{Im}\left[\langle\psi_{\mathbf{k}m}|\,\hat{\mathcal{T}}_x\,|\psi_{\mathbf{k}n}\rangle\,\langle\psi_{\mathbf{k}n}|\,\hat{v}_x\,|\psi_{\mathbf{k}m}\rangle\right]}{(\epsilon_m - \epsilon_n)^2} \end{aligned}$$

This expression boils down to the imaginary part of a complex number being equal to the imaginary part of its conjugate. This is possible only if this imaginary part is zero. As a consequence, from those symmetry rules, $t_{xx}^{inter}$ is null, meaning there is no interband contribution to field-like torque. However, there is no such constraint on $t_{xy}^{inter}$.

Regarding the intraband contribution, symmetry rules unfold as :

$$\begin{aligned} t_{xy}^{intra} &= \frac{e\hbar}{2\Gamma} \sum_{\mathbf{k}}^{n=\text{occ}} \mathrm{Re}\left[\langle\psi_{\mathbf{k}n}|\,\hat{\mathcal{T}}_y\,|\psi_{\mathbf{k}n}\rangle\,\langle\psi_{\mathbf{k}n}|\,\hat{v}_x\,|\psi_{\mathbf{k}n}\rangle\right]\delta\left(\epsilon_F - \epsilon_n\right) \\ &\underset{\mathfrak{TM}_y}{=} -\frac{e\hbar}{2\Gamma} \sum_{\mathbf{k}}^{n=\text{occ}} \mathrm{Re}\left[\langle\psi_{\mathbf{k}n}|\,\hat{\mathcal{T}}_y\,|\psi_{\mathbf{k}n}\rangle\,\langle\psi_{\mathbf{k}n}|\,\hat{v}_x\,|\psi_{\mathbf{k}n}\rangle\right]\delta\left(\epsilon_F - \epsilon_n\right) \end{aligned}$$

This means that $t_{xy}^{intra}$ real part has to be zero in this case which implies that the intraband contribution contributes only to field-like torque.

We are brought to the conclusion that in a system with a symmetry plane orthogonal to the sample layers and time reversal symmetry, the field-like torque originates from the intraband term whereas the damping-like torque results from the interband contribution.

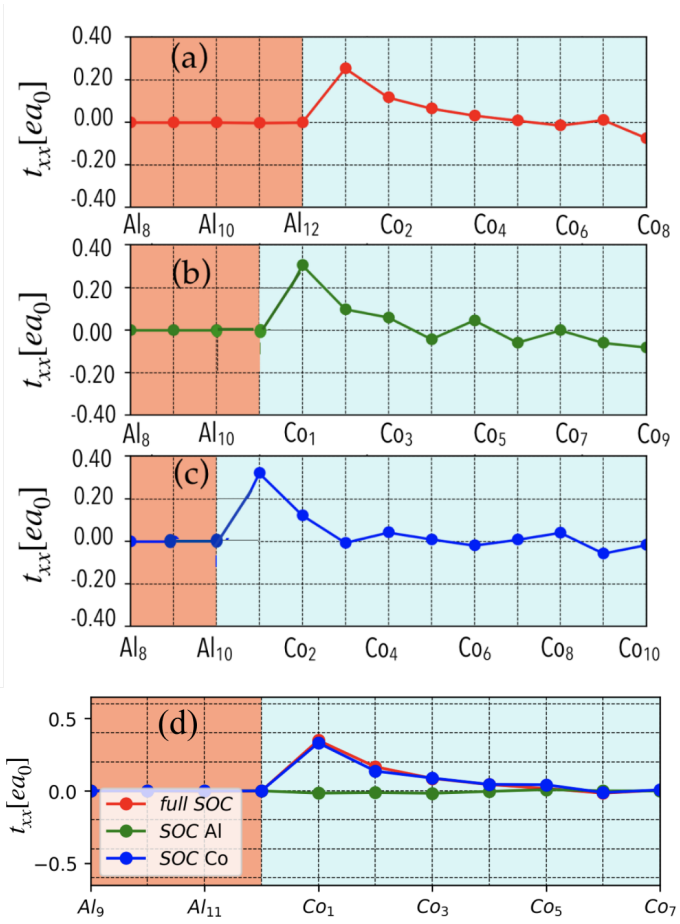


Figure 7.3 – $t_{xx}$ (field like torkance) computed in bilayers made of **a**) Al(12)|Co(12), **b**) Al(11)|Co(13) and **c**) Al(10)|Co(14). **d**) represents $t_{xx}$ computed under three different assumptions : *full SOC* where SOC is on in Co and Al, *SOC Al* with SOC on only in Al and *SOC Co* with SOC on only in Co. *Adapted from Ref. [Pezo et al., 2025]*

### Quantitative results

The torkance tensor is computed in our Ref. [Pezo et al., 2025], assuming that $t_{xx}^{inter}$ and $t_{xy}^{intra}$ are zero. The integrated torque acting on a volume unit of Co (per unit surface) are given in unit of [e$a_0$] ($a_0$ is the Bohr radius). The corresponding effective SOT magnetic fields $\mathbf{B}_{SOT}$ are then given by : $\mathbf{B}_{SOT} = \left(\frac{[e\ a_0]}{M_{s,at}^{Co}\ N_{Co}}\right)\ t_{xx}\mathbf{E}$ with $M_{s,at}$ the atomic magnetization and $N_{Co}$ the number of Co planes in the thickness.

A value of $t_{xx} = 1$ gives $\mathbf{B}_{SOT} = 4.5$ mT for $\mathbf{E} = 2.5 \times 10^4$ V/m (current density in Pt of $J_c = 10^{11}$ A/m$^2$). The average over the whole Co thickness presents a factor of 10 between the component associated to field like $t_{xx} = 0.37\ [ea_0]$ and the damping like component $t_{xy} = -0.04\ [ea_0]$. This confirms that SOT emerging at Co|Al interface are prominently of field-like symmetry.

Figure 7.3, we plot the $t_{xx}$ torkance as a function of the atomic layer obtained from DFT under different assumption relative to Co|Al bilayer. In 7.3 **a, b** and **c**, we present the outcome of the calculations for, respectively Al(12)|Co(12), Al(11)|Co(13)and Al(10)|Co(14) bilayers where the numbers in parenthesis are the number of atomic planes. Changing the number of atomic planes results in changing the configuration of the atomic planes in contact at the interface between Co and Al.

For all three configurations represented figure 7.3 **a,b** and **c**, the same profile is observed. This indicates that the *ab initio* results in Co|Al are largely independent on stacking order at the interface. Co|Al exhibits a large torkance on the Co atomic plane next to Al. The torkance then decreases monotonously as the distance to the interface is increased. Integrated torque value $\sum t_{xx} \simeq 0.5\ [ea_0]$ over the two first Co atomic planes gives then a sot field close to $\mathbf{B}_{SOT}$ =2.5 mT for 0.9 nm thick Co (and $10^{11}$ A.m$^{-2}$ current density). This is of the order of the experimental values.

The monotonous decay of the torkance throughout the Co layer is the signature of the torques being generated by an angular momentum accumulation localized in an interfacial layer, as suggested and explored in our Rashba model developed chapter 6. Indeed torques originating from an angular momentum current (as from SHE for instance) are subjected to precession around the magnetization which manifests in oscillations of the torkance. However, here, the torkance diminishes monotonously. It does as if it results from the coupling of Co to interfacial evanescent electronic states.

The torkance was also computed in cases where SOC was turned-off in both Co or Al (figure 7.3 **d**). It is zero when SOC is off in Co (green line figure 7.3 **d**), while removing SOC from only Al yields the same results as when all SOC is on (blue and red lines figure 7.3 **d**). This demonstrates that all the torque is generated inside Co from coupling with the out-of equilibrium orbital accumulation. SOC in Al does not play any role because of the absence of any magnetic moment induced in Al by proximity effects as emphasized previously.

Those ab-initio calculations of the SOT at Co|Al interface show that those torques are very

localized onto the very first Co layer, mostly generated in the very first layers of Co, due to a large out-of-equilibrium orbital angular momentum giving rise to a mostly field-like symmetry torque. This brings us to confirm that they are caused by OREE.

### 7.5.3 . Comparing Spin-Hall (SHE) and Rashba Effects (REE) efficiencies

We discuss in this section how to directly compare the respective efficiencies of the spin Hall effect and the Rashba-Edelstein effect, particularly in relation to the experiments described. Even though SHE is more related to the damping like torque whereas REE is the main source of the field like torque, such comparison is mandatory to compare the DFT calculations within the linear response theory framework that we lead next chapter 8.

We rephrase this question as : which value of the Rashba-Edelstein response $\chi^{\mathcal{L}}_{xy}$ at the Co|Al interface gives rise to field like torque exceeding the damping like torque generated by Pt at Co|Pt interface? Our answer follows from the arguments :

- The SHE current from Pt scales as $\mathcal{J}_{SHE} = \sigma^{SHE}_{xy}\ \mathbf{E}$ with $\sigma^{SHE}_{xy} = \theta_{SHE}\ \sigma_{xx}$ the corresponding spin-Hall conductivity (SHC).
- Correspondingly, the equivalent REE current (accumulation flow) is given by $\mathcal{J}_{REE} = \left(\frac{e\chi^{s}_{xy}\mathbf{E}}{\tau_{dwell}}\right)$ with $\chi^{s}_{xy}\mathbf{E}$ the 2-D carrier **spin density** (in unit of m$^{-2}$) and $\tau_{dwell} = \frac{\hbar}{2\gamma_F}$ the typical dwell time of carrier in the localized state at the Co|Al interface ($\gamma_F$ is the typical elastic broadening energy near the Fermi level).
- From perturbation calculations, the spin density ($\chi^{s}_{xy}\mathbf{E}$) is related to the orbital density ($\chi^{\mathcal{L}}_{xy}\mathbf{E}$) and estimated from the typical ratio $\epsilon_{SO} = \left(\frac{\Delta_{SOC}}{\Delta E_n}\right) \simeq 0.1$ between the spin-orbit strength and the crystal-field splitting between two consecutive energy levels ($\Delta E_n$).

Equating $\mathcal{J}_{SHE}$ and $\mathcal{J}_{REE}$, we then get the value of the orbital-Rashba response giving rise to the same efficiency than the SHE of Pt :

$$\chi^{\mathcal{L}}_{xy} \simeq \sigma^{SHE}_{xy}\left(\frac{\hbar}{e\epsilon_{SO}\gamma}\right) \simeq 10^{11}\ (\hbar)/(V.m) \simeq 10^{-9}(\hbar)/(atom.V/m) \tag{7.10}$$

considering that $\sigma^{SHE}_{xy} \simeq 10^{5}\ S/m$ for Pt and $\gamma \simeq 0.1$ eV (dwell scattering time of the order of 10 fs).

In Table 7.1, we report values for $\chi^{\mathcal{L}}_{xy}$ as large as $6 \times 10^{-10}\hbar/atom$. We thus confirm that our resulting DFT calculations are in line with the expected order of magnitude for $\chi^{\mathcal{L}}_{xy}$.

## 7.6 . Conclusion

Through this chapter, we pursue our investigation of the Co|Al system by *ab-initio* calculations in collaboration with Sergey Nikolaev of Osaka University and Armando Pezo from Laboratoire Albert Fert. Using two different simulation packages this calculations have consistent results. They exhibit a peculiar hybridization between Al and Co interfacial electronic states compared to Co|Cu. This hybridization induces OML at Co|Al interface.

From this OML demonstration, we quantify the expected SOT following two approach. On one hand, we first estimate the linear response of orbital accumulation, and then translate this in terms of SOT : $B_{FL} \simeq 4$ mT (for $j_{Pt} = 10^{11} A/\text{m}^2$). On the other hand, we are able to directly implement linear response theory of the SOT (the torkance) inside DFT framework ($B_{FL} \simeq 2.5$ mT for $j_{Pt} = 10^{11} A/\text{m}^2$). This values are of the order of the measurements reported chapter 6. Finally, we demonstrate that the orbital response that we predict with DFT in Co|Al is comparable to Pt|Co SHE.

Along chapter 6, the present chapter provide theoretical and experimental demonstrations of OREE at Co|Al interface. Reckoning this acquired knowledge on Co|Al, we will bring experimental modifications to this system in the next chapters to test our hypothesis and envision applications.

# 8 - Probing orbital torque via interfacial Pt insertion

## 8.1 . Introduction

In this section, from the knowledge acquired in the previous chapter on the occurrence of OREE and subsequent orbital torque (OT) acting on the ultrathin Co, we propose to test the OT on Co by varying the properties of the Co|interface via Pt insertion ($\tilde{Pt}$) at the atomic scale by introducing a $\tilde{Pt}$ layer of nominal thickness down to 0.25 nm. This challenges our Rashba model developed chapter 6 based on the typical tunneling escape properties out of a fictitious interfacial layer host to OREE. In this perspective, we distinguish between two competitive effects. First, a possible loss of the orbital-Rashba texture due to Pt introduction if this texture originates from the direct Co|Al bonding. Second, a possible enhancement of the OREE via SOC enhancement introduced by $\tilde{Pt}$.

To this aim, we provide experimental results as well as density functional theory (DFT) calculations developed at the laboratory concerning the electronic band structure and the linear response expected for the torque. In particular, in light of these new series of experimental results, the DFT should give us the answer of the strong localization (or not) of the orbital polarization generated by an external electric field from the model developed chapter 7.

## 8.2 . Modification of Co|Al interface : Pt dusting

### 8.2.1 . Motivation

The significant orbital torque (OT) arising from OREE at the metallic Co|Al interface is unique because it involves only a combination of light metals and, consequently, only involves weak spin-orbit coupling (SOC). To validate this interpretation of our experiments, we propose to introduce additional SOC into the system and measure its impact on spin transport properties within the multilayers.

In order to conduct these experiments, we grew a sequence of samples with the following structure $\mathrm{Ta(5\ nm)|Pt(8\ nm)|Co(0.9\ nm)|\tilde{Pt}(t_{\tilde{Pt}})|Al(3\ nm)|Pt(3\ nm)}$ with $t_{\tilde{Pt}}$ in the range 0.25-3 nm. In the initial samples series, the nominal $\mathrm{\tilde{Pt}}$ layer is thinner than crystalline Pt atomic lattice parameter, leading us to refer to this layer as "dusting Pt".

Since $\mathrm{\tilde{Pt}}$ itself possesses strong SOC and a resulting SHE, it will also actively generate SOT, with however an opposite contribution to the main one coming from the bottom 8 nm Pt. As we transition from multilayers without dusting Pt to those with a relatively thick $\mathrm{\tilde{Pt}}$, the system should exhibit a shift from SOT originating from OREE to SOT dominated by SHE. The transitory regime will provide insights into how SOC-mediated electron diffusion between Co and Al influences orbital torque generation.

### 8.2.2 . First characterizations of Pt-dusting structures

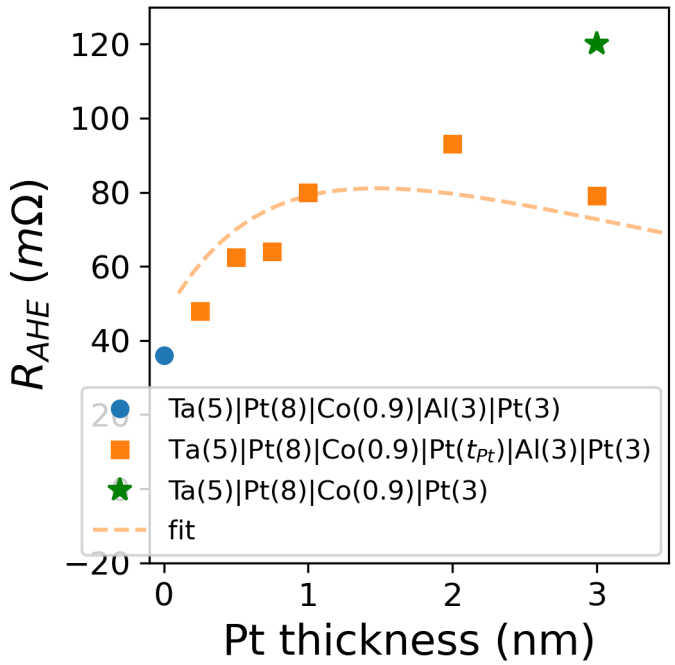


Figure 8.1 – AHE amplitude measured in Ta(5 nm)|Pt(8 nm)|Co(0.9 nm)|$\tilde{Pt}(t_{\tilde{Pt}})$|Al(3 nm)|Pt(3 nm) structures. Comparison with sample without Al, Ta(5 nm)|Pt(8 nm)|Co(0.9 nm)|Pt(3 nm), green star, and without dusting Pt, Ta(5 nm)|Pt(8 nm)|Co(0.9 nm)|Al(3 nm)|Pt(3 nm), blue dot. The dotted line represents our model fitted to the data.

### Anomalous Hall effect

AHE resistance measured in this sample series is very instructive. The results are reported on figure 8.1 for different $\tilde{Pt}$ thicknesses together with the results of our modeling described in chapter 6. When a very thin $\tilde{Pt}$ is inserted between Co and Al, $\mathrm{R_{AHE}}$ gradually increases from $36\ \mathrm{m\Omega}$ (Pt|Co|Al|Pt) to $48\ \mathrm{m\Omega}$ for 0.25 nm $\tilde{Pt}$ and reaches a maximum of $93\ m\Omega$ for 2 nm $\tilde{Pt}$. AHE then decreases mainly due to current shunting introduced by $\tilde{Pt}$ in its "thick limit".

Such AHE enhancement produced by the insertion of $\tilde{Pt}$ originates from a pure spin current proximity effect. This adds a contribution of spin-polarized electrons scattering inside $\tilde{Pt}$ with enhanced efficiency due to Pt large SOC compared to Co. Indeed, the additional spin-charge conversion in $\tilde{Pt}$ is very efficient compared to Co whose spin Hall angle, previously measured to be around 0.007 [Bony et al., 2025]. First, this feature explains why the maximum $R_{AHE}$ with added $\tilde{Pt}$ is more than twice the $R_{AHE}$ measured in Pt|Co|Al|Pt. Second, these measurements clearly emphasize the low electronic transmission amplitude at the Co|Al interface as previously suggested when discussing AHE effects in the seminal Pt|Co|Al series.

Above 2 nm $\tilde{\mathrm{Pt}}$, AHE decreases. Indeed $\tilde{\mathrm{Pt}}$ layer is then thicker than the electronic mean-free path in Pt, $\lambda_{Pt}$, the typical lengthscale of the spin-current proximity effects in $\tilde{\mathrm{Pt}}$. Consequently, the added $\tilde{\mathrm{Pt}}$ layer does not contribute more to the transverse conductivity while providing clear current shunting.

The rise of AHE originating from Co|Pt interfaces becomes even more apparent ($\mathrm{R_{AHE}} = 120\ m\Omega$) in $\mathrm{Ta}(5)|\mathrm{Pt}(8)|\mathrm{Co}(0.9)|\mathrm{Pt}(3)$. In this sample, there is no current shunting by the Al layer and an intermediate $\tilde{\mathrm{Pt}}$ layer.

### Saturation magnetization

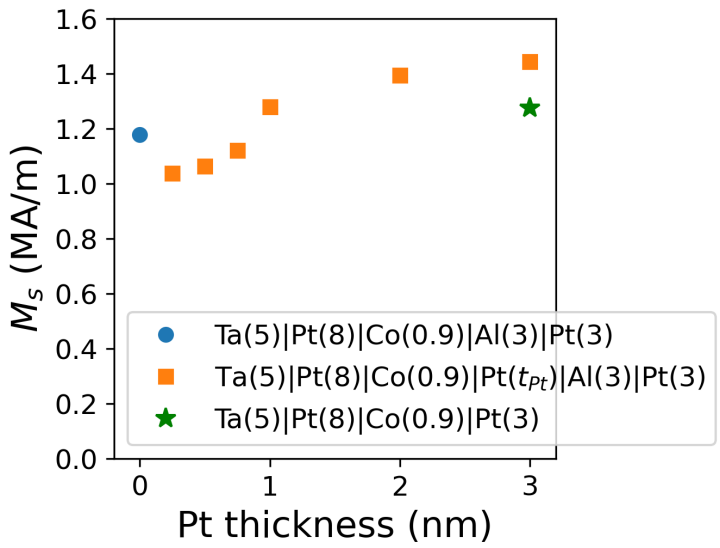


Figure 8.2 – Room temperature magnetization saturation $M_s$ measured by SQUID for Ta(5 nm)|Pt(8 nm)|Co(0.9 nm)|$\tilde{Pt}(t_{\tilde{Pt}})$|Al(3 nm)|Pt(3 nm) (orange squares), Ta(5 nm)|Pt(8 nm)|Co(0.9 nm)|Al(3 nm)|Pt(3 nm) (blue dot) and Ta(5 nm)|Pt(8 nm)|Co(0.9 nm)|Pt(3 nm) (green star)

We report figure 8.2 the saturation magnetizations measured by SQUID in the different Ta(5 nm)|Pt(8 nm)|Co(0.9 nm)|$\tilde{Pt}(t_{\tilde{Pt}})$|Al(3 nm)|Pt(3 nm) samples and compare them to Ta(5 nm)|Pt(8 nm)|Co(0.9 nm)|Al(3 nm)|Pt(3 nm) and the reference Ta(5 nm)|Pt(8 nm)|Co(0.9 nm)|Pt(3 nm). We note that the saturation magnetization in the series where an additional $\tilde{\mathrm{Pt}}$ layer is added between Co and Al increases from $\simeq 1$ MA/m to $\simeq 1.4$ MA/m as this $\tilde{\mathrm{Pt}}$ layer is grown thicker. We attribute this feature to some magnetic moments emerging in $\tilde{\mathrm{Pt}}$ [Wilhelm et al., 2000].

Compared to this series, we note that sample with Co(0.9 nm)|Al(3 nm) interface (blue dot figure 8.2) and reference sample Pt|Co|Pt have an intermediate $M_s$ value. They were both measured to have $M_s \simeq 1.2$ MA/m.

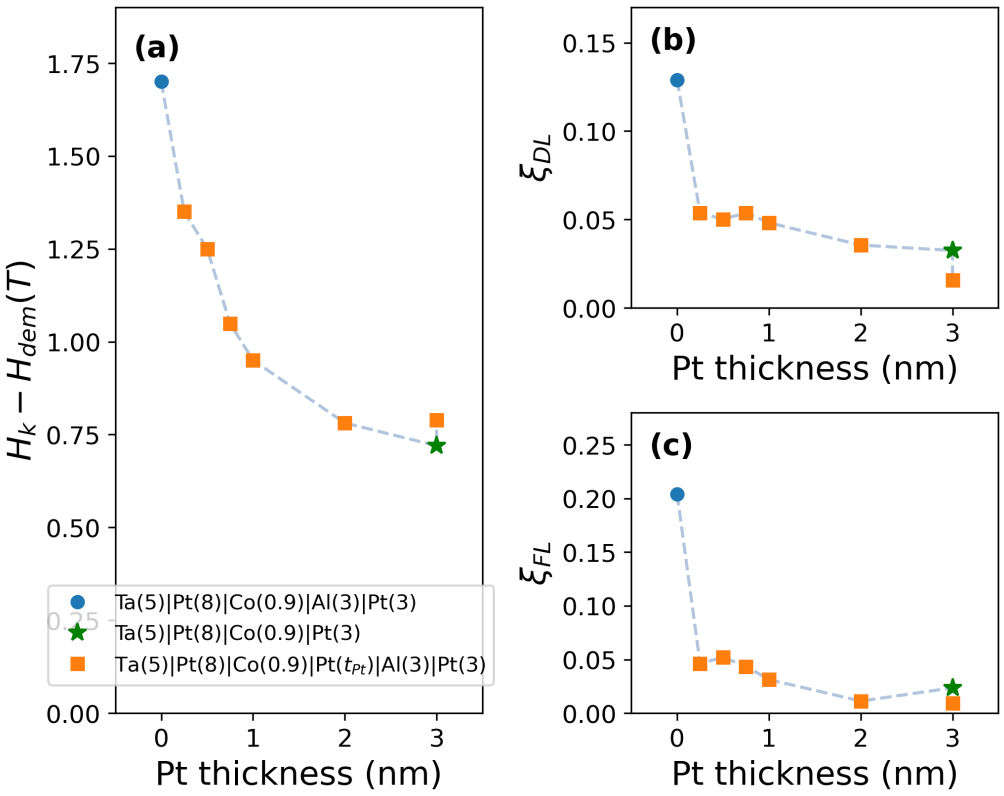


Figure 8.3 – **a**) Anisotropy effective fields for Ta(5 nm)|Pt(8 nm)|Co(0.9 nm)|$\tilde{Pt}(t_{\tilde{Pt}})$|Al(3 nm)|Pt(3 nm). Room temperature saturation magnetization in shown in inset. **b**) Damping-like and **c**) field-like torque efficiencies in this sample series. For comparison, the blue dots are representing the sample with Co|Al without $\tilde{\mathrm{Pt}}$ dusting : Ta(5 nm)|Pt(8 nm)|Co(0.9 nm)|Al(3 nm)|Pt(3 nm) and the green star is the reference sample without Al, Ta(5 nm)|Pt(8 nm)|Co(0.9 nm)|Pt(3 nm).

## 8.3 . Results of SOT on Pt dusting series

All the samples of the $\tilde{\mathrm{Pt}}$ series exhibit PMA. This indicates a good interface quality. Figure 8.3 **a**) displays the effective anisotropy fields $H_K^{eff} > 0$ measured in the 0.25 to 3 nm $\tilde{\mathrm{Pt}}$ thickness range. We observe that the effective anisotropy field $H_k^{eff}$ decreases from 1.75 T in the sample free of any $\tilde{\mathrm{Pt}}$ (blue dot) to 1.35 T for 0.25 nm $\tilde{\mathrm{Pt}}$ and down to 0.79 T for 3 nm $\tilde{\mathrm{Pt}}$. This coincides with the $H_K^{eff}$ value measured in Pt(8)|Co(0.9)|Pt(3) (0.75 T, green star).

We now turn to the discussion of the damping-like and field-like torque components measurements in this samples (figure 8.3 **b-c**). As a 0.25 nm dusting $\tilde{\mathrm{Pt}}$ is inserted between Co and Al layers, we observe a steep decrease of both torque components : by a factor of four for the field-like torque ($\xi_{FL}$ drops from 0.22 to 0.055) and by a factor of two regarding the damping-like torque component ($\xi_{DL}$ falls from 0.13 to 0.065). The

ratio $\frac{H_{FL}}{H_{DL}}$ reaches a value lower than 1, as would be expected when the Rashba induced field-like torque component becomes small compared to the SHE (as introduced by $\tilde{\text{Pt}}$). As the Pt dusting gradually increases up to 3 nm, the two torque components continuously decrease, as expected, down to their value ($\xi_{DL}^{\tilde{\text{Pt}}=3} = 0.02$) corresponding to almost perfectly compensated reference structure Pt(8)|Co(0.9)|Pt(3). An experimental ratio for $\tilde{\text{Pt}} = 3$ nm is then reached $H_{FL}/H_{DL} \simeq 0.3$, as expected from our reference data and theory [Stiles and Zangwill, 2002, Krishnia et al., 2023].

The ensemble of these experimental data, and notably the fact that the amplitude of the drop of the field-like torque is twice that of the damping-like component (for as thin as 0.25 nm $\tilde{\text{Pt}}$) indicates that the full $\tilde{\text{Pt}}$-thickness dependency of the torque may be explained by three subsequent phenomena :

1. The orbital Rashba momentum locking at Co|$\tilde{\text{Pt}}|Al$ interface disappears rapidly due to band structure modification introduced by $\tilde{\text{Pt}}$. This suggests that the large OML at Co|Al interface requires pristine Co|Al interface. The consequence of modifying the band structure is a vanishing field-like torque.
2. the occurrence of enhanced electronic spin-flip scattering onto $\tilde{\text{Pt}}$ for small $\tilde{\text{Pt}}$. This reduces the reflection of spin propagating at the top Co interface and therefore reduces the lifetime of spins incoming from bottom Pt in Co. Hence damping like shrinks.
3. Finally, for the thicker $\tilde{\text{Pt}}$ layers, the rise of an SHE contribution opposite to the bottom Pt layer leads to a partial torque compensation (mainly of damping-like torque symmetry).

## 8.4 . Ab-initio calculations of Co|$\tilde{\text{Pt}}$|Al

This experimental study is completed by ab-initio calculations performed in collaboration with Armando Pezo using the framework described chapter 7. DFT and linear response theory furnish guidance on how to interpret in details the consequences of dusting $\tilde{\text{Pt}}$ insertion between Co and Al. We describe here how it predicts a transition from a system governed by orbital accumulation to a system governed by SHE induced torques.

### 8.4.1 . OML disappearance with $\tilde{\text{Pt}}$ insertion

Figure 8.4 **a**) and **b**) display the average values of the orbital angular momentum (respectively $l_x$ and $l_y$) computed in the Brillouin zone in Al(11)|Pt(1)|Co(12) (numbers in parenthesis here are simulated atomic planes). Despite an OML texture being visible, we clearly observe that its amplitude is ten times weaker than that of Co|Al reported in figure 7.2. DFT hence shows that $\tilde{\text{Pt}}$ dusting is detrimental to the observation of the OML arising between Co and Al.

In line with these observation, the out-of-equilibrium orbital angular momentum density (accumulation) response to an applied electric field is dramatically reduced in simulated Co|Pt|Al compared to that found for Co|Al. We compute in figure 8.4 **g**) that it drops by

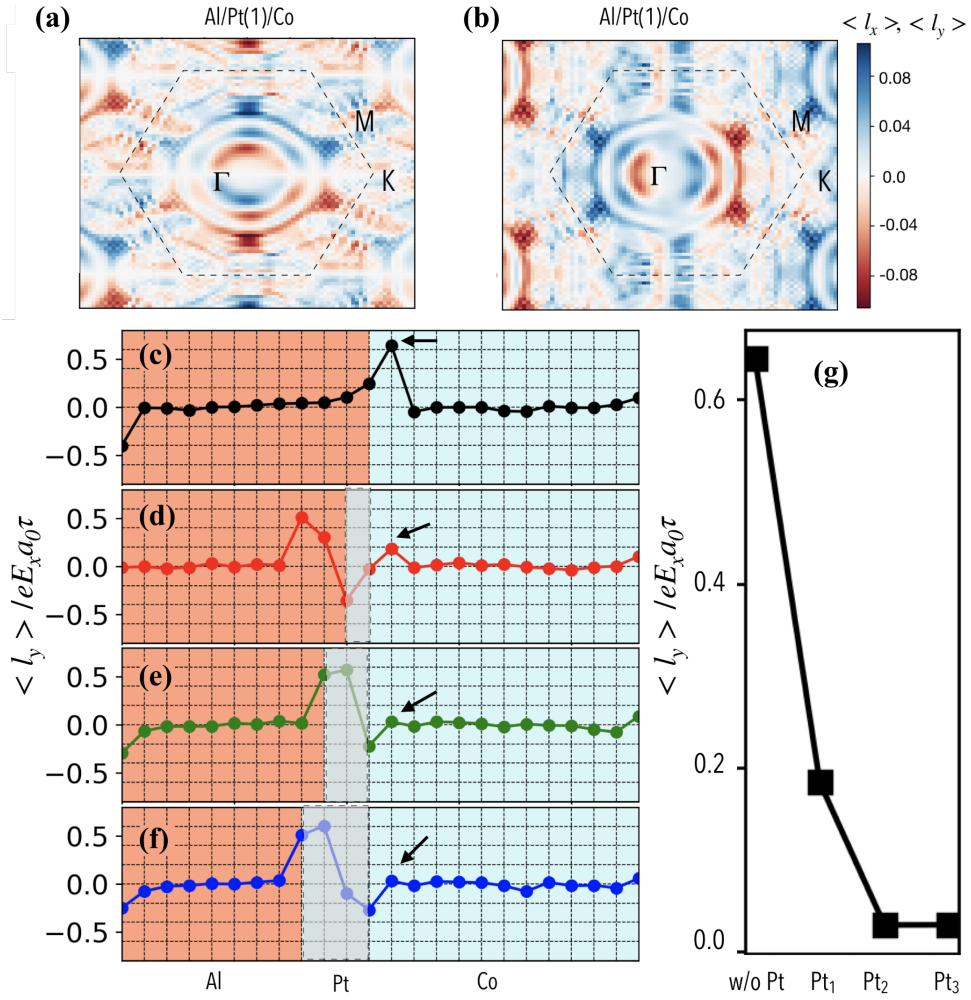


Figure 8.4 – Equilibrium **a**) $\langle l_x \rangle$ and **b**) $\langle l_y \rangle$ operators over the Brillouin zone in Al|Pt(1)|Co. Out of equilibrium orbital accumulation emerging under an applied electric field projected on the different atomic layers in **c**) Al|Co, **d**) Al|Pt(1)|Co, **e**) Al|Pt(2)|Co, **f**) Al|Pt(3)|Co. **g**) Integrated orbital accumulation response over the full Co thickness in those four simulated stacks. *Extracted from Ref. [Pezo et al., 2025].*

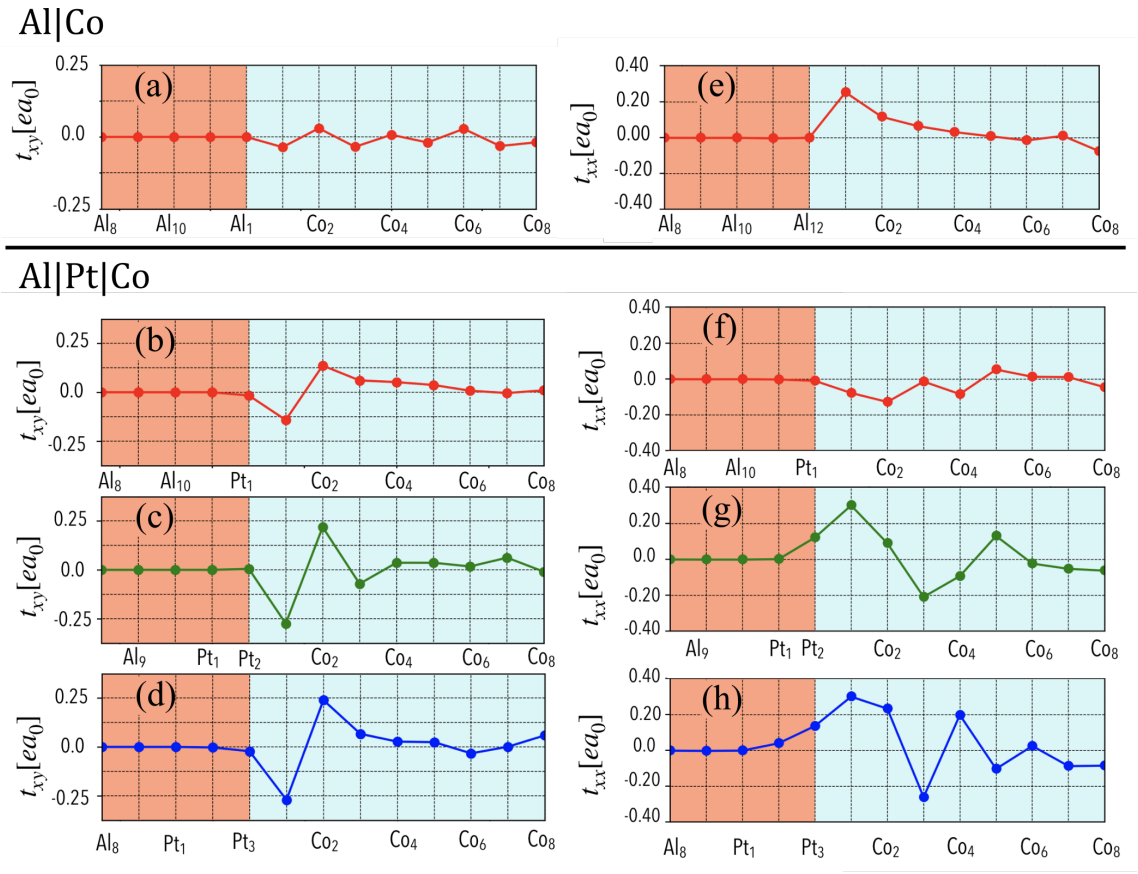


Figure 8.5 – Profile of the damping-like torquance ($t_{xy}$) torquance projected on each atomic layer in **a**) Al|Co, **b**) Al|Pt(1)|Co, **(c)** Al|Pt(2)|Co, **d**) Al|Pt(3)|Co. Profile of the field-like torquance ($t_{xx}$) projected on each atomic layer in **e**) Al|Co, **f**) Al|Pt(1)|Co, **g**) Al|Pt(2)|Co, **h**) Al|Pt(3)|Co. *Extracted from Ref. [Pezo et al., 2025].*

about a factor of three when only one dusting $\tilde{\text{Pt}}$ atomic plane is inserted between Co and Al. It is nearly fully suppressed when $\tilde{\text{Pt}}$ becomes thicker.

On figure 8.4 **c-f**), we report on the orbital accumulation expected to arise in each atomic layer when an electric field is applied. In **c**), we reproduce the strong orbital accumulation arising in the first Co layer of Al|Co as stated chapter 7. In **d,e,f**, 1,2 and 3 $\tilde{\text{Pt}}$ layers are inserted between Co and Al. We clearly observe an extinction of the orbital accumulation inside Co, source of the orbital-torque (of field-like symmetry). However, this accumulation is non zero over the whole metallic stacking since it presents an oscillating behavior over Pt and Al layers. The non zero torkance projected in the Pt layer is a signature local magnetic moment arising due to proximity effect.

### 8.4.2 . Anatomy of Torques in Co|$\tilde{\text{Pt}}$|Al systems.

We now turn to the expectation values of the torkance for each structures. We remind, from the previous chapter, that they have been derived from the linear response

| | $t_{xx}$ $(ea_0)$ | $t_{xy}$ $(ea_0)$ |
|---|---|---|
| Co\|Al | 0.37 | -0.04 |
| Co\|Pt(1)\|Al | -0.08 | 0.33 |
| Co\|Pt(2)\|Al | 0.10 | -0.08 |
| Co\|Pt(3)\|Al | 0.15 | 0.13 |

Table 8.1 – Torkance integrated over the whole Co layers in the different investigated multilayers.

theory and Kubo formula adapted to the torque operator acting on the local spin density [Pezo et al., 2025].

The torkance profiles projected on each layer atomic plane are displayed in figure 8.5 under different conditions. The two top graphs (**a** and **b**) exhibit the already discussed case of Co|Al interface. The torque response is primarily of a field-like torque symmetry ($t_{xx}$) and monotonously evanescent in Co, due to OREE. Its evanescent character is indicated by the localization of the torque on the only two-first planes of Co whereas it is clearly noticeable that no torques occurs inside Al because of the absence of any local magnetic moment. However, this stands in stark contrast to simulated Al|Pt|Co trilayer as soon as one atomic plane of Pt is inserted.

With Pt between Al and Co, both $t_{xx}$ and $t_{xy}$ torkances have significant values and are of oscillatory behavior inside the Co layer (figure 8.5 **b** to **h**). This is the expected signature of a spin-current propagating inside Co and experimenting Larmor precession around the local magnetization. In addition, the integrated torkance over the Co layer is also shown table 8.1 to be balanced between $t_{xx}$ and $t_{xy}$ components.

This calculation thus illustrates how different in nature are torques due to OREE and those due to Pt SHE. It also displays how sensitive OREE is, in agreement with our experiments and interpretation reported in section 8.3. As far as a single atomic plane of Pt inserted, orbital character is lost. It is replaced by an SOT response governed by Pt SOC.

Regarding the torkance unit, we remind here, from chapter 7, that an integrated torkance on the FM side of 0.37 $[ea_0]$ is equivalent to a field torque $B_{FL} = \left(\frac{e^* a_0}{M_s N}\right) t_{xx} \mathcal{E}$ ($M_s$ is the atomic magnetic moment and $N$ the number of Co atomic planes) giving $B_{FL} \approx 2$ mT (for an applied electric field $\mathcal{E} = 2.5 \times 10^4$ V/m or equivalently, effective current density in bottom 8 nm Pt of $\mathcal{J}_c^{Pt} = 10^{11}$ $A/\text{m}^2$, a typical value in our experiments).

## 8.5 . Conclusion

The experimental and theoretical investigation of adding dusting Pt between Co and Al that we reported so far in this chapter sheds light on the peculiarity of Co|Al interface. When a layer of Pt as thin as 0.25 nm is inserted between Co and Al, SOT efficiencies shrink by factor of two in damping like and four in field like. This ultrathin Pt layer is thus

detrimental to SOT despite bringing SOC to the multilayers. It reinforces our interpretation of SOT at Co|Al interface originating because of OREE occurring in the atomic layer of Co next to Al and that the resulting orbital accumulation is converted to SOT inside Co. Adding Pt suppresses this angular momentum source.

Furthermore, we are able to reproduce our experimental observations in DFT calculations, following the principles described chapter 7. Those DFT calculations disclose the transition from OREE governed torques in Co|Al to SHE dominated system Co|$\tilde{\mathrm{Pt}}$|Al. A striking difference that emerges is the precessional behavior of diffusive SHE spin currents contrasting to thee evanescent decay of interfacial Rashba electronic states.

In the following chapter, we no longer try to modify the non magnetic layers of our structure but rather investigate if we can keep large SOT while changing the ferromagnetic material to CoFeB alloy that is more suited to industry requirements.

# 9 - Impact of CoFeB substitution on PMA and orbital torques

## 9.1 . Harnessing orbital torque in CoFeB based systems

Investigations conducted in the previous chapters focus on samples where the ferromagnetic layer consists of pure Co. However, CoFeB alloys have become in the last decades a cornerstone in industrial spintronics due to their superior properties compared to pure Co, particularly in terms of magnetic anisotropy, interfacial characteristics, its perfect integration in MgO-based magnetic tunnel junctions, tunnel spin-polarization and overall device performance. For these reasons and given that one objective of my PhD is to explore new strategies for reducing the writing energy cost in SOT-MRAM, we propose to investigate the implementation of the orbital torque (added to the SOT) in equivalent CoFeB-based structures made from $Co_{40}Fe_{40}B_{20}$ material.

One of the key advantages of CoFeB is its ability to promote strong PMA when interfaced with MgO [Hirohata et al., 2020, Dieny and Chshiev, 2017]. This interfacial anisotropy is essential for memory technologies such as STT- or SOT- MRAM. In contrast, Co lacks the same level of tunability in interfacial PMA, which limits its scalability for such applications.

In addition to its magnetic anisotropy, CoFeB is known for enabling exceptionally high TMR in MgO-based magnetic tunnel junctions (MTJs), surpassing 150 % at room temperature in seminal works [Yuasa et al., 2004, Parkin et al., 2004]. TMR ratios of 600 % have later been achieved [Ikeda et al., 2008]. This remarkable performance is assigned to the high spin-polarization of CoFeB and its ability to form an epitaxial relationship with MgO upon annealing, thus facilitating efficient spin-dependent tunneling. In contrast, pure Co generally suffers from poorer interfacial crystallization and cannot reach similar TMR levels.

Another advantage of CoFeB is its tunable magnetic properties, achieved by varying B concentration. At a B contents above 6 atomic percent, CoFeB remains amorphous, which is ideal for creating smooth and uniform interfaces. When the boron content is reduced below this threshold, the alloy can crystallize into a body-centered cubic (bcc) CoFe phase with controlled magnetic properties, including saturation magnetization ($M_s$), damping constant ($\alpha$), and exchange stiffness [Kim et al., 2022]. This tunability allows device engineers to optimize performance parameters such as switching energy, which is not possible with the fixed composition of pure Co. In this thesis, we chose to investigate samples made with $Co_{40}Fe_{20}B_{20}$ because it was reported to be a good trade-off between damping and anisotropy of the free layer [Dieny and Chshiev, 2017].

From a magnetization dynamics standpoint, CoFeB offers low Gilbert damping, typically around $5 \times 10^{-3}$, which supports ultrafast magnetization switching processes at the nanosecond timescales [Weber et al., 2019]. This characteristic is essential for developing energy-efficient memory devices and spin-torque nano-oscillators. In comparison, the higher damping of pure Co hampers high-speed performance and leads to larger energy dissipation [Zhu and Zhu, 2007].

From the ensemble of those considerations, CoFeB presents numerous advantages over

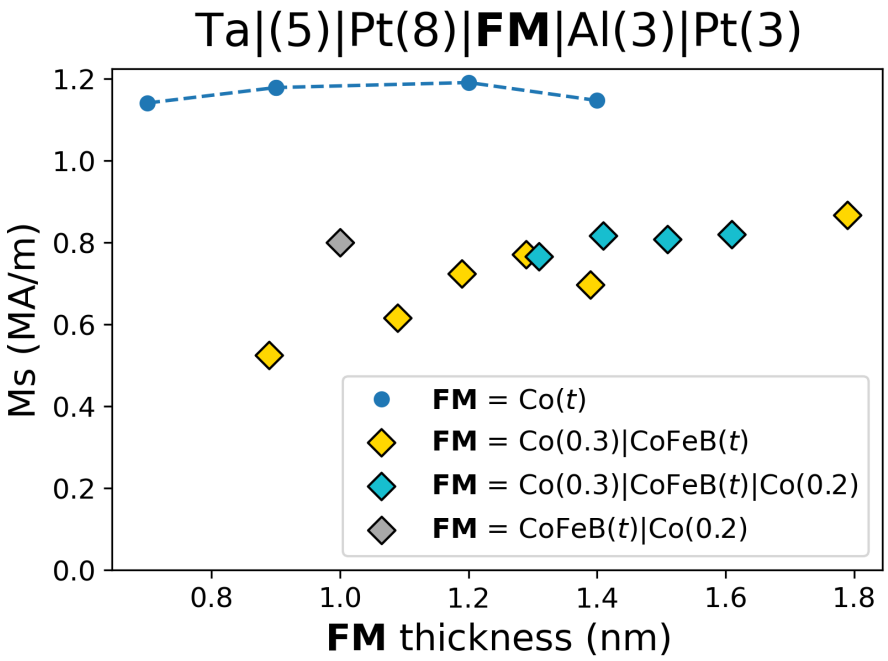


Figure 9.1 – Saturation magnetization $M_s$ measured in series of samples Ta(5 nm)|Pt(8 nm)|**FM**|Al(3 nm)|Pt(3 nm) where **FM** is a varying ferromagnetic layer. The *FM thickness* in the X axis is the total ferromagnetic thickness in the samples.

Co in the development of industrial spintronic devices. In order to see if the OREE we identified at the Co|Al interface could be reproduced with this ferromagnetic alloy, I have grown four samples series made of the same Pt|Co|Al structure than previously investigated where Co is replaced by a ferromagnetic layer based on $Co_{40}Fe_{40}B_{20}$ accompanied, or not, by ultrathin Co layers :

- Ta(5 nm)|Pt(8 nm)|$Co_{40}Fe_{40}B_{20}(t_{CoFeB})$|Al(3 nm)|Pt(3 nm)
- Ta(5 nm)|Pt(8 nm)|Co(0.3 nm)|$Co_{40}Fe_{40}B_{20}(t_{CoFeB})$|Al(3 nm)|Pt(3 nm)
- Ta(5 nm)|Pt(8 nm)|$Co_{40}Fe_{40}B_{20}(t_{CoFeB})$|Co(0.2 nm)|Al(3 nm)|Pt(3 nm)
- Ta(5 nm)|Pt(8 nm)|Co(0.3 nm)|$Co_{40}Fe_{40}B_{20}(t_{CoFeB})$|Co(0.2 nm)|Al(3 nm)|Pt(3 nm)

The magnetic and transport properties of the resulting multilayers have been studied through AHE, PHE, anisotropy and SOT measurements. In the next sections of this manuscript, if the concentrations of the different elements are not specified, CoFeB designates $Co_{40}Fe_{40}B_{20}$.

## 9.2 . Magnetic properties

### 9.2.1 . Saturation magnetization

We measured via SQUID the saturation magentization $M_s$ of the samples combining ultrathin Co and CoFeB. The results are presented figure 9.1. The samples with pure Co fer-

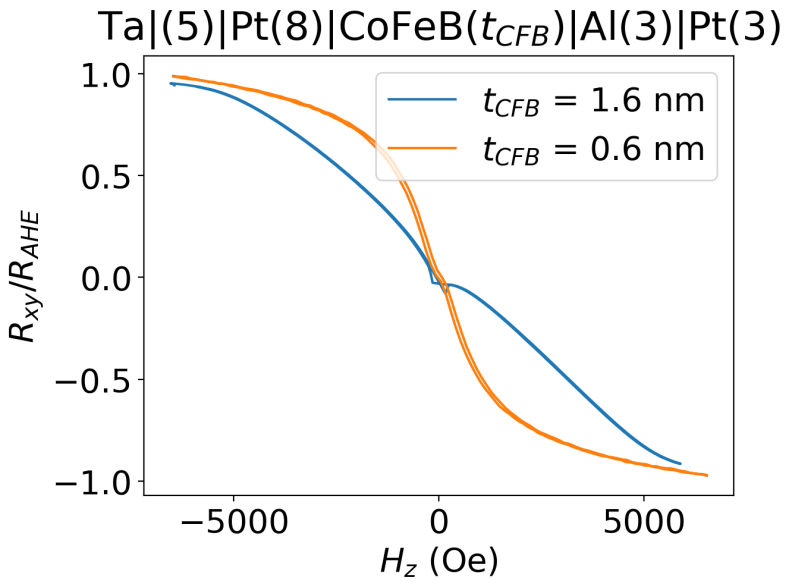


Figure 9.2 – Renormalized transverse AHE resistance $R_{xy}$ vs. OOP field scan in Ta|(5 nm)|Pt(8 nm)|CoFeB(0.6 (orange) and 1.6 nm (blue))|Al(3 nm)|Pt(3 nm).

romagnetic layer $M_s$ are reported on the same graph. They exhibit a saturation magnetization around 1.2 MA/m measured mostly independent on the Co thickness. We observe smaller $Ms$ than Co in the CoFeB based samples (as expected) with values comprised between 0.6 and 0.8 MA/m. Those values are similar to previous reports concerning CoFeB thin films [Devolder et al., 2013]. We note that the series with Co(0.3 nm)|CoFeB($t$) and Co(0.3 nm)|CoFeB($t$)|Co(0.2 nm) (yellow and blue diamonds) have very close $M_s$ as a function of the total ferromagnetic thickness. The sample without Co deposited under CoFeB (grey diamond) has a $M_s$ of 0.8 MA/m, larger than the two other series for $t_{FM} = 1.0nm$, which $M_s$ is around 0.6 MA/m.

We observe an increasing trend of $M_s$ while thickening the ferromagnetic layer in the series Co(0.3 nm)|CoFeB($t$) and Co(0.3 nm)|CoFeB($t$)|Co(0.2 nm). This increase with $t_{CoFeB}$ has been already reported in $Co_{20}Fe_{60}B_{20}$ ultrathin limit (under 3 nm thickness) [Panda et al., 2019] and in $Co_{40}Fe_{40}B_{20}$|Pd multilayers whose $Co_{40}Fe_{40}B_{20}$ thicknesses were less than 5 Å [Silva et al., 2021].

Therefore, from these magnetization characterizations, we conclude that mixed ferromagnetic layers made of CoFeB grown onto or under an ultrathin Co layer are of a particular interest to engineer PMA toward anisotropy weaker than pure Co.

### 9.2.2 . Magnetic anisotropy

In terms of anisotropy, all samples of the Ta|Pt(8 nm)|CoFeB($t_{CoFeB}$)|Al(3 nm)|Pt(3 nm) series were found to exhibit in-plane anisotropy. Figure 9.2 displays the transverse resistance $R_{xy}$ vs. the out-of plane applied magnetic field for both the thinnest and thickest

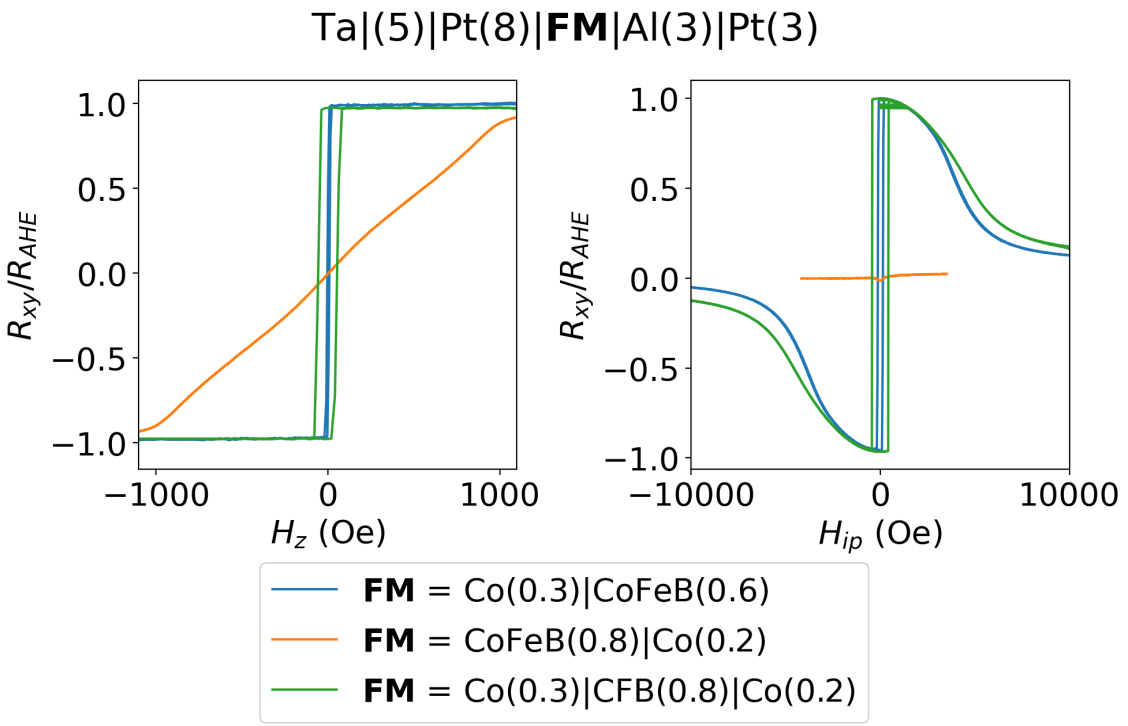


Figure 9.3 – Transverse resistance renormalized by AHE during an out of plane field scan in Ta(5 nm)|Pt(8 nm)|Co(0.3 nm)|CoFeB(0.6 nm)|Al (3 nm)|Pt(3 nm) (blue), Ta(5nm)|Pt(8 nm)|CoFeB(0.8 nm)|Co(0.2 nm)|Al(3 nm)|Pt(3 nm) (orange), Ta(5 nm)|Pt(8 nm)|Co(0.3 nm)|CoFeB(0.8 nm)|Co(0.2 nm)|Al(3 nm)|Pt(3 nm) (green).

samples in this series. The two measurements clearly demonstrate the absence of any hysteresis behavior and any remnant magnetization.

Hence, the chosen strategy to achieve PMA in samples based on CoFeB has been to include an ultrathin Co at the outer interfaces. Then, in order to distinguish the role of each interface, we have elaborated three series of such samples : Ta(5 nm)|Pt(8 nm)|Co(0.3 nm)|CoFeB($t_{CFB}$)|Al(3 nm)|Pt(3 nm), Ta(5 nm)|Pt(8 nm)|CoFeB($t_{CFB}$)|Co(0.2 nm)|Al(3 nm)|Pt(3 nm), Ta(5 nm)|Pt(8 nm)|Co(0.3 nm)|CoFeB($t_{CFB}$)|Co(0.2 nm)|Al(3 nm)|Pt(3 nm).

Our idea is that increasing the Co content at the interfaces might recover the properties measured previously in Pt|Co|Al system, with, however, a reduced anisotropy size. On one hand, we anticipate a surface anisotropy to arise at both interfaces. On the other hand, a higher Co concentration interfacing Al is expected to enable OREE.

The OOP magnetic hysteresis of some samples of these series are displayed in figure 9.3. We note that two samples out of three possess a PMA property : those with Co interfacing Pt, whereas the thinnest CoFeB with Co interfacing only Al still possesses an in plane magnetization (FM = CoFeB(0.8)|Co(0.2)). This shows that the surface anisotropy at the

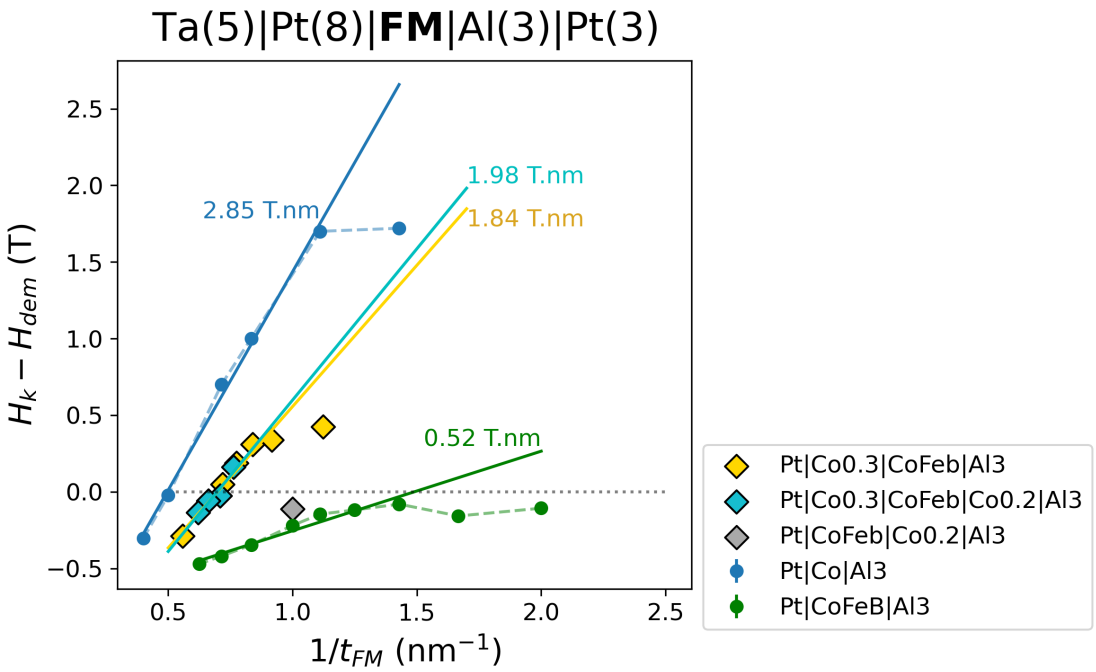


Figure 9.4 – Effective anisotropy field measured in different series of samples Ta(5 nm)|Pt(8 nm)|**FM**|Al(3 nm)|Pt(3 nm) as a function of the ferromagnetic layer thickness inverse. **FM** is a varying ferromagnetic layer. The *FM thickness* in the X axis is the total ferromagnetic thickness. Each sample series is fitted to a straight line. Each line's slope is indicated in T.nm.

Pt|Co interface is really required for observing the magnetic transition from IP to PMA. Moreover, PMA is further increased with Al interfacing Co, as observed from the higher value of the coercive field for the sample FM = Co(0.3)|CoFeB(0.8)|Co(0.2).

The magnetic anisotropy strength are gathered in figure 9.4. We observe that all the CoFeB based samples present an IP magnetization while the samples with pure Co present large PMA up to 2 nm Co thickness. As demonstrated in figure 9.3, adding an ultrathin Co layer between CoFeB and Pt enables PMA in the ultrathin limit (ferromagnetic thickness comprised between 0.75 and 1.5 nm). Still, those samples exhibit a significantly reduced effective anisotropy field compared to Co ones. In Ta(5 nm)|Pt(8 nm)|Co(0.3 nm)|CoFeB(0.6 nm)|Al(3 nm)|Pt(3 nm), we deduce an effective anisotropy field of 0.4 T whereas the sample with 0.9 nm of pure Co as a ferromagnetic layer possesses an anisotropy of 1.7 T.

In figure 9.4, we present the evolution of the effective anisotropy vs. the inverse of the (total) ferromagnet thickness, and fit the anisotropy with a line (with exception of some of the thinnest samples), similarly to figure 6.9. According to the model of equation 6.2, the slope of the lines corresponds to the surface anisotropy and the offset to saturation

magnetization. This model renders :

$$H_k^{eff} = \left(H_k^{\mathcal{V}} - M_s\right) + \frac{H_k^s(FM|Pt)}{t_{FM}} + \frac{H_k^s(FM|Al)}{t_{FM}} \tag{9.1}$$

The comparison between the two FM = Co and FM = CoFeB series demonstrates that the sum of Al- and Pt- induced interface anisotropies is much smaller for CoFeB (0.52 T.nm slope) than for pure Co (2.85 T.nm slope) as expected from the softer CoFeB magnetic material.

We only measured the anisotropy of the FM = CoFeB|Co(0.2) series thinnest sample because we found out it does not posses PMA (grey diamond in figure 9.4. Still, we note that the anisotropy in this sample is close to that of the CoFeB series. We thus conclude that Co|Al interface grown on our CoFeB does not induce a large interface PMA.

Nevertheless, we measure that the slopes in $H_k$ vs. $t_{FM}$ for the series FM = Co(0.3)|CoFeB (yellow diamond in the Figure 9.4 and FM = Co(0.3)|CoFeB|Co(0.2) (blue diamond), respectively 1.84 T.nm and 1.98 T.nm, are four times larger compared to sole CoFeB (0.52 T.nm). This suggests that a Co insertion on top of Pt generates a pretty large interface anisotropy at the scale of about a single atomic plane (0.3 nm). This clearly goes in favor of a very good quality of the sputtering growth maintaining the interface memory between both Co|CoFeB and Pt|CoFeB. Regarding the opposite 'top' interface, the small difference in the anisotropy between FM = Co(0.3)|CoFeB and FM = Co(0.3)|CoFeB|Co(0.2) seems to indicate that Co does not enhance anisotropy when inserted between CoFeB and Al.

The overall measurements reveal that the magnetic anisotropies emerging at Pt and Al are significantly smaller, by a factor of almost 6, for CoFeB thin films compared to pure Co films. Adding a thin Co layer at the Pt interface restores a large surface anisotropy while inserting Co between CoFeB and Al has a minimal effect onto the magnetic anisotropy. We conclude that the interface between Pt and an ultrathin Co is of very good quality while the Co|Al grown onto our CoFeB thin films does not reproduce the properties observed in section 6.3.1.

On the one hand, we note that the anisotropy reduction can be of interest in the perspective of magnetization switching as, for a given SOT amplitude, a sample with lower anisotropy switches at lower critical current. On the other hand, the anisotropy dependence on the ferromagnetic film thickness suggests the FM|Al interface has different SOC related properties when Co is replaced by CoFeB. We thus conduct SOT measurements in this series of samples in order to investigate how they compare to the pure Co case.

## 9.3 . Transport analyses via AHE

In the figure 9.5, we show the evolution of the transverse resistance $R_{AHE}$ vs. the FM thickness. It follows a different trend than observed for Co. We first no-

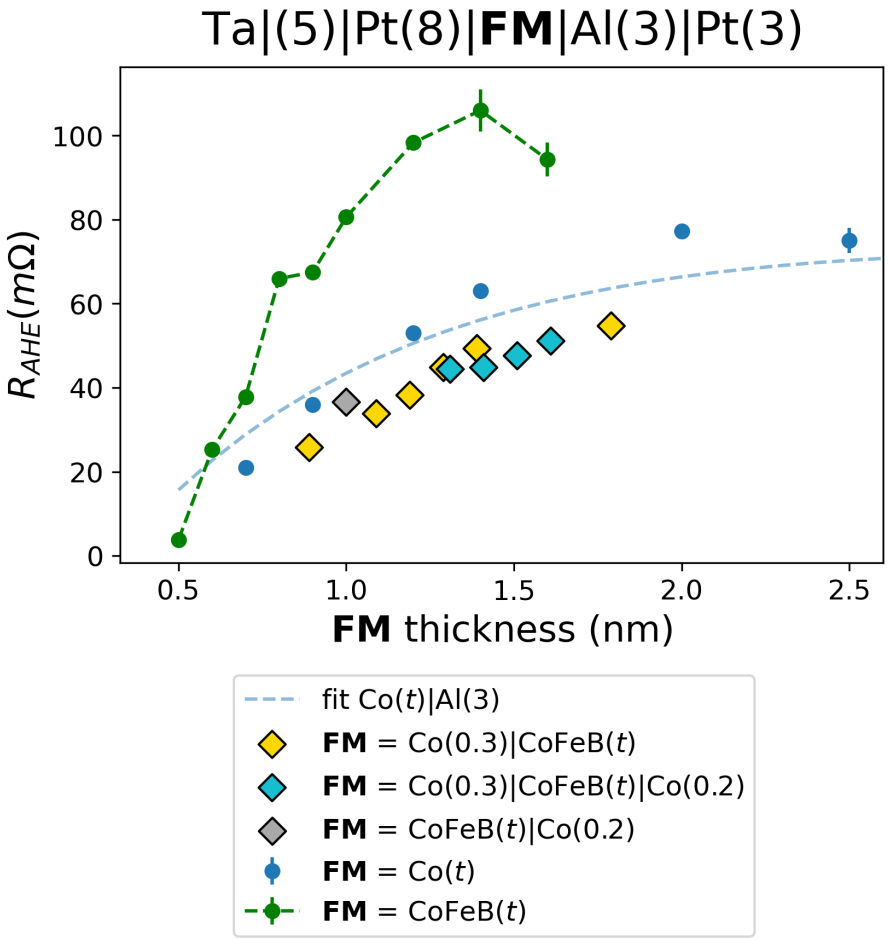


Figure 9.5 – $R_{AHE}$ measured in series of samples Ta(5 nm)|Pt(8 nm)|**FM**|Al(3 nm)|Pt(3 nm) where **FM** is a varying ferromagnetic layer. The *FM thickness* in X axis is the total ferromagnetic thickness in the samples. The blue dotted lines are a fit according to the model described section 6.4.2

tice larger AHE in the samples made of pure CoFeB ferromagnetic layer than in samples made of sole Co. Ta(5)|Pt(8)|Co(1.2)|Al(3)|Pt(3) yields $R_{AHE}$ of 53 $\mathrm{m}\Omega$ whereas Ta(5)|Pt(8)|CoFeB(1.2)|Al(3)|Pt(3) $R_{AHE}$ is as large as 98.3 $\mathrm{m}\Omega$. We can interpret this as a manifestation of a larger spin-polarization of free carriers in CoFeB. This has been reported in [Huang et al., 2008] where the author make the most of Andreev reflections to assess a polarization of 63 % in $Co_{40}Fe_{40}B_{20}$ while polarization in Co was measured to 45 % using the same technique [Strijkers et al., 2001].

Yet, we additionally propose another explanation for the presently higher AHE. Indeed, only increasing the spin-polarization in our model didn't allow to fit AHE data acquired on the CoFeB series as well as the pure Co series. The shift of the maximum AHE towards lower CoFeB thickness of about 1.5 nm (figure 9.5) suggests either a decrease of the (spin-dependent) electron mean-free path, owing to the larger resistivity of CoFeB compared to Co or a larger electron specularity at CoFeB|Al interface as emphasized below.

In the samples with a mixed ferromagnetic layer made of CoFeB and interfacial ultrathin Co layer, we find smaller AHE amplitudes, slightly weaker than those measured in Co. Such reduction in the AHE when an ultrathin Co layer is inserted at both CoFeB|Pt and CoFeB|Al interfaces is a signature of a partial loss of the spin-dependent transport properties at those interfaces. This implies here a loss of the scattering specularity and/or the introduction of a spin-memory loss effect unlike the aforementioned case of homogeneous CoFeB layer.

From our simulations (see figure 9.5) in pure Co samples, the amplitude difference between Pt|CoFeB|Al AHE and Pt|Co|Al stems from lower specularity in reflection at Co|Al interface compared to CoFeB|Al. In Pt|CoFeB|Al trilayers, part of AHE is due to CoFeB conduction electrons reflected at the interface with Al, crossing CoFeB and transmitted into the bottom Pt. In Pt, they produce a substantial transverse AHE current due to Pt enhanced spin-orbit scattering. If the reflection at the Al interface is specular, the electrons contribute significantly to AHE due to the large Pt SHE.

However, this contribution is suppressed in two cases. Either $t_{CoFeB}$ is thicker than the (spin) mean free path and, consequently the maximum in AHE is reached at about two times this length (around 1.5 nm from figure 9.5) and then, AHE decreases for thicker CoFeB layer; or the reflectivity at the **FM**|Al interface is reduced or made less specular, as for Co|Al. Therefore, the AHE reduction with ultrathin Co layers inserted at the interfaces of CoFeB reciprocally validates the memory of the grown sputtered interfaces at the scale of 0.3 nm in thickness.

## 9.4 . SOT quantification

### 9.4.1 . Pt|CoFeB|Al compared to Pt|Co|Al

The SOT efficiencies extracted in Pt(8)|CoFeB($t_{CoFeB}$)|Al(3)|Pt(3) samples (green dots) are reported in figure 9.6 **a)** besides Pt(8)|Co($t_{Co}$)|Al(3)|Pt(3) samples (blue dots) with pure

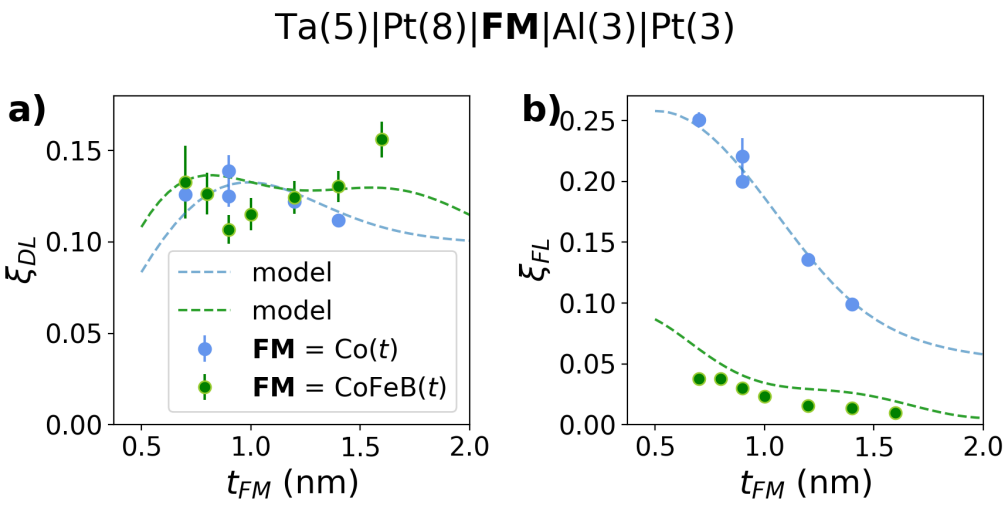


Figure 9.6 – **a)** Damping like and **b** field like SOT efficiencies measured in Ta(5)|Pt(8)|Co($t_{Co}$)|Al(3)|Pt(3) (blue dots) and Ta(5)|Pt(8)|CoFeB($t_{CoFeB}$)|Al(3)|Pt(3) (green dots) series. Dotted lines reproduce the model presented in chapter 6.

Co already presented in chapter 6. The Damping-like efficiency vs. the CoFeB thickness first decreases from 0.13 to 0.1 from $t_{CoFeB} = 0.7$ nm to $t_{CoFeB} = 0.9$ nm. It then monotonously increases to $\xi_{DL} = 0.15$ for $t_{CoFeB} = 1.6$ nm. This dependence on the ferromagnetic thickness is different from the Pt(8)|Co($t_{Co}$)|Al(3)|Pt(3) samples. Indeed, the latter (blue dots) instead present a maximum of $\xi_{DL} = 0.13$ at $t_{Co} = 0.9$ nm. Despite these opposite trends, the two series of samples have damping like efficiencies of the same order, around $\xi_{DL} = 0.12$. Consequently, the samples series in which CoFeB replaces Co displays as large Damping-like torque despite their much weaker magnetic anisotropy up to in-plane magnetization.

Regarding the Field-like torques reported in figure 9.6 **a)**, we measured significantly lower efficiencies in the CoFeB series (green dots) compared to Co (blue dots). The two series exhibit the same monotonously decreasing trend vs. the ferromagnetic layer thickness. However, at $t_{FM} = 0.9$ nm, the Field-like torque efficiency is 4.5 times larger when $\mathbf{FM} =$ Co ($\xi_{FL} = 0.13$) compared to the case of CoFeB ($\xi_{FL} = 0.03$).

This difference between the two sample series strongly suggests a weaker (orbital) Rashba character in Pt|CoFeB|Al compared to Pt|Co|Al. We managed to reproduce the experimental thickness-dependence using our semi-classical torque model described in chapter 6. The green dotted line figure 9.6 represent the outcome of this model involving no (zero) Rashba induced torques and the modification of some characteristic lengths compared to Co discussed hereafter. The blue dashed line is reported for comparison. It conveniently reproduces the model adapted to Pt|Co|Al. Even though we could not adapt our transport model to CoFeB experimental data as well as to Co, we capture some of the observed feature. Notably, figure 9.6 **a**), the model reproduces the non monotonous be-

havior of the measured $\xi_{DL}$. This is permitted by a reduction of the exchange length $\lambda_J$ set to the model : from 0.6 nm in Co to 0.4 nm in CoFeB.

In Figure 9.6 **b**), we then reproduce the Field-like efficiency reduction in CoFeB by suppressing the Rashba source of the SOT. We also have to extend the transverse decoherence length $\lambda_\Delta$ from 1.2 nm in Co to 2.5$\pm$0.5 nm in CoFeB. A factor two in this characteristic length between CoFeB and Co may reveal a better interface quality at CoFeB|Al interface allowing a longer ballistic transport length as expressed previously in the AHE experimental data.

### 9.4.2 . SOT in series incorporating ultrathin Co layers at interfaces with CoFeB

In figure 9.7, we summarize our SOT measurements in Pt|Co|Al, Pt|Co|CoFeB|Al, and Pt|Co|CoFeB|Co|Al series. The Pt|Co(0.3)|CoFeB($t_{CoFeB}$)|Al(3)|Pt(3) series (yellow diamonds figure 9.7) exhibit a similar dependence of Damping-like efficiency as for the series incorporating solely CoFeB, as described in section 9.4.1. Figure 9.7 **a**), although we do not observe any decreasing at the lowest thicknesses, we measure an increase in $\xi_{DL}$ in the $t_{FM} = 1 - 1.8$ nm window.

Regarding the Field-like efficiency however (figure 9.7 **b**), even though the trend is a monotonous decay with increasing thickness as with sole CoFeB, the amplitude is substantially larger. It is comparable to what was observed in Pt|Co|Al|Pt. For instance, at $t_{FM} = 1.2$ nm, $\xi_{FL} = 0.136$ with pure Co and $\xi_{DL} = 0.1$ in Pt(8 nm)|Co(0.3 nm)|CoFeB(0.9 nm)|Al(3 nm)|Pt(3 nm)

In the samples with ultrathin Co inserted at the two CoFeB interfaces, we measured the highest Damping-like torque efficiencies (blue diamonds figure 9.7 **a**). For instance, in Ta(5 nm)|Pt(8 nm)|Co(0.3 nm)|CFB(0.9 nm)|Co(0.2 nm)|Al(3 nm)|Pt(3 nm), we measured $\xi_{DL}$ as large as 0.18.

In parallel, the Field-like torque efficiency of this samples series (blue diamonds figure 9.7 **b**) overlap very well with those measured for the Pt|Co(0.3)|CoFeB($t_{CoFeB}$)|Al(3)|Pt(3) series (yellow diamonds). We then tried to adapt our model parameters in order to reproduce the experimental data. Now, the (orbital) Rashba torques are not set to zero but is reduced by a factor of two compared to the pure Co case. By additionally extending the transverse decoherence length to 3 nm, we are able to reproduce well the experimental trends between within the $t_{CoFeB} = 1.3 - 2$ nm window.

Moreover, in Figure 9.4.1 **c**), we plot the ratio of the two torque components as a function of the ferromagnet thickness. We note that our model does not match the two thinnest samples of Pt|Co(0.3)|CoFeB($t_{CoFeB}$)|Al(3)|Pt(3) series. Indeed, figure 9.4.1 **a**), we observe that the model does not reproduce the decrease of $\xi_{DL}$ at the lower thicknesses. Still, with the parameters adapted to the samples in the range 1.3-2 nm, the model yields a steep increase of the ration $\xi_{FL}/\xi_{DL}$ to values larger than one. This is strongly indicative

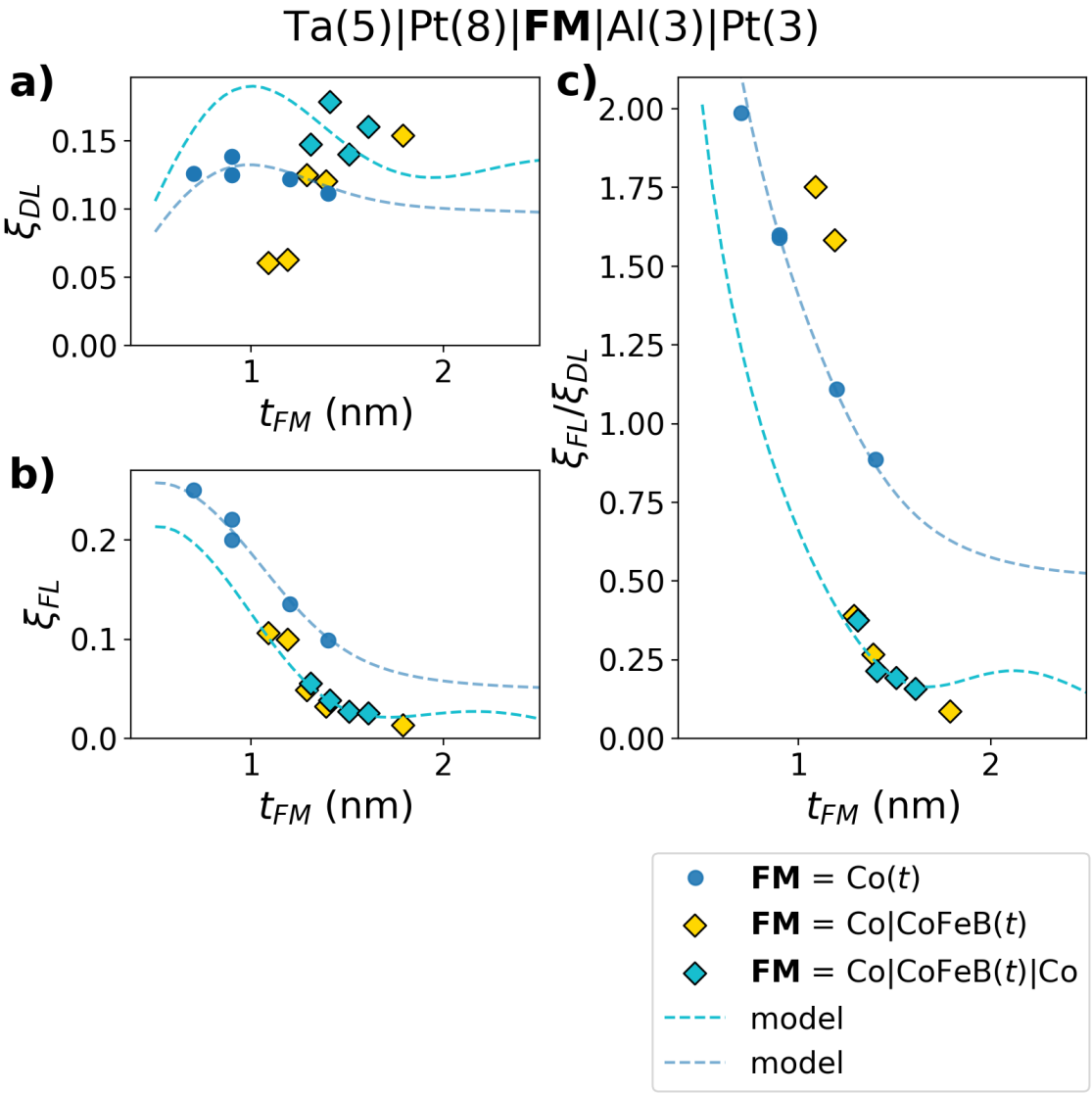


Figure 9.7 – Summary of the SOT efficiencies measured in the Ta(5 nm)|Pt(8 nm)|Co($t_{Co}$)|Al(3 nm)|Pt(3 nm), Ta(5 nm)|Pt(8 nm)|Co(0.3 nm)|CoFeB($t_{CoFeB}$)|Al(3 nm)|Pt(3 nm) and Ta(5 nm)|Pt(8 nm)|Co(0.3 nm)|CoFeB($t_{CoFeB}$)|Co(0.2 nm)|Al(3 nm)|Pt(3 nm) series. The dotted lines are our transport model.

of the existence of Rashba induced SOT in this system as emphasized in this section.

### 9.4.3 . Evaluation of orbital Rashba from DFT

Besides this experimental investigation, we have led DFT calculation of the orbital and spin momentum lockings, corresponding Rashba-Edelstein response and torque efficiencies in CoFe|Al and Fe|Al. The calculations were performed by Armando Pezo. Calculations have been then performed assuming epitaxial bilayers. The results are reported on table 9.1.

| | $\chi_l^{intra}[10^{-10}\hbar\, m/V]$ | $\chi_l^{inter}[10^{-10}\hbar\, m/V]$ | $t_{xx}\,[ea_0]$ |
|---|---|---|---|
| Co/Al | $\mathbf{5.94}$ | 0.20 | $\mathbf{0.37}$ |
| Fe/Al | $\mathbf{2.05}$ | 0.25 | $\mathbf{0.13}$ |
| $Co_{0.5}Fe_{0.5}$/Al | $\mathbf{3.85}$ | 0.19 | $\mathbf{0.26}$ |
| | $\chi_s^{intra}[10^{-10}\hbar\, m/V]$ | $\chi_s^{inter}[10^{-10}\hbar\, m/V]$ | $t_{xy}\,[ea_0]$ |
| Co/Al | 0.12 | -0.002 | -0.04 |
| Fe/Al | 0.18 | 0.07 | 0.05 |
| $Co_{0.5}Fe_{0.5}$/Al | 0.38 | 0.08 | -0.05 |

Table 9.1 – Rashba-Eldelstein response and orbital torques (Field-like $t_{xx}$ and Damping-like $t_{xy}$ torques) for Co/Al and $Co_{1-x}Fe_xB$/Al ($x = 0.5, 1$) structures.

We observe that progressively alloying Co with Fe, the orbital Rashba-Edelstein (intra-band) response decreases from 5.94 $[10^{-10}\hbar\, m/V]$ for pure Co to about half value, 3.85 $[10^{-10}\hbar\, m/V]$ for $Co_{50}Fe_{50}$, and to 2.05 $[10^{-10}\hbar\, m/V]$ for pure Fe. Correspondingly, the Field-like torque ($t_{xx}$) decreases from 0.37 $ea_0$ for pure Co to 0.26 $ea_0$ for $Co_{50}Fe_{50}$ and to 0.13 $ea_0$ for pure Fe proportionally to the orbital Rashba response. Note that in all cases, the spin response is still much smaller than the orbital counterpart.

Our conclusions is that DFT output calculations for the linear response theory are in agreement with the previous conclusions raised concerning the regular decrease of the (orbital) Rashba contribution to the SOT when Co is alloyed with Fe.

## 9.5 . Conclusions and short-term perspectives

We grew metallic multilayers with the same non-magnetic structure as the samples investigated in chapter 6 but integrating $Co_{40}Fe_{40}B_{20}$ instead of pure Co as the ultrathin ferromagnetic layer. We show that contrarily to the Co case, this samples do not possess PMA and are characterized by in-plane magnetization. However, adding an ultrathin Co layer on the interfaces of the CoFeB layer, we were able to demonstrate restored PMA, however significantly weaker than in the pure Co multilayers. Through this engineering of the ferromagnetic layer, we thus manage to tune the magnetic anisotropy.

Regarding SOT, we measured large Damping-like efficiencies in all the CoFeB based samples, in the range of the values measured for pure Co and even larger in some cases. Regarding the Field-like component, it is largely suppressed with CoFeB as ferromagnetic

layer but partially restored by the addition of Co ultrathin layers at each interface. We can approximately adapt the transport model described in the chapter 6 to those series of samples. To do so, besides relaxation lengths modification in the ferromagnet, in order to fit with experiments, we have to suppress the (orbital) Rashba contribution in the samples with only CoFeB and partially restore it, although reduced compared to pure Co, in the samples with ultrathin interfacial Co layers. Those result indicates that CoFeB|Al interface is not host to Rashba states but the growth of ultrathin Co layers may allow to restore part of this character. The experimental results are in agreement with the DFT calculations of the orbital torque from the linear response theory framework.

In the view of magnetization switching experiments, we make the most of the anisotropy reduction compared to pure Co as well as the large Damping-like efficiencies in order to target lower switching critical currents. We thus selected the sample Ta(5 nm)|Pt(8 nm)|Co(0.3 nm)|CoFeB(0.8 nm)|Co(0.2 nm)|Al(3 nm)|Pt(3 nm) to include in our switching study chapter 10. This sample possesses among the largest Damping-like efficiencies ($\xi_{DL} = 0.15$) as well as out of plane anisotropy, but reduced compared to Co ($H_k^{eff} = 0.2$ T). Experimental results and the interpretations are presented in the next chapter 10.

# 10 - Orbital torque assisted magnetization switching in Pt|Co|Al elements

## 10.1 . Introduction

This chapter presents our key findings on magnetization switching experiments in Pt|Co|Al and Pt|CoFeB|Al systems using current injection across the GHz frequency range with short-term perspectives aiming at THz range. These experiments are realized on deep submicronic lithographed pillars and results were compared to reference structures, e.g. Pt|Co systems, to assess the impact of the orbital torque enhancement from OREE introduced at the Co|Al interface. This enhancement aims to reduce the critical current density required for switching. Orbitally induced spin–orbit torques (SOTs) have already shown promise for enabling more energy-efficient magnetization switching, see [Gupta et al., 2025, Huang et al., 2023].

## 10.2 . Field-like torque in magnetization switching

Different approaches have been proposed to model SOT-driven magnetization switching according to the two SOT components efficiency, magnetic anisotropy, damping parameter and DMI strength. Macrospin simulations, assuming coherent dynamics of the magnetization over the whole magnetic sample, show that the damping-like torque causes the magnetization to rotate toward a given hemisphere, whereas the field-like torque triggers precessional motion [Lee et al., 2013, Park et al., 2014]. [Lee et al., 2013] derives a formula for the critical switching current :

$$J_C = \frac{2e}{\hbar}\frac{M_s t_F}{\theta_{SHE}}\left(\frac{H_k^{eff}}{2} - \frac{H_x}{\sqrt{2}}\right) \tag{10.1}$$

with $H_x$ the constant magnetic field applied along the injected current.

However, it is known that the macrospin model represents an oversimplified approximation for magnetic elements of size larger than approximatively 50 nm. In our context, models that account for the role of the Dzyaloshinskii–Moriya interaction (DMI) are more appropriate, as supported by previous work [Mikuszeit et al., 2015]. These models have been validated through time- and space- resolved experimental investigations [Baumgartner et al., 2017] in which the switching process of a 500 nm wide magnetic pillar has been studied using time-resolved XMCD. Their results revealed that switching initiates with the nucleation of a magnetic domain at the edge of the pillar, followed by the propagation of a domain wall across the structure, as illustrated in figure 10.1 **a**). In particular, one of the key observations is that the nucleation of the domain wall takes place deterministically in one of the four quadrants of the magnetic pillar depending on the signs of the current and applied magnetic field $H_x$. They explain this feature by considering the various effective fields contributing to the domain-wall mediated reversal. Owing to energy minimization, DMI induces a significant canting of the spin at the edges of the magnetic pillar (figure 10.1 **b**). The applied in-plane field $H_x$ is parallel to this canting on one side of the pillar and enhances it (left side figure 10.1 **c**).

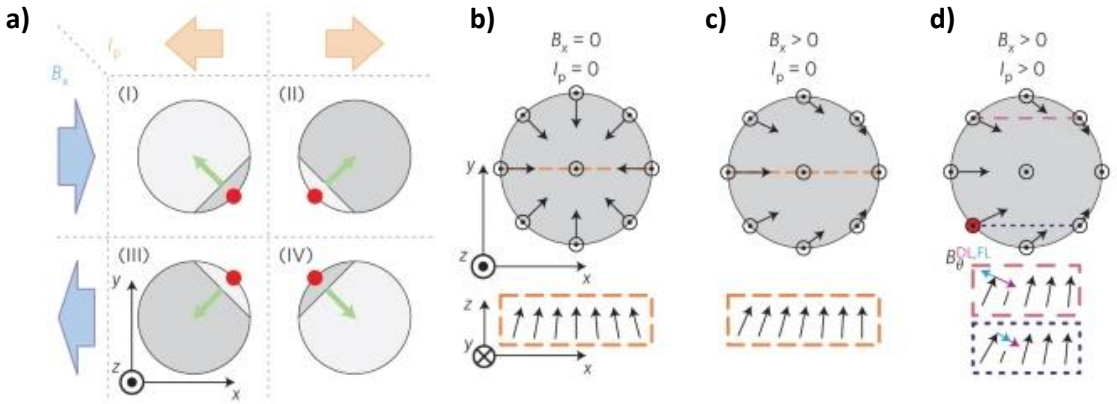


Figure 10.1 – **a**) domain nucleation (red dot) and domain wall propagation (green arrow) observed in [Baumgartner et al., 2017] for all combination of current and applied field signs. **b**) Spin canting in the magnetic nanopillar due to DMI, **c**) Canting configuration due to the addition of an in plane field. **c**) In red, the preferred point of domain nucleation determined by the competition between field-like and damping like effective fields polar components. Extracted from [Baumgartner et al., 2017].

On the dot side, the local magnetization thus possess the maximal in-plane component of the whole nanopillar. The action of the damping-like torque on that in plane spin component is to destabilize it into nucleating a magnetic domain opposite to the main magnetization direction. We thus expect to observe domain nucleation along the dashed line parallel to the applied field figure 10.1 **c)**. However, experimentally, domain nucleation is observed to appear in one of the red points shown in figure 10.1 **a)**.

To understand this, we need to account for damping-like (DL) torque competition with the field-like (FL) torque. Both SOT effective fields i.e. DL and FL, have a finite projection on the canted spin polar direction (the direction causing nucleation). On top of the dashed line in figure 10.1 **c**, those two components are opposite according to the convention chosen in [Baumgartner et al., 2017]. Under this line, they add constructively (inset below the nanopillar figure 10.1 **d**). In this configuration, the spins of the nanopillar that are the most destabilized into nucleating a magnetic domain are lying in the lower left quadrant (red dot figure 10.1 **d**).

Once a domain wall has nucleated in a favorable configuration, it may propagate across the magnetic pillar. The observed angle between the propagation front and the current is consistent with domain wall propagation under an effective field along the $y$ axis [Martinez et al., 2015]. It is thus a signature of the role of the effective field associated to field-like torque. In [Baumgartner et al., 2017], the authors explain by using this argument supported by a micromagnetic model, that nucleation and domain wall propagation symmetry may be consistent or not depending on the sign of the ratio $H_{FL}/H_{DL}$. In the consistent case (represented figure **a**), starting from the nucleation point, domain

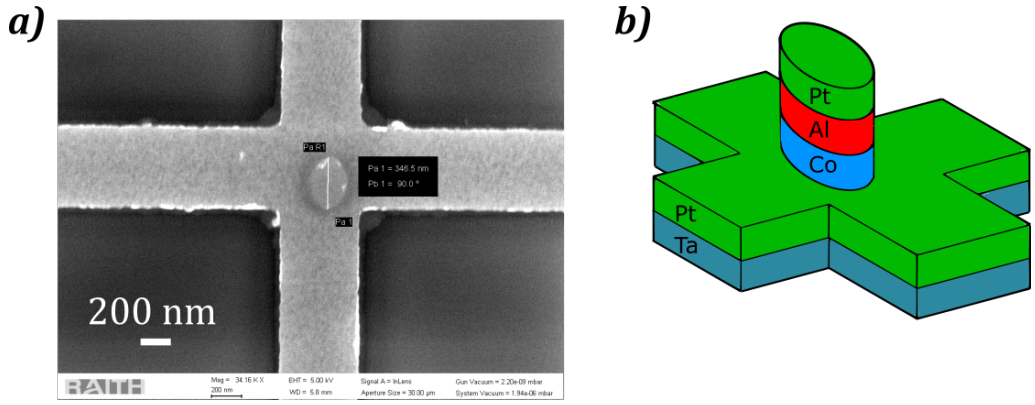


Figure 10.2 – **a**) SEM image of a magnetic pillar at the intersection of two arms of a Hall cross obtained by e-beam lithography. **b**) Scheme of the metallic structure.

wall propagation direction points towards the rest of the pillar. SOT driven switching is hence made more efficient by the action of the FL component $H_{FL}$. However, for opposite $H_{FL}/H_{DL}$ sign, domain wall propagation is hindered and the switching critical current largely increases.

## 10.3 . Submicronic nanopillars fabrication using e-beam lithography

In chapters 6, 8 and 9, we have employed second-harmonic SOT measurement technique to characterize the magnetic and spin-transport properties arising from Co|Al interfaces. Building on this, we aim to compare the efficiency of SOT-driven magnetization switching across our various metallic structures. In particular, a key challenge in studying the magnetization switching properties in nanopillars is to clearly identify and benchmark the dominant physical mechanisms (such as magnetic torques) against theoretical models.

To this purpose, we have patterned our multilayers into pillars of an ultrathin magnetic element deposited onto a SOT track as represented in figure 10.2, equivalent to the SOT-MRAM geometry. For that, we use the e-beam lithography and ion beam etching. The first step consists in patterning 500 nm wide Hall crosses of the full metallic stack. Then, in a second e-beam lithography step, we define an ellipse at the center of this cross and etched the surrounding area of the cross down to the exact 8 nm thick bottom Pt layer. This etching step is monitored through the secondary ion mass spectrometer (SIMS) available in our etching system. The resulting device is then observed with Scanning Electron Microscopy (SEM) as shown in figure 10.2 **a**).

## 10.4 . Magnetization switching experiment protocol

Among the two Hall cross arms, one is used as a conduction line to apply electrical pulses while the other allows the acquisition of the transverse resistance $R_{xy}$ of the pillar. In this

manner, we track the normal component of the magnetization through AHE. For each sample, our investigation consists in the quantitative evaluation of the critical switching current as a function of a "writing" electrical pulse width. The protocol we have adopted is thus the following :

1. Saturate the magnetization along a given direction perpendicular to the sample's plane (either $\pm z$) by the application of a magnetic field $H_z = 6400$ Oe.
2. Apply a magnetic field $H_x$ parallel to the "current injection" arm of the Hall cross along the applied current direction.
3. Apply a "writing" pulse electric current of a given amplitude and width along the same "current injection" arm of the Hall cross.
4. Apply an electric current "reading" pulse of typically 1 ms and 100 µA intensity to probe the transverse AHE resistance $R_{xy}$ of the pillar.
5. Steps 3 and 4 are repeated varying the "writing" pulse amplitude. We typically perform a cycle where the first "writing" pulse has a small amplitude. It is then increased up to a maximum value before being decreased down to the opposite of this maximum value in the negative amplitudes. We conclude a full cycle by applying pulses of increasing amplitude back to 0. (An experimental cycle is typically described in figure 10.3 **c**).

These experiments use a combination of quasi-static currents (with pulse duration around 1 ms, referred to as the "reading" pulse) and RF currents (or 'writing' pulses, which can be as short as a few tens of nanoseconds). Consequently, the measurement setup includes a bias-T to combine the two current sources along with an oscilloscope to probe the pulse shape (the circuit is represented in figure 10.3 **a**).

For each studied sample, we verify that reversing the in-plane magnetic field $H_x$ leads to a reversal in the polarity of the magnetization switching cycle (as shown in figure 10.3 **d**). This behavior confirms that the switching process is primarily governed by the SOT mechanism.

From one experimental cycle of a given "writing" pulse duration, we extract the critical switching current as the minimal "writing" pulse amplitude after which $R_{xy} > 0.4$ R$_{AHE}$ for a switching from "down" to "up" states or $R_{xy} < -0.4$ R$_{AHE}$ for a switching from "up" to "down" states (the scheme is represented in figure 10.4 **a**). Assuming that the magnetic configuration within the pillar consists solely of 'up' and 'down' domains, this criterion corresponds to 70 % of the pillar's total magnetization having switched. Red dots in figure 10.4 **b**) represent the critical switching currents extracted from one experimental realization.

## 10.5 . Benchmarking the critical switching currents

As described in section 10.3, we have fabricated small dots on four different metallic stacks, respectively : Ta(5)|Pt(8)|Co(0.9)|Al(1.4)|Pt(3),

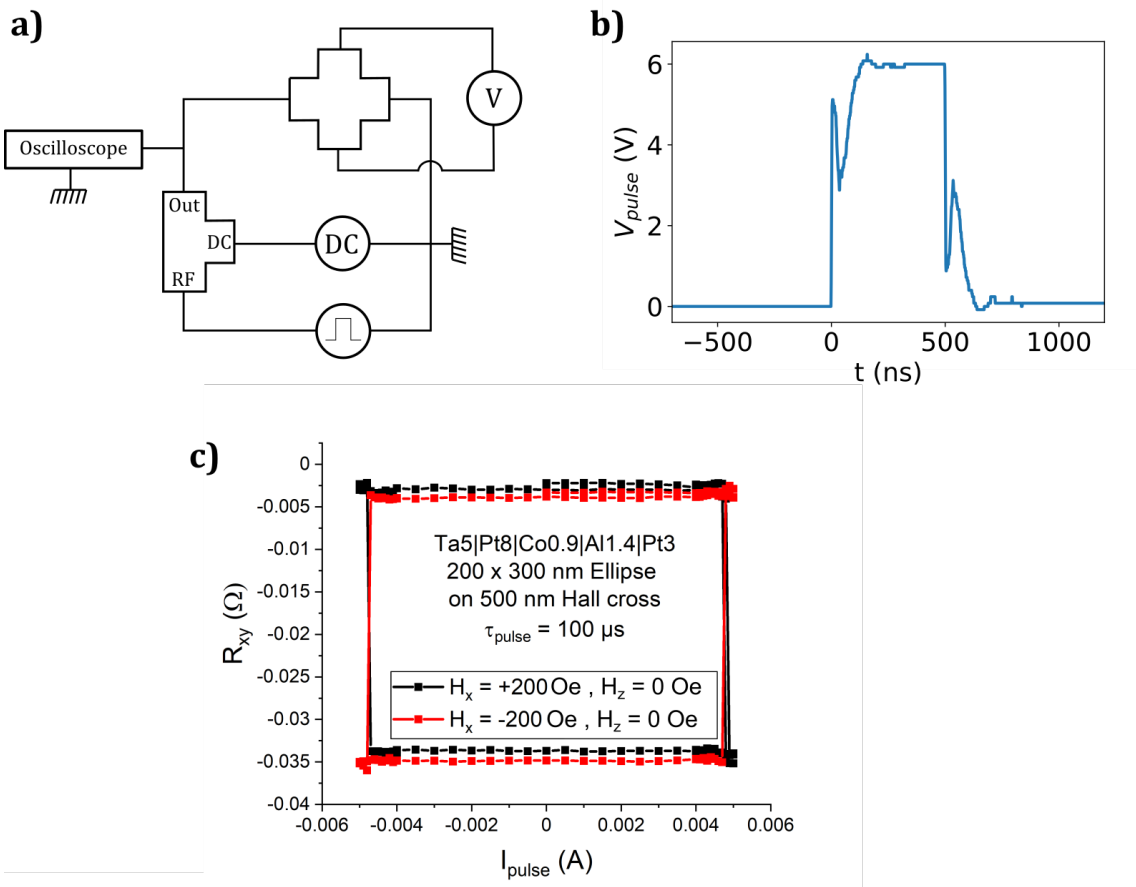


Figure 10.3 – **a**) Scheme of the setup for the application of the electrical pulses to the samples and the measurement of the magnetization state through $R_{xy}$. **b**) A typical 500 ns width electrical pulse measured by the oscilloscope. **c**) Magnetization switching cycles obtained for two opposite in-plane magnetic field $H_x$ and o perpendicular field $H_z$.

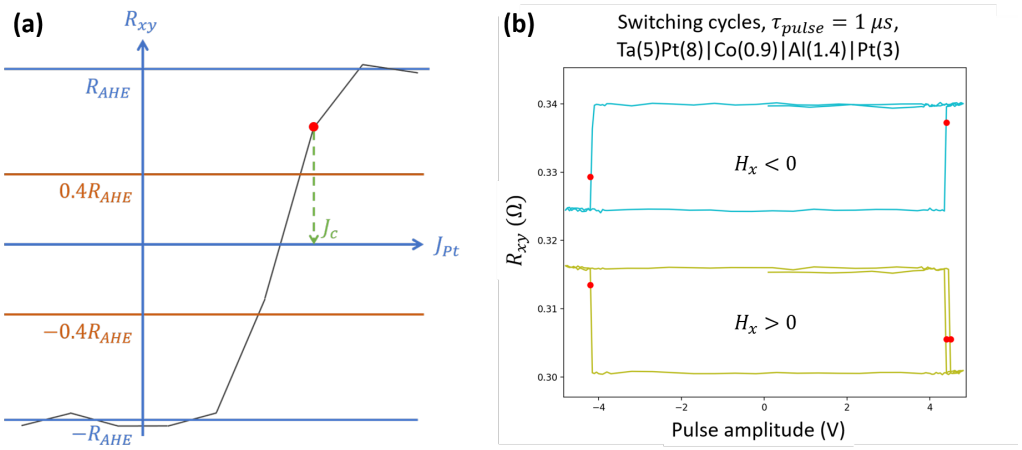


Figure 10.4 – **a**) Estimation of the characteristic critical switching currents from a given switching cycle. **b**) Outcome on two experimental cycles acquired at room temperature. $H_x = \pm 6.3$ kOe.

Ta(5)|Pt(8)|Co(0.9)|Al(3)|Pt(3) Co|Al based samples differing by their Al thickness, Ta(5)|Pt(8)|Co(0.3)|CoFeB(0.8)|Co(0.2)|Al(1.4)|Pt(3) sample comprising CoFeB characterized by a reduced PMA compared to Co and Ta(5)|Pt(8)|Co(0.9)|Pt(3) reference sample.

### 10.5.1 . Impact of the fabrication onto the material properties

During the nanopillar fabrication process (Figure 10.2), which involves two electron beam lithography steps, we observed that the procedure has a measurable influence on the magnetic anisotropy of the samples. As shown in figure 10.5, PMA is moderately reduced following the e-beam processing. For instance,in the (Ta(5)|Pt(8)|Co(0.9)|Al(3)|Pt(3)) structure, the effective anisotropy field $H_k^{eff}$, previously measured at 1.7 T in UV lithography samples, was found to decrease to $H_k^{eff}$=1.4 T after nanopillar patterning. Similar trends were observed across other sample compositions, with $H_k^{eff}$ values measured at 1.1 T for Ta(5)|Pt(8)|Co(0.9)|Al(1.4)|Pt(3), 0.5 T for Ta(5)|Pt(8)|Co(0.9)|Pt(3) and 0.16 T for Ta(5)|Pt(8)|Co(0.3)|CoFeB(0.8)|Co(0.2)|Al(3)|Pt(3).

### 10.5.2 . 100 µs-long pulse width

Figure 10.6 displays the switching cycles obtained at room temperature with 100 µs long pulses and for a $H_x = 200$ Oe in-plane magnetic field for the four different samples. In figure 10.6 **a**), we report the switching cycles for two samples, namely Pt|$\mathbf{FM}$|Al(3 nm)|Pt where $\mathbf{FM}$ denotes either for Co(0.9 nm) or the hybrid ferromagnetic layer Co(0.3 nm)|CoFeB(0.8 nm)|Co(0.2 nm). Notably, the sample incorporating the $Co_{40}Fe_{40}B_{20}$ ferromagnetic layer exhibits the lowest critical current. This enhanced switching efficiency is primarily attributed to its significantly reduced magnetic anisotropy, combined with a damping-like torque comparable in magnitude to that observed in Pt|Co|Al structures.

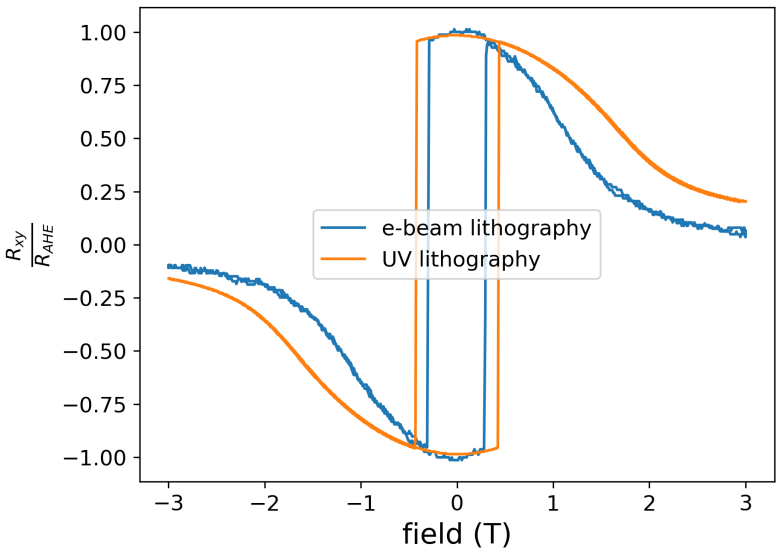


Figure 10.5 – Transverse rescaled by $R_{AHE}$ vs. the applied magnetic field in the sample plane for two samples. Both are made from Ta(5)|Pt(8)|Co(0.9)|Al(3)|Pt(3) metallic structure. One (in orange) was patterned in Hall bars through UV lithography. The other was fabricated into nanopillars via electron beam lithography.

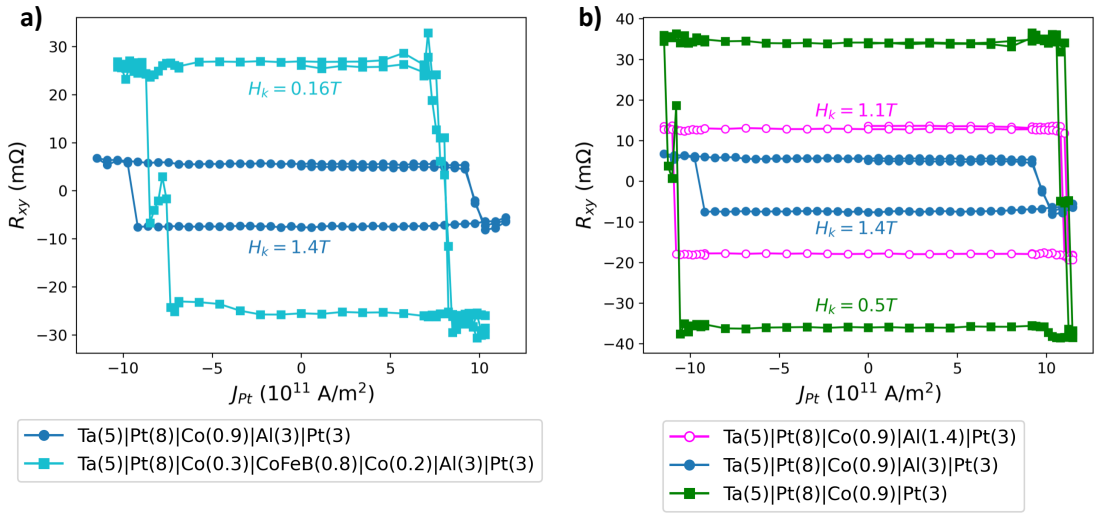


Figure 10.6 – Switching cycles obtained for 100 µs long pulses in varying metallic structures patterned as nanopillars. An in-plane field $H_x = 200$ Oe is applied. **a**) Samples Pt|$\mathbf{FM}$|Al(3 nm)|Pt where $\mathbf{FM}$ = Co(0.9 nm) and Co(0.3 nm)|CoFeB(0.8 nm)|Co(0.2 nm). **b**) Samples having the same magnetic layer Co(0.9 nm), with either 3 nm Al grown on top, 1.4 nm Al, or no Al and directly the 3 nm Pt capping.

In figure 10.6 **b**), we display the 100 $\mu$s switching cycles for the samples constituted of the same Co(0.9 nm) ferromagnetic layer. The sample with the lowest critical current is Ta(5)|Pt(8)|Co(0.9)|Al(3)|Pt(3) integrating the 3 nm Al layer, despite possessing the largest magnetic anisotropy (1.4 T) of the present series : $J_{Pt} = 10 \pm 0.5\ 10^{11} A/m^2$. This critical current is lower than for the sample containing 1.4 nm of Al on top of Co ($J_{Pt} = 11 \pm 0.510^{11} A/m^2$).

Finally, the two samples, Ta(5)|Pt(8)|Co(0.9)|Al(1.4)|Pt(3) and the reference Ta(5)|Pt(8)|Co(0.9)|Pt(3), exhibit similar critical current density for magnetization switching. However, since the sample with Al layer has about twice the anisotropy of the reference sample, this comparison provides further evidence that incorporating Al can significantly reduce the critical current required for switching. In this case, this improvement is attributed to the suppression of the partial compensation of SOT originating from the 3 nm capping Pt as well as the emergence of OREE with 1.4 nm Al. Despite the higher magnetic anisotropy, the reduced critical current highlights the beneficial role of the Co|Al interface in enhancing SOT efficiency, leading to improved energy performance in magnetization switching.

### 10.5.3 . Orbital-assisted switching at shorter pulse duration

The experiments presented in the previous section were performed using relatively long pulses (100 µs). To better understand the specific influence of the orbital related effects on magnetization switching under conditions relevant to SOT-MRAM applications, we extended our investigation to shorter pulse duration, down to the 50 ns range.

As expected, reducing the pulse width necessitated higher pulse amplitudes to reach the switching threshold, consistent with previous observations [Garello et al., 2014]. However, such high amplitudes can pose a risk of device degradation. To avoid this and keep current amplitudes within a moderate range, we applied a relatively strong in-plane magnetic field (6 kOe), thereby facilitating the switching process without compromising device integrity.

In figure 10.7, we present the switching cycles for Ta(5)|Pt(8)|Co(0.9)|Al(1.4)|Pt(3) and Ta(5)|Pt(8)|Co(0.9)|Al(3)|Pt(3) samples under 500 ns pulses. A clear reduction in the required pulse amplitude for magnetization switching is observed in the sample with 3 nm Al compared to the 1.4 nm Al sample. This result is in contrast to what is expected from the difference in magnetic anisotropy between the two samples, and is consistent with the behavior observed under 100 $\mu$s pulses.

We repeated this experiment gradually decreasing the pulse width. In figure 10.8, we show the resulting critical current densities in Pt for switching. The error bars are estimated as the standard deviation of 20 different switching cycles of alternating polarity. Both samples exhibit an increasing trend in critical current with decreasing pulse width. Across all pulse widths, the sample with 3 nm Al consistently requires a lower critical current than the one with 1.4 nm Al. This confirms that SOT generated by OREE at Co|Al interface,

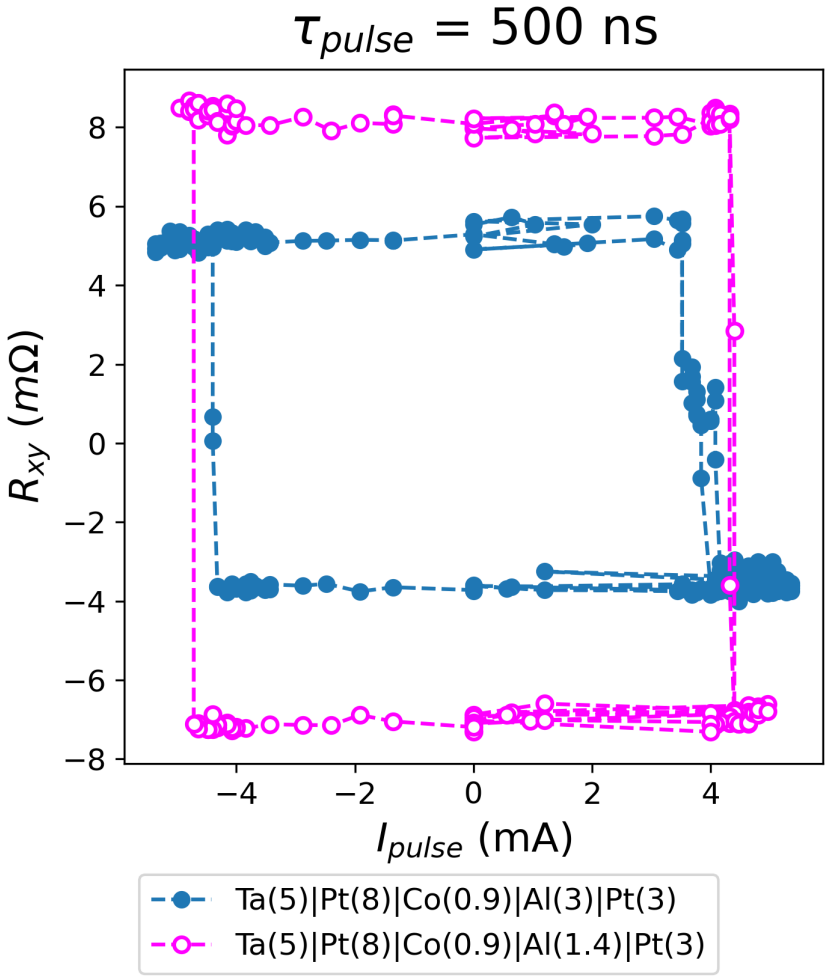


Figure 10.7 – Magnetization switching cycles observed at room temperature for 500 ns long pulses in Ta(5)|Pt(8)|Co(0.9)|Al(1.4)|Pt(3) (open pink dots) and Ta(5)|Pt(8)|Co(0.9)|Al(3)|Pt(3) (filled blue dots). An in plane field $H_x = 6$ kOe is applied.

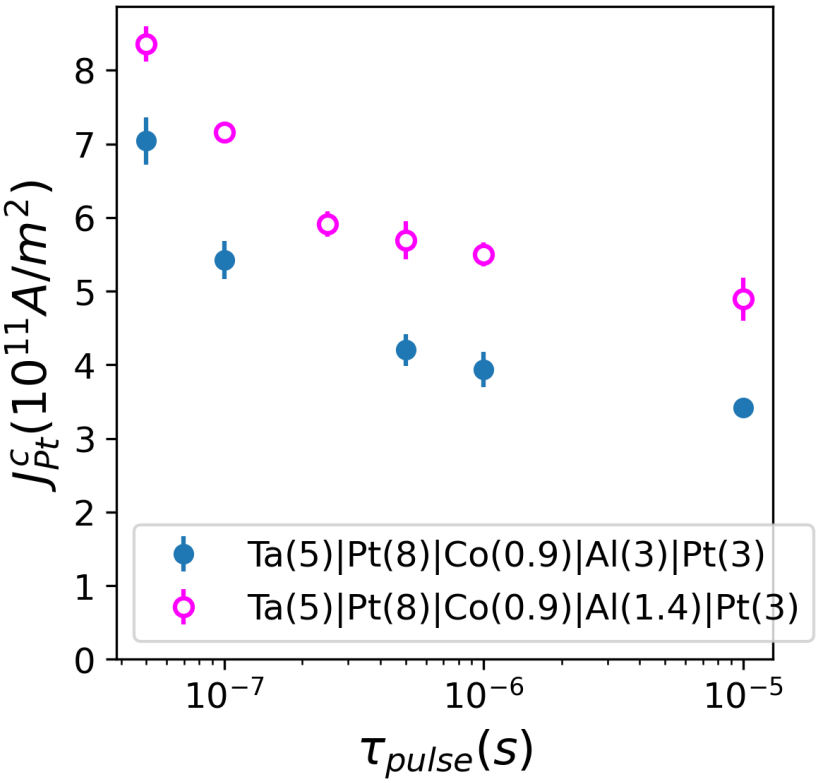


Figure 10.8 – Critical current density in Pt for magnetization switching Vs. the pulse width. An in-plane field $H_x = 6$ kOe is applied. The error bars are based on the standard deviation of 20 switching cycles with alternating sign of the in-plane field.

more than compensates for the increase in the magnetic anisotropy enabling efficient magnetization switching.

### 10.5.4 . Impact of the Rashba torques on the Damping-like field and critical currents

An important conclusion is that the reduction of the critical switching current for Ta(5)|Pt(8)|Co(0.9)|Al(3)|Pt(3) sample cannot be attributed to an increased field-like component of SOT. In fact, this component typically acts against domain wall displacement in presence of DMI. Therefore, the reduced critical current in systems with larger PMA must result from an enhanced damping-like torque. This raises the question : what mechanism is responsible for this enhancement in our Al-based samples ?

The answer lies in the additional damping-like torque component generated by the OREE mechanism at Co|Al interface. While OREE primarily promotes a strong field-like torque due to quantum confinement effects at the Co|Al Rashba states, between field-like and damping-like components becomes possible through leakage currents towards the bulk Co electronic states. These currents are parameterized by the $\mathcal{T}_{il}$ transmission coefficient defined in chapter 6.

From our torque data (f-2f) and from our theoretical modelling, we have performed numerical simulations able to explain the evolution of the two torques components, in particular comparing Ta(5)|Pt(8)|Co(0.9)|Al(1.4)|Pt(3) and Ta(5)|Pt(8)|Co(0.9)|Al(3)|Pt(3) samples. This enables us to quantify the proportions of each SOT component induced by OREE or SHE. We list here after the main assumption and conclusions :

- The spin Hall effect (SHE) arising from the bottom Pt|Co layer is parameterized by a bare spin-angle angle of $\theta_{SHE} = 0.20 \pm 0.02$ and a spin-memory loss coefficient $\delta = 0.4$. Such SHE spin current is also subject to spin-backflow at this interface. The efficiency of the torques calculated for $t_{Co} = 0.9$ nm are respectively $\xi_{DL}^{SHE} = 0.045$ and $\xi_{FL}^{SHE} = 0.03$.
- The Ta(5)|Pt(8)|Co(0.9)|Al(1.4)|Pt(3) sample experiments OREE giving rise to *additional torque* components $\xi_{DL}^{OREE} = 0.03$ and $\xi_{FL}^{OREE} = 0.075$. The Field-like torque (FLT) by OREE then represents 70% of this additional OREE torque (DLT represents 30%) showing the major role of REE to generate the Field-like torque component. This ratio is parameterized by the $T_{iL} \simeq 0.2$ transmission coefficient (coupling) from the Rashba virtual layer to bulk Co states as largely previously emphasized (chapter 6). The OREE represents then 40% of the total DLT and 70% of the total FLT.
- The Ta(5)|Pt(8)|Co(0.9)|Al(3)|Pt(3) sample experiments OREE giving rise to additional torque components $\zeta_{DL}^{OREE} = 0.07$ and $\xi_{FL}^{OREE} = 0.21$, still compared to SHE. The Field-like torque by OREE then represents 75% of this additional OREE torque (DLT is only 25%). This ratio is parameterized by a coupling $T_{iL} \simeq 0.15$ (transmission coefficient) from the Rashba to bulk Co states.
- Those calculations reproduce then well the amplitude of the experimental

torques reported on the previous chapter 6. The final conclusion is that, Ta(5)|Pt(8)|Co(0.9)|Al(1.4)|Pt(3) and Ta(5)|Pt(8)|Co(0.9)|Al(3)|Pt(3) samples, the total DLT efficiency increases from $\xi_{DL} = 0.075$ to $\xi_{DL} = 0.12$ whereas for the FLT , the increase goes from $\xi_{FL} = 0.11$ to $\xi_{FL} = 0.23$.

The reduced critical switching current observed in the Co|Al sample can thus be attributed to the ability of the OREE to enhance the damping-like component of the spin–orbit torque. While OREE is typically associated with a dominant field-like torque, our switching experiments demonstrate its effectiveness as a powerful tool for probing the damping-like torque and, more broadly, for torque metrology. Table 10.1 summarizes the measured values and relative contributions of both torque efficiencies, $\xi_{FL}$ and $\xi_{DL}$ efficiencies for the two samples.

| | $\xi_{FL}$ | | | $\xi_{DL}$ | | |
|---|---|---|---|---|---|---|
| Ta(5)\|Pt(8)\|Co(0.9)\|Al(1.4)\|Pt(3) | SHE | OREE | total | SHE | OREE | total |
| | 0.03 | 0.075 | 0.105 | 0.045 | 0.03 | 0.075 |
| | 29 % | 71 % | 100 % | 56 % | 44 % | 100 % |
| Ta(5)\|Pt(8)\|Co(0.9)\|Al(3)\|Pt(3) | SHE | OREE | total | SHE | OREE | total |
| | 0.03 | 0.21 | 0.24 | 0.045 | 0.07 | 0.115 |
| | 13 % | 87 % | 100 % | 39 % | 61 % | 100 % |

Table 10.1 – Values and relative contributions of OREE and Pt SHE in both torque $\xi_{FL}$ and $\xi_{DL}$ efficiencies for the two samples. For instance, in Ta(5)|Pt(8)|Co(0.9)|Al(3)|Pt(3), SHE induces 0.03 field like efficiency and OREE 0.21. OREE thus induces 87 % of the field like torque.

## 10.6 . Conclusion

Using electron beam lithography, we patterned the samples into nanopillars to emulate the configuration of a SOT MRAM free layer. We then compared the critical switching currents for the various metallic multilayers that we investigated in my PhD. Due to its lower anisotropy compared to the other samples, the sample with a CoFeB magnetic layer exhibits significantly lower critical current. In contrast, the Co-based samples with a Co|Al interface demonstrate enhanced switching efficiency despite higher anisotropy. By comparing two such Co|Al samples under pulse widths as short as 50 ns, we confirm that the OREE mechanism is responsible for the observed reduction in critical switching current.

This result is not immediately expected from our SOT analysis. While we have shown that the OREE primarily enhances the field-like torque component, theoretical models of magnetization switching generally indicate that this component contributes less to switching efficiency and can even be detrimental. Nevertheless, as discussed at the end of this chapter, our results reveal that OREE also leads to a significant enhancement of the damping-like torque in our samples, which accounts for the improved switching performance.

# 11 - Conclusions & perspectives

## 11.1 . Conclusion

The main objective of my PhD has been to thoroughly investigate the peculiar magnetic torque properties of Co|Al metallic interface, notably related to the contribution of orbital angular momentum, and to evaluate how much it could help to reduce the energy cost of the writing operation in a MRAM bit. Our initial interest in Co|Al system stems from an unexpectedly large PMA in samples in which this interface is fully metallic, compared to the seminal Co|AlOx surface anisotropy. Our main experimental tool is SOT metrometry, enabling us, through the precise measurement of the damping-like and field-like SOT components, to conduct rich comparisons from sample to sample.

Strikingly, we discover large SOT arising at Co|Al interface, notably for the field like geometry. To gain further insight on the microscopic mechanisms at play, we model spin dependent transport and resulting SOT inside our multilayers using a semiclassical framework parameterized by complex diffusion lengths representing precession around the magnetization vector. We fit this model as close as possible to our fabricated samples considering transport parameters extracted experimentally from AHE measurements and demonstrate then the occurrence of a Rashba effect at Co|Al interface.

To understand better the origin of this Rashba effect, and in the light of our semi-classical model fitting, we compare our results to recent first principles calculations of Co|Al done in the lab. Setting these DFT calculations with different assumptions, we find that they all converge to showing an orbital angular momentum locking at Co|Al interface electronic states. This enables us to demonstrate the emergence of a strong orbital Rashba Edelstein effect (OREE) at Co|Al. We then apply linear response theory to estimate the orbital torques on the magnetization induced by this OREE conversion mechanism. One of the important result of my PhD is that the outcome is in close agreement with our experimental data and is comparable in amplitude to the expected SOT induced by Pt through SHE.

Building on our understanding of the Co|Al interface, we introduce an ultrathin Pt layer between Co and Al to deliberately modify the interfacial properties. With these experiments, we aim at probing how OREE is affected by enhanced SOC electron scattering. Measuring SOT in those samples, we clearly see that both damping-like and field-like components drop when as thin as 0.25 nm Pt is inserted. We can reproduce this behavior with our DFT model. The fact that the addition of Pt—despite increasing the overall SOC—suppresses the increase of SOT highlights the unique interfacial character of the OREE in the Co|Al system.

To explore materials more suitable for integration into SOT-MRAM devices, we further modify our multilayer stacks by replacing pure Co by $Co_{40}Fe_{40}B_{20}$. In addition to being more compatible with industrial applications, this alloy exhibits reduced perpendicular magnetic anisotropy (PMA). CoFeB alloys are, in fact, among the most widely adopted materials for magnetic tunnel junction (MTJ) fabrication due to their favorable properties. Our measurements reveal that the surface anisotropy in Pt|CoFeB|Al is significantly lower

than in Pt|Co|Al, to the extent that PMA is no longer observed in these samples. They also indicate that OREE at CoFeB|Al is strongly reduced as far as Co species is replaced by Fe atoms. We then fabricate samples with an ultrathin pure Co layer inserted at CoFeB interface. This modification partially restores PMA, although its magnitude remains lower than in pure Co|Al systems. Furthermore, our transport model reveals the emergence of Rashba-type interaction in this samples series. Overall, from this study, we are able to tune the PMA of our magnetic multilayers while preserving a strong SOT. It represents an important step toward optimizing materials for SOT-driven magnetization switching.

Provided all these experimental and theoretical insights, we compare the efficiency of magnetization switching for different series of samples. As anticipated, the sample comprising CoFeB reduced PMA switches with the lowest critical current. Among the other samples investigated, we find that Co|Al OREE reduces critical currents for pulse widths comprised between 50 ns and 100 $\mu$s. This occurs despite an increase in PMA and a dominant enhancement of the field-like SOT component over the damping-like one.

It is worth recalling that my PhD work was carried out within the framework of the PEPR Electronics program and was the first to receive funding under this initiative. One of the goals of this support was to demonstrate that spintronic approaches—based on emerging and fundamental physical phenomena—can offer concrete prospects for reducing the energy cost of writing operations in next-generation spintronic devices.

Through the studies conducted and the obtained results, particularly on the role of orbital effects and the fine engineering of magnetic interfaces, I hope to have convinced that this PhD has contributed significant advances at the state of the art. These results align closely with the ambitions of the EMCOM project from PEPR Electronics, which aims to establish spintronic solutions as a lasting part of national strategies in microelectronics.

## 11.2 . Perspectives

In the following, I outline several perspectives stemming from my PhD work, aimed at deepening our understanding of orbital- and interface-related effects in spintronic materials, with the goal of further reducing the current densities required for magnetization switching in SOT-MTJ devices. An important open question concerns the ultimate timescale over which the SOT enhancement observed in this study remains effective. Lastly, a promising avenue for future research lies in the post-growth engineering of thin film properties, offering additional flexibility for device optimization.

### 11.2.1 . Toward ultrafast dynamics assisted by orbital torques?

In the prolongation of the previous chapter dealing with the magnetization switching in the ns timescale, ultrafast switching and magnetization control up to the THz frequency (picosecond characteristic time for switching) is a key challenge to bring spintronics into high-speed communication devices. This is an opportunity of the SOT-MRAM device since the thin free ferromagnetic layer may be subject to fast dynamics via coupling to sub-

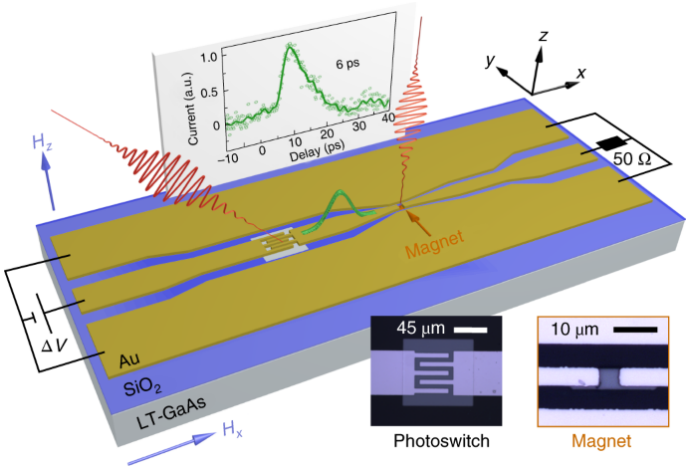


Figure 11.1 – Scheme of the picosecond pulse circuit. We note the Auston switch on which is shone a trigger optical pulse as well as the magnetic element composed of the metallic structure under study, whose magnetization is probed optically. The plot in the back reproduces the time profile of the electrical current pulse. *From Ref. [Jhuria et al., 2020].*

picosecond spin-currents. The present section reports briefly on the preliminary results of a collaboration with Institut Jean Lamour team in Nancy (IJL). This type of experiment will improve our understanding of OREE by probing magnetization response in the ultrafast regime. At the same time, the development of this experiment itself will benefit from samples having larger field-like torque than damping-like, offering possibilities to tune SOT.

### Experiment principle of picosecond switching experiments

IJL team developed a setup to probe ultrafast SOT induced magnetization switching. Ultrashort pulses of a few picoseconds are generated by shining a photoconductive Auston switch with a femtosecond laser. The amplitude of the electrical pulse flowing through the magnetic sample is adjusted via the voltage $\Delta V$ figure 11.1. The magnetic element magnetization state is probed via time resolved magneto-optical Kerr effect (MOKE) through a pump-probe process. The setup is extensively described in [Jhuria et al., 2020].

This experiment is a powerful framework to investigate ultrafast magnetization response to an electric pulse. When an in plane magnetic field is applied, magnetization switching occurs for sufficient bias voltage. Without this in plane field, or with reduced biased voltage, full switching does not occur but the electrical pulse triggers magnetization precession or oscillations.

Combined with micromagnetic simulation, this experiment gives another quantitative insight into current induced torques. The model developed by Nancy team includes thermal induced demagnetization, SOT as well as torques due to thermal anisotropy fluctuation. The micromagnetic simulation can then be fitted to the measured oscillations to estimate

the different torques strengths.

## 11.3 . Materials engineering through film irradiation

### Light ions irradiation to tune magnetic properties

As anticipated, the results obtained during this PhD on SOT-assisted switching—whether or not assisted by orbital contributions—have underscored the critical role of the magnetic layer properties in governing this effect. It is therefore of great interest to explore additional methods for tuning these properties, even after the material design and sample growth are complete. To this end, we conducted a preliminary study on the use of light ion irradiation as a post-growth modification technique for our metallic multilayers. This method, carried out in collaboration with Yanis Sassi, Noël Montblanc, and Dafiné Ravelosona from Spin Ion Technologies, has proven to be a powerful tool for tailoring the magnetic properties of thin films.

Using ion energies in the range of 5 to 150 keV, irradiation can alter structural parameters such as chemical composition, crystallinity, and grain morphology. One of the key advantages of this approach is its ability to decouple modifications of magnetic properties from changes in surface topology. Moreover, ion irradiation can be applied locally with spatial resolutions down to 50 nm, allowing for selective tuning of magnetic behavior without affecting neighboring regions. A comprehensive review of the potential of light ion irradiation for magnetic materials engineering can be found in [Fassbender et al., 2004].

#### 11.3.1 . Preliminary results on Co|Al

Light ion irradiation has been performed on our Ta(5 nm)|Pt(8 nm)|Co(0.9 nm)|Al(3 nm)|Pt(3 nm) sample with increasing fluence (energy irradiated per surface unit). We display the $M_s$ and $H_k^{eff}$ that we measured in those samples in figure 11.2. The blue dot is a reference sample without irradiation. The orange dots are irradiated samples subjected to increasing irradiation fluence. Sample "a" underwent the smallest irradiation fluence while sample "h" the largest.

In figure 11.2 **a**), we show the saturation magnetization in the irradiated samples. While $M_s$ appears to be relatively insensitive to irradiation fluence, it exhibits a significant reduction between the non-irradiated sample ($M_s = 1.18$ MA/m) and the irradiated ones ($M_s \simeq 0.78$ MA/m). This $M_s$ degradation may arise from a loss of Co structural quality or irradiation induced intermixing.

In Figure 11.2 **b**), we display the anisotropy effective fields measured in these samples. All samples still possess PMA but $H_k^{eff}$ amplitude plummets as the irradiation fluence increases. Reference sample has an anisotropy effective field of 1.7 T while the most irradiated sample exhibits $H_k^{eff} = 0.3$ T. This decline in anisotropy suggests that interface modifications might have occurred. If these samples maintain large SOT, it opens opportunities to enhance the efficiency of SOT-driven magnetization switching in combination

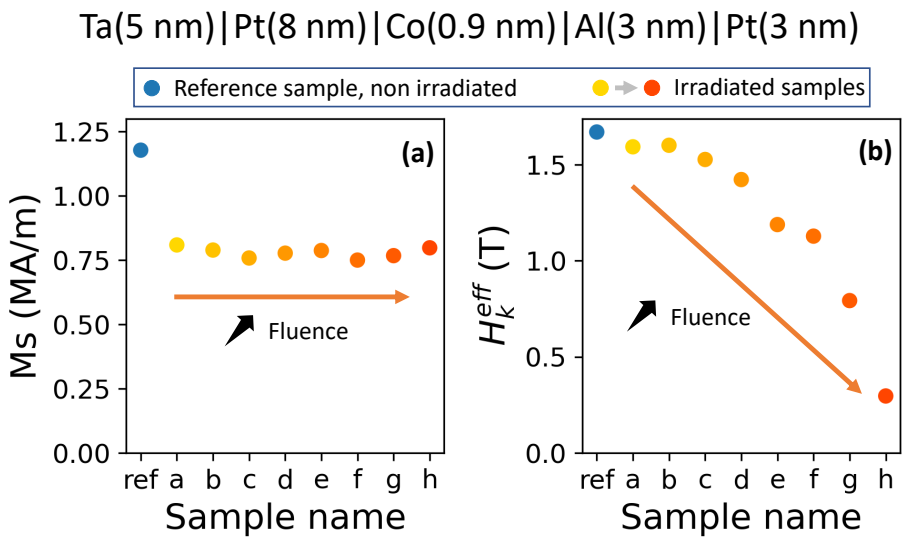


Figure 11.2 – **(a)** Saturation magnetization measured via room temperature SQUID in reference sample "ref" Ta(5 nm)|Pt(8 nm)|Co(0.9 nm)|Al(3 nm)|Pt(3 nm) (blue dots) and samples "a" to "h" which were exposed to light ions irradiation of increasing fluence (yellow and orange dots). **(b)** $H_k^{eff}$ effective fields obtained in the same samples during the SQUID measurements.

to torque enhancement at Co|Al interfaces. SOT characterization of irradiated films will soon shed light on the possibilities offered by light ion irradiation.

# Bibliographie


[Ajejas et al., 2022] Ajejas, F., Sassi, Y., Legrand, W., Collin, S., Peña Garcia, J., Thiaville, A., Pizzini, S., Reyren, N., Cros, V., and Fert, A. (2022). Interfacial potential gradient modulates dzyaloshinskii-moriya interaction in pt/co/metal multilayers. *Phys. Rev. Mater.*, 6 :L071401.

[Albert et al., 2000] Albert, F., Katine, J., Buhrman, R., and Ralph, D. (2000). Spin-polarized current switching of a co thin film nanomagnet. *Applied Physics Letters*, 77(23) :3809–3811.

[Amin and Stiles, 2016] Amin, V. P. and Stiles, M. D. (2016). Spin transport at interfaces with spin-orbit coupling : Phenomenology. *Phys. Rev. B*, 94 :104420.

[An et al., 2016] An, H., Kageyama, Y., Kanno, Y., Enishi, N., and Ando, K. (2016). Spin–torque generator engineered by natural oxidation of cu. *Nature communications*, 7(1) :13069.

[Ando et al., 2008] Ando, K., Takahashi, S., Harii, K., Sasage, K., Ieda, J., Maekawa, S., and Saitoh, E. (2008). Electric manipulation of spin relaxation using the spin hall effect. *Phys. Rev. Lett.*, 101 :036601.

[Ast et al., 2007] Ast, C. R., Henk, J., Ernst, A., Moreschini, L., Falub, M. C., Pacilé, D., Bruno, P., Kern, K., and Grioni, M. (2007). Giant spin splitting through surface alloying. *Physical Review Letters*, 98(18) :186807.

[Avci et al., 2014] Avci, C. O., Garello, K., Gabureac, M., Ghosh, A., Fuhrer, A., Alvarado, S. F., and Gambardella, P. (2014). Interplay of spin-orbit torque and thermoelectric effects in ferromagnet/normal-metal bilayers. *Phys. Rev. B*, 90 :224427.

[Baibich et al., 1988] Baibich, M. N., Broto, J. M., Fert, A., Van Dau, F. N., Petroff, F., Etienne, P., Creuzet, G., Friederich, A., and Chazelas, J. (1988). Giant magnetoresistance of (001)fe/(001)cr magnetic superlattices. *Phys. Rev. Lett.*, 61 :2472–2475.

[Balan et al., 2024] Balan, C., Fischer, J., Gueneau, C., Fassatoui, A., Rueff, J.-P., Ceolin, D., De-Santis, M., Vogel, J., Ranno, L., Béa, H., and Pizzini, S. (2024). Using hard-x-ray photoelectron spectroscopy to measure the oxidation state of gated $\mathrm{Co}/\mathrm{AlO}_x$ interfaces. *Phys. Rev. Appl.*, 21 :064023.

[Barnaś et al., 2005] Barnaś, J., Fert, A., Gmitra, M., Weymann, I., and Dugaev, V. (2005). From giant magnetoresistance to current-induced switching by spin transfer. *Physical Review B—Condensed Matter and Materials Physics*, 72(2) :024426.

[Barnes et al., 2014] Barnes, S. E., Ieda, J., and Maekawa, S. (2014). Rashba spin-orbit anisotropy and the electric field control of magnetism. *Scientific reports*, 4(1) :4105.

[Bauer et al., 2012] Bauer, G. E., Saitoh, E., and Van Wees, B. J. (2012). Spin caloritronics. *Nature materials*, 11(5) :391–399.

[Baumgartner et al., 2017] Baumgartner, M., Garello, K., Mendil, J., Avci, C. O., Grimaldi, E., Murer, C., Feng, J., Gabureac, M., Stamm, C., Acremann, Y., et al. (2017). Spatially and

time-resolved magnetization dynamics driven by spin–orbit torques. *Nature nanotechnology*, 12(10) :980–986.

[Belabbes et al., 2016] Belabbes, A., Bihlmayer, G., Blügel, S., and Manchon, A. (2016). Oxygen-enabled control of dzyaloshinskii-moriya interaction in ultra-thin magnetic films. *Scientific reports*, 6(1) :24634.

[Belmeguenai et al., 2015] Belmeguenai, M., Adam, J.-P., Roussigné, Y., Eimer, S., Devolder, T., Kim, J.-V., Cherif, S. M., Stashkevich, A., and Thiaville, A. (2015). Interfacial dzyaloshinskii-moriya interaction in perpendicularly magnetized pt/co/alo$_x$ ultrathin films measured by brillouin light spectroscopy. *Phys. Rev. B*, 91 :180405.

[Berger, 1996] Berger, L. (1996). Emission of spin waves by a magnetic multilayer traversed by a current. *Physical Review B*, 54(13) :9353.

[Bhatti et al., 2017] Bhatti, S., Sbiaa, R., Hirohata, A., Ohno, H., Fukami, S., and Piramanayagam, S. (2017). Spintronics based random access memory : a review. *Materials today*, 20(9) :530–548.

[Binasch et al., 1989] Binasch, G., Grünberg, P., Saurenbach, F., and Zinn, W. (1989). Enhanced magnetoresistance in layered magnetic structures with antiferromagnetic interlayer exchange. *Phys. Rev. B*, 39 :4828–4830.

[Bony et al., 2025] Bony, B., Krishnia, S., Xu, Y., Collin, S., Fert, A., George, J. M., Viret, M., Cros, V., and Jaffrès, H. (2025). Quantitative analysis of vectorial torques in thin 3d co ferromagnet using orbital-spin conversion.

[Bose et al., 2023] Bose, A., Kammerbauer, F., Gupta, R., Go, D., Mokrousov, Y., Jakob, G., and Kläui, M. (2023). Detection of long-range orbital-hall torques. *Phys. Rev. B*, 107 :134423.

[Brataas et al., 2006] Brataas, A., Bauer, G. E., and Kelly, P. J. (2006). Non-collinear magnetoelectronics. *Physics Reports*, 427(4) :157–255.

[Bruno, 1993] Bruno, P. (1993). *Physical Origins and Theoretical Models of Magnetic Anisotropy*, pages 24.1–24.8. Dederichs, P.H. and Grünberg, P. and Zinns W., Forschungszentrum Jülich.

[Bräuer et al., 2010] Bräuer, G., Szyszka, B., Vergöhl, M., and Bandorf, R. (2010). Magnetron sputtering – milestones of 30 years. *Vacuum*, 84(12) :1354–1359. Selected Papers from the Proceedings of The Tenth International Symposium on Sputtering and Plasma Processes (ISSP 2009), 8th–10th July 2009, Kanazawa, Japan.

[Camley and Barnaś, 1989] Camley, R. E. and Barnaś, J. (1989). Theory of giant magnetoresistance effects in magnetic layered structures with antiferromagnetic coupling. *Phys. Rev. Lett.*, 63 :664–667.

[Campbell et al., 1967] Campbell, I., Fert, A., and Pomeroy, R. (1967). Evidence for two current conduction iron. *Philosophical magazine*, 15(137) :977–983.

[Chappert et al., 2007] Chappert, C., Fert, A., and Van Dau, F. N. (2007). The emergence of spin electronics in data storage. *Nature materials*, 6(11) :813–823.

[Chen et al., 2013] Chen, Y.-T., Takahashi, S., Nakayama, H., Althammer, M., Goennenwein, S. T., Saitoh, E., and Bauer, G. E. (2013). Theory of spin hall magnetoresistance. *Physical Review B—Condensed Matter and Materials Physics*, 87(14) :144411.

[Choi et al., 2017] Choi, J.-G., Lee, J. W., and Park, B.-G. (2017). Spin hall magnetoresistance in heavy-metal/metallic-ferromagnet multilayer structures. *Phys. Rev. B*, 96 :174412.

[Coey, 2010] Coey, J. M. (2010). *Magnetism and magnetic materials*. Cambridge university press.

[Cosset-Cheneau, 2022] Cosset-Cheneau, M. (2022). *Spin to charge current interconversion in Rasha interfaces and topological insulators*. Theses, Université Grenoble Alpes [2020-....].

[Cosset-Chéneau et al., 2021] Cosset-Chéneau, M., Vila, L., Zahnd, G., Gusakova, D., Pham, V. T., Grèzes, C., Waintal, X., Marty, A., Jaffrès, H., and Attané, J.-P. (2021). Measurement of the spin absorption anisotropy in lateral spin valves. *Phys. Rev. Lett.*, 126 :027201.

[Crewe and Wall, 1970] Crewe, A. and Wall, J. (1970). A scanning microscope with 5 Å resolution. *Journal of Molecular Biology*, 48(3) :375–393.

[Dang et al., 2020] Dang, T. H., Barbedienne, Q., To, D. Q., Rongione, E., Reyren, N., Godel, F., Collin, S., George, J. M., and Jaffrès, H. (2020). Anomalous hall effect in $3d/5d$ multilayers mediated by interface scattering and nonlocal spin conductivity. *Phys. Rev. B*, 102 :144405.

[Demidov et al., 2017] Demidov, V., Urazhdin, S., De Loubens, G., Klein, O., Cros, V., Anane, A., and Demokritov, S. (2017). Magnetization oscillations and waves driven by pure spin currents. *Physics Reports*, 673 :1–31.

[Devolder et al., 2013] Devolder, T., Barisic, I., Eimer, S., Garcia, K., Adam, J.-P., Ockert, B., and Ravelosona, D. (2013). Irradiation-induced tailoring of the magnetism of cofeb/mgo ultrathin films. *Journal of applied Physics*, 113(20).

[Devolder et al., 2008] Devolder, T., Hayakawa, J., Ito, K., Takahashi, H., Ikeda, S., Crozat, P., Zerounian, N., Kim, . f. J.-V., Chappert, C., and Ohno, H. (2008). Single-shot time-resolved measurements of nanosecond-scale spin-transfer induced switching : Stochastic versus deterministic aspects. *Physical review letters*, 100(5) :057206.

[Dieny and Chshiev, 2017] Dieny, B. and Chshiev, M. (2017). Perpendicular magnetic anisotropy at transition metal/oxide interfaces and applications. *Rev. Mod. Phys.*, 89 :025008.

[Dieny et al., 1993] Dieny, B., Gurney, B. A., Lambert, S. E., Mauri, D., Parkin, S. S. P., Speriosu, V. S., and Wilhoit, D. R. (1993). Magnetoresistive sensor based on the spin valve effect.

[Dieny et al., 2020] Dieny, B., Prejbeanu, I. L., Garello, K., Gambardella, P., Freitas, P., Lehndorff, R., Raberg, W., Ebels, U., Demokritov, S. O., Akerman, J., et al. (2020). Opportunities and challenges for spintronics in the microelectronics industry. *Nature Electronics*, 3(8) :446–459.

[Ding et al., 2022] Ding, S., Liang, Z., Go, D., Yun, C., Xue, M., Liu, Z., Becker, S., Yang, W., Du, H., Wang, C., et al. (2022). Observation of the orbital rashba-edelstein magnetoresistance. *Physical review letters*, 128(6) :067201.

[Ding et al., 2020] Ding, S., Ross, A., Go, D., Baldrati, L., Ren, Z., Freimuth, F., Becker, S., Kammerbauer, F., Yang, J., Jakob, G., et al. (2020). Harnessing orbital-to-spin conversion of interfacial orbital currents for efficient spin-orbit torques. *Physical review letters*, 125(17) :177201.

[Eid et al., 2002] Eid, K., Portner, D., Borchers, J. A., Loloee, R., Al-Haj Darwish, M., Tsoi, M., Slater, R. D., O'Donovan, K. V., Kurt, H., Pratt, W. P., and Bass, J. (2002). Absence of mean-free-path effects in the current-perpendicular-to-plane magnetoresistance of magnetic multilayers. *Phys. Rev. B*, 65 :054424.

[El Hamdi et al., 2023] El Hamdi, A., Chauleau, J.-Y., Boselli, M., Thibault, C., Gorini, C., Smogunov, A., Barreteau, C., Gariglio, S., Triscone, J.-M., and Viret, M. (2023). Observation of the orbital inverse rashba–edelstein effect. *Nature Physics*, 19(12) :1855–1860.

[Fan et al., 2016] Fan, X., Mellnik, A. R., Wang, W., Reynolds, N., Wang, T., Celik, H., Lorenz, V. O., Ralph, D. C., and Xiao, J. Q. (2016). All-optical vector measurement of spin-orbit-induced torques using both polar and quadratic magneto-optic kerr effects. *Applied Physics Letters*, 109(12).

[Fassbender et al., 2004] Fassbender, J., Ravelosona, D., and Samson, Y. (2004). Tailoring magnetism by light-ion irradiation. *Journal of Physics D : Applied Physics*, 37(16) :R179.

[Fert, 1990] Fert, A. (1990). Magnetic and transport properties of metallic multilayers. In *Metallic Multilayers*, volume 59 of *Materials Science Forum*, pages 439–480. Trans Tech Publications Ltd.

[Fert and Campbell, 1968] Fert, A. and Campbell, I. (1968). Two-current conduction in nickel. *Physical Review Letters*, 21(16) :1190.

[Fert and Campbell, 1971] Fert, A. and Campbell, I. (1971). Transport properties of ferromagnetic transition metals. *Le Journal de Physique Colloques*, 32(C1) :C1–46.

[Fert et al., 2013] Fert, A., Cros, V., and Sampaio, J. (2013). Skyrmions on the track. *Nature nanotechnology*, 8(3) :152–156.

[Fukunaga et al., 2023] Fukunaga, R., Haku, S., Hayashi, H., and Ando, K. (2023). Orbital torque originating from orbital hall effect in zr. *Phys. Rev. Res.*, 5 :023054.

[Gao et al., 2018] Gao, T., Qaiumzadeh, A., An, H., Musha, A., Kageyama, Y., Shi, J., and Ando, K. (2018). Intrinsic spin-orbit torque arising from the berry curvature in a metallic-magnet/cu-oxide interface. *Physical review letters*, 121(1) :017202.

[Garello et al., 2014] Garello, K., Avci, C. O., Miron, I. M., Baumgartner, M., Ghosh, A., Auffret, S., Boulle, O., Gaudin, G., and Gambardella, P. (2014). Ultrafast magnetization switching by spin-orbit torques. *Applied Physics Letters*, 105(21).

[Garello et al., 2013] Garello, K., Miron, I. M., Avci, C. O., Freimuth, F., Mokrousov, Y., Blügel, S., Auffret, S., Boulle, O., Gaudin, G., and Gambardella, P. (2013). Symmetry and magnitude of spin–orbit torques in ferromagnetic heterostructures. *Nature Nanotechnology*, 8(8) :587–593.

[Garello et al., 2018] Garello, K., Yasin, F., Couet, S., Souriau, L., Swerts, J., Rao, S., Van Beek, S., Kim, W., Liu, E., Kundu, S., et al. (2018). Sot-mram 300mm integration for low power

and ultrafast embedded memories. In *2018 IEEE symposium on VLSI Circuits*, pages 81–82. IEEE.

[Givord et al., 1996] Givord, D., McGrath, O., Meyer, C., and Rothman, J. (1996). Interface magnetic anisotropy. *Journal of magnetism and magnetic materials*, 157 :245–249.

[Go et al., 2020] Go, D., Freimuth, F., Hanke, J.-P., Xue, F., Gomonay, O., Lee, K.-J., Blügel, S., Haney, P. M., Lee, H.-W., and Mokrousov, Y. (2020). Theory of current-induced angular momentum transfer dynamics in spin-orbit coupled systems. *Phys. Rev. Res.*, 2 :033401.

[Go et al., 2017] Go, D., Hanke, J.-P., Buhl, P. M., Freimuth, F., Bihlmayer, G., Lee, H.-W., Mokrousov, Y., and Blügel, S. (2017). Toward surface orbitronics : giant orbital magnetism from the orbital rashba effect at the surface of sp-metals. *Scientific reports*, 7(1) :46742.

[Go et al., 2021] Go, D., Jo, D., Gao, T., Ando, K., Blügel, S., Lee, H.-W., and Mokrousov, Y. (2021). Orbital rashba effect in a surface-oxidized cu film. *Phys. Rev. B*, 103 :L121113.

[Go et al., 2018] Go, D., Jo, D., Kim, C., and Lee, H.-W. (2018). Intrinsic spin and orbital hall effects from orbital texture. *Physical Review Letters*, 121(8).

[Go et al., 2023] Go, D., Jo, D., Kim, K.-W., Lee, S., Kang, M.-G., Park, B.-G., Blügel, S., Lee, H.-W., and Mokrousov, Y. (2023). Long-range orbital torque by momentum-space hotspots. *Phys. Rev. Lett.*, 130 :246701.

[Go and Lee, 2020] Go, D. and Lee, H.-W. (2020). Orbital torque : Torque generation by orbital current injection. *Phys. Rev. Res.*, 2 :013177.

[Goering*, 2005] Goering*, E. (2005). X-ray magnetic circular dichroism sum rule correction for the light transition metals. *Philosophical Magazine*, 85(25) :2895–2911.

[Goldberg and Davis, 1954] Goldberg, C. and Davis, R. E. (1954). New galvanomagnetic effect. *Phys. Rev.*, 94 :1121–1125.

[Goldstein et al., 2017] Goldstein, J. I., Newbury, D. E., Michael, J. R., Ritchie, N. W., Scott, J. H. J., and Joy, D. C. (2017). *Scanning electron microscopy and X-ray microanalysis*. springer.

[Grollier et al., 2001] Grollier, J., Cros, V., Hamzic, A., George, J.-M., Jaffrès, H., Fert, A., Faini, G., Ben Youssef, J., and Legall, H. (2001). Spin-polarized current induced switching in co/cu/co pillars. *Applied Physics Letters*, 78(23) :3663–3665.

[Guo et al., 2008] Guo, G. Y., Murakami, S., Chen, T.-W., and Nagaosa, N. (2008). Intrinsic spin hall effect in platinum : First-principles calculations. *Phys. Rev. Lett.*, 100 :096401.

[Gupta et al., 2025] Gupta, R., Bouard, C., Kammerbauer, F., Ledesma-Martin, J. O., Bose, A., Kononenko, I., Martin, S., Usé, P., Jakob, G., Drouard, M., et al. (2025). Harnessing orbital hall effect in spin-orbit torque mram. *Nature Communications*, 16(1) :130.

[Hayashi et al., 2014] Hayashi, M., Kim, J., Yamanouchi, M., and Ohno, H. (2014). Quantitative characterization of the spin-orbit torque using harmonic hall voltage measurements. *Phys. Rev. B*, 89 :144425.

[Heide et al., 2009] Heide, M., Bihlmayer, G., and Blügel, S. (2009). Describing dzyaloshinskii–moriya spirals from first principles. *Physica B : Condensed Matter*, 404(18) :2678–2683.

[Hirohata et al., 2020] Hirohata, A., Yamada, K., Nakatani, Y., Prejbeanu, I.-L., Diény, B., Pirro, P., and Hillebrands, B. (2020). Review on spintronics : Principles and device applications. *Journal of Magnetism and Magnetic Materials*, 509 :166711.

[Huang et al., 2023] Huang, Q., Liu, S., Yang, T., Xie, R., Cai, L., Cao, Q., Lü, W., Bai, L., Tian, Y., and Yan, S. (2023). Current-induced magnetization switching in light-metal-oxide/ferromagnetic-metal bilayers via orbital rashba effect. *Nano Letters*, 23(23) :11323–11329.

[Huang et al., 2008] Huang, S., Chen, T., and Chien, C. (2008). Spin polarization of amorphous cofeb determined by point-contact andreev reflection. *Applied Physics Letters*, 92(24).

[Ikeda et al., 2008] Ikeda, S., Hayakawa, J., Ashizawa, Y., Lee, Y., Miura, K., Hasegawa, H., Tsunoda, M., Matsukura, F., and Ohno, H. (2008). Tunnel magnetoresistance of 604% at 300k by suppression of ta diffusion in cofeb/ mgo/ cofeb pseudo-spin-valves annealed at high temperature. *Applied Physics Letters*, 93(8).

[Jhuria et al., 2020] Jhuria, K., Hohlfeld, J., Pattabi, A., Martin, E., Arriola Córdova, A. Y., Shi, X., Lo Conte, R., Petit-Watelot, S., Rojas-Sanchez, J. C., Malinowski, G., et al. (2020). Spin–orbit torque switching of a ferromagnet with picosecond electrical pulses. *Nature Electronics*, 3(11) :680–686.

[Johansson, 2024] Johansson, A. (2024). Theory of spin and orbital edelstein effects. *Journal of Physics : Condensed Matter*, 36(42) :423002.

[Julliere, 1975] Julliere, M. (1975). Tunneling between ferromagnetic films. *Physics letters A*, 54(3) :225–226.

[Jungwirth et al., 2002] Jungwirth, T., Niu, Q., and MacDonald, A. H. (2002). Anomalous hall effect in ferromagnetic semiconductors. *Phys. Rev. Lett.*, 88 :207208.

[Jungwirth et al., 2014] Jungwirth, T., Wunderlich, J., Novák, V., Olejník, K., Gallagher, B. L., Campion, R. P., Edmonds, K. W., Rushforth, A. W., Ferguson, A. J., and Němec, P. (2014). Spin-dependent phenomena and device concepts explored in (ga,mn)as. *Rev. Mod. Phys.*, 86 :855–896.

[Kanai et al., 2014] Kanai, S., Tsujikawa, M., Miura, Y., Shirai, M., Matsukura, F., and Ohno, H. (2014). Magnetic anisotropy in ta/cofeb/mgo investigated by x-ray magnetic circular dichroism and first-principles calculation. *Applied Physics Letters*, 105(22) :222409.

[Karplus and Luttinger, 1954] Karplus, R. and Luttinger, J. M. (1954). Hall effect in ferromagnetics. *Phys. Rev.*, 95 :1154–1160.

[Kato et al., 2004] Kato, Y. K., Myers, R. C., Gossard, A. C., and Awschalom, D. D. (2004). Observation of the spin hall effect in semiconductors. *science*, 306(5703) :1910–1913.

[Kelly and Arnell, 2000] Kelly, P. and Arnell, R. (2000). Magnetron sputtering : a review of recent developments and applications. *Vacuum*, 56(3) :159–172.

[Khang et al., 2018] Khang, N. H. D., Ueda, Y., and Hai, P. N. (2018). A conductive topological insulator with large spin hall effect for ultralow power spin–orbit torque switching. *Nature materials*, 17(9) :808–813.

[Kim et al., 2021] Kim, J., Go, D., Tsai, H., Jo, D., Kondou, K., Lee, H.-W., and Otani, Y. (2021). Nontrivial torque generation by orbital angular momentum injection in ferromagnetic-metal/cu/al 2 o 3 trilayers. *Physical Review B*, 103(2) :L020407.

[Kim et al., 2023] Kim, J., Uzuhashi, J., Horio, M., Senoo, T., Go, D., Jo, D., Sumi, T., Wada, T., Matsuda, I., Ohkubo, T., Mitani, S., Lee, H.-W., and Otani, Y. (2023). Oxide layer dependent orbital torque efficiency in ferromagnet|Cu|oxide heterostructures. *Phys. Rev. Mater.*, 7 :L111401.

[Kim et al., 2022] Kim, J.-S., Kim, G., Jung, J., Jung, K., Cho, J., Kim, W.-Y., and You, C.-Y. (2022). Control of crystallization and magnetic properties of cofeb by boron concentration. *Scientific Reports*, 12(1) :4549.

[Kim et al., 2017] Kim, N.-H., Han, D.-S., Jung, J., Park, K., Swagten, H. J. M., Kim, J.-S., and You, C.-Y. (2017). Dependence of interfacial dzyaloshinskii–moriya interaction and perpendicular magnetic anisotropy on the thickness of the heavy-metal layer. *Applied Physics Express*, 10(10) :103003.

[Kim et al., 2014] Kim, P., Kang, K. T., Go, G., and Han, J. H. (2014). Nature of orbital and spin rashba coupling in the surface bands of $\mathrm{srtio_3}$ and $\mathrm{ktao_3}$. *Phys. Rev. B*, 90 :205423.

[Kokado et al., 2012] Kokado, S., Tsunoda, M., Harigaya, K., and Sakuma, A. (2012). Anisotropic magnetoresistance effects in fe, co, ni, fe4n, and half-metallic ferromagnet : A systematic analysis. *Journal of the Physical Society of Japan*, 81(2) :024705.

[Kresse and Furthmüller, 1996] Kresse, G. and Furthmüller, J. (1996). Efficient iterative schemes for ab initio total-energy calculations using a plane-wave basis set. *Phys. Rev. B*, 54 :11169–11186.

[Kresse and Joubert, 1999] Kresse, G. and Joubert, D. (1999). From ultrasoft pseudopotentials to the projector augmented-wave method. *Phys. Rev. B*, 59 :1758–1775.

[Krishnia et al., 2024] Krishnia, S., Bony, B., Rongione, E., Vicente-Arche, L. M., Denneulin, T., Pezo, A., Lu, Y., Dunin-Borkowski, R., Collin, S., Fert, A., et al. (2024). Quantifying the large contribution from orbital rashba–edelstein effect to the effective damping-like torque on magnetization. *APL Materials*, 12(5).

[Krishnia et al., 2023] Krishnia, S., Sassi, Y., Ajejas, F., Sebe, N., Reyren, N., Collin, S., Denneulin, T., Kovács, A., Dunin-Borkowski, R. E., Fert, A., George, J.-M., Cros, V., and Jaffrès, H. (2023). Large interfacial rashba interaction generating strong spin–orbit torques in atomically thin metallic heterostructures. *Nano Letters*, 23(15) :6785–6791. PMID : 37524333.

[Krishnia et al., 2025] Krishnia, S., Vojáček, L., Gomes, T. d. C. S. C., Sebe, N., Ibrahim, F., Li, J., Vicente-Arche, L. M., Collin, S., Denneulin, T., Dunin-Borkowski, R. E., Nikolaev, S. A., Ohresser, P., Jaouen, N., Thiaville, A., Fert, A., Jaffrès, H., Chshiev, M., Reyren, N., and Cros, V. (2025). Interfacial spin-orbitronic effects controlled by different oxidation levels at the Co|Al interface. *Phys. Rev. Appl.*, 24 :024055.

[Krizakova et al., 2022] Krizakova, V., Perumkunnil, M., Couet, S., Gambardella, P., and Garello, K. (2022). Spin-orbit torque switching of magnetic tunnel junctions for memory applications. *Journal of Magnetism and Magnetic Materials*, 562 :169692.

[Kuepferling et al., 2023] Kuepferling, M., Casiraghi, A., Soares, G., Durin, G., Garcia-Sanchez, F., Chen, L., Back, C. H., Marrows, C. H., Tacchi, S., and Carlotti, G. (2023). Measuring interfacial dzyaloshinskii-moriya interaction in ultrathin magnetic films. *Rev. Mod. Phys.*, 95 :015003.

[Kurt et al., 2002] Kurt, H., Loloee, R., Eid, K., Pratt Jr, W., and Bass, J. (2002). Spin-memory loss at 4.2 k in sputtered pd and pt and at pd/cu and pt/cu interfaces. *Applied Physics Letters*, 81(25) :4787–4789.

[Landau and Lifchits, 1958] Landau, L. D. and Lifchits, E. M. (1958). *Quantum mechanics, non relativistic theory. Volume 3 of a course of theoretical physics*. Pergamon Press, Oxford.

[Lee et al., 2013] Lee, K.-S., Lee, S.-W., Min, B.-C., and Lee, K.-J. (2013). Threshold current for switching of a perpendicular magnetic layer induced by spin hall effect. *Applied Physics Letters*, 102(11) :112410.

[Lesne et al., 2016] Lesne, E., Fu, Y., Oyarzún, S., Rojas-Sánchez, J. C., Vaz, D., Naganuma, H., Sicoli, G., Attané, J.-P., Jamet, M., Jacquet, E., et al. (2016). Highly efficient and tunable spin-to-charge conversion through rashba coupling at oxide interfaces. *Nature materials*, 15(12) :1261–1266.

[Liang et al., 2014] Liang, S. H., Zhang, T. T., Barate, P., Frougier, J., Vidal, M., Renucci, P., Xu, B., Jaffrès, H., George, J.-M., Devaux, X., Hehn, M., Marie, X., Mangin, S., Yang, H. X., Hallal, A., Chshiev, M., Amand, T., Liu, H. F., Liu, D. P., Han, X. F., Wang, Z. G., and Lu, Y. (2014). Large and robust electrical spin injection into GaAs at zero magnetic field using an ultrathin CoFeB|MgO injector. *Phys. Rev. B*, 90 :085310.

[Liu et al., 2012a] Liu, L., Lee, O., Gudmundsen, T., Ralph, D., and Buhrman, R. (2012a). Current-induced switching of perpendicularly magnetized magnetic layers using spin torque from the spin hall effect. *Physical review letters*, 109(9) :096602.

[Liu et al., 2011] Liu, L., Moriyama, T., Ralph, D. C., and Buhrman, R. A. (2011). Spin-torque ferromagnetic resonance induced by the spin hall effect. *Phys. Rev. Lett.*, 106 :036601.

[Liu et al., 2012b] Liu, L., Pai, C.-F., Li, Y., Tseng, H., Ralph, D., and Buhrman, R. (2012b). Spin-torque switching with the giant spin hall effect of tantalum. *Science*, 336(6081) :555–558.

[Lo Conte et al., 2017] Lo Conte, R., Karnad, G. V., Martinez, E., Lee, K., Kim, N.-H., Han, D.-S., Kim, J.-S., Prenzel, S., Schulz, T., You, C.-Y., et al. (2017). Ferromagnetic layer thickness dependence of the dzyaloshinskii-moriya interaction and spin-orbit torques in pt\co\alox. *AIP Advances*, 7(6).

[Manchon et al., 2008] Manchon, A., Ducruet, C., Lombard, L., Auffret, S., Rodmacq, B., Dieny, B., Pizzini, S., Vogel, J., Uhlíř, V., Hochstrasser, M., et al. (2008). Analysis of oxygen induced anisotropy crossover in pt/co/mox trilayers. *Journal of Applied Physics*, 104(4) :043914.

[Manchon et al., 2019] Manchon, A., Železný, J., Miron, I. M., Jungwirth, T., Sinova, J., Thiaville, A., Garello, K., and Gambardella, P. (2019). Current-induced spin-orbit torques in ferromagnetic and antiferromagnetic systems. *Rev. Mod. Phys.*, 91 :035004.

[Martinez et al., 2015] Martinez, E., Torres, L., Perez, N., Hernandez, M. A., Raposo, V., and Moretti, S. (2015). Universal chiral-triggered magnetization switching in confined nanodots. *Scientific reports*, 5(1) :10156.

[Mellnik et al., 2014] Mellnik, A. R., Lee, J., Richardella, A., Grab, J. L., Mintun, P. J., Fischer, M. H., Vaezi, A., Manchon, A., Kim, E.-A., Samarth, N., et al. (2014). Spin-transfer torque generated by a topological insulator. *Nature*, 511(7510) :449–451.

[Mikuszeit et al., 2015] Mikuszeit, N., Boulle, O., Miron, I. M., Garello, K., Gambardella, P., Gaudin, G., and Buda-Prejbeanu, L. D. (2015). Spin-orbit torque driven chiral magnetization reversal in ultrathin nanostructures. *Physical Review B*, 92(14) :144424.

[Miron et al., 2011] Miron, I. M., Garello, K., Gaudin, G., Zermatten, P.-J., Costache, M. V., Auffret, S., Bandiera, S., Rodmacq, B., Schuhl, A., and Gambardella, P. (2011). Perpendicular switching of a single ferromagnetic layer induced by in-plane current injection. *Nature*, 476(7359) :189–193.

[Mohn, 2006] Mohn, P. (2006). *Magnetism in the solid state : an introduction*. Springer.

[Monkhorst and Pack, 1976] Monkhorst, H. J. and Pack, J. D. (1976). Special points for brillouin-zone integrations. *Phys. Rev. B*, 13 :5188–5192.

[Monso et al., 2002] Monso, S., Rodmacq, B., Auffret, S., Casali, G., Fettar, F., Gilles, B., Dieny, B., and Boyer, P. (2002). Crossover from in-plane to perpendicular anisotropy in pt/cofe/alo x sandwiches as a function of al oxidation : A very accurate control of the oxidation of tunnel barriers. *Applied physics letters*, 80(22) :4157–4159.

[Muller, 2009] Muller, D. A. (2009). Structure and bonding at the atomic scale by scanning transmission electron microscopy. *Nature materials*, 8(4) :263–270.

[Murakami et al., 2003] Murakami, S., Nagaosa, N., and Zhang, S.-C. (2003). Dissipationless quantum spin current at room temperature. *Science*, 301(5638) :1348–1351.

[Néel, 1954] Néel, L. (1954). Anisotropie magnétique superficielle et surstructures d'orientation. *Journal de Physique et le Radium*, 15(4) :225–239.

[Nguyen et al., 2014] Nguyen, H. Y. T., Pratt Jr, W., and Bass, J. (2014). Spin-flipping in pt and at co/pt interfaces. *Journal of magnetism and magnetic materials*, 361 :30–33.

[Niimi and Otani, 2015] Niimi, Y. and Otani, Y. (2015). Reciprocal spin hall effects in conductors with strong spin–orbit coupling : a review. *Reports on progress in physics*, 78(12) :124501.

[Nikolaev et al., 2024] Nikolaev, S. A., Chshiev, M., Ibrahim, F., Krishnia, S., Sebe, N., George, J.-M., Cros, V., Jaffrès, H., and Fert, A. (2024). Large chiral orbital texture and orbital edelstein effect in co/al heterostructure. *Nano Letters*, 24(43) :13465–13472. PMID : 39433297.

[Noël et al., 2020] Noël, P., Trier, F., Vicente Arche, L. M., Bréhin, J., Vaz, D. C., Garcia, V., Fusil, S., Barthélémy, A., Vila, L., Bibes, M., et al. (2020). Non-volatile electric control of spin–charge conversion in a srtio3 rashba system. *Nature*, 580(7804) :483–486.

[Otten, 1991] Otten, M. T. (1991). High-angle annular dark-field imaging on a tem/stem system. *Journal of Electron Microscopy Technique*, 17(2) :221–230.

[Panda et al., 2019] Panda, S., Mondal, S., Sinha, J., Choudhury, S., and Barman, A. (2019). All-optical detection of interfacial spin transparency from spin pumping in $\beta$-ta/cofeb thin films. *Science advances*, 5(4) :eaav7200.

[Park et al., 2014] Park, J., Rowlands, G., Lee, O., Ralph, D., and Buhrman, R. (2014). Macrospin modeling of sub-ns pulse switching of perpendicularly magnetized free layer via spin-orbit torques for cryogenic memory applications. *Applied Physics Letters*, 105(10).

[Park et al., 2013] Park, J.-H., Kim, C. H., Lee, H.-W., and Han, J. H. (2013). Orbital chirality and rashba interaction in magnetic bands. *Phys. Rev. B*, 87 :041301.

[Park et al., 2012] Park, S. R., Han, J., Kim, C., Koh, Y. Y., Kim, C., Lee, H., Choi, H. J., Han, J. H., Lee, K. D., Hur, N. J., et al. (2012). Chiral orbital-angular momentum in the surface states of bi 2 se 3. *Physical Review Letters*, 108(4) :046805.

[Park et al., 2011] Park, S. R., Kim, C. H., Yu, J., Han, J. H., and Kim, C. (2011). Orbital-angular-momentum based origin of rashba-type surface band splitting. *Physical review letters*, 107(15) :156803.

[Parkin et al., 2004] Parkin, S. S., Kaiser, C., Panchula, A., Rice, P. M., Hughes, B., Samant, M., and Yang, S.-H. (2004). Giant tunnelling magnetoresistance at room temperature with mgo (100) tunnel barriers. *Nature materials*, 3(12) :862–867.

[Pauyac et al., 2018] Pauyac, C. O., Chshiev, M., Manchon, A., and Nikolaev, S. A. (2018). Spin hall and spin swapping torques in diffusive ferromagnets. *Phys. Rev. Lett.*, 120 :176802.

[Petersen and Hedegård, 2000] Petersen, L. and Hedegård, P. (2000). A simple tight-binding model of spin–orbit splitting of sp-derived surface states. *Surface science*, 459(1-2) :49–56.

[Petitjean et al., 2012] Petitjean, C., Luc, D., and Waintal, X. (2012). Unified drift-diffusion theory for transverse spin currents in spin valves, domain walls, and other textured magnets. *Phys. Rev. Lett.*, 109 :117204.

[Pezo et al., 2024] Pezo, A., George, J.-M., and Jaffrès, H. (2024). Theory of spin and orbital charge conversion at the surface states of $\mathrm{bi}_{1-x}\mathrm{sb}_x$ topological insulator. *Phys. Rev. Res.*, 6 :043332.

[Pezo et al., 2025] Pezo, A., Sebe, N., Manchon, A., Cros, V., and Jaffrès, H. (2025). Anatomy of torques from orbital rashba textures : the case of co/al interfaces.

[Pi et al., 2010] Pi, U. H., Won Kim, K., Bae, J. Y., Lee, S. C., Cho, Y. J., Kim, K. S., and Seo, S. (2010). Tilting of the spin orientation induced by rashba effect in ferromagnetic metal layer. *Applied Physics Letters*, 97(16).

[Rodmacq et al., 2003] Rodmacq, B., Auffret, S., Dieny, B., Monso, S., and Boyer, P. (2003). Crossovers from in-plane to perpendicular anisotropy in magnetic tunnel junctions as a function of the barrier degree of oxidation. *Journal of Applied Physics*, 93(10) :7513–7515.

[Rojas-Sánchez and Fert, 2019] Rojas-Sánchez, J.-C. and Fert, A. (2019). Compared efficiencies of conversions between charge and spin current by spin-orbit interactions in two- and three-dimensional systems. *Physical Review Applied*, 11(5) :054049.

[Rojas-Sánchez et al., 2014] Rojas-Sánchez, J.-C., Reyren, N., Laczkowski, P., Savero, W., Attané, J.-P., Deranlot, C., Jamet, M., George, J.-M., Vila, L., and Jaffrès, H. (2014). Spin pumping and inverse spin hall effect in platinum : The essential role of spin-memory loss at metallic interfaces. *Phys. Rev. Lett.*, 112 :106602.

[Rousseau et al., 2021] Rousseau, O., Gorini, C., Ibrahim, F., Chauleau, J.-Y., Solignac, A., Hallal, A., Tölle, S., Chshiev, M., and Viret, M. (2021). Spin-charge conversion in ferromagnetic rashba states. *Physical Review B*, 104(13) :134438.

[Rupp, 2022] Rupp, K. (2022). Microprocessor trend data. https://github.com/karlrupp/microprocessor-trend-data.

[Sagasta et al., 2016] Sagasta, E., Omori, Y., Isasa, M., Gradhand, M., Hueso, L. E., Niimi, Y., Otani, Y., and Casanova, F. (2016). Tuning the spin hall effect of pt from the moderately dirty to the superclean regime. *Phys. Rev. B*, 94 :060412.

[Sala and Gambardella, 2022] Sala, G. and Gambardella, P. (2022). Giant orbital hall effect and orbital-to-spin conversion in $3d$, $5d$, and $4f$ metallic heterostructures. *Phys. Rev. Res.*, 4 :033037.

[Salemi et al., 2021] Salemi, L., Berritta, M., and Oppeneer, P. M. (2021). Quantitative comparison of electrically induced spin and orbital polarizations in heavy-metal/$3d$-metal bilayers. *Phys. Rev. Mater.*, 5 :074407.

[Salemi and Oppeneer, 2022] Salemi, L. and Oppeneer, P. M. (2022). First-principles theory of intrinsic spin and orbital hall and nernst effects in metallic monoatomic crystals. *Phys. Rev. Mater.*, 6 :095001.

[Sánchez et al., 2013] Sánchez, J. R., Vila, L., Desfonds, G., Gambarelli, S., Attané, J., De Teresa, J., Magén, C., and Fert, A. (2013). Spin-to-charge conversion using rashba coupling at the interface between non-magnetic materials. *Nature communications*, 4(1) :2944.

[Sangiao et al., 2015] Sangiao, S., De Teresa, J., Morellon, L., Lucas, I., Martínez-Velarte, M. C., and Viret, M. (2015). Control of the spin to charge conversion using the inverse rashba-edelstein effect. *Applied Physics Letters*, 106(17).

[Sharma et al., 2008] Sharma, A., Theodoropoulou, N., Haillard, T., Acharyya, R., Loloee, R., Pratt, W. P., Bass, J., Zhang, J., and Crimp, M. A. (2008). Current-perpendicular-to-plane magnetoresistance of ferromagnetic $f$/Al interfaces ($f$ = Py, co, fe, and $co_{91}fe_9$) and structural studies of co/al and py/al. *Phys. Rev. B*, 77 :224438.

[Shchelushkin and Brataas, 2005] Shchelushkin, R. V. and Brataas, A. (2005). Spin hall effect, hall effect, and spin precession in diffusive normal metals. *Phys. Rev. B*, 72 :073110.

[Silva et al., 2021] Silva, A. S., Sá, S. P., Bunyaev, S. A., Garcia, C., Sola, I. J., Kakazei, G. N., Crespo, H., and Navas, D. (2021). Dynamical behaviour of ultrathin [cofeb (t cofeb)/pd] films with perpendicular magnetic anisotropy. *Scientific Reports*, 11(1) :43.

[Sinova et al., 2004] Sinova, J., Culcer, D., Niu, Q., Sinitsyn, N., Jungwirth, T., and MacDonald, A. H. (2004). Universal intrinsic spin hall effect. *Physical review letters*, 92(12) :126603.

[Sinova et al., 2015] Sinova, J., Valenzuela, S. O., Wunderlich, J., Back, C. H., and Jungwirth, T. (2015). Spin hall effects. *Rev. Mod. Phys.*, 87 :1213–1260.

[Slonczewski, 1996] Slonczewski, J. C. (1996). Current-driven excitation of magnetic multilayers. *Journal of Magnetism and Magnetic Materials*, 159(1-2) :L1–L7.

[Smit, 1955] Smit, J. (1955). The spontaneous hall effect in ferromagnetics i. *Physica*, 21(6-10) :877–887.

[Smit, 1958] Smit, J. (1958). The spontaneous hall effect in ferromagnetics ii. *Physica*, 24(1-5) :39–51.

[Soler et al., 2002] Soler, J. M., Artacho, E., Gale, J. D., García, A., Junquera, J., Ordejón, P., and Sánchez-Portal, D. (2002). The siesta method for ab initio order-n materials simulation. *Journal of Physics : Condensed Matter*, 14(11) :2745.

[Sondheimer, 2001] Sondheimer, E. H. (2001). The mean free path of electrons in metals. *Advances in physics*, 50(6) :499–537.

[Stewart et al., 2003] Stewart, D. A., Butler, W. H., Zhang, X.-G., and Los, V. F. (2003). Interfacial scattering in magnetic multilayers and spin valves. *Phys. Rev. B*, 68 :014433.

[Stiles and Zangwill, 2002] Stiles, M. D. and Zangwill, A. (2002). Anatomy of spin-transfer torque. *Phys. Rev. B*, 66 :014407.

[Strijkers et al., 2001] Strijkers, G. J., Ji, Y., Yang, F. Y., Chien, C. L., and Byers, J. M. (2001). Andreev reflections at metal/superconductor point contacts : Measurement and analysis. *Phys. Rev. B*, 63 :104510.

[Taniguchi et al., 2015] Taniguchi, T., Mitani, S., and Hayashi, M. (2015). Critical current destabilizing perpendicular magnetization by the spin hall effect. *Phys. Rev. B*, 92 :024428.

[Taniguchi et al., 2008] Taniguchi, T., Yakata, S., Imamura, H., and Ando, Y. (2008). Penetration depth of transverse spin current in ferromagnetic metals. *IEEE Transactions on Magnetics*, 44(11) :2636–2639.

[Thiaville et al., 2012] Thiaville, A., Rohart, S., Jué, É., Cros, V., and Fert, A. (2012). Dynamics of dzyaloshinskii domain walls in ultrathin magnetic films. *Europhysics Letters*, 100(5) :57002.

[Tinkham, 2003] Tinkham, M. (2003). *Group theory and quantum mechanics*. Courier Corporation.

[Tsai et al., 2018] Tsai, T.-Y., Chen, T.-Y., Wu, C.-T., Chan, H.-I., and Pai, C.-F. (2018). Spin-orbit torque magnetometry by wide-field magneto-optical kerr effect. *Scientific reports*, 8(1) :5613.

[Tsoi et al., 1998] Tsoi, M., Jansen, A., Bass, J., Chiang, W.-C., Seck, M., Tsoi, V., and Wyder, P. (1998). Excitation of a magnetic multilayer by an electric current. *Physical Review Letters*, 80(19) :4281.

[Valenzuela and Tinkham, 2006] Valenzuela, S. O. and Tinkham, M. (2006). Direct electronic measurement of the spin hall effect. *Nature*, 442(7099) :176–179.

[Valet et al., 2025] Valet, T., Jaffres, H., Cros, V., and Raimondi, R. (2025). Quantum kinetic anatomy of electron angular momenta edge accumulation.

[Weber et al., 2019] Weber, R., Han, D.-S., Boventer, I., Jaiswal, S., Lebrun, R., Jakob, G., and Kläui, M. (2019). Gilbert damping of cofe-alloys. *Journal of Physics D : Applied Physics*, 52(32) :325001.

[Wilhelm et al., 2000] Wilhelm, F., Poulopoulos, P., Ceballos, G., Wende, H., Baberschke, K., Srivastava, P., Benea, D., Ebert, H., Angelakeris, M., Flevaris, N. K., Niarchos, D., Rogalev, A., and Brookes, N. B. (2000). Layer-resolved magnetic moments in $\mathrm{Ni}/\mathrm{Pt}$ multilayers. *Phys. Rev. Lett.*, 85 :413–416.

[Xu et al., 2025] Xu, Y., Bony, B., Krishnia, S., Torrão Victor, R., Collin, S., Fert, A., George, J.-M., Cros, V., and Jaffrès, H. (2025). Alternative harmonic detection approach for quantitative determination of spin and orbital torques. *Applied Physics Letters*, 126(20).

[Yang et al., 2018] Yang, H., Boulle, O., Cros, V., Fert, A., and Chshiev, M. (2018). Controlling dzyaloshinskii-moriya interaction via chirality dependent atomic-layer stacking, insulator capping and electric field. *Scientific reports*, 8(1) :12356.

[Yang et al., 2022] Yang, H., Valenzuela, S. O., Chshiev, M., Couet, S., Dieny, B., Dlubak, B., Fert, A., Garello, K., Jamet, M., Jeong, D.-E., et al. (2022). Two-dimensional materials prospects for non-volatile spintronic memories. *Nature*, 606(7915) :663–673.

[Yao et al., 2025] Yao, Y., Xiao, C., Ning, X., Cai, W., Guo, X., Guo, Z., Yang, K., Xiong, D., Yan, Z., Lu, S., Zhang, H., Cheng, S., Xu, R., Ma, D., Wang, C., Wang, Z., Zhu, D., Cao, K., Liu, H., Manchon, A., and Zhao, W. (2025). Giant orbital torque-driven picosecond switching in magnetic tunnel junctions.

[Yasaka, 2010] Yasaka, M. (2010). X-ray thin-film measurement techniques. *Rigaku J.*, 26 :1–9.

[Yasin et al., 2024] Yasin, F., Palomino, A., Kumar, A., Pica, V., Van Beek, S., Talmelli, G., Nguyen, V., Cosemans, S., Crotti, D., Wostyn, K., Kar, G. S., and Couet, S. (2024). Extremely scaled perpendicular SOT-MRAM array integration on 300mm wafer. In *2024 IEEE Symposium on VLSI Technology and Circuits (VLSI Technology and Circuits)*, pages 1–2.

[Yu et al., 2014] Yu, G., Upadhyaya, P., Fan, Y., Alzate, J. G., Jiang, W., Wong, K. L., Takei, S., Bender, S. A., Chang, L.-T., Jiang, Y., et al. (2014). Switching of perpendicular magnetization by spin–orbit torques in the absence of external magnetic fields. *Nature nanotechnology*, 9(7) :548–554.

[Yuasa et al., 2004] Yuasa, S., Nagahama, T., Fukushima, A., Suzuki, Y., and Ando, K. (2004). Giant room-temperature magnetoresistance in single-crystal fe/mgo/fe magnetic tunnel junctions. *Nature materials*, 3(12) :868–871.

[Zhang et al., 2002] Zhang, S., Levy, P. M., and Fert, A. (2002). Mechanisms of spin-polarized current-driven magnetization switching. *Phys. Rev. Lett.*, 88 :236601.

[Zhang and Butler, 1995] Zhang, X.-G. and Butler, W. H. (1995). Conductivity of metallic films and multilayers. *Phys. Rev. B*, 51 :10085–10103.

[Zhang and Butler, 2004] Zhang, X.-G. and Butler, W. H. (2004). Large magnetoresistance in bcc $\mathrm{Co}|\mathrm{MgO}|\mathrm{Co}$ and $\mathrm{FeCo}|\mathrm{MgO}|\mathrm{FeCo}$ tunnel junctions. *Phys. Rev. B*, 70 :172407.

[Zhu and Zhu, 2007] Zhu, X. and Zhu, J.-G. (2007). Effect of damping constant on magnetic switching in spin torque driven perpendicular mram. *IEEE transactions on magnetics*, 43(6) :2349–2351.